ANALYTICAL STUDIES OF STANDING SHOCKS IN ACCRETION FLOWS AROUND COMPACT OBJECTS

Thesis submitted for the degree of
Doctor of Philosophy (Science)
of the
Jadavpur University

Santabrata Das

Satyendranath Bose National Centre
for Basic Sciences
JD Block, Sector-III, Salt Lake City
Kolkata 700098, INDIA

ANALYTICAL STUDIES OF STANDING SHOCKS IN ACCRETION FLOWS AROUND COMPACT OBJECTS

Thesis submitted for the degree of
Doctor of Philosophy (Science)
of the
Jadavpur University

Santabrata Das
Satyendranath Bose National Centre
for Basic Sciences
JD Block, Sector-III, Salt Lake City
Kolkata 700098, INDIA

CERTIFICATE FROM THE SUPERVISOR

This is to certify that the thesis entitled **"Analytical Studies of Standing Shocks in Accretion Flows Around Compact Objects"**, submitted by Sri **Santabrata Das** who got his name registered on **23.07.01** for the award of Ph.D.(Science) degree of Jadavpur University, absolutely based upon his own work under the supervision of **Professor Sandip K. Chakrabarti** and that neither this thesis nor any part of it has been submitted for any degree/diploma or any other academic award anywhere before .

16.2.05

Sandip K. Chakrabarti
Professor,
S.N.Bose National Centre for Basic Sciences,
JD-Block, Sector-III, Salt Lake, Calcutta, India.

DR. SANDIP K CHAKRABARTI
Professor
S N Bose National Centre
For Basic Sciences
Block JD, Salt Lake, Kolkata-700 098

ABSTRACT

In the isolated and binary systems, matter accretion is taking place from the surrounded medium or from the companion star. This matter forms a disk-like depository which is widely known as the *accretion disk*. In the presence of sufficient angular momentum, slowly moving matter at the outer edge of the disk gradually gains radial velocity while getting accreted towards the compact object and becomes super-sonic. At some point, super-sonic matter may make discontinuous transition to the sub-sonic branch. This discontinuous transition is known as a *shock*. If Rankine-Hugoniot relations are satisfied, this shock is called a standing shock. At a shock, matter slows down and piles up. This causes a puffed up torus like structure called CENtrifugal pressure supported BOundary Layer (CENBOL) to form. Soft-photons originated from the low temperature Keplerian disk are reprocessed by the hot electrons of CENBOL through the inverse-Comptonization process. They are emitted as hard X-rays. Thermal pressure gradient force at the shock location becomes significant in the transverse direction which drives matter upward and downward in the from of jets or outflows. These X-rays and outflows are observed. Therefore, it is generally believed that *shocks* are essential ingredients of the accretion disks around black holes and neutron stars.

In Chapter 1, we classify the nature of the compact objects. We demonstrate that the order of magnitude estimation of observed luminosities of compact object could be explained by assuming the accretion process. Historical study of spherical accretion process through various approaches are briefly highlighted . A qualitative discussion on the development of disk accretion process is also presented. The chapter ends with a short note on the nature of the generalized advective accretion disk models.

In Chapter 2, we present a more realistic advective disk model. We present the sonic point analysis and compute the standing shock locations. We discuss the process of jet formation and estimate the mass outflow rate considering a toy model for the disk-jet system.

In Chapter 3, we compute the location of sonic points and shocks in a *hybrid model* completely analytically in the special case when viscosity and other dissipative processes are negligible. We compare our analytical results with those obtained numerically. The agreement is generally good. We calculate the frequency of shock oscillation which is directly related to the quasi-periodic oscillation of hard X-rays. We analytically calculate the transonic properties of the accretion flow for different flow models. We show that all the flow models are basically identical in nature provided the polytropic index is suitably adjusted in different models. We self-consistently estimate the outflow rate from the inflow parameters for a two component advective model. We show that for a high value of compression ratio (R), the outflow rate

is small but significant whereas the outflow rate is negligible for lower compression ratio. For an intermediate value of R, the outflow rate is maximum. We also show how the spectral state of a black hole is directly related to the outflow rate.

In the course of development of the accretion disk models we study the effects of viscosity which must be present in the differentially rotating accretion disk. In Chapter 4, we include different types of cooling mechanisms, such as bremsstrahlung and synchrotron coolings, in succession. We show that standing shocks can form in an accretion flow having substantial amount of angular momentum and low viscosity. We identify the region of parameter space which produces multiple sonic points and shocks separately in presence of heating and cooling effects. We quantify two critical viscosity parameters and a critical cooling factor which separate the flow topologies. We mention that the cooling induces opposite contribution to the heating obtained by viscosity as far as the transonic properties are concerned. But these two effects can never be exactly balanced due to their dissimilar dependence on the dynamic and thermodynamic flow variables. We find that the shock moves closer to the black hole when the viscosity parameter is increased. This implies an enhancement of the quasi-periodic oscillation frequency due to an increase in viscosity.

In Chapter 5, we draw the conclusions.

In the Appendix (Chapter 6), the formalism to solve the quartic equation is discussed.

ACKNOWLEDGMENTS

I would first like to express my sincerest gratitude to my supervisor Professor Sandip K. Chakrabarti. I am grateful to him for introducing me to the fabulous world of astrophysics especially to the subject of black holes. His enthusiastic guidance, valuable suggestions, immense patience, unremitting discipline and lucid way of teaching always evoke me awe-inspiring during the Ph. D. period and helped me to reach a much awaited and cherished destination. Close proximity with him has helped me to learn a lot and opened up a rare window of black hole worlds.

I would like to thank all the academic and non-academic staff of the S. N. Bose National Centre For Basic Sciences for their enthusiastic support during my Ph. D period. I express my gratitude to the director of SNBNCBS, Prof. S. Dattagupta for giving me the opportunity to work here. My special acknowledgment goes to the Centre for Space Physics, Kolkata for providing me to attend many seminars and presenting lectures which gives me a broad view of the subject. I express my sincerest greetings to Prof. Diego Molteni of University of Palermo, Italy, for hosting me at his place and sharing his expertise in numerical simulation. I would like to thank Prof. Paolo Goldoni of C.E.A. Saclay, France, for his kind collaboration with me. My special thanks goes to Prof. A. R. Rao of TIFR, India, for his constant support during my Ph. D. period. I would like to thank the organizer of 4th. MicroQuasar Workshop for giving me the opportunity to attend the conference at Corsica. I would also like to acknowledge Abdus Salam International Centre For Theoretical Physics, Trieste, Italy, for giving me the opportunity to participate in the Summer School on Astroparticle Physics in summer 2002. Experienced gained from all of these visits improved the quality of my thesis.

I express my heartiest greetings to all my friends of S. N. Bose National Centre for Basic Sciences for sharing many memorable moments during my Ph. D. period. I specially remember Mr. Abhishek Chaudhuri and Ms. Swarnali Bandopadhyay in this regard.

I thank all my former and present colleagues in the astrophysics group of S. N. Bose National Centre for Basic Sciences. Specially I would like to mention Dr. Indranil Chattopadhyay for his generous help and friendly behaviour which boosted me to carry on my research work. I would also thank Mr. Soumen Mandal for his continuous support. I express my heartiest gratitude to Mr. Anuj Nandi, my colleague, batch met, room met and bosom friend who has shared every moment with me during the entire Ph. D. period. His fruitful suggestions and effective collaboration helped me to finish my work. I would also like to remember Mr.

Samir Mandal and Mr. Kinsuk Acharyaa of Centre for Space Physics for their useful discussion on various aspects of Astrophysics.

I offer special thanks to my wife, Anupama, for her continuous encouragement and unfailing support which drove me to complete my work smoothly and successfully.

Lastly, though it does not worth mentioning, I am ever indebted to my parents and my other family members for their tireless endeavor to help me for the completion of my work.

PUBLICATIONS

1. ***Standing Shocks around Black Holes: An Analytical Study***, by Santabrata Das, Indranil Chattopadhyay and Sandip K. Chakrabarti, in *ApJ*, **557**, 983 (2001).

2. ***Model dependence of transonic properties of accretion flows around black holes***, by Sandip K. Chakrabarti and Santabrata Das, in *MNRAS*, **327**, 808 (2001)

3. ***Computation of Outflow Rates from Accretion Disks Around Black Holes***, by Santabrata Das, Indranil Chattopadhyay, A. Nandi and Sandip K. Chakrabarti, in *A & A*, **379**, 683 (2001).

4. ***Analytical study of standing shock around black hole***, by Santabrata Das and Sandip K. Chakrabarti, in *Bulletin of the Astronomical Society of India*, **30**, 321 (2001).

5. ***On the Ejection Mechanism of Bullets in SS 433***, by Sandip K. Chakrabarti, P. Goldoni, P. J. Wiita, Anuj Nandi and Santabrata Das, in *ApJ*, **576**, L45 (2002).

6. ***Standing shocks around black holes and estimation of outflow rates***, by Santabrata Das and Sandip K. Chakrabarti, in *Journal of Astrophysics and Astronomy*, **23**, 143 (2002).

7. ***Parameter space for accretion flow around black holes: effects of energy dissipation***, by Santabrata Das and Sandip K. Chakrabarti, in *New Views on MICROQUASARS, the Fourth Microquasars Workshop*, Institut d'Etudes Scientifiques de Cargse, Corsica, France, May 27 - June 1, 2002. Edited by Ph. Durouchoux, Y. Fuchs, and J. Rodriguez. Published by the Center for Space Physics: Kolkata (India), p. 115 (2002).

8. ***Analytical solution of studying shocks around black hole***, by Santabrata Das and Sandip K. Chakrabarti, in *Proceedings of the National Space Science Symposium*, p. 386 (2002).

9. ***Behaviour of Standing Shocks around Black Holes and Determination of the outflow rates***, by Santabrata Das and Sandip K. Chakrabarti, in *Recent Trends in Astro and Plasma Physics in India*, Edited by Sandip K.

Chakrabarti, Santabrata Das, B. Basu and M. Khan, Published by the Centre for Space Physics: Kolkata (India), p. 70 (2003).

10. ***Analytical Investigation of Mass Outflow Rate in Quasars***, by **Santabrata Das** and Sandip K. Chakrabarti, in *Quasar Cores and Jets*, 25th meeting of the IAU, Joint Discussion 18, 23-24 July 2003, Sidney, Australia (2003).

11. ***Radiatively driven electron-positron jets from two-component accretion flows***, by Indranil Chattopadhyay, **Santabrata Das** and Sandip K. Chakrabarti, in *MNRAS*, **348**, 846C (2004).

12. ***Properties of accretion shock waves in viscous flows around black holes***, by Sandip K. Chakrabarti and **Santabrata Das**, in *MNRAS*, **349**, 649C (2004).

13. ***Properties of accretion shocks in viscous flows with cooling effect***, by **Santabrata Das** and Sandip K. Chakrabarti, in *IJMPD*, **13**, 1955(2004).

Contents

Chapter 1

Introduction

The present thesis contains the study of various properties of accretion disk around a compact object. In a broad point of view, the analysis of accretion physics is done in two different modes—the first one is for the idealistic non-dissipative accretion flow system and the second one is for the more realistic dissipative accretion flow system.

The present Chapter starts by giving an account of wide variety of compact objects. In §1.2, we point out that accretion processes could produce the observed luminosity of AGNs, quasars and micro-quasars etc. In §1.3, we study the dynamics of the accreted matter. In §1.4.1, we demonstrate the steady hydrodynamic spherical accretion process around a Newtonian star. Subsequently, we repeat the similar study around a non-rotating black hole in pure general relativity (§1.4.3). In §1.4.4, we obtain a simple pseudo-potential for a non-rotating black hole to avoid mathematical complexity. This pseudo-potential successfully mimics the space-time geometry around a non-rotating black hole. The historical developments of disk accretion processes are described in §1.5. In the same Section, we discuss the properties of thin, thick and slim disk respectively. In §1.6, we present the nature of advective disk models by considering different geometric disk structure.

1.1 Compact objects: end products of normal stars

'Compact Object's are born when normal stars die. These stars are the ashes of the luminous stars. Compact stars are broadly grouped as white dwarfs, neutron stars and black holes. The key factor for determining whether a star ends up as a white dwarf, neutron star or black hole is believed to be the star's mass. Compact stars are created when the massive stars have exhausted most of their nuclear fuel in their core. In general, this stars differ from the ordinary stars because of their exceedingly small size. Compact stars of comparable mass with normal star are very very small in radii that effectively produce stronger gravitational attraction.

On the other hand, since compact stars do not burn nuclear fuel they cannot support themselves against the inward gravitational collapse by generating the internal thermal pressure. In the case of white dwarfs, inward gravitational pressure at the core is supported by the electron degeneracy pressure while for neutron stars the same support comes from the pressure of degenerate neutrons. On the other hand, black holes are completely collapsed stars— inside it there is nothing to neutralize the inward gravitational pull and therefore, collapse to singularity.

White dwarfs are believed to originate from light stars of mass $M \lesssim 4M_{\odot}$. There is a maximum allowed mass limit for white dwarfs which is around $1.4M_{\odot}$. Neutron stars and black holes are believed to be originated from the more massive stars. However, the basic difference between the formation of neutron stars and black holes is very uncertain because the final stage of evolution of massive stars is poorly understood. Those stars also have some maximum mass limit in the range $1.4-3M_{\odot}$. A black hole is probably the fate of the most massive star, an inaccessible region of space-time into which the entire star, ashes and everythings, fall at the end of the luminous phase.

1.2 Accretion process: general consideration

When diffuse gases or matters are accumulated around a compact object under the influence of gravity we call this process as 'accretion'. In the early days (twentieth century) of astrophysical study, it was widely believed that non-gravitational process (nuclear reaction) was the only conceivable source of energy for the celestial objects. Later on, this idea was abandoned while people look for the origin of the most energetic sources in the universe. They end up with the conclusion that extraction of the gravitational potential energy from the accreted matter on to the gravitating body is the only source of power supply for luminous objects like active galactic nuclei, quasars, micro-quasars, etc. Thus, as a natural process, gravity plays a powerful role for the production of the electromagnetic radiations ranging from infrared to γ-rays and this shows a new window in observational astronomy.

Now, we present a simple order of magnitude estimation of energy release through the above mentioned process. Let us consider a star of mass M_* and radius R_*. The gravitational potential energy release on the surface of the star due to the accretion of unit mass of matter is given by,

$$\delta E_{acc} = \frac{GM_*}{R_*}, \tag{1.1}$$

where, G is the gravitational constant and c is the speed of light. This energy is expected to be released mainly in the form of electromagnetic radiation.

For comparison, we consider the energy that could be extracted by nuclear fusion process from a unit mass of matter. We assume that the material is initially composed of hydrogen only. Now, if all the hydrogen is converted to helium through the nuclear fusion, the burning of unit mass of the hydrogen yields an energy release which is given by,

$$\delta E_{nuc} = 0.007c^2 \approx 6.3 \times 10^{18} \text{ergs g}^{-1}. \tag{1.2}$$

At present, it is not easy to make comment about the superiority of the above mentioned process as the accretion process strongly depends on the compactness of the accreting star; the larger the ratio M_*/R_*, the greater is the efficiency.

For the Sun, the gravitational potential energy release per unit mass comes out to be,

$$\delta E_{acc} \approx 1.9 \times 19^{15} \text{ergs g}^{-1}, \tag{1.3}$$

where, $R_* = R_\odot$ and $M_* = M_\odot$ have been used. This indicates that $\delta E_{acc} \ll \delta E_{nuc}$. For a $1M_\odot$ neutron star of radius $R* \approx 10^6$cm, the released energy is about $\delta E_{acc} \approx 10^{20}$ergs g^{-1}. This is twenty times greater than the nuclear burning process. Accretion on to the black holes produces even higher gravitational potential energy as they are more compact than the neutron stars. This released energy would emit in the form of electromagnetic radiation from the vicinity of the compact stars. Therefore, the accretion process on to the compact stars would be the possible explanation for the emission of the high energy radiation as well.

An accreting object is characterized by it's luminosity which is defined to be the amount of radiant power emitted from the star's surroundings. This implies that the luminosity is mainly dictated by the amount of matter accreted on to the star surface in unit time, *i.e. accretion rate* ($\dot{M}_{acc}$). Thus the formal definition of the accretion luminosity (L_{acc}) is given by,

$$L_{acc} = \frac{GM_*\dot{M}_{acc}}{R_*} \tag{1.4}$$

Let us now define a useful benchmark for the luminosity which is known as *Eddington Luminosity*. We consider a steady spherically symmetric accretion on to a Newtonian star. The accreting matter is supposed to compose only of hydrogen which is fully ionized. Electrons experience an outward force by radiation due to momentum deposition through the Thomson scattering process. These electrons are also dragging protons by exerting a force via coulomb coupling. On the other hand, protons are attracted by the inward gravitational pull. Under this circumstance, this two forces would be exactly balanced for a certain limiting accretion rate and the accretion process would be ceased. This accretion rate gives a limiting luminosity called Eddington Luminosity and is given by,

$$L_{Edd} = \frac{4\pi G M_* m_p c}{\sigma_T} \cong 1.3 \times 10^{38} \frac{M_*}{M_\odot} \text{erg s}^{-1}. \quad (1.5)$$

Although the above estimation is based on some very idealistic approximation, still it provides a crude estimate which is acceptable.

1.2.1 Geometric structure of the accreted matter: accretion disk

Accretion is a process in which the gas and dust are accumulated around massive celestial object which could be stars, planets or any massive objects. These matters are collected in a relatively flat sheet on the equatorial plane of the attracting object.

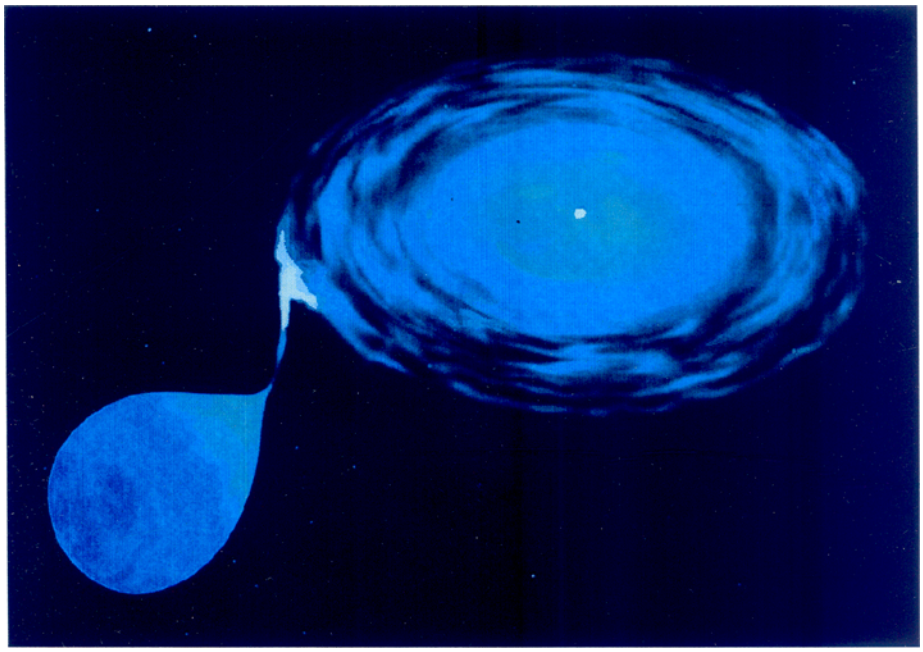

Figure 1.1: Artist's visualization of a binary system. Figure has been taken from http://antwrp.gsfc.nasa.gov/apod/ap991219.html

Fig. 1.1 shows an accretion disk in a binary system. Blue star at the left is filling its Roche lobe and matter is therefore streaming over the compact object at the right. Since accreted matter possesses significant amount of angular momentum, it cannot fall directly on to the compact object, instead it forms an accretion disk surrounding the compact object.

In general, the matter is rotated in Keplerian orbits inside an accretion disk. This implies that the matter is in a perfect equilibrium by the balance between the gravity

and the centrifugal force. If this were all, nothing would have ever happened inside the accretion disk. In this situation, matter would just go on revolving around the accreting star forever. But there is always some viscosity present inside the disk. The role of the viscosity is to transfer angular momentum from one gas layer to another gas layer which is further out from the accreting object. The first gas layer will then move a bit closer to the accreting object as it's new angular momentum corresponds to a smaller orbit. Repeating this process many times, the gas element eventually falls down to the central object and forms an accretion disk.

1.2.2 Efficiency of the accretion processes

Let us now make an order of magnitude estimation for the luminosity using Eq. (1.5). Considering the typical values of mass and radius for white dwarfs ($M_{WD} \sim M_{\odot}, R_{WD} \sim 10^9$ cm) and neutron stars ($M_{NS} \sim M_{\odot}, R_{NS} \sim 10^6$ cm), one could easily obtain the luminosity $L_{WD} \approx 10^{33}$ ergs s^{-1} for white dwarfs and $L_{NS} \approx 10^{36}$ ergs s^{-1} for neutron stars. In fact, in the above luminosity approximation, the accretion rate is chosen to be of the order of 10^{16} gm s^{-1} which is the typical value of accretion rate for a close binary system that includes the similar kind of stars.

In the case of a black hole accretion, the situation is rather different as the black holes do not have any *hard surface boundary*. The black hole boundary is defined by it's 'event horizon' and is given by the distance $r_g = \frac{2GM_{BH}}{c^2}$, where M_{BH} represents the mass of the black hole and r_g denotes the Schwarzschild radius. Accretion on to the black hole does not produce much of the radiated energy as significant amount of accreted matter is sucked by the hole itself. Therefore, it is useful to re-express Eq. (1.4) for the accretion on to the black hole through the introduction of a dimensionless parameter, η, known as efficiency factor, that measures the conversion efficiency of energy from gravitational head to radiation head. Thus, Eq. (1.4) takes the form as,

$$L_{acc} = \frac{\eta' G M_* \dot{M}_{acc}}{R_*} = \eta \dot{M}_{acc} c^2, \tag{1.6}$$

where, $\eta = \frac{\eta'}{2}, M_* = M_{BH}$ and $R_* = r_g$. Now it is important to estimate the realistic value of the conversion factor, η. The acceptable value of η for a non-rotating black hole is ~ 0.06 and for a extremely rotating black hole η is ~ 0.42. So it is reasonable to estimate the value of η is around 0.1. This value is comparable to the value $\eta \sim 0.15$ that comes from Eq. (1.6) assuming a $1M_{\odot}$ neutron star. This indicates that a neutron star of similar mass as a black hole is more efficient for converting energy from one head (gravitation) to other (radiation) though a neutron star is less compact than a black hole.

In fact, the accretion luminosity plays an important role while investigating the

core structure of the celestial objects, like active galaxies, quasars etc. For these systems, luminosity is very large ($L_{acc} \sim 10^{47}$ ergs s^{-1}). At the sub-Eddington accretion rate limit, such a high luminosity would be possible if the mass of the central object exceeds it's value around $10^9 M_\odot$ or more. White dwarfs and neutron stars do not have such extreme mass limits. Therefore, it would automatically indicate the presence of super-massive black holes at the centre of active galactic nuclei.

1.2.3 Emitted spectra

Let us now proceed to classify the different varieties of the compact stars by analyzing their various observed features. It is assumed that the photon energy, $h\overline{\nu}$, would be the order of kT_{rad}, where T_{rad} characterizes the continuum spectrum of the emitted radiation.

Now one can define the black body temperature, T_b, for a source of radius R and luminosity L_{acc}. If the total power which corresponds to the source itself radiates through the black body radiation, then the effective temperature of the source will be,

$$T_b = \left(\frac{L_{acc}}{4\pi R_*^2 \sigma}\right)^{1/4}. \tag{1.7}$$

Finally, we assume that each electron-proton pair (of masses m_e and m_p, where $m_e \ll m_p$) is accreted on to the compact object where the potential energy release is $\sim GMm_p/R_*$. Simultaneously, the thermal energy is $2 \times \frac{3}{2}kT$ for the same accreted pair. Now, if all the gravitational energy of the accreted matter is completely converted to the thermal energy, this will result a temperature, T_{th}, which is given by,

$$T_{th} = \frac{GMm_p}{3kR_*}. \tag{1.8}$$

Let us now look at the extreme limit of temperature for the matter that is accreting on to the compact stars. In an optically thick accretion flow, radiation achieves thermal equilibrium with the accreted material before escaping from the system which implies that $T_{rad} \sim T_b$. On the other hand, when the intervening material is optically thin, the accretion energy is converted to radiation which escapes from the system without further interaction and we have, $T_{rad} \sim T_{th}$. So it is clear that radiation temperature lie in between the thermal and the black body temperatures, $T_b \leq T_{rad} \leq T_{th}$. For one solar mass ($M = M_\odot$) neutron star or black hole the upper limit of temperature comes about $T_{th} \sim 5.5 \times 10^{11} K$ which is equivalent to the energy, $kT_{th} \sim 50 MeV$. The lower limit can be estimated by considering a typical luminosity ($L_{acc} \sim 10^{36}$ ergs s^{-1}) of a $1 M_\odot$ neutron star and it will be

around $T_b \sim 10^7 K$ or $kT_b \sim 1KeV$. Therefore, the photon which is emitted from the accreted matter belongs to the energy band ranging from $1KeV$ to $50MeV$.

This result gives a hint that a $1M_\odot$ neutron star or a black hole may be the source of hard X-ray photons. In a similar way, one could easily show that a stellar mass white dwarf is responsible for the emission of optical and ultraviolet radiations.

1.3 Fluid dynamics

In an accretion disk, matter is composed of constituent particles, such as free electrons and ions. These particles exert forces onto each other only by collision. In general, particles are expected to maintain their original state of motion up to a certain distance before colliding with some other particles. This collision free distance is called as mean free path, l. If the gas particles travel uniformly upto a certain distance which is of the order of several mean free path distance, it is possible to characterize the particles by a mean velocity, $\mathbf{v}$. Under these circumstances, a gaseous system with length scale $L \gg l$ can be treated as a continuous fluid having velocity ($\mathbf{v}$), temperature (T) and density (ρ). Here onwards, our goal is to study the dynamics of the fluid flow where the flow variables, such as velocity, temperature, density etc., will be expressed in terms of position and time by considering conservation law of mass, momentum and energy.

1.3.1 Basic equation

In the present Section, we briefly discuss the various conservation laws in fluid dynamics. These conservation laws explicitly describe the nature of the flow dynamics when the equation of state of the fluid is known. Of course, the flow characteristics must depend on the initial boundary conditions of the system under consideration.

The conservation of mass of the fluid flow is described by the *continuity equation* for the density ρ and fluid velocity $\mathbf{v}$ which is given by,

$$\frac{\partial \rho}{\partial t} + \nabla.(\rho \mathbf{v}) = 0. \tag{1.9}$$

The momentum conservation of gas elements can be expressed by the Newton's second law for the continuous fluid and is obtained from *Euler equation* as,

$$\rho \frac{\partial \mathbf{v}}{\partial t} + \rho \mathbf{v}.\nabla \mathbf{v} = -\nabla P + f, \tag{1.10}$$

where, P is the gas pressure at each point aroused because of the thermal motion of the gas particles and f denotes the external forces like gravity, viscosity etc.

The energy equation for the gas element is given by,

$$\frac{\partial}{\partial t}\left(\frac{1}{2}\rho v^2 + \rho\varepsilon\right) + \nabla.\left[\left(\frac{1}{2}\rho v^2 + \rho\varepsilon + P\right)\mathbf{v}\right] = f.\mathbf{v} - \nabla.F_{rad} - \nabla.q, \qquad (1.11)$$

where, the terms $\frac{1}{2}\rho v^2$ and $\rho\varepsilon$ measure the kinetic energy density and internal energy density respectively. In the right hand side, F_{rad} represents the radiative flux vector and q denotes the conductive heat flux. In general, q estimates the rate of transport of thermal energy inside the gas due to random motions.

Apart from these conservation laws, an equation of state is necessary to describe an astrophysical gas flow. The most useful idea for this purpose is to assume the astrophysical flow as a *perfect gas* and the so called equation of state of the perfect gas is given by,

$$P = \frac{\rho kT}{\mu m_p}, \qquad (1.12)$$

where, k is the Boltzmann constant, m_p is the mass of the hydrogen atom and μ is the mean molecular weight—for neutral hydrogen, $\mu = 1$ and for fully ionized hydrogen, $\mu = \frac{1}{2}$.

The set of Eqs. (1.9—1.12) along with the specific form of f give a complete description of the behaviour of the flow when the appropriate boundary conditions are known. Of course, it is really difficult to solve these set of equations retaining all the generalities. In the subsequent Sections we shall highlight some of the solutions of these set of equations considering reasonable approximations.

1.3.2 Steady flow: adiabatic & isothermal

In the present thesis, we are concentrating on the *stationary flow* in which flow variables are not varying with time. Here, we consider a special fluid flow for which no heat flows into or out of the gas element. Then the first law of thermodynamics takes the following form,

$$dU = -PdV;\ dQ = 0, \qquad (1.13)$$

where, U is the internal energy and V is the volume involved into the system. Specific heats of the gas element are connected by the relations which are given by,

$$C_P - C_V = R \ \text{ and } \ \frac{C_P}{C_V} = \gamma, \qquad (1.14)$$

where, R and γ denote the universal gas constant and adiabatic index respectively. In the ideal gas law, pressure (P) is expressed in term of volume (V) and temperature (T) and is given by,

$$PV = RT.$$

After some simple manipulation with Eqs (1.13) we have,

$$\gamma \frac{dV}{V} = -\frac{dP}{P}.$$

Solution of the above differential equation leads to the adiabatic gas law for a fluid of unit mass which is given by,

$$P = K\rho^{\gamma}, \tag{1.15}$$

where, K is a constant that measures the entropy of the flow.

Another special type of a flow could be obtained from the assumption that the gas temperature T remains constant throughout the region of interest. This is called isothermal flow. In a similar way expressed above, one can easily obtain the isothermal gas law as $P = K\rho$ with $\gamma = 1$. In future, we shall use both the flows separately while studying the flow characteristics.

1.4 Steady hydrodynamic spherical accretion

In 1939, Hoyel & Lyttleton first studied the problem of axisymmetric particle accretion through a shock front. The problem was to quantify the amount of matter which was accumulated on the star surface while coming from the interstellar medium. The result was not satisfactory as the pressure effect was ignored. Several years later, Bondi (1952) published his pioneering work on spherical accretion process. He considered the situation where an isolated star was at rest inside an ambient medium and matter was accreted onto the star's surface spherically symmetrically due to the gravitational attraction of the isolated star. He studied the effect of finite pressure in more detail and concluded that the temperature of the accreted matter had a vital role in this problem. In the next Section, we present a short review on the Bondi flow problem.

1.4.1 Bondi flow in Newtonian geometry

Here, we briefly illustrate the Bondi accretion flow problem (Bondi 1952). We start with a Newtonian star of mass M_* which is accreting matter spherically symmetrically from an infinite cloud. This cloud is at rest at infinity with uniform density ρ_∞ and pressure P_∞ in a Newtonian force field. The motion of the gas is steady and the gas dose not possess any angular momentum or magnetic field. The increase of mass of the central star due to the matter accretion on to the star surface is neglected. This leaves the external force field unchanged.

The equation of motion for an unit mass which is accreted towards the central star in the steady state condition is obtained from the Euler equation. Here, gravity

gives the only contribution to the external force, f. Due to the spherical symmetry the flow variables have only radial component and then, the equation of motion reduces to a form which is given by,

$$v\frac{dv}{dr}+\frac{1}{\rho}\frac{dP}{dr}+\frac{1}{r^2}=0, \tag{1.16}$$

where, v is the radial velocity, r is the radial distance, ρ is the matter density and P is the isotropic pressure.

The mass flux conservation is ensured by the continuity equation and in the spherical polar geometry it is given by,

$$\frac{1}{r^2}\frac{d}{dr}\left(\rho v r^2\right)=0. \tag{1.17}$$

While writing these equations we have chosen the geometric units $G = c = M_* = 1$, where G is the gravitational constant, c is the velocity of light and M_* is the mass of the central star. Thus the unit of length, mass, velocity and time would be GM_*/c^2, M_*, c and GM_*/c^3 respectively.

Moreover, matter is considered to be adiabatic in nature that follows from the equation of state $P = K\rho^\gamma$, where γ is the adiabatic index and K is a constant measures the specific entropy of the matter. We integrate radial momentum equation using adiabatic sound speed, $a = \sqrt{\gamma P/\rho}$, to obtain the *Bernoulli integral* which is given by,

$$\mathcal{E}=\frac{1}{2}v^2+na^2-\frac{1}{r}=na_\infty^2, \tag{1.16a}$$

where, $\mathcal{E}$ and n $[= (\gamma-1)^{-1}]$ denote the specific energy and polytropic index of the flow respectively.

Integrating Eq. (1.17) we get the mass flux equation as,

$$\dot{M}=\rho v r^2, \tag{1.17a}$$

where, $\dot{M}$ is a constant called as mass accretion rate. We re-express polytropic equation of state in terms of adiabatic sound speed as

$$\rho=\left(\frac{a^2}{\gamma K}\right)^n. \tag{1.18}$$

Using Eq.(1.18), Eq.(1.17a) can be written as,

$$\dot{\mathcal{M}}=a^{2n}vr^2. \tag{1.19}$$

The new term $\dot{\mathcal{M}}(=\gamma^n K^n \dot{M})$ first introduced by Chakrabarti (1989a) is also a conserved quantity in the flow known as the *entropy accretion rate*.

Differentiating Eqs. (1.16a) and (1.17a) and eliminating da/dr, we get the gradient of radial velocity as

$$\frac{dv}{dr} = \frac{\frac{2a^2}{r} - \frac{1}{r^2}}{v - \frac{a^2}{v}} = \frac{N}{D}, \tag{1.20}$$

where, N and D stand for numerator and denominator respectively.

According to the boundary conditions flow must be smooth at every point. Interestingly, if at some point the denominator vanishes, the numerator must also vanish there as dv/dr is finite always. Such a special point is called as *critical point* of the flow. We, therefore, have the critical point conditions which are given by,

$$v_c^2(r_c) = a_c^2(r_c) \text{ and } r_c = \frac{1}{2a_c^2}. \tag{1.21}$$

The subscript 'c' identifies the flow variables at the critical point. In fluid dynamics, the Mach number is defined as the ratio of the flow radial velocity to the sound speed at the same location. In fact, at the critical point Mach number $M(r_c)\,(= v_c/a_c)$ is unity and therefore, the critical point is renamed as the sonic point (r_c). This sonic point, r_c, would then correspond to a spherical surface called *sound horizon*, as any acoustic disturbance created at downstream region $(r < r_c, u < a)$ will not be carried out to the upstream $(r > r_c, u > a)$.

Let us concentrate on the length scale of the accretion flow problem. Define the 'accretion radius', r_{acc}, to be that radius at which the kinetic energy of matter is balanced by its potential energy. Thus, the accretion radius is given by,

$$r_{acc} \equiv \frac{2}{v_\infty^2}. \tag{1.22}$$

This length scale gives the range of influence of the central star onto the gas cloud.

From Eq. (1.16a), it is clear that for $r \to \infty$, contribution of gravity is negligible and flow does not feel any inward pull as gravity is the only responsible attracting force there. But at the same location sound speed have some considerable value which asymptotically approaches to a_∞. As one now proceeds towards the central star the flow velocity increases and the flow must be sub-sonic at a large r. In an accretion process, the gradient of radial velocity must be negative throughout the flow. In the vicinity of the accreting star, since gravity dominates over all other forces numerator becomes negative as well. Therefore, accretion is possible if $D > 0$ that implies $v > a$, *i.e.* flow is super-sonic in nature at that region. Thus accretion flow solutions are always transonic and transonic transition between sub- and super-sonic branches occurs at the sonic point. Limitation of the transonic flow solutions

could be clearly understood when flow variables (u or a) at the critical point are expressed in terms of a_∞ which is given by,

$$a_c = \left(\frac{n}{n-3/2}\right)^{1/2} a_\infty. \tag{1.23}$$

This indicates that transonic flow exits if and only if $n > 3/2$, *i.e.*, for $\gamma < 5/3$.

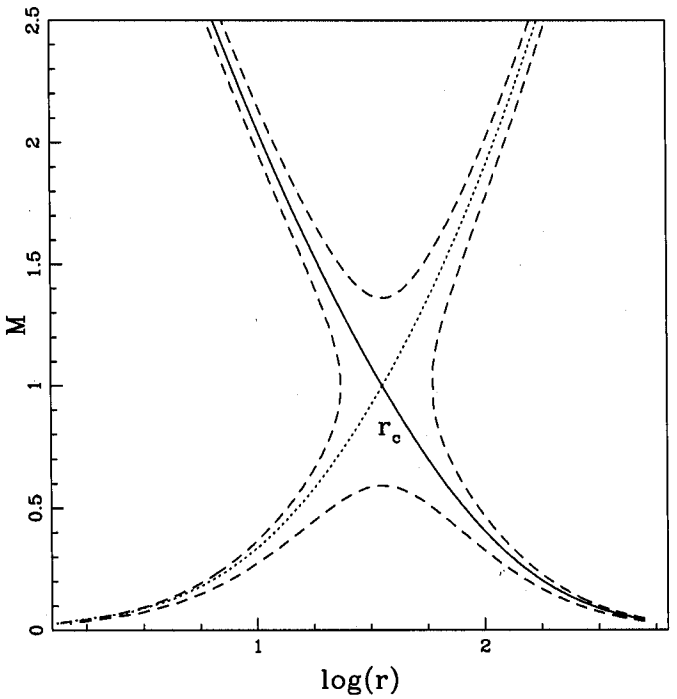

Figure 1.2: Plot of the phase space diagram of the Bondi flow around a Newtonian star for $n = 3$ and $\mathcal{E} = 0.01$. Solid, dotted and dashed curves are the contours of constant $\dot{M}$. The solid curve represents the accretion flow solution while the dotted curve is drawn for wind solution. Solid and dotted curves are the only physically acceptable solutions as they are transonic in nature while the dashed curves are not transonic anyway. Among the dashed curves, one branch is sub-sonic at every point and the other branch is super-sonic always and could be excluded for any realistic flow.

More importantly, the conserved quantities $\mathcal{E}$ and $\dot{\mathcal{M}}$ can be expressed in terms of a unknown variable, r_c, by using two critical point conditions. Therefore, $\mathcal{E}$

and $\dot{\mathcal{M}}$ cannot be independent and this will provide a single parameter family of solutions. Beside this, the accretion rate $\dot{\mathcal{M}}$ can be estimated from a_∞ as,

$$\dot{\mathcal{M}}_c = \frac{1}{4}\left(\frac{na_\infty^2}{n-3/2}\right)^{n-3/2}. \tag{1.24}$$

In Fig. 1.2, we present the variation of Mach number with logarithmic radial distance for a set of fixed input parameters $n = 3$ and $\mathcal{E} = 0.01$. The solid and dotted curves connect the flow solution from infinity to the star surface and hence consider to be physically significant. Details of figure descriptions are given in the Figure captions.

The nature of the Bondi solutions can be understood by studying the radial velocity gradient $[(dv/dr)_c]$ at the critical point. At this point $dv/dr = 0/0$, so one must apply l'Hospital rule to understand the behaviour of the flow properly. Thus, using the critical point conditions one obtains the radial velocity gradient at r_c as,

$$\left(\frac{dv}{dr}\right)_c = -\frac{4a_c^3}{2n+1}\left[1 \mp \sqrt{n(n-3/2)}\right]. \tag{1.25}$$

The nature of the critical point is dictated by the discriminant $\mathcal{D} = n(n - 3/2)$. A transonic flow solution is possible when velocity gradient at the critical point becomes real and it happens for $n > 3/2$. Classification of the critical points mainly depends on the exact value of the discriminant ($\mathcal{D}$) and Chakrabarti (1990a, hereafter C90a) have done a detail study on it which will not be repeated here once again. For $n > 2$, saddle type sonic point exists since derivatives $(dv/dr)_c$ at the critical point are real and of opposite sign. When $n < 3/2$, $\mathcal{D} < 0$ and the critical point is of spiral type. Critical point becomes nodal when n lie in the range $2 > n > 3/2$. Therefore, in Bondi flow, the behaviour of the critical point strongly depends on the polytropic index (n) and it's nature is highly sensitive on the numerical value of n.

1.4.2 Limitations of spherical symmetry

Now it is clear that the accretion flow variables could be expressed in terms of radial distance only and using these variables one can easily understand the emission properties of the flow. Due to the fact that black hole does not have its own hard surface, the outgoing radiation is produced by the accreted matter and the radiation spectrum is determined by the various radiation processes.

In general, most of the radiations are originated from the vicinity of the region just outside the event horizon. The flow variables, such as velocity , density etc.,

possess their maximum values at the region close to the black hole. In this particular environment, thermal bremsstrahlung radiation process will be important where relativistic electrons collide with heavy ions inelastically and generate radiation spectrum. Considering the relativistic effect due to the motion of the infalling gas, the so called total luminosity (L_{brem}) is computed and the efficiency of conversion of rest mass energy into radiation is estimated (Shapiro & Teukolsky, 1983) as,

$$\eta = \frac{L_{brem}}{\dot{M}c^2} \sim 6 \times 10^{-11} \left(\frac{n_\infty}{1 \text{ cm}^{-3}}\right) \left(\frac{T_\infty}{10^4 K}\right)^{-3/2} \left(\frac{M_B}{M_\odot}\right), \tag{1.26}$$

where, n_∞ and T_∞ represent the number density and temperature of the gas at continuum. Eq. (1.26) represents a very low efficiency for the conversion of rest-mass energy into the radiation. This efficiency may increase only by 15% when the central object rotates with its maximum allowed angular momentum. In this scenario, spherical accretion of interstellar gas by a stellar mass black hole gives minimal contribution to the emitted radiation and cannot be treated as a possible mechanism of radiation process for quasar and AGN as their efficiency factor ranges from 0.057-0.42 for Schwarzschild and maximally rotating Kerr black hole.

1.4.3 General relativistic Bondi flow

It is worthwhile to study the stationary spherical accretion flow problem for a non-rotating black hole in pure general relativity. The metric around a Schwarzschild black hole is given by,

$$ds^2 = -\left(1 - \frac{2}{r}\right) dt^2 + \left(1 - \frac{2}{r}\right)^{-1} dr^2 + r^2 d\theta^2 + r^2 sin^2\theta d\phi^2. \tag{1.27}$$

Here, we have used geometrical units similar to the earlier Section. Presently we are dealing with a steady, radial flow where $\partial/\partial t = \partial/\partial\theta = \partial/\partial\phi = 0$ and $u^\theta = u^\phi = 0$ as well. The radial velocity is defined as,

$$v^2 = -\frac{u_r u^r}{u_t u^t}, \tag{1.28}$$

where, u^t and u^r denote the time- and radial-component of four velocity. Using the normalization relation, $u_\mu u^\mu = -1$, and Eq. (1.27) one can easily compute u_t and u^r which are given by,

$$u_t = \left(\frac{1 - \frac{2}{r}}{1 - v^2}\right)^{1/2}, \tag{1.29}$$

and

$$u^r = \frac{v}{\sqrt{1-v^2}}\sqrt{1-\frac{2}{r}}. \tag{1.30}$$

In our present study, we consider the accretion flow which has negligible viscosity. Therefore, the conserved energy equation (Chakrabarti 1996a, hereafter C96a) is obtain as,

$$hu_t = \frac{p+\epsilon}{\rho}u_t = \mathcal{E}, \tag{1.31}$$

where, h $[= (p+\epsilon)/\rho]$ is the specific enthalpy, ϵ is the mass energy density, ρ is the mass density and p is the isotropic pressure of the flow respectively. Here, u_t represents the time-component of velocity which is also considered as the specific binding energy of the flow.

In the steady state, the conserved mass flux equation is calculated from the continuity equation as,

$$\dot{M} = \rho r^2 u^r. \tag{1.32}$$

Using the Chakrabarti's definition for *entropy accretion rate* (C90a) we get,

$$\dot{\mathcal{M}} = \gamma^n K^n \dot{M} = \left(\frac{a^2}{1-na^2}\right)\frac{vr^2}{\sqrt{1-v^2}}\sqrt{1-\frac{2}{r}}, \tag{1.33}$$

where, γ and n denote the adiabatic index and the polytropic index respectively. Here, we have used the definition of sound speed as $a = \sqrt{\gamma p/(\epsilon+p)}$. Since no energy exchange is taken place in the flow we consider the flow to be adiabatic in nature. Therefore, the flow follows the adiabatic equation of state, $p = K\rho^\gamma$, where K is a constant measures the change of entropy of the flow.

Differentiating Eqs. (1.31 and 1.32) and eliminating da/dr, we get,

$$\frac{dv}{dr} = \left[\frac{2a^2(1-v^2)}{r} - \frac{(1-a^2)(1-v^2)}{r(r-2)}\right] \Big/ \left[\frac{a^2}{v} - v\right] \tag{1.34}$$

Similar to Newtonian approach, Eq. (1.34) is integrated to obtain the solution topologies for different flow parameters. In Fig. 1.3a, we show the variation of radial velocity of the accreted matter (solid curve) as a function of logarithmic radial distance around a non-rotating black hole. The corresponding wind velocity variation is denoted by dotted curve. The specific energy of the flow is chosen as $\mathcal{E} = 1.02$ which identifies the sonic point (r_c) at 41.53. Polytropic index $n = 3$ is used here. Note that, matter velocity approaches to unity (in units of c) while crossing the black hole horizon ($2GM_{BH}/c^2$). We plot the phase space diagram of spherically symmetric accreted matter for the same flow parameters used in Fig.1.3b.

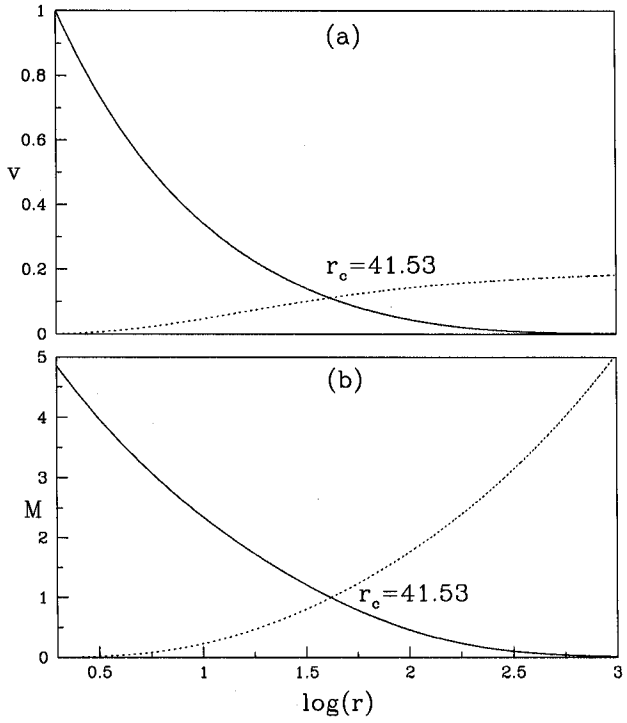

Figure 1.3: Spherically symmetric transonic flow solutions obtain from pure general relativistic calculation. Fig. (a) show the velocity variation with logarithmic radial distance for both the accretion (solid) and the wind solution (dotted). We present the Mach number ($M = v/a$) variation as a function of the logarithmic radial distance for accretion (solid) and wind (dotted) for the same set of flow parameters in Fig. (b). The figure details are mentioned in the text.

There we show both the transonic flow solutions for wind (dotted) and accretion (solid) separately. The important point is that the nature of solutions obtained from Newtonian approach are exactly identical with the pure general relativistic calculations. But the only difference is that sonic point forms further away from the black hole horizon in the Newtonian case.

1.4.4 Space-time around Black holes and pseudo-Newtonian potential

The physics of black holes is described by the space-time geometry around it. Due to compactness, the black hole geometry differs from the ordinary star and it can

be successfully described by the general theory of relativity. In most of the astrophysical systems where a neutron star or a black hole is involved, one can avoid complicated full general relativistic treatment when the interesting astrophysical processes are not occurring extremely close (within $r \lesssim 2r_g$) to the black hole horizon. Accordingly, accretion disk problem can be tackled with Newtonian concept by introducing pseudo-Newtonian potential which retains all the salient features of black hole geometry well out side the black hole horizon. In 1980, Paczyński & Wiita (Paczyński & Wiita, 1980, hereafter PW80) suggested the expression of pseudo-Newtonian potential which mimics the black hole environment quite satisfactorily within the acceptable error bar. Therefore, from now and onwards, we shall use this potential to account the general relativistic effects around the black hole surroundings.

In the present study, we are interested to find out a suitable pseudo-potential which successfully mimics the basic features of actual non-rotating black hole geometry. For this, we explore Schwarzschild metric which properly describes the external field of a non-rotating black hole. The so called metric with -,+,+,+ signature is given by,

$$ds^2 = -\left(1-\frac{2}{r}\right)dt^2 + \left(1-\frac{2}{r}\right)^{-1}dr^2 + r^2d\theta^2 + r^2\sin^2\theta d\phi^2. \tag{1.35}$$

Here, we choose the geometric units $G = M_{BH} = c = 1$, where G is the universal gravitational constant, M_{BH} is the mass of the black hole and c is the velocity of light respectively. We use r, θ and ϕ as the coordinates of spherical geometry. The motion of a freely moving test particle will be along the geodesics of space time and the geodesic equations are obtained from the Lagrangian which is given by,

$$2L = -\left(1-\frac{2}{r}\right)\dot{t}^2 + \left(1-\frac{2}{r}\right)^{-1}\dot{r}^2 + r^2\dot{\theta}^2 + r^2\sin^2\theta\dot{\phi}^2, \tag{1.36}$$

where, $\dot{t} \equiv dt/d\tau = u^t$ is the t-component of 4-momentum and so on, for a particle of unit mass and τ is simply the proper time.

The equation of motions corresponding to θ, ϕ and t coordinates are respectively given by,

$$\frac{du_\theta}{d\tau} = \frac{d}{d\tau}(r^2u^\theta) = r^2\sin\theta\cos\theta(u^\phi)^2, \tag{1.37}$$

$$\frac{du_\phi}{d\tau} = \frac{d}{d\tau}(r^2\sin^2\theta u^\phi) = 0, \tag{1.38}$$

$$\frac{du_t}{d\tau} = \frac{d}{d\tau}\left[\left(1-\frac{2}{r}\right)u^t\right] = 0. \tag{1.39}$$

Taking integration of Eqs.(1.37—1.39) we get u_μ as a constant of motion. Eq. (1.37) clearly indicates that if we orient the coordinate system so that initially the

particle is moving in a equatorial plane (i. e. $\theta = \pi/2, \dot{\theta} = 0$), then the particle remains in the equatorial plane. Therefore, it gives $u^\theta = 0$ all throughout. Now with $\theta = \pi/2$, Eqs.(1.38) and (1.39) become

$$u_\phi = r^2 u^\phi = l = \text{constant of motion} \tag{1.40}$$

and

$$-u_t = \left(1 - \frac{2}{r}\right) u^t = E = \text{constant of motion.} \tag{1.41}$$

The above set of equations and the normalization relation of four-velocities ($u_\mu u^\mu = -1$) together give us,

$$\left(\frac{dr}{d\tau}\right)^2 = E^2 - \left(1 - \frac{2}{r}\right)\left(1 + \frac{l^2}{r^2}\right). \tag{1.42}$$

The general nature of a freely moving test particle orbit could be ascertained while considering the second term of the r.h.s. of Eq.(1.42) as an 'effective potential' of the particle and is given by,

$$V_{eff}^2 \equiv \left(1 - \frac{2}{r}\right)\left(1 + \frac{l^2}{r^2}\right). \tag{1.43}$$

Eq.(1.43) identifies a remarkable feature that $V_{eff} = 0$ at the event horizon of the Schwarzschild black hole ($r = 2$). Fig. 1.4 shows the plot of V_{eff} as a function of radial distance (r) where we compare the effective potentials obtained from different approaches. In Fig. 1.4, the solid curves are drawn for general relativistic effective potential for (from bottom curve to top one) $l = 0, 3, 2\sqrt{3}, 4,$ and 4.5 respectively. Long dashed curves represent pseudo-Newtonian effective potential for $l = 4$ (bottom) and $l = 4.5$ (top) and the dotted curve indicates the Newtonian inverse square law. The incoming matter with sufficient energy ($E > V_{eff}$) does not feel any obstruction from the pseudo-Newtonian and general relativistic potential barrier—implies that matter can fall into a black hole as easily as a spherical flow. On the other hand, a Newtonian potential presents an infinitely high barrier to the flow even when matter possesses a significant amount angular momentum. The particles that enter into the black hole travel in a trajectory which is known as 'capture orbit'. Presently we focus on these bound particles. Particles on a 'circular orbit' can also be captured into the black hole even with a slight perturbation. Mathematically, circular orbit could be derived by setting the conditions, namely, (A)$\frac{\partial V_{eff}}{\partial r} = 0$ and (B)$\frac{\partial r}{\partial \tau} = 0$. Accordingly, from condition (A) we have the relation,

$$r^2 - l^2 r + 3l^2 = 0. \tag{1.44}$$

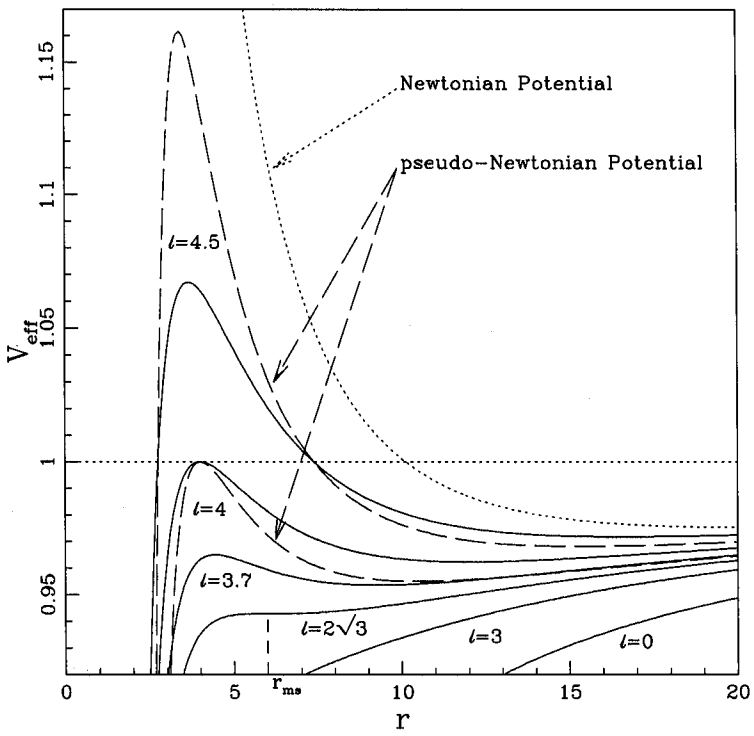

Figure 1.4: Plot of the effective potential V_{eff} with radial distance for the a set of values of specific angular momentum marked in the figure. The dotted curve denotes the Newtonian inverse square law. Solid curves are drawn for general relativistic effective potential while long dashed curves represent the pseudo-Newtonian effective potential.

The real value of radial distance, r, is possible whenever $l \geqq 2\sqrt{3}$ and the potential has a extremity for $l \geqq 2\sqrt{3}$. $l_{ms} = 2\sqrt{3}$ is known as marginally stable angular momentum, since closed orbits can not be formed below this l. At $r = r_{ms} = 6GM_{BH}/c^2, V_{eff}(l = l_{ms})$, specially indicated in the Fig 1.4, has a point of inflection called the marginally stable orbit (r_{ms}). This closed orbit is the last stable orbit nearer to the black hole horizon. For $r < r_{ms}$, matter cannot stay in a stable orbit and must dive into the black hole. For $l_{mb} = 4GM_{BH}/c^2, V_{eff} = 1$ at $r_{mb} = 2GM_{BH}/c^2$ and the orbits are marginally bound located at r_{mb}.

Angular momentum of the test particle can be calculated from Eq.(1.44) which is given by,

$$l^2 = \frac{r^2}{(r-3)}. \tag{1.45}$$

Moreover, specific angular momentum is defined as $-u_\phi/u_t$ and the Keplerian angular momentum distribution is obtained by joining the locus of the extremity of V_{eff} which is written as,

$$l^2_{Kep} = \left(-\frac{u_\phi}{u_t}\right)^2 = \frac{r^3}{(r-2)^2}. \tag{1.46}$$

Using Eq. (1.45) and condition (B) we get the energy of the particle after some simplified algebra as

$$E^2 = \frac{(r-2)^2}{r(r-3)}. \tag{1.47}$$

The numerical value of the effective potential $[V_{eff}(r_{ms})]$ at the marginally stable orbit is obtained by using $r = 6$ and $l = 2\sqrt{3}$ in Eq. (1.43) and is given by,

$$V_{eff}(r_{ms}) = \sqrt{\frac{8}{9}}. \tag{1.48}$$

Thus, using Eq. (1.48), one can easily compute the binding energy per unit mass of a particle at the last stable orbit, $r = r_{ms} = 6$, which is obtain as,

$$E_{bind} = 1 - V_{eff}(r_{ms}) = 1 - \sqrt{8/9} = 5.72\%. \tag{1.49}$$

Therefore, when a particle at rest at infinity plunges into the black hole through the inner most stable circular orbit it will release the above fraction ($\sim 6\%$) of its rest-mass energy in the form of radiation.

Black hole space-time environment could also be described by using pseudo-Newtonian potential first proposed by Paczyński and Wiita in 1980. This pseudo potential roughly reproduces the essential features of a black hole space-time and also allow us to avoid the more complicated general relativistic treatment. The prescribed effective potential along with the matter rest mass energy is given by,

$$V_{eff}(PW) = 1 + \frac{\ell^2}{2r^2} - \frac{1}{(r-2)}, \tag{1.50}$$

where, the last term in the r.h.s. represents the pseudo-Newtonian potential ($\Phi_{PW} = -\frac{1}{(r-2)}$) and ℓ is the angular momentum of the matter which plays a similar role of l used earlier. The two different notations are used to indicate the different approaches.

Setting the condition (A) in Eq. (1.50), one can easily obtain the expression of Keplerian angular momentum distribution as,

$$\ell^2_{Kep} = \frac{r^3}{(r-2)^2}. \tag{1.51}$$

This indicates that pseudo-Newtonian potential (Φ_{PW}) gives exactly identical expression for the Keplerian angular momentum distribution as obtained in GR approach. Moreover, the minimum of the Keplerian angular momentum distribution also occurs at the marginally stable orbit, (r_{ms}). The efficiency of energy conversion in pseudo-Newtonian description is obtain as,

$$\eta = 1 - V_{eff}(PW) \mid_{r_{ms}} = 6.25\%. \tag{1.52}$$

Note that η is also very close to the earlier result. Thus, from the above discussion it is clear that pseudo-Newtonian approach is quite correct and the error lies within the acceptable range. Therefore, satisfactory results are expected if we restrict our interest in a region well outside the black hole horizon. In the next part of the thesis, we shall use this pseudo-Newtonian potential to take care of the general relativistic effects.

1.4.5 Bondi flow in pseudo-Newtonian geometry

In §1.4.1, we have studied the transonic astrophysical flow on to a Newtonian star. In reality, astrophysical flow cannot be so simple which can be tackled with Newtonian geometry—instead, the general relativistic approach must be incorporated. So far, we have dealt with a very simple system using the general relativity and the governing equations of the flow are not very tedious. However, in general, a rigorous study of a more complex system, such as the flow with angular momentum, viscosity, magnetic field etc. is almost impossible in full general relativity. The problem is solved by incorporating a pseudo-Newtonian potential ($\Phi_{PW} = -\frac{1}{x-2}$) often used in the literature (PW80). This pseudo-Newtonian potential successfully takes care the essential features of Schwarzschild geometry. This treatment is very similar but little bit harder compared to the Newtonian approach. In this Section, we shall revisit the Bondi flow problem with pseudo-Newtonian potential. Accordingly, one could obtain Schwarzschild solutions without going through the general relativistic treatment.

In the present context, we assume that the adiabatic matter is collected spherically symmetrically around a non-rotating black hole. In addition, we consider that the viscosity and other dissipative processes are negligible. Therefore, the energy of the flow remains constant all throughout. The flow is governed by the energy and mass conservation equations which are given by,

Energy Equation :

$$\mathcal{E} = \frac{v^2}{2} + na^2 - \frac{1}{r-2}, \tag{1.53}$$

and, *Mass Flux Equation* :

$$\dot{M} = \rho v r^2; \text{ apart from the geometrical factor.} \tag{1.54a}$$

Entropy-accretion rate is calculated from the relation $\dot{\mathcal{M}} = \gamma^n K^n \dot{M}$ and is obtained from Eq. (1.54a) as,

$$\dot{\mathcal{M}} = a^{2n} v r^2, \tag{1.54b}$$

where, the quantities carry the same meaning mentioned previously.

Following the similar procedure as described in §1.4.1, the radial velocity gradient at any point can be obtained as,

$$\frac{dv}{dr} = \frac{\frac{1}{(r-2)^2} - \frac{2a^2}{r}}{\frac{a^2}{v} - v} = \frac{N}{D}. \tag{1.55}$$

According to the boundary conditions, since the flow is smooth everywhere, radial velocity gradient must be finite always at each point of the flow. This indicates that whenever denominator vanishes numerator must also vanish simultaneously at the same point. Such a special point is called as sonic point. Under this consideration, one can easily derive the sonic point conditions as,

$$v_c = a_c, \Rightarrow M(r_c) = 1, \tag{1.56a}$$

and

$$r_c = 2 + \frac{1}{4a_c^2} + \frac{\sqrt{16a_c^2 + 1}}{4a_c^2}. \tag{1.56b}$$

Eq. (1.56b) represents the location of the sonic point which could be anywhere ranging from inner boundary to outer edge of the disk depending on the value of sound speed. In Newtonian geometry, sound speed is allowed to become infinity at its maximum value. This indicates a closest approach of sonic point at the black hole horizon ($r = 2$) which is consistent with the result obtained from the pure Schwarzchild geometry (§1.4.3). The flow solutions obtained from the present approach are very similar to the original Bondi solution in the Newtonian geometry.

1.5 Disk accretion

In the earlier Section, we have pointed out that emitted radiation which originates from the rapidly infalling matter onto a compact object, is not found to be strong

enough to explain the high luminosity of AGNs and quasars. However, the presence of tangled magnetic field, leading to the synchrotron radiation in addition with bremsstrahlung radiation can improve luminosity but the result does not reach in the highest expectation level. In this floating age, accreted material was found to produce a disk like temporary depositary around the compact objects. Later on, disk like structure of such accreted flow around the compact object was suggested to resolve the mystery of high luminous radiation sources (Lynden-Bell, 1969 and Pendergest & Burbidge, 1968).

In the early days of accretion disk physics, accretion in a binary system was first investigated where one of the components of the binary system was treated as a compact object (primary component). In the present study, we are mainly interested in the accretion process on to a black hole. In what follows, primary component would strip out matter due to tidal disruption either from the ambient wind of the surrounding stars or through the Roche lobe overflow from the binary companion. Hence, the accreted matter would possess substantial amount of intrinsic angular momentum with respect to the black hole. As the accreting matter does have a significant amount of angular momentum it would revolve around the black hole that results lower infall velocity and much higher density compared to the spherical accretion. Therefore, the infall timescale becomes longer. This would help the flow to dissipate angular momentum and energy well outside the event horizon through the viscosity. Actually, viscosity automatically comes into play due to the differential rotation of the infalling matter inside the disk. Moreover, since angular momentum is a conserved quantity, loss of angular momentum through the viscosity drifts matter into a closer orbit with larger infall velocity towards the black hole. Therefore, the infalling matter gradually falls into the black hole following a spiral trajectory before forming a temporary depositary of disk like structure around the black hole and preferably settles down into an orbital plane of it. As more and more matter dives into the deeper gravitational potential well of the black hole, it would radiate more efficiently corresponds to high luminosity radiation spectra. In the case of the Schwarzschild black hole, an accreting disk can radiate up to 6% of the rest mass of the infalling matter and for Kerr black hole it could be around 40% depending upon the rotation parameter of the black hole. In fact, the real energy conversion efficiency factor does depend upon the heating and cooling processes inside the accretion disk. This energy is released through the entire electromagnetic spectrum and the success of the disk model depends on it's ability to describe the emitted energy which is distributed in various frequency bands. The temperature, density as well as the geometrical shape of the disk dictate the nature of the emerging radiation spectrum as well. The disk variables explicitly depend on the outer boundary conditions, namely, the rate of matter supply, specific angular momentum as well as the energy content of the matter.

In a binary system, in general, accreting matter encircles around a compact star and forms a quasi-stationary structure of matter around it which is widely known as accretion disk. Due to viscosity, matter transports angular momentum from the inner part to the outer part of the disk. Therefore, the accreted matter has an angular momentum distribution inside the disk. In general, this accreted matter settles down in the equatorial plane of the gravitating object. This kind of matter distribution is usualy described by the standard 'thin' disk model which is commonly known as the Keplerain disk. Of course, some matter will be accreted by the black hole from the winds of the companion star. Therefore, a Keplerian flow could become sub- or super-Keplerian close to the black hole when the terms, such as, advection, pressure, cooling factor etc. are included in the flow equations. Thus, the flow close to the compact object will be a mixture of Keplerian and sub-Keplarian matter. Behavior of such disk will be discussed in §3.3.6. However, the accretion mechanism on to AGNs and quasars is intrinsically different where infalling matter is supplied to the central star from the winds of the ambient star cluster. Therefore, the infalling matter possesses angular momentum sufficiently lower than the Keplerian value. Thus, the flow is expected to have a higher infall velocity, *i.e.*, the matter is mostly advecting. Matter travels with almost free fall velocity until it interacts with the centrifugal barrier that causes a sharp discontinuous transition of the flow variables. This sharp discontinuity is called a shock. At the base of the shock, the post-shock flow has a negligible infall velocity and relatively high temperature. In this region, the infall velocity is dominated by the orbital motion of the flow and flow density becomes high. Such special type of matter distribution can be described by the so-called 'thick' accretion disk model. This disk model has very little viscosity and radiation efficiency which could be somewhat intermediate between a spherical flow and a Keplerian thin disk model. Properties of all such disks will be discussed in the subsequent Section.

1.5.1 Standard thin disk

In general, standard accretion disk forms in a binary system where the companion feeds gas to the compact star via Roche-lobe overflow. In this Section, the structure of such a disk around a central star will be briefly discussed. Usually this disk is known as the Keplerian accretion disk. Prendergast et al. (1968) first realized the importance of angular momentum of accretion flow in the binary system. They incorporated it to visualize the system precisely. Meanwhile, Lynden-Bell (1969) gave a tentative suggestion that super-massive black hole might be centered at the galaxy core surrounded by the accreted matter. Subsequently, Shakura (1972), Pringle & Rees (1972), Shakura & Sunyaev (1973, SS73 from here onwards) and Novikov & Thorne (1973) proposed several accretion disk models around the compact objects considering Newtonian geometry. In 1973, Novikov & Thorne (1973) extended their

work in general relativity while solving the inner part of the accretion disk. In addition, Shapiro & Teukolsky (1983) reviewed the thin accretion disk model in a great detail. In the next, we present a brief note on the thin accretion disk model.

Let us begin with a qualitative overview of a disk accretion where the matter is accreted onto a black hole very slowly. Accreted matter possesses substantial amount of intrinsic angular momentum. Therefore, matter will be distributed in Keplerian orbit and will not be drifted further inward as angular momentum is a conserved quantity. But the viscosity is always present inside the disk which transports angular momentum outwards and allows matter to move in. Following this process matter ultimately dives into the black hole. As the matter moves in a Keplerian orbit, it settles down in an equatorial plane of the black hole and forms a disk which is assumed to be *thin*, *i.e.* the local height of the disk is much smaller than the local radial distance ($h(r) \ll r$). In this thin disk approximation, it is reasonable to ignore the vertical velocity component compared to the radial or orbital velocities. So, the vertical equations could be solved separately from the radial equations. Along with this, accretion rate is assumed to lie in the sub-Eddington regime. Local heat is produced due to viscosity which is easily radiated away through the disk surface. As a result, the disk becomes cooler compared to the spherical accretion. Therefore, we assume that the disk is highly non-adiabatic in nature. In addition, the pressure effect is also ignored which implies that the angular momentum distribution of matter is purely Keplerian. Thus, the radial velocity is negligible compared to the orbital velocity ($v_r \ll v_\phi$). Therefore, the angular velocity of matter around an accreting star of mass M_{BH} is given by,

$$\Omega = \Omega_K(r) = \sqrt{\frac{GM_{BH}}{r^3}}, \tag{1.57}$$

which gives the Keplerian orbital velocity,

$$v_\phi = r\Omega = \sqrt{\frac{GM_{BH}}{r}}. \tag{1.58}$$

In presence of significant viscosity, the gas is assumed to possess a small inward radial drift velocity v_r which ensures that matter is being accreted. The angular momentum of the gas element at the same radius r is obtained as,

$$\lambda_k = \sqrt{GM_{BH}r}. \tag{1.59}$$

Eq.(1.59) clearly indicates that angular momentum $[\lambda_K(r_{ms})]$ at the marginally stable orbit (r_{ms}) is very very less than the same $[\lambda_K(r_{out})]$ at the outer edge (r_{out}) of the disk. Therefore, in the steady state, the rate of angular momentum transport from the disk would be,

$$\dot{J} = \sqrt{GM_{BH}r_{out}}\dot{M}, \tag{1.60}$$

where, $\dot{M}$ represents a constant gas deposition rate into the disk in the steady state. Moreover, disk is characterized by it's *surface density* (Σ) which measures the mass per unit surface area of the disk, obtained by integrating the gas density ρ at the equatorial plane (z=0) in the vertical direction (z-direction) and is given by,

$$\Sigma = \int_{-h}^{h} \rho dz \approx 2h\rho, \tag{1.61}$$

where, h is considered to be the half thickness of the disk.

For a Keplerian disk, viscous stress tensor is obtained as,

$$t_{r\phi} = \eta r \frac{d\Omega}{dr} = -\frac{3}{2}\eta\Omega, \tag{1.62}$$

where, η denotes the dynamic viscosity coefficient. The viscous stress, f_ϕ, acted in the ϕ direction between the adjacent fluid layers is related to the viscous stress tensor as,

$$f_\phi = -t_{r\phi} = \frac{3}{2}\eta\sqrt{GM_{BH}/r^3}. \tag{1.63}$$

A detail overview of a steady state thin disk structure could be computed by solving the four conservation equations, namely, the conservation of mass, specific energy, specific angular momentum and vertical momentum respectively. In addition, possible dissipation processes (i.e. viscosity, radiation etc.) must also be specified for the shake of completeness of the problem.

Inside the disk, matter experiences more and more compression due to the geometric structure of the disk as it gradually moves in towards the compact star. Hence, density is increased and the variation of density can be identified from the integral of the continuity equation in the steady state. Under this circumstances, the mass accretion rate ($\dot{M}$) is obtained as,

$$\dot{M} = 2\pi r v_r \Sigma. \tag{1.64}$$

The factor 2π appears in the r.h.s. due to the geometric structure of the disk.

As the matter approaches the black hole, a fraction of angular momentum is consumed by the star itself and the rest is transported outwards. Let us denote $\dot{J}^+ = \dot{M}\sqrt{GM_{BH}r}$ as the inward rate of angular momentum transported across the radius r in the disk due to infalling matter. Since the angular momentum consumed by the black hole cannot exceed the value $\lambda(r_{ms})$ at the inner edge of the disk, the rate at which angular momentum is deposited in the compact star is given by,

$$\dot{J}^- = \beta\dot{M}\sqrt{GM_{BH}r_{ms}} \quad (\beta \ll 1; \text{for black hole } \beta = 1). \tag{1.65}$$

We have already mentioned that viscosity distributes angular momentum of gas element in a Keplerian value. Conservation of angular momentum demands that

the net change of rate of angular momentum within a fluid element at r must be balanced with the torque exerted by the viscous stress and we may have

$$\mathcal{G} = f_\phi \, 2\pi r.2h \; r = \dot{J}^+ - \dot{J}^- = \dot{M}\left[\sqrt{GM_{BH}r} - \beta\sqrt{GM_{BH}r_{ms}}\right]. \tag{1.66}$$

Eq.(1.66) indicates that f_ϕ could be identified uniquely in the steady state as a function of M_{BH} and $\dot{M}$ respectively. In addition, viscous dissipation process generates heat at a rate

$$\dot{Q}_+ = \rho T\frac{ds}{dt} \approx \frac{(t_{r\phi})^2}{\eta} = -\frac{f_\phi t_{r\phi}}{\eta}. \tag{1.67}$$

After some simplified algebra with Eq.(1.63), Eq. (1.66) and Eq. (1.67) one obtains,

$$2h\dot{Q}_+ = \frac{3\dot{M}}{4\pi r^2}\frac{GM_B}{r}\left[1 - \beta\left(\frac{r_{ms}}{r}\right)^{1/2}\right]. \tag{1.68}$$

Since the disk is thin, heat easily radiated away vertically through the disk surface and the radiated heat flux from the either side of the disk is given by,

$$F(r) = \frac{1}{2} \times h\dot{Q}_+ = \frac{3\dot{M}}{8\pi r^2}\frac{GM_B}{r}\left[1 - \beta\left(\frac{r_{ms}}{r}\right)^{1/2}\right]. \tag{1.69}$$

An important point is that the radiated heat flux does not depend on the nature of the viscosity prescription. The total disk luminosity is thus given by,

$$L = \int_{r_{ms}}^{\infty} 2F(r)\times 2\pi r dr = \left(\frac{3}{2} - \beta\right)\frac{GM_B\dot{M}}{r_{ms}}. \tag{1.70}$$

For a black hole, luminosity $L = GM_{BH}\dot{M}/2r_{ms}$ and it is exactly half of the potential energy of matter at the marginally stable orbit.

In the thin disk approximation, vertical velocity component v_ϕ is negligible with respect to other velocity components that puts matter in a hydrostatic equilibrium in the vertical direction. Thus, one can drop the advection term in the vertical component of the momentum balance equation and one obtains,

$$\frac{1}{\rho}\frac{dP}{dz} = \frac{d}{dz}\left[\frac{GM_{BH}}{\sqrt{r^2+z^2}}\right].$$

For a thin disk, $z \ll r$ and the above expression reduces to

$$\frac{1}{\rho}\frac{dP}{dz} = -\frac{GM_{BH}}{r^2}\frac{z}{r}. \tag{1.71}$$

If the typical scale height of the disk in the z-direction is h, one may set $dP/dz \sim P/h$ and $z \sim h$ and obtains

$$h \approx \left(\frac{P}{\rho}\frac{r^3}{GM_{BH}}\right)^{1/2} \approx \frac{a_s}{\Omega}, \tag{1.72}$$

where, $a_s(=P/\rho)$ denotes the sound speed of matter. Now, we can rewrite Eq. (1.58) as

$$\frac{h}{r} \approx \frac{a_s}{v_\phi}.$$

Therefore, the thin disk approximation ($h \ll r$) requires that the local Keplerian velocity should be highly *super − sonic* with respect to the azimuthal velocity (v_ϕ).

It is evident that a complete theory of disk accretion requires a prior knowledge of the nature of viscosity. Unfortunately the exact nature of viscosity prescription inside the accretion disk is still not very well known. One of the major problems is to explain the origin of large viscosity which is usually present inside the accretion disk. Moreover, in general, most of the well understood momentum transfer mechanisms, such as the molecular viscosity, radiative viscosity etc., are very slow processes compared to the viscosity that is estimated from observation. The most promising possibility is that the viscosity may be originated due to the magnetic transport of angular momentum or due to small scale turbulence in the gas-dynamical flow. Random magnetic fields may also contribute significantly to the viscosity as the fields are sheared by the disk differential motion and again reconnect at the boundary of the chaotic cells. Velikhov (1959), Chandrasekar (1960), Fricke (1969) and Balbus & Hawley (1991) intensely investigated the proper explanation of viscosity through the study of magnetic instability known as the *Balbus − Hawley instability*. This instability is responsible to give rise to a turbulence motion. Therefore, it is generally believed that the viscosity may be originated due to the small scale turbulence in a gas dynamical flow. With this consideration, the coefficient of dynamic viscosity η is estimated as,

$$\eta \approx \rho v_{turb} l_{turb}, \tag{1.73}$$

where, v_{turb} denotes the velocity of the turbulent cells relative to the mean gas motion and l_{turb} represents the size of the largest turbulent cells. For the supersonic motion of the gas, the turbulent kinetic energy is converted into heat at the shock which is possible when $v_{turb} \ll a_s$. Due to scale height restriction, turbulent cell size (l_{turb}) must be less than the disk height (h) as well. Hence, we may express the viscous stress as,

$$f_\phi = t_{r\phi} \leqslant \rho a_s h\Omega \sim \rho a_s^2 \sim P. \tag{1.74}$$

Thus, in general, the viscous stress may be approximated as,

$$f_\phi = \alpha P, \tag{1.75}$$

where, α is the non-dimensional viscosity parameter and $\alpha \leqslant 1$ to maintain causality condition. This is the well known α-disk prescription of Shakura & Sunyeav (1973).

Let us focus on the opacity property of the standard accretion disk model that contains a compact star of mass $M \sim M_{\odot}$. Most of the gravitational energy is released at the innermost part of the disk closest to the compact star which produces a high temperature in that region. Thus the disk becomes fully ionized there. Accordingly, opacity may be assumed to be dominated by the Thomson electron scattering process with the coefficient

$$\kappa_{scatt} = 0.4 \text{ cm}^2 \text{ g}^{-1}.$$

The frequency averaged Rossland mean absorption opacity is given by (Shapiro & Teukolsky, 1983),

$$\kappa_{abs} \sim \kappa_{ff} \sim 0.64 \times 10^{23} \rho T^{-7/2} \text{ cm}^2 \text{ g}^{-1}.$$

At the outer edge of the disk, the temperature of the gas is relatively lower compared to the inner edge. So absorption dominates over scattering in the outer regions. However, close to the accreting star the situation is completely opposite. Therefore, on an average, the Rossland mean opacity for the whole disk is obtain as

$$\frac{1}{\kappa_{mean}} = \frac{1}{\kappa_{scatt}} + \frac{1}{\kappa_{abs}}. \tag{1.76}$$

The accreting matter experiences a total pressure which is sum of the radiation and thermal gas pressure. For a fully ionized hydrogen gas, the total pressure is given by,

$$P = \frac{\rho k T}{\mu m_p} + P_{rad}, \tag{1.77}$$

where, $\mu = 0.5$ for fully ionized hydrogen. When the gas is in a thermodynamical equilibrium, the radiation pressure can be estimated as $P_{rad} \simeq \sigma T^4/3$. In general, gas pressure dominates over the radiation pressure all over the disk except at the innermost region where temperature is relatively high.

Inside the disk, radiation process plays an important role. Viscosity generates heat which is transported vertically through the disk before being radiated away from the disk surface. In the optically thick region, $\tau \gg 1$, radiations are transported via diffusion. Thus, in local thermodynamical equilibrium, the radiation flux $F(r, z)$ in the vertical direction is expressed by the following differential equation as

$$F(r, z) = -\frac{c}{3}\frac{d}{d\tau}(aT^4). \tag{1.78}$$

Here, τ ($= \int_0^h \kappa_{mean}\rho dz \sim \kappa_{mean}\Sigma$) is the optical depth computed from the Rosslandmean opacity and it is measured in the vertical direction only. Replacing differentials by finite differences, Eq. (1.78) takes the form at the surface of the disk as

$$F(r) \approx \frac{acT^4}{\tau} = \frac{acT^4}{\kappa\Sigma}. \tag{1.79}$$

Here, the flow variables are calculated at the disk equatorial plan (z=0). When the disk becomes optically thin, the radiations can escape almost freely from their emission point without suffering any scattering or absorption. In this particular situation, radiation flux strongly depends on the radiation emissivity which may arise due to the free-free emission or Comptonization.

Structure of a standard disk

In the previous Section, we have discussed about the various physical processes which occur inside the disk. We solve Eqs. (1.63, 1.64, 1.66, 1.69, 1.72, 1.75, 1.76, 1.79) for nine unknown disk variables, namely, $\rho(r), h(r), \Sigma(r), v_r(r), P(r), T(r), f_\phi(r), \kappa_{mean}(r)$ and $F(r)$ as a function of radial distance (r), mass of the central star (M_{BH}) and mass accretion rate ($\dot{M}$) following the prescription proposed by Shakura & Sunyeav (1973) and Novikov & Throne (1973). For specified values of (M_{BH}) and ($\dot{M}$) the solutions are distinctly subdivided in three different region, depending on r. Far away from the central star, *i.e.*, at the outer edge, contribution to the total pressure mainly comes from gas pressure and free-free absorption controls the disk opacity. In the intermediate location, gas pressure still dominates over the radiation pressure but opacity is dictated by the electron scattering. The condition $\kappa_{ff} \sim \kappa_{abs}$ identifies the transition radius between these two regions. At the innermost region, radiation pressure is high enough with respect to the gas pressure and scattering is the main cause for opacity. The boundary of the these regions is described by the condition $P_{gas} \sim P_{rad}$.

The final expression of the flow variables are as follows:

$F(r) = 5.0 \times 10^{26} M_{BH}^{-2} \dot{M}_{17} r^{-3}[1 - \sqrt{6/r}]$erg cm^{-2} s^{-1},

$\Sigma(r) = 7.0\alpha^{-1} M_{BH} \dot{M}_{17}^{-1} r^{3/2}[1 - \sqrt{6/r}]^{-1}$gm cm^{-2},

$h(r) = 1.0 \times 10^{-5} \dot{M}_{17}[1 - \sqrt{6/r}]$ cm,

$\rho(r) = 3.0 \times 10^{-5} \alpha^{-1} M_{BH} \dot{M}_{17}^{-2} r^{-3/2}[1 - \sqrt{6/r}]^{-2}$g cm^{-3},

$T(r) = 5.0 \times 10^{7} \alpha^{-1/4} M_{BH}^{-1/4} r^{-3/4} K$,

$\tau_{abs}(r) = 3.0\alpha^{-1} M_{BH} \dot{M}_{17}^{-1} r^{3/2}[1 - \sqrt{6/r}]^{-1}$, where, M_{BH} is measured in units of the mass of the Sun ($M_\odot$), $\dot{M}_{17}$ is in units of 10^{17}gm s^{-1} and r is measured in units of $GM_{BH}M_\odot/c^2$.

Emitted spectrum

So far, we have mentioned about the temperature (T) of the disk that belongs to the disk equatorial plane (z=0). In reality, surface temperature (T_s) of the disk is always somewhat lower than the temperature at the equatorial plan (T). For an optically thin disk, T and T_s are roughly comparable but for absorption dominated optically thick disk the emission process is followed by the black body radiation and the surface temperature of the disk is computed from the local effective temperature which given by,

$$T_s(r) = \left[\frac{4F(r)}{a}\right]^{1/4} \approx 5.0 \times 10^7 \left(\frac{M_{BH}}{M_\odot}\right)^{-1/2} \dot{M}_{17}^{1/4} r^{-3/4}[1-\sqrt{6/r}]^{1/4} \quad K,$$

where, $\sigma = ac/4$, and a is the radiation density constant. Therefore, whenever we know the temperature profile it is easy to estimate the emitted spectrum.

The standard thin disk model is thus able to explain the observational features of close binaries, quasars, AGNs etc. (Frank et al. 2002, Shapiro & Teukolsky, 1983) successfully. The drawback of this model is that disk is terminated at the marginally stable orbit (r_{ms}) and the inner boundary conditions are not satisfied as the advection term is ignored in the momentum balance equation. However, this disk model gives an insight that matter has to deviate from the Keplerian orbit to maintain the inner boundary conditions. In the subsequent Sections, we shall present more realistic disk model considering advection term and show that all the boundary conditions are perfectly satisfied there.

1.5.2 Thick accretion disk

In the previous Section, we have extensively discussed the theory of thin accretion disk model. The simplified assumptions accounted for the thin disk model are inadequate at the innermost region of the accretion disk around the black holes as the radiation pressure may cause disk to be thicken ($h(r) \sim r$) for super-Eddington accretion rate. Indeed, the inner part of the disk is usually called as accretion torus. Therefore, pressure effect (either due to radiation or hot ion) must be included to understand the behaviour of thermodynamical flow variables inside the disk which are believed to be responsible for determining the disk structure. Moreover, this model must also incorporate the significant infall velocity which ensures that matter should accrete more rapidly while falling into the black holes. Simultaneously, disk should also be shifted from Keplerian orbit to below the marginally stable orbit ($r = r_{ms}$) as well. The angular momentum distribution of the infalling matter would be modified from the Keplerian value when radiation pressure is included in the radial momentum equation — the angular momentum is super (sub) Keplerian wherever the pressure gradient term is positive (negative). Lynden-Bell (1978)

constructed a qualitative model with constant angular momentum considering the effect of radiation pressure and showed that disk is puffed up close to the black hole. They also pointed out that matter with considerable amount of angular momentum could not reach the vicinity of spinning axis of the disk and a funnel wall would be created around the rotation axis of the black hole. In that region, radiation pressure is sufficiently high which drives the accreted matter vertically outward and downward. This region is considered to be the suitable place to accelerate matter in the form of outflows or jets often observed in powerful radio sources. Latter on, Paczyński (Paczyński 1982) studied thick accretion disk model by incorporating rotation and advection terms together with various combinations of angular momentum in *ad hoc* basis. They studied the thick accretion disk model under a potential $\phi = -GM_{BH}/(r - 2GM_{BH}/c^2)$, where G and M_{BH} are the universal gravitational constant and mass of the black hole respectively and c is the velocity of light. This potential provides exactly identical Keplerian angular momentum distribution as obtained in Schwarzchild geometry. They also found that the thick disk smoothly merges with the standard thin disk at the outer edge. In some of the astrophysical models, accretion disks are equipped with coronae similar to solar surfaces where matter is anchored by magnetic flux tubes inside the disk. Isothermal thick accretion disk could successfully explain this structure. But the dynamical structure of the thick accretion disk is highly insensitive to the viscosity and the efficiency of accretion reduces sharply. However, for a stellar mass black hole, the temperature of the radiation pressure dominated disk is sufficiently high to ignite the possible nuclear reaction inside the disk. It is observed (Chakrabarti 1986a, 1988a, 1988b and Chakrabarti et al. 1987) that the nuclear reaction around the black hole is significant when the disk viscosity is negligible. Accordingly, nuclear reaction may change the composition of disk materials and outgoing jets for a stellar mass black hole (Chakrabarti et al. 1987 and Chakrabarti 1988b) and the observed metalicity of the galaxy which must contains number of stellar mass black holes could be understood. The qualitative nature of the angular momentum distribution is changed when mass of the disk is comparable or more than the central black hole, *i.e.* self-gravity cannot be neglected. A stable thick accretion disk is expected to be much hotter when self-gravity is important since the deviation of matter from the Keplerian origin is going to be higher. More realistic model of radiation supported thick accretion disk including self-gravity has recently been studied in full general relativity (Wiita 1982; Chakrabarti 1985, 1988b; Lanza, 1992) and similar conclusion is drawn. Indeed, one of the most attractive features of the thick accretion disk model is that it produces super-Eddington luminosity as the effective gravity is very strong compared to the centrifugal force close to the black hole horizon and therefore, the luminosity exceeds several times the Eddington luminosity. The spectrum emitted from the thick accretion disk is obtained in an identical manner as in the case of thin accretion disk by adding local black body contributions and it is slightly shifted towards the

higher effective temperature region due to opacity effects. Relativistic jet electrons Comptonize the ambient radiations and produce soft X-rays. This soft X-rays are observed in some optically selected radio quiet QSO sources which are believed to be originated due to this effect. Under this circumstances, an optical/UV bump is observed when the accretion torus is viewed at an high inclination (i.e. nearly perpendicular to the jet axis), whereas at low inclinations an excess in the UV/soft X-ray band is detected (Frank et al. 2002).

The effect of magnetic field in the form of the axisymmetric flux tube inside the thick accretion disk has recently been studied analytically (Nandi et al. 2001 and references therein). The toroidal flux tubes are expected to move along with the infalling matter and the extraction of magnetic flux tubes are taking place through the funnel due to the combined effects of drag force, Coriolis force, magnetic tension, buoyancy force and of course gravity force. Therefore, a significant amount of matter is supposed to emerge out vertically from the inner part of the disk in the form of jets. Since the inner part of the disk is disappeared by this magnetic activity, reduction of the emitted flux is expected. Observational result of the black hole candidate, GRS 1915+105, shows this feature clearly (Mirabel and Rodriguez 1994).

From the above discussion it is clear that the thick accretion disk model has a couple of interesting features such as the ability to collimate jet, to produce metalicity in galaxy by nucleosynthesis, activity in the funnel for the explanation of the rapid variability in BL-Lacs, production of supercritical luminosity etc. (Chakrabarti 1985). However, the strong anisotropic nature of the emission properties of a thick accretion disk is still a major disadvantage. And also non-accreting thick disk is found to be dynamically and globally unstable due to non-axisymmetric perturbations. Moreover, an ideal thick accretion disk requires the flow to have sufficiently high accretion rate involving very low angular momentum and negligible infall velocity. This picture could be constructed by including shock wave in an accreting matter of low angular momentum. At the shock, matter has very high temperature. This causes a puffed up torus which resembles the standard thick accretion disk. In the present context, we are not discussing this issue further.

Meanwhile, Abramowicz et al. (1988) proposed a treatment of accretion disk model assuming optically thick cooling with electron scattering and free-free opacities. In this model, the local solution instabilities at the inner most part of the disk are removed by introducing the advection term. The local vertical disk thickness is computed from the solution of this model — it produces small thickness for low accretion rate and tends to become of the order of radial distance ($h \sim r$) as the accretion rate approaches to the critical Eddington limit. In fact, the solution of this model makes the disk thickness intermediate between the standard thin and thick disk and is widely known as 'slim' disk.

1.6 Advective disk

In the earlier Section, we have already investigated the two extremity of the accretion models, namely, the Bondi flow and Keplerian disk model. In a Bondi flow, the matter does not possess any rotation but it has significant advection while in the Keplerian, the disk matter is mainly rotation dominated with a negligible advection. In reality, accretion flow must possesses both rotation and advection terms together. Thus, a self-consistent approach is required for exact modeling of the accretion flow problem. Now, we discuss the foundation of such a model in a qualitative manner.

So far, we focused our attention on to a more idealistic spherically symmetric model to keep our first step on to the subject. However, a realistic astrophysical flow is more complex and a number of different physical processes must be taken into account for the detailed study of the flow. In general, the flow must contain a significant amount of angular momentum that could be transported outwards due to presence of viscosity inside the flow. When the amount of the accumulating matter is comparable with the central star, self-gravity becomes important. In fact, flow may have dynamical magnetic fields and it may interact with radiations also. Since the flow is sufficiently hot close to the central star, thermonuclear reactions must play an important role inside the disk. Thus we improve the theory of accretion flow problem by considering many such physical processes in order of increasing complexity.

The fundamental criteria which must be satisfied is that the matter has to enter into the black hole super-sonically and it must be sub-Keplerian in nature at the black hole horizon. In fact, matter crosses the black hole boundary with the velocity of light, c. In a flow with a realistic equation of state, the maximum allowed value of sound speed is $c/\sqrt{3}$. On the other hand, both the standard thin and thick disk models are terminated before or at the marginally stable radius ($r_{ms} = 6$) and do not satisfy the inner boundary conditions. Inner boundary conditions demand that disk has to deviate from the Keplerian origin and matter must enter into the black hole with the super-sonic speed. To take care the inner boundary conditions we, therefore, include the advection term in the momentum balance equation which was absent in both these models.

Self-consistent study of the accretion disk problem was started in the late eighties by Chakrabarti and his collaborators. In 1989, Chakrabarti (Chakrabarti 1989a, hereafter C89a) presented a global solution for the astrophysical flow which is widely known as 'Chakrabarti solution'. Indeed, the present thesis is developed on the basis of such solutions. According to Chakrabarti's approach, the various properties of astrophysical flow can be understood through a systematic study of the basic flow equations. This is done through the several steps. Firstly, the initial flow parameters, namely, specific energy, specific angular momentum, accretion rate,

viscosity parameter etc., determine the number, nature and location of the sonic points of the accreted flow. This separates a region of parameter space for multiple sonic points from the single sonic point. The parameter space is spanned by the specific energy and specific angular momentum of the flow. Secondly, we look all the possible flow topologies for different set of initial parameters which specifically show how the flow originating from the outer edge of the disk is connected with the inner boundary of the black hole. And finally, we seek a special solution where the local flow variables make a discontinuous transition from the super-sonic branch to the sub-sonic branch and this discontinuous transition of flow variables is widely known as the 'shock'. In general, this shock is believed to be the fundamental ingredient for explaining the various aspects of the astrophysical observations around black holes.

Non-dissipative accretion disk around a black hole could be modeled in different ways depending on the flow geometry. In the astrophysical literature, three models, namely, Conical model, Constant Height model and Vertical Equilibrium model (C90a) are mostly highlighted. In the next two Sections, we shall briefly discuss the properties of Conical and Constant Height models and in Chapter 3, we shall illustrate the superiority of Vertical Equilibrium model over the other models when the transonic property of the accretion flow is considered.

1.6.1 Conical model

This toy model is specially designed in such a way that the accreted matter is confined within a conical shape container. We assume that non-viscous adiabatic matter accretes axisymetrically around a non-rotating black hole. We study the accretion flow problem within this frame work following the traditional approach, *i.e.*, finding sonic points, shock locations and its strengths etc. We use geometrical units ($G = M_{BH} = c = 1$) all throughout where radial distance is measured in units of GM/c^2 and so on. The basic equations in this model is described as (C90a),

(a) Energy equations:

$$\mathcal{E} = \frac{v^2}{2} + na^2 + \frac{\lambda^2}{2x^2} - \frac{1}{x-2}. \tag{1.80}$$

and

(b) accretion rate equations:

$$\dot{\mathcal{M}} = a^{2n} v x^2, \tag{1.81a}$$

where, the quantities have the same meaning as mentioned before.

We deduce the radial velocity gradient term by differentiating Eqs. (1.80-1.81a) and eliminating sound speed gradient which is given by,

$$\frac{dv}{dx} = \frac{\frac{2a^2}{x} + \frac{\lambda^2}{x^3} - \frac{1}{(x-2)^2}}{v - \frac{a^2}{v}}. \tag{1.82}$$

Sonic point conditions are obtained when both the numerator and the denominator vanish simultaneously at the same location and setting this criteria one gets the sonic point conditions which are given by,

$$v_c = a_c; \quad M(x_c) = 1, \tag{1.83a}$$

and

$$a_c^2 = \frac{x}{2(x-2)^2} - \frac{\lambda^2}{2x^2} = \frac{\lambda_K^2 - \lambda^2}{2x^2}, \tag{1.83b}$$

where, λ_K is Keplerian angular momentum which is defined as $\lambda_K = \sqrt{x^3/(x-2)^2}$. Eq. (1.83a) shows that in the phase space plot Mach number of the flow becomes unity at the location of the sonic point. Eq. (1.83b) gives the expression of sound speed at the sonic point which must be positive for any initial flow parameters. This indicates that angular momentum of the flow at the sonic point must be always lower than the Keplerian value, *i.e.*, matter angular momentum must be sub-Keplerian always.

More importantly, the behaviour of the flow variables at the critical points could be illustrated by using the sonic point conditions in the governing equations [Eq. (1.80)]. Following this criteria one could express specific energy of the flow in terms of angular momentum and location of the sonic points which is given by,

$$\mathcal{E} = \frac{(2n+1)}{4}\frac{x_c}{(x_c-2)^2} - \frac{1}{x_c-2} - \left(\frac{2n-1}{4}\right)\frac{\lambda^2}{x_c^2}. \tag{1.84}$$

Fig. 1.5 shows a three dimensional plot of a function $\mathcal{E} = \mathcal{E}(x_c, \lambda)$ where variation of specific energy at the sonic points is shown for different values of angular momentum and sonic point locations when polytropic index is set at $n = 3$. Note that in the higher angular momentum regime, specific energy of the flow has both the minima ($\mathcal{E}_{min}$) and maxima ($\mathcal{E}_{max}$). This indicates that flow may possess multiple sonic points when angular momentum of the flow is chosen beyond a critical value. Among these sonic points two are 'X'-type flanking a 'O'-type one. An 'X'-type point closer to the black hole horizon is called as *inner* sonic point and the furthest one is termed as *outer* sonic point. All these sonic points merge at a single point which is known as *cusp* for a particular angular momentum called as critical angular momentum of the flow. Moreover, existence of the 'X'-type sonic point ensures a topological connection in between the black hole horizon and infinity through this

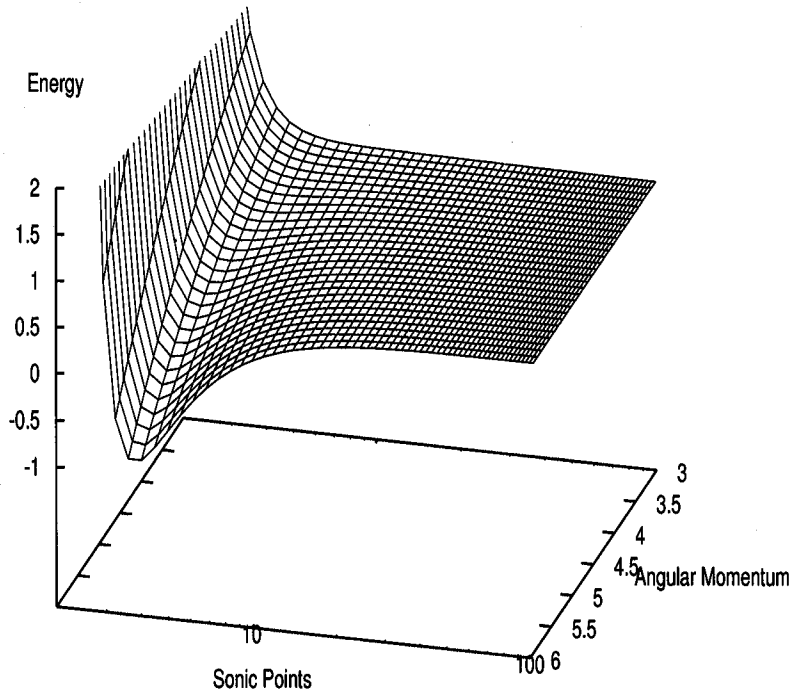

Figure 1.5: Plot of the surface $\mathcal{E} = \mathcal{E}(x_c, \lambda)$. Note that, energy of the flow is not in the proper scale.

point provides a unique solution of the problem. The two 'X'-type sonic points may also be linked through the shock which forms in between them. We shall present a detail shock study in the next Chapter.

1.6.2 Constant height model

The description of this model is very similar to the Conical model. It differs from the earlier one only from the geometrical structure of the disk under consideration. Here we assume that the disk height remains constant irrespective of the radial distance of the disk (C90a and Chakrabarti & Molteni 1993). Since the geometry of the present model is different form the earlier one, the entropy-accretion rate equation will be modified but the energy equation will remain unchanged.

In the cylindrical coordinate system, the entropy-accretion rate equation becomes

$$\dot{\mathcal{M}} = a^{2n} v x. \tag{1.81b}$$

Now, one can easily calculate the accretion flow properties using the governing equations of the flow following the similar method discussed in the earlier Section. In this model, multiple sonic points as well as shocks form for relatively higher values of initial flow parameters compared to the Conical model. Interestingly, Constant Height model also provides much larger area in the parameter space, which is spanned by the energy and the angular momentum of the flow, for multiple sonic points and shocks.

So far, we have discussed astrophysical flows with different toy models which do not have any real physical importance. In spite of that it successfully gives some important insight of the transonic behaviour of the flow. In the next Chapter, we shall rigorously study a more realistic astrophysical flow considering most successful accretion disk model in the literature which is commonly known as the *Vertical Equilibrium Model*.

Chapter 2

Hybrid Model for Advective Flow

In Chapter I, we have discussed various accretion disk models which are very simplistic in nature. In this Chapter, we study a more complex astrophysical system for explaining the essential observational features of the black hole candidates. A self-consistent study of the astrophysical flow around the black holes comes in the literature in the late eighties. Chakrabarti (C89a) presented a most general transonic flow model usually called as *hybrid model* which started a new era in accretion disk physics. A solution is easily obtained following the general method described earlier and the problem associated with the thick accretion flow is circumvented by the proper choice of the shock conditions. Modeling of a three dimensional flow around a back hole is done by assuming the flow to be rotating, thin, axisymmetric, and non-dissipative in nature. Moreover, in the present model, accreted matter is supposed to be mostly advection dominated, *i.e.*, radial velocity dominated. In addition, we consider that the flow may be in a hydrostatic equilibrium in a direction transverse to the flow motion. The governing equations are written down in the disk equatorial plane where vertically averaged pressure and density at the equatorial plane identify their exact values at the disk surface. In this context, we investigate all the stationary flow solutions of this model with or without shock. This flow solutions strictly depend on the initial flow parameters, such as specific energy, specific angular momentum, accretion rate etc. and successfully illustrate the different properties of the astrophysical flow.

2.1 Governing equations and the sonic point analysis

We begin with the assumption that non-dissipative, adiabatic, sub-Keplerian, inviscid matter is accreted on to a Schwarzschild black hole. The general relativistic effect is taken care of by the Paczyński-Wiita (PW80) potential. Basic equations are written on the equatorial plane of the accretion disk while the radial momentum balance equation which must be satisfied at the shock is vertically integrated (Mat-

sumoto et al., 1984). Flow equations are made dimensionless considering unit of length, time and the mass as $2GM_{BH}/c^2$, $2GM_{BH}/c^3$ and M_{BH} respectively where G, M_{BH} and c represent their usual meaning mentioned earlier.

In the steady state, the dimensionless energy equation can be written as (C90a)

$$\mathcal{E} = \frac{1}{2}v_e^2 + \frac{a_e^2}{\gamma - 1} + \frac{\lambda^2}{2x^2} - \frac{1}{2(x-1)}, \tag{2.1}$$

where, $\mathcal{E}$ is the specific energy, v_e is the radial velocity and a_e is the adiabatic sound speed defined as $a_e = \sqrt{\gamma P_e/\rho_e}$. Since the viscosity is considered to be negligible in the present study, specific angular momentum (λ) of the flow will remain conserved all throughout. Here, x represents the radial distance from the black hole when the black hole itself is considered to be located at the origin of the cylindrical coordinate system. The subscript 'e' refers to the quantities measured on the equatorial plane. The mass flux conservation equation (C90a) in the steady state apart from the geometric factor is given by,

$$\dot{M} = v_e \rho_e x h, \tag{2.2}$$

where, $\dot{M}$ is the mass accretion rate considered to be constant, ρ_e is the density of the flow and h represents the half-thickness of the flow at a radial distance x. The present model is constructed in such a way that the disk is assumed to be in hydrostatic equilibrium in the vertical direction and therefore, local disk height is obtained by equating the pressure gradient force in the vertical direction with the component of the gravitational force in that direction. The analytical expression of half thickness of the disk is thus obtained as,

$$h = a_e x^{1/2}(x-1). \tag{2.3}$$

In Eq. (2.3), we drop a constant factor $\sqrt{2/\gamma}$ since the adiabatic index (γ) is considered to be a constant all throughout. Hydrostatic equilibrium condition of matter in the vertical direction is justified as the infall time exceeds the local sound crossing time in the transverse direction of the flow. Since the flow is adiabatic in nature, the flow is characterized by the polytropic equation of state, $P = K\rho^\gamma$, where K is a constant related to the specific entropy of the flow which can vary only at the shock. For a non-dissipative accretion flow, Chakrabarti (C89a) defines a new conserved quantity of the flow which is connected with the mass accretion rate ($\dot{M}$) through the relation $\dot{\mathcal{M}} = \gamma^n K^n \dot{M}$. The new conserved quantity is known as the 'entropy-accretion rate' and it is expressed in terms of the flow variables as,

$$\dot{\mathcal{M}} = v_e a_e^\nu x^{3/2}(x-1), \tag{2.4}$$

where, $\nu = (\gamma+1)/(\gamma-1)$. In the present thesis, we are interested to study the properties of the shock wave. In an accretion flow, shock forms when the flow

becomes supersonic at some point, *i.e.*, stationary flow definitely passes through the sonic point. We derive the sonic point conditions following the traditional way. We, therefore, differentiate Eq. (2.1) and Eq. (2.4) and eliminate da/dx from them to obtain radial velocity gradient which is given by,

$$\frac{dv}{dx} = \left\{ \frac{2a^2}{(\gamma+1)} \frac{5x-3}{2x(x-1)} - \frac{d}{dx}\left[\frac{\lambda^2}{2x^2} - \frac{1}{2(x-1)}\right] \right\} \Big/ \left[v - \frac{2a^2}{(\gamma+1)v} \right], \tag{2.5}$$

where, we drop the subscript 'e' to avoid confusion. In order to have the flow smooth everywhere, the numerator and the denominator in Eq. (2.5) must vanish simultaneously which give the sonic point conditions. Setting denominator equal to zero, we may have,

$$v_c^2(x_c) = \frac{2}{(\gamma+1)} a_c^2(x_c) \quad \Rightarrow \quad M_c^2 = \frac{2}{\gamma+1}. \tag{2.6a}$$

The subscripts 'c' denotes the quantity at the sonic points. Note that the Mach number $[M(x_c)]$ at the sonic point is not unity as in the other models since the vertical equilibrium model is considered. The other condition comes while setting the numerator equal to zero and is given by,

$$a_c^2(x_c) = \frac{(\gamma+1)(x_c-1)}{x_c^2} \frac{(\lambda_K^2 - \lambda^2)}{(5x_c-3)}. \tag{2.6b}$$

Here, λ_K is the Keplerian angular momentum defined as $\lambda_K = \sqrt{\frac{1}{2}x^3/(x-1)^2}$. From Eq. (2.6b) one can easily calculate the sound speed at the sonic point and it must be always positive. This demands that angular momentum of the stationary flow must be sub-Keplerian at the sonic point, *i.e.*, $\lambda(x_c) < \lambda_K$. We solve Eqs.(2.1-2.6b) to obtain a full set of flow solutions where shock may present.

In order to model the astrophysical flow, we have introduced three conserved quantities, namely, specific energy ($\mathcal{E}$), accretion rate ($\dot{\mathcal{M}}$) and specific angular momentum (λ) respectively. These three conserved quantities are not strictly independent to each other as we have two additional conditions (sonic point conditions) which must be obeyed by the stationary flow. Hence, either the energy or the accretion rate can be expressed in terms of the other two conserved quantities. Therefore, the parameter space for a steady astrophysical flow solution lie on a hyper surface,

$$\mathcal{F}(\mathcal{E}, \dot{\mathcal{M}}, \lambda) = 0. \tag{2.7}$$

This indicates that the conserved quantities are the 'eigenvalues' of the problem.

Sub-sonic matter coming from infinity becomes super-sonic while passing through the sonic point before entering into the black hole. Thus, black hole accretion flow

solutions are always transonic. In the present context, we discuss the behaviour of sonic points in a great detail. The specific angular momentum of the flow at the sonic point can be evaluated using sonic point conditions [Eqs. (2.6a-b)] in Eq. (2.1) and is given by,

$$\lambda^2 = \frac{\{2\mathcal{E}(x_c-1)+1\}(5x_c-3)x_c^2 - 2(n+1)x_c^3}{\{(5x_c-3)-4(n+1)(x_c-1)\}(x_c-1)}. \tag{2.8a}$$

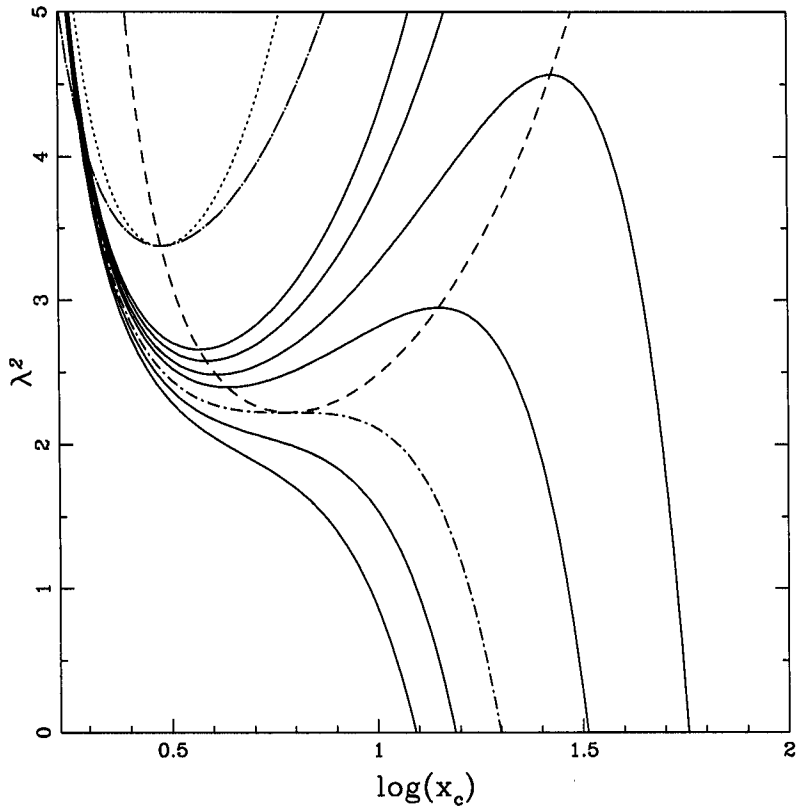

Figure 2.1: Plot of λ^2 with the sonic point for a set of different energies. Details of the figure are described inside the text.

Fig. 2.1 describes the variation of λ^2 with logarithmic location of the sonic point, $\log(x_c)$, as obtained from Eq. (2.8a) for a set of energies of the flow. The dot-long dashed curve is plotted for the Keplerian angular momentum distribution. The dotted curve is drawn for the marginally stable energy, $\mathcal{E} = -0.0625$ which touches the Keplarian value at the marginally stable orbit, $x_{ms} = x_c = 3$ (in units of r_g). Solid curves (top to bottom) correspond to the energy $\mathcal{E} = -0.005, 0.0, 0.0055, 0.01, 0.023$

and 0.03 respectively while the dot-short dashed curve represents a critical plot for $\mathcal{E}_{cri} = 0.017176$. Negative energy curves are drawn for the bound solutions. It is clear that the flow has multiple sonic points when $0 \leq \mathcal{E} \leq \mathcal{E}_{cri}$ and all the sonic points merge to a single point when the flow energy matches exactly with critical energy parameter $\mathcal{E}_{cri} = 0.017176$. Above this critical energy $\mathcal{E} > \mathcal{E}_{cri}$, the flow has only one sonic point (Bondi like solution). In addition, the locus of the extrema of the curves is indicated by the short-dashed curve. In the present context, polytropic index is chosen as $n = 3$ and we use this value in the rest of the discussion.

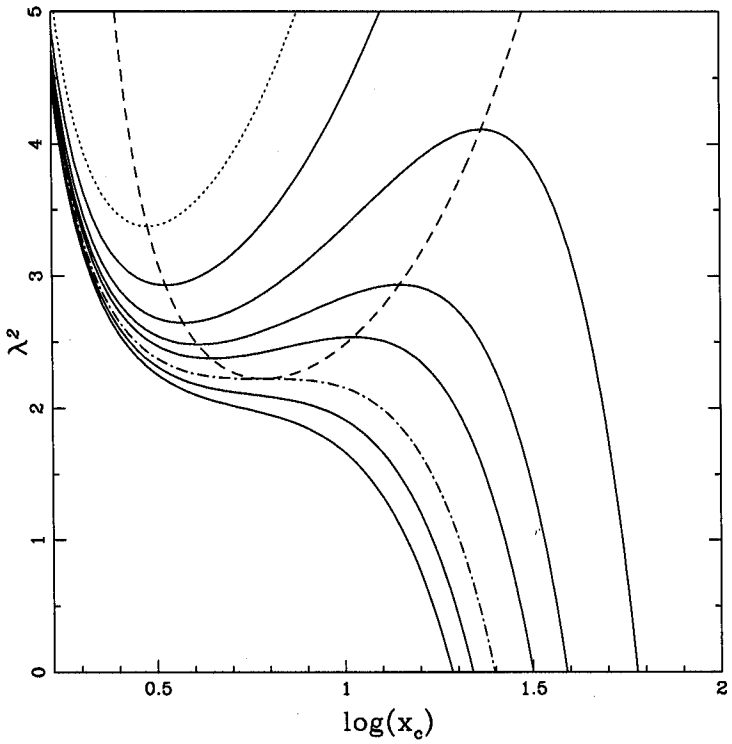

Figure 2.2: Plot of (λ^2) with the sonic point for various accretion rates. Details of the figure are illustrated inside the text.

On the other hand, specific angular momentum of the flow at the sonic point can also be expressed in terms of the other flow parameter, namely, the accretion rate $(\dot{\mathcal{M}})$ and is obtained as,

$$\lambda^2 = \left\{ \frac{(2n+1)}{nx_c^2} \frac{x_c - 1}{5x_c - 3} \lambda_K^2 - \left[\sqrt{\frac{2n+1}{2n}} \frac{\dot{\mathcal{M}}}{x_c^{3/2}(x_c - 1)} \right]^{1/(n+1)} \right\} \left[\frac{(2n+1)}{nx_c^2} \frac{x_c - 1}{5x_c - 3} \right]^{-1} \tag{2.8b}$$

Fig. 2.2 shows a similar plot $[\lambda^2 - \log(x_c)]$ as in Fig. 2.1 for a set of constant accretion rates ($\dot{\mathcal{M}}$). The lower value of the accretion rate in transonic accretion flow is obviously zero which provides the Keplerian angular momentum distribution identified with the dotted curve. The solid curves (from top to bottom) are drawn for various accretion rates (in units of 10^{-5}), namely, $\dot{\mathcal{M}} = 0.1, 0.6, 1.2, 1.7, 3.2$ and 4.0 respectively while the dot-dashed curve corresponds to the critical accretion rate $\dot{\mathcal{M}}_{cri} = 2.731$ above which ($\dot{\mathcal{M}} > \dot{\mathcal{M}}_{cri}$) flow does not have multiple critical points. Moreover, the short-dashed curve represents the locus of the extrema of the curves as described earlier.

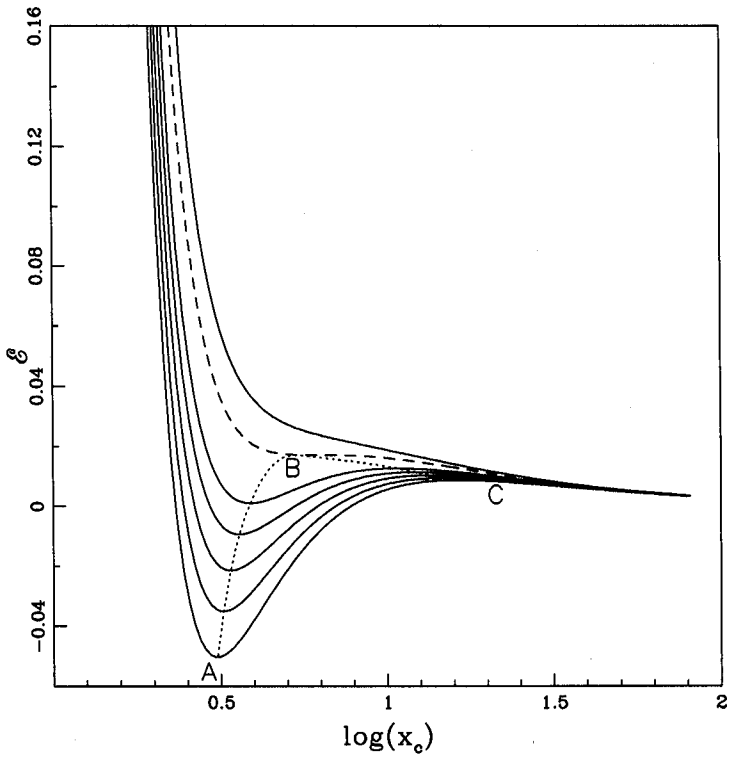

Figure 2.3: Variation of specific energy ($\mathcal{E}$) as a function of logarithmic sonic point locations $[\log(x_c)]$ for a set of λ.

The specific energy of the flow at the sonic point is obtained from Eq. (2.8a) while the specific angular momentum (λ) of the flow is treated as a flow parameter. Thus, we have the expression of specific energy as,

$$\mathcal{E} = \frac{(n+1)x_c}{(x_c-1)(5x_c-3)} + \frac{\lambda^2}{2x_c^2}\left[1 - \frac{4(n+1)(x_c-1)}{(5x_c-3}\right] - \frac{1}{2(x_c-1)}. \qquad (2.8c)$$

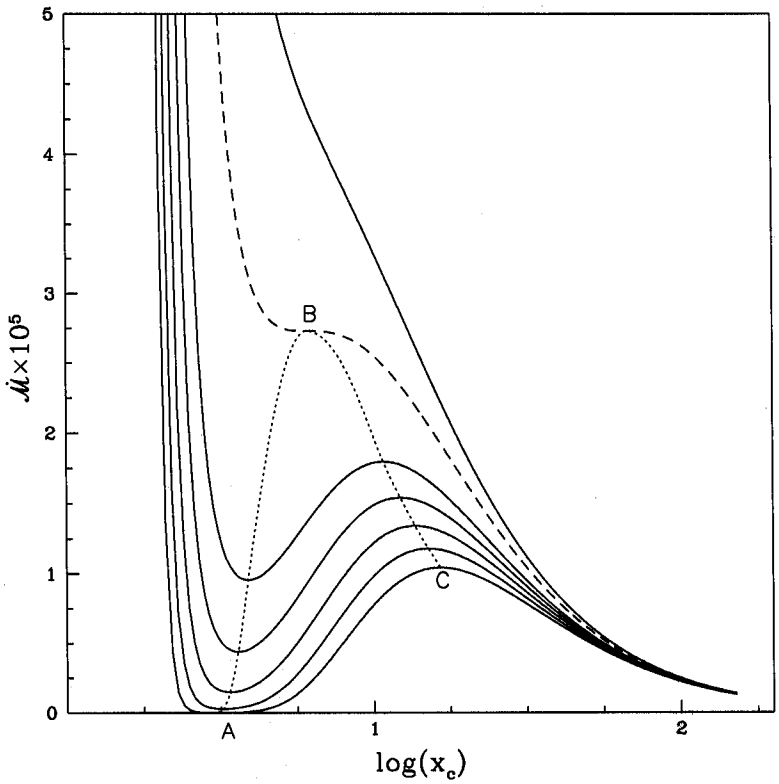

Figure 2.4: Variation of accretion rate is plotted against logarithmic sonic point locations for a set of λ.

The generic behavior of Eq. (2.8c) could be understood well when the specific energy of the flow is plotted against the location of the sonic points. This is done in Fig. 2.3 where energy distribution is shown for a set of constant angular momentum (λ). Similarly, in Fig. 2.4, variation of accretion rate at the sonic point for a set of fixed λ is also presented. Solid curves are drawn for a set of $\lambda = 1.4, 1.6, 1.65, 1.7, 1.75, 1.8$ respectively (from top to bottom curve) and the dashed curve corresponds to the critical angular momentum $\lambda_{cri} = 1.491$ in both the Figures. Dotted curve (ABC) represents the locus of the extrema of the curves. Note that, for a given angular momentum (λ) multiple critical points exist for a distinct energy or accretion rate range which is given by $\mathcal{E}_{min} < \mathcal{E} < \mathcal{E}_{max}$ or $\dot{\mathcal{M}}_{min} < \dot{\mathcal{M}} < \dot{\mathcal{M}}_{max}$. Moreover, a flow with $\lambda < \lambda_{cri}$ has only one critical point (Bondi like). The locus of the extrema (ABC) of the curves can be identified separately when it is viewed from the different angles in a $\lambda^2 - \dot{\mathcal{M}}$ plane.

Fig. 2.5 shows the projection of such a plot where the region bounded by ABC

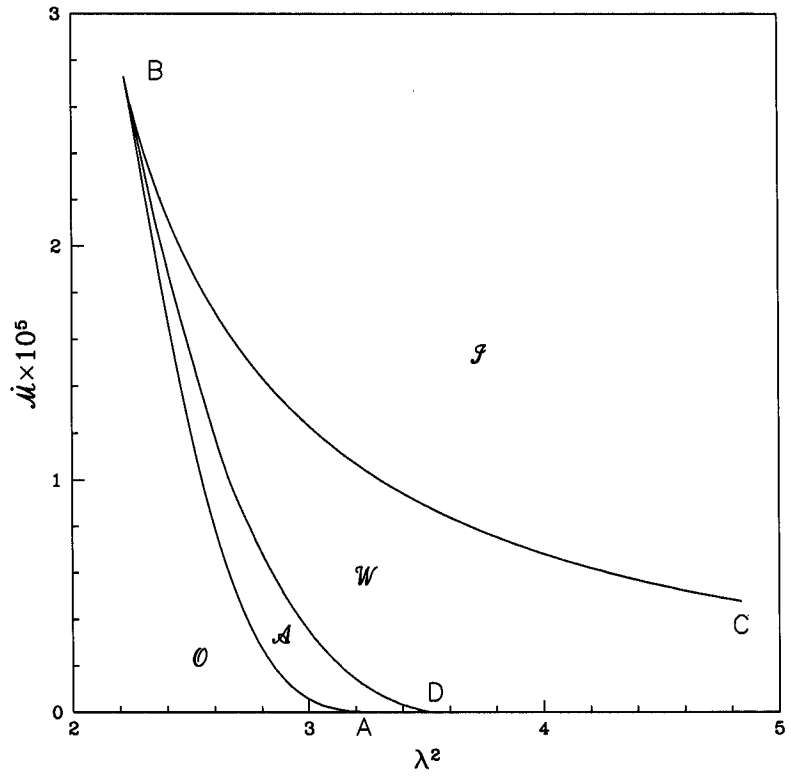

Figure 2.5: Division of the parameter space for multiple sonic points region for accretion and winds.

separates the multiple sonic points region from the single sonic point region. For a given set of initial flow parameter $(\mathcal{E}, \lambda)$ one can uniquely determine the multiple sonic points. Among the multiple sonic points two are 'X'-type sonic points. The point closer to the black hole horizon is known as the inner sonic point (x_{ci}) and the farthest one is termed as the outer sonic point (x_{co}). At these two sonic points entropy is not in general equal and consequently, the entropy accretion rate is also different there. It is already mentioned that the entropy accretion rate of the stationary transonic flow can be obtained as a function of specific energy and specific angular momentum (Eq. 2.7) of the flow. Moreover, for a given λ, there exists an energy $\mathcal{E}_s$, such that $\dot{\mathcal{M}}_s(\mathcal{E}_s, \lambda, x_{ci}) = \dot{\mathcal{M}}_s(\mathcal{E}_s, \lambda, x_{co})$. Thus the stationary flow with $(\dot{\mathcal{M}}_s, \mathcal{E}_s)$ has the same entropy at the inner and the outer sonic points and the flow will cross both the sonic points before falling into the black hole. In Fig. 2.5, such a special locus of accretion rates $(\dot{\mathcal{M}}_s)$ is indicated by the curve BD and at the same time this curve also divides the multiple sonic points boundary

in two regions—the region bounded by the curves BD and BC corresponds to the multiple sonic points for wind ($\mathcal{W}$) where $\dot{\mathcal{M}}(\mathcal{E}, \lambda, x_{ci}) < \dot{\mathcal{M}}(\mathcal{E}, \lambda, x_{co})$ whereas the curves BA and BD separate the region of parameter space for accretion ($\mathcal{A}$) where $\dot{\mathcal{M}}(\mathcal{E}, \lambda, x_{ci}) > \dot{\mathcal{M}}(\mathcal{E}, \lambda, x_{co})$. In the region $\mathcal{I}$ above BC, the flow possesses a single sonic point nearer to the black hole horizon and in region $\mathcal{O}$ below AB, the flow has only outer sonic points (Bondi like).

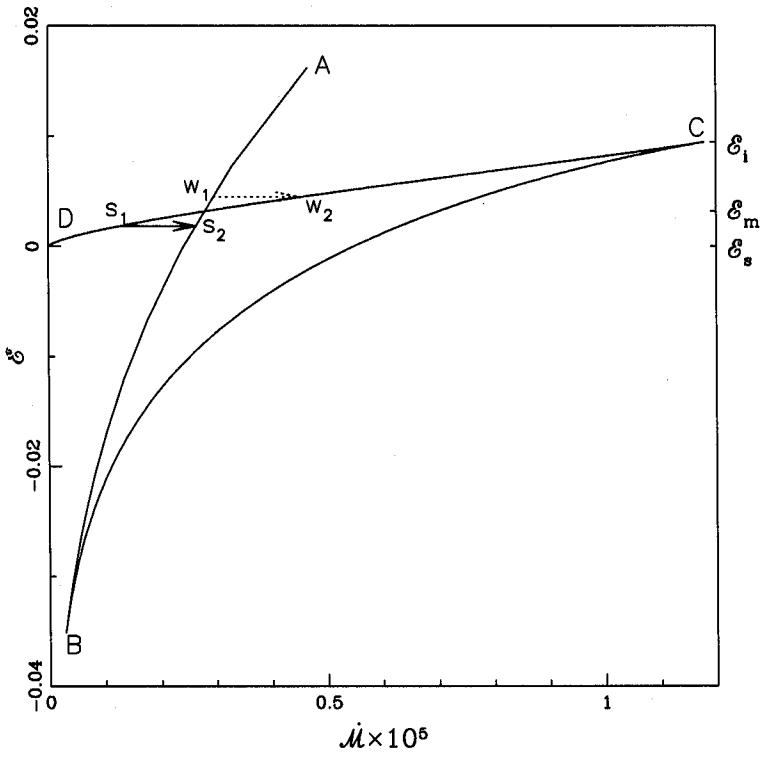

Figure 2.6: Variation of the energy with the accretion rate for a fixed angular momentum ($\lambda = 1.675$). Details of the figure are described inside the text.

For the shake of completeness of the sonic point analysis, we further study the variation of $\mathcal{E}$ as a function of $\dot{\mathcal{M}}$ for a given λ for all possible stationary solutions. Fig. 2.6 shows such plot when $\lambda = 1.675$ is chosen. A transonic flow with initial flow parameters which lies on the branch AB passes through the inner 'X'-type sonic point and a flow with parameters belonging to the branch CD has the outer 'X'-type sonic point. The parameters chosen from BC branch give the 'O'-type sonic point. A stationary flow avoids to have the 'O'-type sonic point as radial velocity gradient at this point becomes complex. The branches AD and CD intersect at a common point where the accretion rates at both the sonic points are equal. Such a critical

accretion rate is denoted by $\dot{\mathcal{M}}_m$ and the corresponding energy is represented by $\mathcal{E}_m$. Note that the flow with energy $\mathcal{E} > \mathcal{E}_i$ has only one inner sonic point whereas flow with energy $\mathcal{E} < \mathcal{E}_s$ passes through the outer sonic points. For $\mathcal{E}_m \leq \mathcal{E} \leq \mathcal{E}_i$, the accretion rate $\dot{\mathcal{M}}_o \geq \dot{\mathcal{M}}_i$ and for $\mathcal{E}_s \leq \mathcal{E} \leq \mathcal{E}_m$, $\dot{\mathcal{M}}_o \leq \dot{\mathcal{M}}_i$, where, the subscripts 'i' and 'o' denote the quantities at the inner and outer sonic points respectively. A similar divisions can be made in terms of the accretion rates also.

2.2 Shock waves

Before going to discuss the implication of shock waves we first highlight the basic physics involved in the formation of shocks in an astrophysical flow. Rotating matter accreted around a black hole experiences mainly two forces which dictate the notion of the particle trajectory. The first one is the inward gravitational force, $F_g \propto 1/(x-1)^2$ and the second one is the outward centrifugal force, $F_{cen} \propto 1/x^3$ for a flow having constant angular momentum. Both the principal forces strictly depend on the radial distance. Therefore, the gravity dominates over the centrifugal force at a distance either close to or far away from the black hole whereas the centrifugal force becomes comparable to gravity at intermediate locations. Accordingly, matter at infinity feels the gravitational pull due to the black hole and accretes toward it with increasing inward velocity which becomes super-sonic at some point. Since matter moves with super-sonic velocity, no information can travel back. As a result, incoming matter is piled up in this region. At a distance of few tens of r_g outward centrifugal force starts to dominate over gravity and thus matter slows down. In fact, the matter virtually stops there. Therefore, density goes up and matter makes a discontinuous transition from super-sonic branch to sub-sonic branch which is termed as a *shock*. Just after the shock, sub-sonic matter is again attracted towards the black hole due to gravity and it crosses the inner sonic point to become super-sonic before crossing the black hole horizon. At the shock, kinetic energy of the pre-shock matter is dissipated which makes the post-shock matter hot. Thus, at the post-shock region disk puffs up in the form of a torus due to the combined effects of matter accumulation and the heat generation and the inner part of the disk behaves like an 'effective boundary layer' (C96a) of the black hole which is widely known as the CENBOL (CENtrifugal pressure supported BOundary Layer).

2.2.1 Shock conditions

In order to have a shock, the flow velocity must jump discontinuously from super-sonic to sub-sonic branch. This discontinuous shock jump is characterized by four flow variables, namely, shock location (x_s), radial velocity (v), sound speed (a) and entropy constant (K) respectively and are given by,

$$x = x_s, \tag{2.9a}$$

$$\Delta v = v_+(x_s) - v_-(x_s), \tag{2.9b}$$

$$\Delta a = a_+(x_s) - a_-(x_s), \tag{2.9c}$$

and

$$\Delta K = K_+ - K_-, \tag{2.9d}$$

where, the subscripts '-' and '+' denote the quantities before and after the shock. Moreover, the conservation of mass flux and momentum flux are guaranteed at the shock transition which impose two extra constraints on the above mentioned flow variables. The conserved quantities at the shock are (C89a and Chakrabarti 1990b, hereafter C90b) given by,

$$\dot{M}_+ = \dot{M}_-, \tag{2.10a}$$

and

$$\tilde{P}_+ + \tilde{\rho}_+ v_+^2 = \tilde{P}_- + \tilde{\rho}_- v_-^2, \tag{2.10b}$$

where, $\tilde{P}$ and $\tilde{\rho}$ represent the average pressure and the density of the flow respectively. Under this circumstances, three different type of shocks are of special interest corresponding to three extreme physical considerations. These are named as Rankine-Hugoniot shock ($\mathcal{E}_+ = \mathcal{E}_-$), isentropic compression wave ($\dot{\mathcal{M}}_+ = \dot{\mathcal{M}}_-$) and isothermal shock ($a_+ = a_-$) (C90b).

In case of a Rankine-Hugoniot shock (Landau & Lifshitz 1959), the energy is not radiated away through the surface boundaries of the flow as the radiative cooling processes are not sufficiently efficient inside the disk. However, since the post-shock temperature is significantly higher than the pre-shock flow, the disk thickness at this region is more compared to the pre-shock disk. The basic condition for this type of shock is $\mathcal{E}_+ = \mathcal{E}_-$, $T_+ > T_-$ and $s_+ > s_-(\dot{\mathcal{M}}_+ > \dot{\mathcal{M}}_-)$ where s denotes the entropy of the flow.

In case of an isentropic compression wave, the entropy does not change in the flow but a considerable part of the energy is lost at the shock. The amount of entropy at the shock front is comparable to the entropy radiated away from the disk which may help to maintain a proper balance of entropy. For this type of shock, $s_+ = s_-$, $\mathcal{E}_+ < \mathcal{E}_-$ and $T_+ > T_-$.

In an isothermal shock, the radiative cooling processes are highly efficient. Some energy and entropy are lost from the surface of the flow at the shock front to maintain uniform pre-shock surface temperature identical to its post-shock value. Accordingly, sound speed and the flow thickness remain unchanged across the shock. For this type of shock, $T_+ = T_-$, $\mathcal{E}_+ < \mathcal{E}_-$ and $s_+ < s_-$.

So far, we have classified different types of shock waves depending on various flow constraints. However, presently we are specially interested to study the non-dissipative inviscid adiabatic flow near a non-rotating black hole. Therefore, at this moment we concentrate on the Rankine-Hugoniot shock conditions which will serve our purpose successfully. We are dealing with a quasi two dimensional flow where pressure and density are averaged over in the vertical direction. In this regards, we recapitulate the Rankine-Hugoniot shock conditions (Landau & Lifshitz 1959) once again which are given by,

(I) the energy conservation equation,

$$\mathcal{E}_+ = \mathcal{E}_-, \tag{2.11a}$$

(II) the self-consistent pressure condition,

$$W_+ + \Sigma_+ v_+^2 = W_- + \Sigma_- v_-^2, \tag{2.11b}$$

and (III) the baryon number conservation equation,

$$\dot{M}_+ = \dot{M}_-. \tag{2.11c}$$

Here, W and Σ denote the vertically averaged pressure and density of the flow (Matsumoto et al. 1984) and is given by,

$$W = \int_{-h}^{h} P dz = 2P_e I_{n+1} h,$$

and

$$\Sigma = \int_{-h}^{h} \rho dz = 2\rho_e I_n h,$$

where, $I_n = (2^n n!)^2/(2n+1)!$ and n is the polytropic index defined earlier. The subscript 'e' denotes the quantities at the equatorial plane and in the subsequent analysis we drop it to avoid further confusion. Note that, in the hybrid model, some equations are written down in the disk equatorial plane and the rest are written with vertically integrated quantities.

2.2.2 Shock solutions

In the earlier Section, we have extensively studied different parts of parameter space for the rotating stationary transonic flow. Suitable flow parameters confirm the existence of multiple sonic points and also provided a possibility of shock formation in a flow. In a stationary accretion flow with shock, the flow must cross the outer sonic point first, then pass through a discontinuity known as the shock and finally

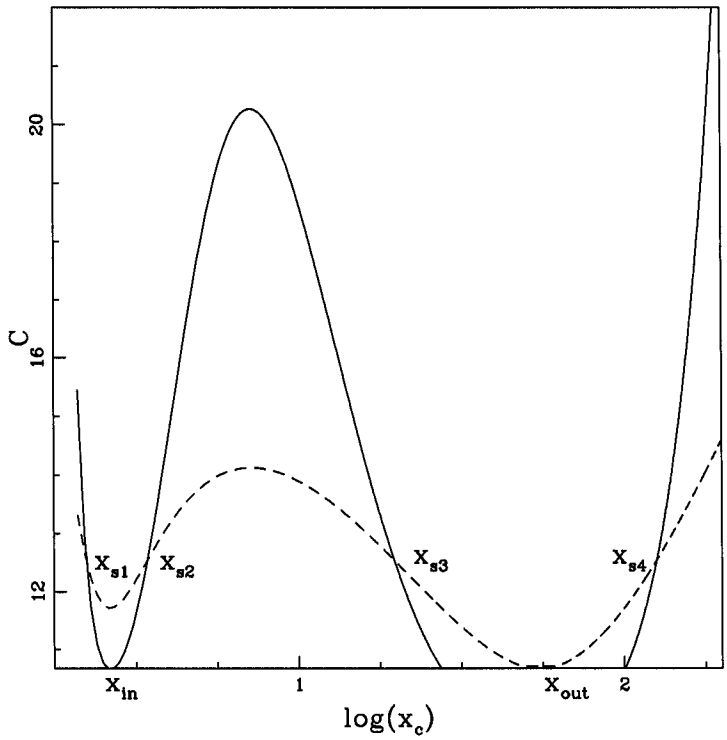

Figure 2.7: Contours of constant $\dot{\mathcal{M}}_-$ and $\dot{\mathcal{M}}_+$ in $C - log(x_c)$ plane for a set of flow parameters ($\mathcal{E} = 0.0047$, $\lambda = 1.69$) which satisfy the shock conditions in accretion flow. Solid and dotted curves are drawn for $\dot{\mathcal{M}}_- = 5.66 \times 10^{-06}$ and $\dot{\mathcal{M}}_+ = 4.88 \times 10^{-06}$. The intersection points represent the shock locations and x_{in} and x_{out} corresponds to the inner and the outer sonic points respectively.

crosses the inner sonic point before entering into the black hole. In the case of shock in wind, the situation is completely opposite. A typical example of such solution are shown in Fig. 2.6 where the shock transition is indicated by the solid (accretion) and dotted (wind) arrows.

In order to have the shock, flow has to satisfy the shock conditions along with all the other criteria mentioned earlier. Using the governing equations and shock conditions, Chakrabarti (C89a) computed an invariant relation at the shock which is given by,

$$C = \frac{[M_+(3\gamma - 1) + \frac{2}{M_+}]^2}{2 + (\gamma - 1)M_+^2} = \frac{[M_-(3\gamma - 1) + \frac{2}{M_-}]^2}{2 + (\gamma - 1)M_-^2}, \tag{2.12}$$

where, M's are the Mach numbers of the flow. We solve the problem in terms of the

initial flow parameters $(\mathcal{E}, \lambda)$ for shock. Shocks are formed for a suitable set of flow parameters. In Fig. 2.7, we have shown four possible shock locations denoted by x_{s1}, x_{s2}, x_{s3} and x_{s4} respectively for a given set of flow parameters ($\mathcal{E} = 0.047, \lambda = 1.69$). Details of the figure description are presented in the Figure captions. In a black hole accretion flow, x_{s2} and x_{s3} are the only possible shock locations.

Recently Das et al. (2001, hereafter, DCC01) have extensively studied the hybrid model analytically considering a two component flow. In the next Chapter, we shall present the analytical solution for the hybrid model in detail.

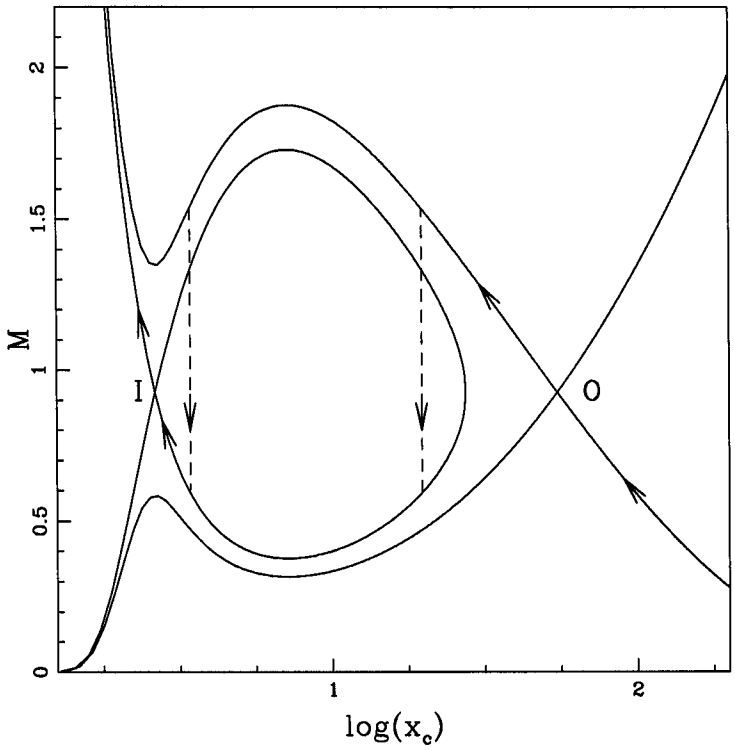

Figure 2.8: Phase space diagram of the accretion flow for the parameters same as $C - log(x_c)$. The inner (I) and outer (O) sonic points are located at 2.634 and 54.88. The shock locations are: $x_{s1} = 2.233, x_{s2} = 3.434, x_{s3} = 19.71$ and $x_{s4} = 126.71$ respectively. The vertical dashed lines represent the possible shock transitions in an accretion flow.

In the case of accretion, matter at rest at infinity accretes toward the black hole due to gravity and gradually gains inward radial velocity up to its maximum value. Thus the sub-sonic matter at the outer edge of the disk becomes super-sonic

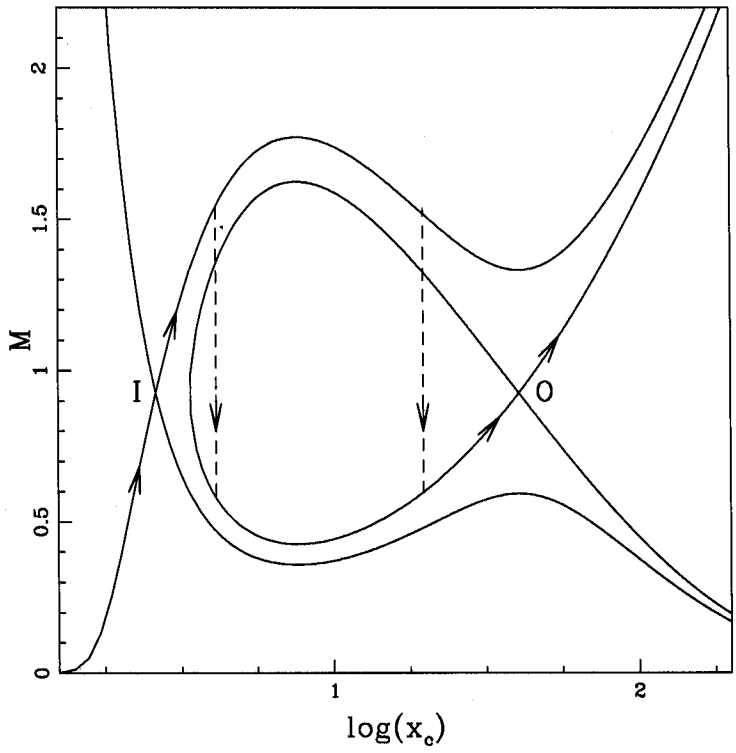

Figure 2.9: Phase space diagram of the wind flow for the parameter $\mathcal{E} = 0.006$ and $\lambda = 1.69$. The inner (I) and outer (O) sonic points are at 2.6201 and 40.604 respectively. The vertical dashed lines represent the possible shock transitions in the wind flow.

while passing through the outer sonic point (O) and makes a discontinuous jump from super-sonic to sub-sonic branch depending on whether the Rankine-Hugoniot shock conditions (hereafter referred to as the R-H conditions) are satisfied or not. After the discontinuous transition, the accreted matter again becomes super-sonic while crossing the inner sonic point (I) before falling into the black hole. If the R-H conditions are not satisfied, the super-sonic matter enters into the black hole directly without making any transition. Fig. 2.8 shows the phase space trajectory of such a flow where the logarithmic radial distance is plotted along the X-axis and the Mach number is plotted along the Y-axis. The vertical dashed lines denote the possible shock locations. Indeed, Chakrabarti & Molteni (1993) showed that the shock location close to the outer sonic point (O) is stable whereas the other one is unstable. Details of the input parameters for Fig. 2.8 are illustrated in the Figure

captions. A similar plot is drawn in Fig. 2.9 for a wind solution where the situation is completely reversed due to the inner boundary condition of the flow. Here, the sub-sonic matter originated from the star surface first passes through the inner sonic point (I) to become super-sonic and makes a shock jump to the sub-sonic branch if the R-H conditions hold and finally becomes supersonic while passing through the outer sonic point (O). Details of figure descriptions are presented in the Figure captions.

2.3 Outflow and jet formation

In the astrophysical context, when a highly collimated matter with relativistic speed emerges out from the vicinity of celestial object, namely micro-quasars , AGNs etc., this ejected matter is usually called the outflows or jets. In 1953, Jenison & Dasgupta (Jenison & Dasgupta (1953)) first identified double radio lobes originated from Cygnus A. In the early eighties, radio and X-ray observations of SS 433 confirm the presence of jets (Watson et al. 1986; Hjellming & Johnston 1981). In the mid nineties, Mirabel & Rodriguez (1994) reported the existence of outflows in stellar mass micro-quasars GRS 1915+105. In addition, jets in X-ray binary like Cygnus X3 are also very common (Schalinski et al. 1995). In this Section, we shall briefly discuss the generation mechanism of outflows and jets from the accretion disks itself (Chakrabarti 1999, hereafter C99; Das & Chakrabarti 1999). Chakrabarti (C99) presented a simple toy model where he considered that accreting matter close to the black hole falls freely with roughly constant angular momentum. In reality, close to the black hole, the infall time scale becomes much smaller compared to the viscous time scale and therefore, matter does not have enough time to transport angular momentum outwards. As pointed out earlier, when matter with sufficient angular momentum accretes towards the black hole, centrifugal force becomes comparable to gravity. This causes a puffed up torus like structure to form where the flow suffers a discontinuous shock transition. At the shock, an excess of thermal pressure gradient force is generated due to the compression of matter which drives some parts of accreting matter in vertical direction in the form of outflows or jets. Chakrabarti (C99) modeled a system which consists of a dense boundary layer (CENBOL) and both the infalling and outflowing matters are confined within a conical shape structure.

A schematic diagram of such a toy model is shown in Fig. 2.10. The incoming flow is compressed and heated in the post-shock region (within CENBOL) and also efficiently radiates the extra heat to maintain the isothermality conditions. Since the outflows are originated from the CENBOL region, it is reasonable to consider the outflows to be isothermal in nature. Following all these considerations, one can easily compute the expression for ratio of mass outflow rate to the inflow rate ($R_{\dot{m}}$) as a function of compression ratio (R) of the infalling matter. Compression ratio is

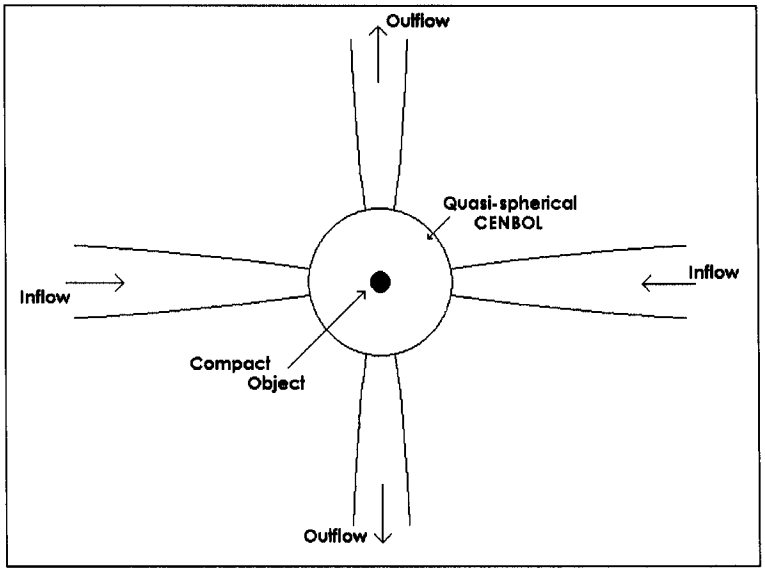

Figure 2.10: Cartoon diagram of the toy model to estimate the outflow rate from the inflow parameter (C99).

usually defined as the ratio of post-shock to pre-shock density and explicitly related with the inflow parameters ($\mathcal{E}$ and λ). Therefore, the ratio of outflow and inflow rate is given by (C99),

$$R_{\dot{m}} = \frac{\dot{M}_{out}}{\dot{M}_{in}} = \frac{\Theta_{in}}{\Theta_{out}} \frac{R}{4} \left[\frac{R^2}{R-1}\right]^{3/2} exp\left(\frac{3}{2} - \frac{R^2}{R-1}\right), \tag{2.13}$$

where, Θ_{in} and Θ_{out} are the solid angles subtended by the inflow and outflow respectively.

Eq. (2.13) indicates that outflow rate can be estimated self-consistently only knowing the initial inflow parameters. Figure 2.11 shows the variation of $R_{\dot{m}}$ with compression ratio R for comparable solid angles subtended by the inflow and outflow ($\Theta_{in} \approx \Theta_{out}$). When a shock is not formed in the accretion flow ($R \rightarrow 1$), the outflow rate $R_{\dot{m}} = 0$ [Eq. (2.13)]. On the other hand, for a strong shock ($R \rightarrow 7$) the outflow rate is negligible. For the intermediate shock strength ($R \sim 4$) the outflow rate is maximum. Thus it is clear that an outflow is possible when there is a shock in the inflow and it is observed that outflows or jets are originated only in the hard states. This features show the originality of the Chakrabarti's model. In 1999, Das & Chakrabarti (Das & Chakrabarti 1999) presented another self-consistent inflow-outflow model where they extensively showed that jets are originated from the inner

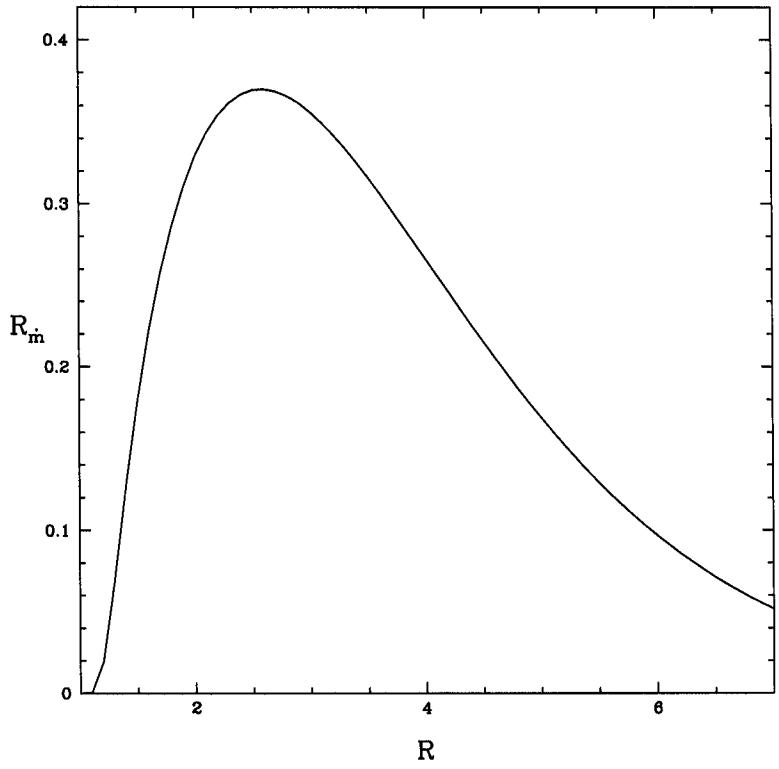

Figure 2.11: Variation of the ratio of outflow to inflow rate ($R_{\dot{m}}$) as a function of compression ratio R (C99).

part of the disk *i.e.*, mainly from CENBOL. Recently Das et al. 2001 (hereafter DCNC01) presented a more advanced disk-jet model where rotation of matter inside the accretion disk is also considered. In the next Chapter, we shall discuss this model in detail.

Chapter 3

Properties of Non-dissipative Accretion Flow

The basic features of the advective accretion flow around a black hole are extensively discussed in Chapter 2. In a non-dissipative accretion system, the stationary flow characteristics are mainly dictated by the flow parameters, namely, specific energy and specific angular momentum. For a suitable set of parameters, the flow possesses multiple sonic points and forms a shock if the Rankine-Hugonoit shock conditions are satisfied. So far, all the attempts are made by numerical means for obtaining the desired solutions. Presently we proceed further to obtain the shock locations solely analytically from which one can easily estimate the other shock properties, such as shock strength, compression ratio etc. There are two motivations for the analytical work—first, from the theoretical point of view it is challenging to find solutions of a large number of non-linear equations that must satisfy a number of conditions mentioned in Chapter 2 and second, from the observer's point of view, any observation which could require standing shock waves could be explained using more fundamental parameters, such as specific energy and angular momentum or even better, using accretion rates of Keplerian and sub-Keplerian flows as in a two-component flow solution of Chakrabarti and Titarchuk (Chakrabarti and Titarchuk 1995, hereafter CT95). Analytical work also gives insight into why the shocks form in the first place. Under this circumstances, we start with a set of governing equations of the flow and look for the analytical solution of these equations for the appropriate boundary conditions. A detail formalism for computing analytical shock solution is presented in the next Section.

3.1 Analytical study of shock waves

The analytical solution of the *hybrid model flow* is based on few simplified assumptions. We consider a steady, thin, axisymmetric, inviscid, rotating flow around a non-rotating black hole. The flow is confined in a special geometrical structure where the flow variables remain in hydrostatic equilibrium in a direction transverse

to the flow motion. In the present Section, we choose similar geometrical units, $M_{BH} = c = 1$; $G = 1/2$, used in Chapter 2.

3.1.1 Model equations

The model equations that govern the motion of matter accreted on to a black hole are usually written down in the disk equatorial plane which are already presented in §2.1. In the present context, our goal is to compute the flow solutions solely analytically and therefore, we proceed with a brief introduction of the flow governing equations once again (C89a, DCC2001). The radial momentum equation for a stationary flow is expressed as,

$$\vartheta\frac{d\vartheta}{dx} + \frac{1}{\rho}\frac{dP}{dx} + \frac{\lambda^2}{x^3} + \frac{1}{2(x-1)^2} = 0. \tag{3.1}$$

In a non-dissipated advective flow, integration of Eq. (3.1) leads to the energy conservation equation which is given by,

$$\mathcal{E} = \frac{\vartheta^2}{2} + \frac{a^2}{\gamma - 1} + \frac{\lambda^2}{2x^2} + g(x), \tag{3.2}$$

where, ϑ and a are the dimensionless radial and sound velocities and x represents the dimensionless radial distance. Here, P and ρ denote the isotropic pressure and the mass density of the flow respectively. The adiabatic index is denoted by γ and it is related to the polytropic index by the relation $n = 1/(\gamma - 1)$. Effect of gravity is taken care of by the pseudo-Newtonian potential introduced by Paczyński & Wiita (PW80), which is given by $g(x) = -\frac{1}{2}(x-1)^{-1}$. In addition, $P = K\rho^\gamma$ is considered to be the equation of state of the flow where K is the measure of the specific entropy. In general, specific entropy remain constant throughout the flow except at the shock location where local turbulence generates some entropy enabling the flow to pass through the inner sonic point.

In the steady state, the flow continuity is dictated by the following equation:

$$\frac{d}{dx}(\vartheta\rho x h) = 0, \tag{3.3}$$

which is integrated to obtain the mass conservation equation in the cylindrical geometry:

$$\dot{M} = \vartheta\rho x h, \tag{3.4}$$

where, h is the half-thickness of the flow at radial coordinate x and the analytical expression of local disk height, h, is presented in Eq. (2.3). Here, $\dot{M}$ is the mass accretion rate apart from a geometric constant. Chakrabarti (C89a) defines a new conserved quantity $\dot{\mathcal{M}}$, known as *entropy accretion rate* which is linked with

the actual accretion rate as $\dot{\mathcal{M}} = K^n \gamma^n \dot{M}$. Therefore, $\dot{\mathcal{M}}$ remains constant for a flow passing through a given sonic point whereas $\dot{M}$ is always constant all throughout independent of flow trajectory. The advantage of this prescription is that $\dot{\mathcal{M}}$ makes a sharp transition at the discontinuities and also identifies the shock location successfully. Subsequently, we write $\dot{\mathcal{M}}$ in terms of the flow variables and obtain:

$$\dot{\mathcal{M}} = \vartheta a^q f(x), \tag{3.5}$$

where, $q = (\gamma + 1)/(\gamma - 1)$ and $f(x) = x^{3/2}(x - 1)$. However, the definition of the adiabatic sound speed, $a^2 = \gamma P/\rho$, is used in this calculation. In the next Section, we present an account of sonic point analysis following the traditional approach and also discuss shock invariants.

3.1.2 Sonic point analysis and shock invariants

In order to satisfy the inner boundary conditions of the black hole accretion process, the flow must be super-sonic at least once at some point of its trajectory. Indeed, the stationary sub-sonic flow becomes super-sonic at a special point known as a sonic point. In the next Section, we present a detail study of the various properties of the sonic point.

Sonic point conditions

Following the usual approach, we derive the sonic point conditions from radial momentum and continuity equations (Eqs. 3.1 and 3.4b) (C89a, C90a). The first derivative of radial velocity with respect to radial distance is given by,

$$\frac{d\vartheta}{dx} = \left[\frac{2a^2}{\gamma+1}\frac{d\ln f}{dx} - \frac{dG}{dx}\right] \Big/ \left[\vartheta - \frac{2a^2}{(\gamma+1)\vartheta}\right] . \tag{3.6}$$

Here, $G(x) = \frac{1}{2}\lambda^2/x^2 - \frac{1}{2}(x-1)^{-1}$ is the effective potential associated with the present problem. Since the denominator must vanish at the sonic points, if the flow is assumed to be smooth everywhere, the numerator must vanish simultaneously. The vanishing of the denominator gives,

$$\vartheta_c^2(x_c) = \frac{1}{\gamma+1} a_c^2(x_c). \tag{3.7}$$

The factor in front of $a_c^2(x_c)$ arises because the flow is assumed to be in vertical equilibrium. The vanishing of the numerator gives,

$$a_c^2(x_c) = \frac{(\gamma+1)(x_c-1)}{x_c^2}\frac{[\lambda_K^2 - \lambda^2]}{5x_c - 3}, \tag{3.8}$$

where, λ_K represents the Keplerian angular momentum. Notice that since sound speed is always positive, flow angular momentum at the sonic point must be sub-Keplerian, *i.e.*, $\lambda(x_c) < \lambda_K$ (C90a and reference therein). Here, the quantities with the subscript 'c' denote their values at the sonic point.

In order to have a shock, the flow must satisfy certain boundary conditions. Since the accretion disk under consideration is non-dissipative, we shall incorporate Rankine-Hugoniot conditions for shock transition. In Chapter 2, we already presented a elaborate discussion on R-H conditions and therefore, will not be repeated here (C89a).

Mach number relation at the shock

We now derive an invariant quantity that must be satisfied at the shock using basic flow equations. At the beginning, we write the shock conditions (Landau and Lifshitz 1959) and Eqs. (3.7-3.8) in terms of Mach number ($M = \vartheta/a$) of the flow which are given by,

$$\frac{1}{2}M_+^2 a_+^2 + \frac{a_+^2}{\gamma - 1} = \frac{1}{2}M_-^2 a_-^2 + \frac{a_-^2}{\gamma - 1}, \tag{3.9}$$

$$\dot{\mathcal{M}}_+ = M_+ a^{\nu'}{}_+ f(x_s); \quad \dot{\mathcal{M}}_- = M_- a^{\nu'}{}_- f(x_s), \tag{3.10}$$

where, $\nu' = 2\gamma/(\gamma - 1)$ and x_s is the shock location and

$$\frac{a_+^\nu}{\dot{\mathcal{M}}_+}\left(\frac{2}{3\gamma - 1} + M_+^2\right) = \frac{a_-^\nu}{\dot{\mathcal{M}}_-}\left(\frac{2}{3\gamma - 1} + M_-^2\right), \tag{3.11}$$

where, $\nu = (3\gamma - 1)/(\gamma - 1)$. Using Eqs. (3.9-3.11), one obtains the following equation relating the pre- and post-shock Mach numbers of the flow at the shock (C89a) as,

$$C = \frac{[M_+(3\gamma - 1) + 2/M_+]^2}{2 + (\gamma - 1)M_+^2} = \frac{[M_-(3\gamma - 1) + 2/M_-]^2}{2 + (\gamma - 1)M_-^2}. \tag{3.12}$$

Here, the constant C remains invariant across the shock. Subsequently, one can rewrite the Mach number of the flow just before and after the shock in terms of C as

$$M_\pm^2 = \frac{2(3\gamma - 1) - C \mp \sqrt{C^2 - 8C\gamma}}{(\gamma - 1)C - (3\gamma - 1)^2}, \tag{3.13}$$

and the product of the Mach numbers is given by,

$$M_+ M_- = -\frac{2}{\sqrt{(3\gamma - 1)^2 - (\gamma - 1)C}}. \tag{3.14}$$

So far, we have derived sonic point conditions and shock invariant relations for a flow which possesses a finite amount of angular momentum. Presently, we intend to investigate the location of the sonic points in terms of the flow parameters such as specific energy ($\mathcal{E}$) and specific angular momentum (λ) and also identify the region of the parameter space for multiple sonic points. In §3.1.3, we present this calculations in detail.

3.1.3 Analytical expression of the sonic points and behavior in the parameter space

In order to obtain the shock locations, we first compute the locations of the sonic points and ensure that at least two of them are X-type (C90a). In §3.1.2, we have derived the sonic point conditions. Using the definition of the Mach number $M = \vartheta/a$ and sonic point conditions (Eqs. 3.7-3.8), we obtain an algebraic equation for the location of sonic points (x_c) as a function of flow parameters which is given by,

$$\mathcal{N}x_c^4 - \mathcal{O}x_c^3 + \mathcal{P}x_c^2 - \mathcal{Q}x_c + \mathcal{R} = 0, \tag{3.15}$$

where, $\mathcal{N} = 10\mathcal{E}$, $\mathcal{O} = 16\mathcal{E} + 2n - 3$, $\mathcal{P} = 6\mathcal{E} + \lambda^2(4n-1) - 3$, $\mathcal{Q} = 8n\lambda^2$, $\mathcal{R} = (1+4n)\lambda^2$ and n is the polytropic index.

We solve Eq. (3.15) analytically (Abramowitz and Stegun, 1970) and obtain the location of the sonic points. Detail formalisms are given in the Appendix. For the purpose of sonic points, D of the Appendix is denoted as D_c. Eq. (3.15) has four roots and equation (A6) can be used to check whether all of them are complex (a pair of complex conjugates). At least two are real and two are complex, or all four are real. A necessary condition to form a shock wave is to have four real roots. Of course, only one would be inside the black hole horizon, and the other three would be outside; out of these, for topological reasons, only two would be X-type or saddle type, and the one in between must be O-type or center type. This is determined by computing derivative $d\vartheta/dx$ at the sonic point by using l'Hospital's rule and checking whether they are real. For our purpose, two derivatives at each sonic point must be real and of opposite signs in order to have the X-type sonic points.

Fig. 3.1 shows the division of the parameter space. Denoting the discriminant D (of Appendix) by D_c, we find that the condition $D_c < 0$ is the necessary condition for having three sonic points. The boundary $D_c = 0$ separates this region, on which two sonic points merge and the third one remains separate. Outside of this region $D_c > 0$, and only one sonic point is possible and the other two roots are complex

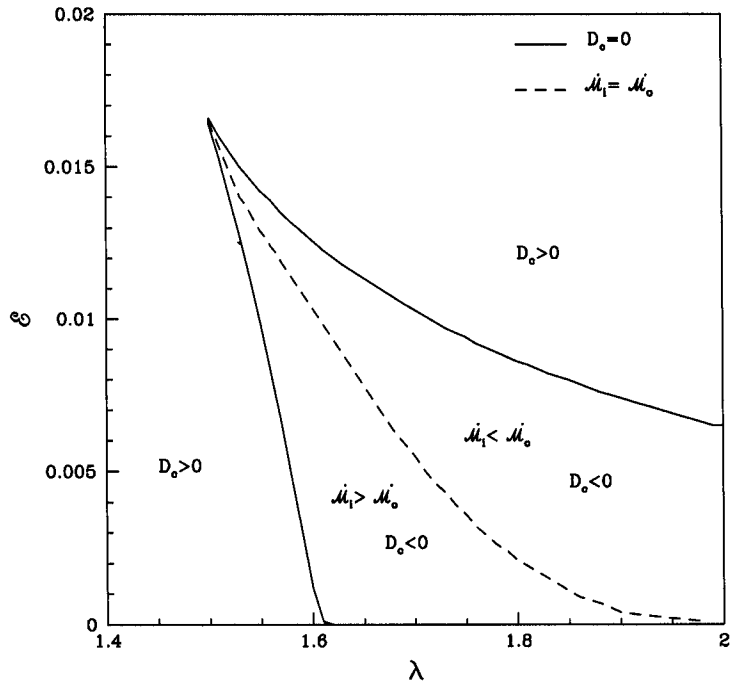

Figure 3.1: Division of the parameter space as spanned by the pair $(\mathcal{E}, \lambda)$ according to the number of sonic points. Solid curve represents $D_c = 0$ which divides the region into $D_c > 0$ (one sonic point) and $D_c < 0$ (three sonic points) regions. The dashed curve further divides the region into two regions where entropy accretion rate $\dot{\mathcal{M}}$ at the two saddle type sonic points behave differently (inner point is denoted by i and outer point is denoted by o).

conjugates of one another. The dotted curve in the middle represents the condition,

$$\dot{\mathcal{M}}_o = \dot{\mathcal{M}}_i,$$

where $\dot{\mathcal{M}}_i$ and $\dot{\mathcal{M}}_o$ are the entropy accretion rates at the inner and outer sonic points, respectively. The region above it contains parameters with $\dot{\mathcal{M}}_i < \dot{\mathcal{M}}_o$ and the region below it contains parameters with $\dot{\mathcal{M}}_i > \dot{\mathcal{M}}_o$. This latter region is suitable for shock formation in accretion flows.

Moreover, one can easily show from Eq. (3.7) that the locations where $dM/dx = 0$ exactly coincide with the sonic points of the flow. Thus, the number of extrema of $M = M(x)$ is the same as that of the sonic points. Therefore, the division in Fig. 3.1 could give an idea about the behaviour of $M = M(x)$ as well.

3.1.4 Analytical expression for the shock location and behavior in the parameter space

A black hole accretion flow, being transonic, must satisfy two sonic point conditions at the cost of one extra unknown, namely, the sonic point. Because of this extra conditions, out of the three constants of motion, namely, $\mathcal{E}$, $\dot{M}$ and λ, only two are supposed to be supplied as free parameters. We deduce shock locations using our past experience derived from numerical methods where we found that only one of the shocks, x_{s3} (see, Chapter 2) is stable. Accordingly our procedure as delineated below attempts to compute only this location.

The flow will have a shock only at those point where the shock invariant condition is satisfied. Simplifying the shock invariant relation (Eq. 3.12), we obtain,

$$2(\gamma-1)(M_+^2+M_-^2)-[(3\gamma-1)^2-2(3\gamma-1)(\gamma-1)]M_+^2M_-^2+4=0. \quad (3.16)$$

We consider a relativistic flow with $\gamma = 4/3$ so that the polytropic index $n = 3$. Then from Eq. (3.16), we obtain,

$$2(M_+^2+M_-^2)-21M_+^2M_-^2+12=0. \quad (3.17)$$

We now expand the post-shock Mach number M_+^2 by a polynomial which must satisfy the following conditions:

1. The derivative dM/dx is zero at the central O-type sonic point. This is a general property of the flow (see discussion at the end of the previous Section).

2. The Mach number M_+ at the location of the middle sonic point matches with the value that derived from approximate analytical solution obtained using the energy equation (Eqs. 3.2 and 3.4).

3. The Solution passes through the position where dM/dx is ∞ and a good guess of this the location (say, from the location of the sonic points) is known.

Similarly, we expand M_-^2 by a polynomial that must satisfy the following conditions:

1. The derivative dM/dx is zero at the outer sonic point (location of which has already been determined above). This is a general condition (see discussion at the end of the previous Section).

2. The Mach Number at the outer sonic point matches the analytical value obtained from the sonic point condition (Eq. 3.7).

3. The Mach Number M_- at the location of the middle sonic point matches with the analytical value derived from approximate analytical solution obtained using the energy equation (Eq. 3.2 and 3.4).

Keeping in mind that an algebraic equation that is beyond quartic cannot be solved analytically (Abramowitz and Stegun 1970), we expand $M_\pm^2$ as quadratic

equation so that Eq. (3.17) may become quartic. We will show, a posteriori, that such an assumption introduces a very small and tolerable error in our computation.

If x_s denotes the shock location, we assume

$$M_{\pm}^2 = \sum_{q=0}^{2} A_{[q,\pm]} x_s^q, \tag{3.18}$$

where, $A_{[q,\pm]}$ are constant co-efficients to be determined from the conditions mentioned above. We find them to be,

$$A_{[2,+]} = \frac{1-\left(M_+^2\right)_{mid}}{(x_{inf}-x_{mid})^2}, \quad A_{[2,-]} = \frac{\left(M_-^2\right)_{mid}-1}{(x_{out}-x_{mid})^2},$$

$$A_{[1,+]} = -2x_{mid}A_{[2,+]}, \quad A_{[1,-]} = -2x_{mid}A_{[2,-]},$$

$$A_{[0,+]} = 1+\left(2x_{mid}x_{inf}-x_{inf}^2\right)A_{[2,+]}, \quad A_{[0,-]} = 1+x_{out}^2 A_{[2,-]},$$

where, x_{mid}, x_{inf} and x_{out} are the middle (O-type) sonic point, the position where first derivative of Mach Number is infinity, and the outer sonic point respectively.

We now substitute the above expression (Eq. 3.18) of the Mach number in the Mach invariant relation (Eq. 3.17) to obtain the following algebraic equation for shock (x_s) and obtain as algebraic equation which is given by,

$$\mathcal{A}x_s^4 + \mathcal{B}x_s^3 + \mathcal{C}x_s^2 + \mathcal{D}x_s + \mathcal{F} = 0, \tag{3.19}$$

where,

$\mathcal{Y} = (3\gamma-1)(\gamma+1)$,
$\mathcal{Z} = 2(\gamma-1)$, $\mathcal{A} = \mathcal{Y}A_{[2,+]}A_{[2,-]}$,
$\mathcal{B} = \mathcal{Y}\left(A_{[1,+]}A_{[2,-]} + A_{[2,+]}A_{[1,-]}\right)$,
$\mathcal{C} = \mathcal{Y}\left(A_{[0,+]}A_{[2,-]} + A_{[1,+]}A_{[1,-]} + A_{[2,+]}A_{[0,-]}\right) - \mathcal{Z}\left(A_{[2,+]} + A_{[2,-]}\right)$,
$\mathcal{D} = \mathcal{Y}\left(A_{[0,+]}A_{[1,-]} + A_{[1,+]}A_{[0,-]}\right) - \mathcal{Z}\left(A_{[1,+]} + A_{[1,-]}\right)$,
$\mathcal{F} = \mathcal{Y}A_{[0,+]}A_{[0,-]} - \mathcal{Z}\left(A_{[0,+]} + A_{[0,-]}\right) - 4$.

We solve this equation for x_s analytically using the same procedure as in §3.1.3 (details are described in the Appendix). We denote the discriminant D by D_s, and Q and R-values as Q_s and R_s respectively for our discussion on the parameter-space behaviour of shocks.

In Fig. 3.2, we redraw the parameter space as in Figure 3.1, but consider the formation of shocks alone. We find that $Q_s > 0$ produces no shock from above, and $Q_s = 0$ with $R_s \neq 0$ gives the boundary of the weakest shock (shocks with

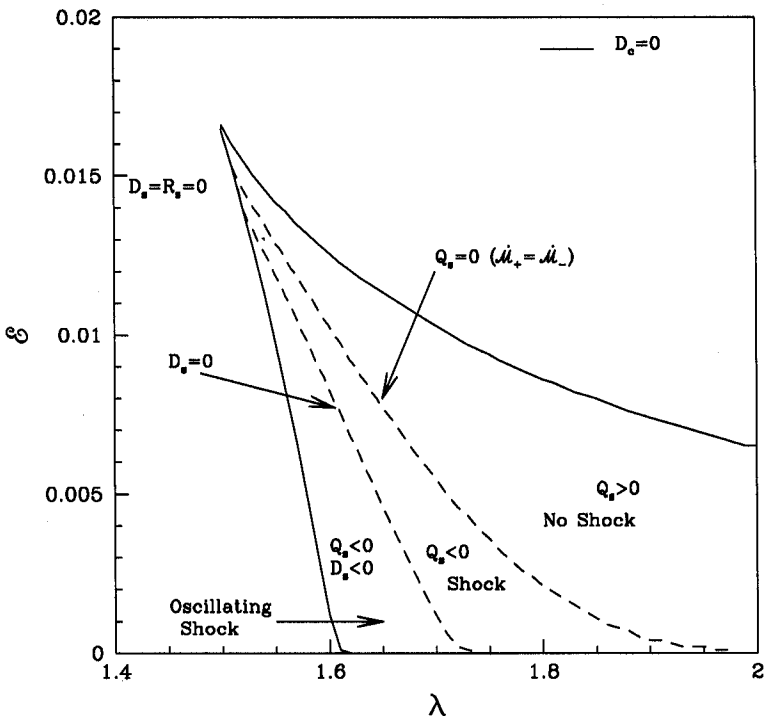

Figure 3.2: Division of the parameter space as spanned by the pair $(\mathcal{E}, \lambda)$ according to whether shocks can form or not. The solid curve represents $D_c = 0$ as in Fig. 3.1. The dashed curve ($D_s = 0$) surrounds the region with shocks in accretion. When $D_s < 0$ and yet there are three sonic points, the shocks are oscillatory, giving rise to quasi-periodically varying hard X-rays.

unit compression ratio). This boundary, although obtained using our approximate analytical method, generally coincides with the dashed curve of Figure 3.1. The edge of the boundary is obtained with an extra condition $R_s = 0$. Thus, R_s progressively decreases towards the edge along the dashed curve. This edge (denoted by $D_s = R_s = 0$) ought to have coincided with the cusp of the $D_c = 0$ curve drawn for the sonic point (see, Fig. 3.1 also) obtained by analytical method. A small shift is the evidence that a small error is present at this corner of the parameter space. We also provide the region of the oscillating shocks ($Q_s < 0$ and $D_s < 0$). Here the shock location is imaginary and therefore, shock continuously oscillates back and forth, causing a very interesting astrophysical effect known as quasi-periodic oscillations, which will be discussed in the next Section. The boundary between the shock and

no-shock region from below is denoted by the dashed curve marked by $D_s = 0$. Below the no-shock region, where the energy and angular momentum of the flow are very low, the flow has only one sonic point.

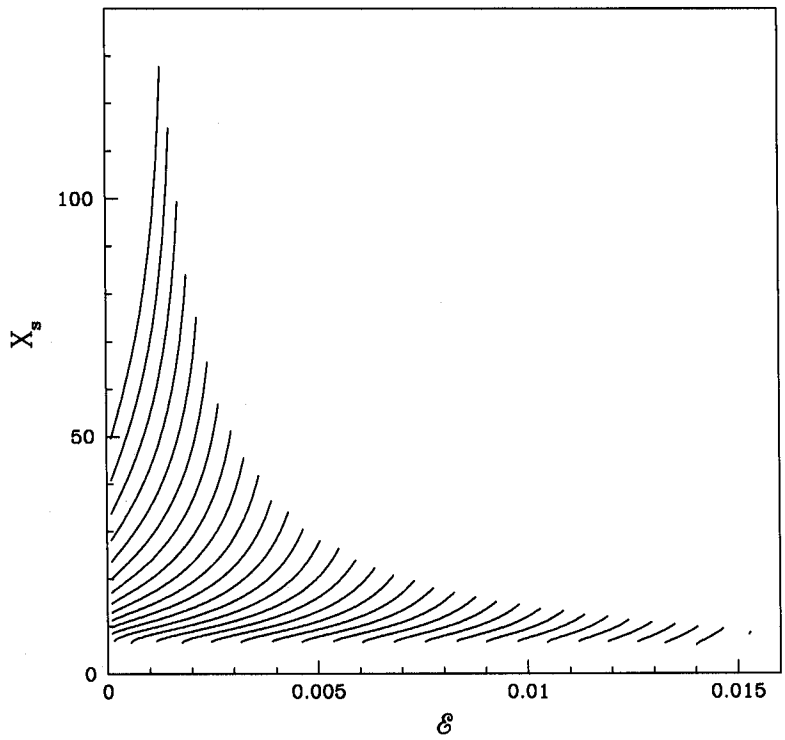

Figure 3.3: Variation of shock location (x_s) with specific energy ($\mathcal{E}$) of the flow. Each curve is drawn for a specific angular momentum λ. From right to left curves are drawn for $\lambda = 1.51,\ 1.52,\ 1.53, ...$ until 1.84. For a given specific energy $\mathcal{E}$, shock location increases with increasing centrifugal force (through λ). Similarly, for a given λ, shock location increases with energy.

In Figure 3.3, we draw shock location (x_s) as a function of specific energy ($\mathcal{E}$). Different curves are drawn for different specific angular momentum of the flow. The rightmost one is for $\lambda = 1.51$ and the leftmost one is for $\lambda = 1.84$, with the remainder drawn at interval of λ is 0.01. As angular momentum increases, the shock is located further from the black hole. Comparing the shock locations from those obtained analytically, one may note that the same shock location is obtained for a specific angular momentum slightly more ($\sim 3\%$) than that used in the numerical method. We, therefore, believe that the obtained results are very much reliable.

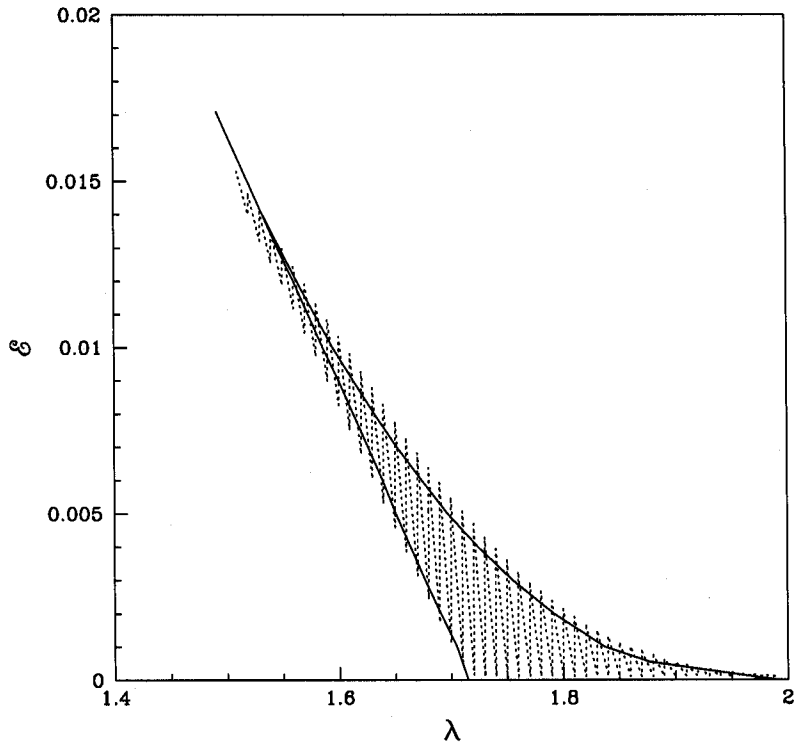

Figure 3.4: Comparison of the boundary of the parameter space in the $(\mathcal{E}, \lambda)$ plane using the numerical (solid curve) and the analytical (dotted region) methods. Except for the region near the cusp (upper left corner) the agreement is very strong.

In Figure 3.4, we present a comparison of the boundary of the parameter space for which standing shocks may form as obtained by our analytical solution (*dotted region*) and by the numerical means (*solid curve*) existing in the literature (C89a). The agreement is very good except in a region near the cusp (as also noted while discussing Fig. 3.2). Since very little parameter space is involved at this edge, we think that this small mismatch is tolerable.

3.1.5 Astrophysical applications

Even though a black hole has no hard surface, it is remarkable that matter forms standing shock around it in the same way a shock is formed when a super-sonic flow encounters a hard boundary. Shock waves heat up a gas and puff it up. This post-shock region intercepts soft photons from the pre-shock matter, particularly from

the Keplerian disk located on the equatorial plane (CT95). In this scenario, the nature of the Comptonized radiation depends on the amount of matter in the sub-Keplerian and in the Keplerian flow: if the intensity of soft photon is very low, they cannot cool the post-shock region by an inverse Compton process, and the spectrum remains very hot. On the other hand, if the intensity of soft photon is very high (i.e., the Keplerian rate is large), they cool down the post-shock region to the extent that the shock cannot be sustained (pressure balance condition breaks down). This produces a soft-state spectrum with a hard tail due to bulk motion Comptonization (CT95). There are several models in the literature which perhaps explain the soft and hard states. However, no model other than CT95 explains the power-law hard-tail in the soft state. Similarly, regarding the question of quasi-periodic oscillations, shock-oscillation model turns out to be a sufficiently satisfactory one (Chakrabarti and Manickam 2000, hereafter CM00).

When the parameters fall in the 'no shock' region of Figure 3.2, the shock location becomes imaginary. However, three sonic points are still present and the entropy of the flow at the inner sonic point continues to be higher compared with that at the outer sonic point. In this case, shock starts oscillating with a time period T_s comparable to the infall time from the post-shock region (Ryu, Chakrabarti and Molteni 1997). Even when shock forms, if the infall time-scale turns out to be comparable to the cooling time, then the resonance condition is satisfied (Molteni, Sponholz and Chakrabarti 1996, hereafter MSC96; CM00) and shock starts oscillation in a timescales of,

$$T_s \sim x_s/v_s,$$

where, $v_s \sim R^{-1}x_s^{-1/2}$ is the infall velocity and R is the compression ratio at the shock (easily obtained analytically from our equations). However, observed QPO frequencies are comparable to $1/T_s$.

So far, we have dealt with a single component flow having a sub-Keplerian angular momentum. Indeed, an accreted flow is originated at the outer edge of the disk almost with a Keplerian angular momentum. Therefore, in reality, accretion flow initially contains only the Keplerian matter. In the intermediate stage, some part of the Keplerian matter are converted to sub-Keplerian. This implies that the matter contains both the components and at few hundred of r_g all matters become completely sub-Keplerian. Under this circumstances, we present an *ad hoc* prescription for obtaining a single component sub-Keplerian flow from the mixture of matter of both the species. When a mixture of the Keplerian and the sub-Keplerian matter is accreted, it is easy to obtain the parameters λ and $\mathcal{E}$ in terms of the Keplerian ($\dot{M}_d$) and sub-Keplerian ($\dot{M}_h$) accretion rates. Suppose, the viscosity parameter is such that the flow is deviated from a Keplerian disk at $x = x_K$ where its energy and angular momentum were $\mathcal{E}_d$ and λ_d respectively. Further suppose that the sub-Keplerian halo has a constant energy $\mathcal{E} \sim 0 \sim \mathcal{E}_h$ and constant angular momentum

λ_h, then the average angular momentum and energy of the transonic flow would be,

$$< \mathcal{E} >= \frac{\dot{M}_d \mathcal{E}_d + \dot{M}_h \mathcal{E}_h}{\dot{M}_d + \dot{M}_h} \quad \text{and} \quad < \lambda >= \frac{\dot{M}_d \lambda_d + \dot{M}_h \lambda_h}{\dot{M}_d + \dot{M}_h}$$

Therefore, it is easy to compute the shock location of the resultant flow using our formalism given above.

Fig. 3.3 indicates that shock solution exists when the flow possesses positive specific energy. In other words, if a flow deviates from a cool Keplerian disk on the equatorial plane, the flow cannot have shocks since the specific energy in such a flow would be negative unless the flow is mixed with a substantial amount of sub-Keplerian matter with positive energy. Typically, $\dot{M}_h \gg \dot{M}_d$, and even with a small energy, the specific energy of the mixture becomes positive, giving rise to shocks and (unbound) winds. In the case when magnetic dissipation is present, flow energy could increase to a positive value, and a solution with a shock would be allowed. The prospect of magnetic energy dissipation has been discussed by several workers in the literature (Shapiro 1973; Bisnovatyi-Kogan and Blinnikov 1976; Bisnovatyi-Kogan 1998). Briefly, since the magnetic field rises as $B_r \propto r^{-2}$ and, therefore, magnetic pressure rises as $P_{mag} \propto r^{-4}$, while the gas pressure in the sub-Keplerian matter goes as $P_{gas} \propto r^{-5/2}$, any magnetic field in excess of the equipartition value would escape from the disk buoyantly and may dissipate at the atmosphere, as in the case of the Sun. If the flow has specific energy $\mathcal{E}_h$ at, say $r = 100 r_g$, where the flow is in equipartition, then at the shock, the energy would be at least $2^4 = 16$ times larger if *all* the magnetic energy is dissipated into the flow. Thus, a basically free-fall matter of $\mathcal{E} \sim 10^{-4}$ would have an energy $\sim 10^{-3}$ and a shock at a few tens of Schwarzschild radii would be expected.

Another interesting feature is that an accreting flow can, in principle, intercept hard X-ray photons emitted from the inner edge of the disk. In a certain circumstances, this pre-heating effect need not be negligible. For instance, a flow emitting isotropically with 6% efficiency will definitely intercept $\theta \sim \Theta_{in}/4\pi$ fraction of radiation in between the shocked region and the Keplerian disk. Here, Θ_{in} denotes the solid angle subtended by the inflow. Assuming $\theta \sim 0.1$, the energy deposition due to pre-heating is 0.6%, which is significant. This would energize Keplerian matter as well, and consequently shocks in the sub-Keplerian flow would be expected.

3.2 Model dependence of transonic accretion flow properties

So far, we have studied the shock properties analytically for vertical equilibrium model. In this Section, we analytically investigate how the behaviour of an accretion flow changes when the flow model is varied. Indeed, we study the transonic

properties of the accretion flow in the conical flow model, the constant height model and the vertical equilibrium model respectively and show that all these models are basically identical provided the polytropic constant is suitably adjusted from one model to another. We show that this behaviour continues even when standing shocks are produced in the flow. The parameter space where the shocks are formed remain roughly identical in all these models when the same transformation among the polytropic indices is used. At the end of this Section we present applications of these findings.

A fully self-consistent study of any astrophysical system is generally prohibitive. Very often, for simplicity, it is necessary to construct models which have all the salient features of the original problem. However, these models need not be unique. In this part of the thesis, we make a pedagogical review of three different models of rotating accretion flow and show that even though they are based on fundamentally different assumptions, they have identical physical properties. What is more, results of one model could be obtained from the other by changing a *physical* parameter, namely, the polytropic constant. In other words, all these models are *identical.*

Chakrabarti (C89a and C90a) studied transonic properties of accretion flows in different models. One of such models is conical in shape in the meridional plane ('Wedge-shaped Flow') and in the other model flows are in vertical equilibrium. Subsequently, Chakrabarti and Molteni (Chakrabarti and Molteni 1993) studied flows of constant height and also verified by time dependent numerical simulations that the flow indeed allows standing shocks in it. In a Bondi (Bondi 1952) flow, to specify a solution one requires exactly one parameter, namely the specific energy ($\mathcal{E}$) of the flow. This is in turn determined by the temperature of the flow at a large distance. In an inviscid, rotating axisymmetric accretion flow, one requires two parameters, namely, specific energy ($\mathcal{E}$) and specific angular momentum (λ). Once they are specified, all the crucial properties of the flow, namely the locations of the sonic points, shock locations, as well as the complete global solutions are determined. C89 numerically studied the properties of the parameter space rather extensively, and divided the parameter space in terms of whether standing shocks can form or not. In the present context, we compare these models completely analytically through the study of these flow properties and show, very interestingly, that one could easily 'map' one model onto another by suitably changing the polytropic index of the flow.

In the next Section, we present a set of equations which govern a steady state flow in all the three models. In §3.2.2, we present the sonic point analysis in different models and obtain the expressions for the energy of the flow in terms of the sonic points. We observe that these expressions are identical provided there is a unique relation among the polytropic indices of these model flows. In §3.2.3, we compare shock locations in all the three models. We also compare the parameter

space which allows shock formation in these models with the regions obtained using purely numerical method. In the same Section, we show that in fact if the relations between the polytropic indices are used, the shock locations in all these models are also roughly identical. Therefore, the apparently disjoint parameter spaces drawn with the same polytropic index overlap almost completely when the aforementioned relations among polytropic indices are used. This remarkable behaviour shows underlying unity in these apparently diverse models.

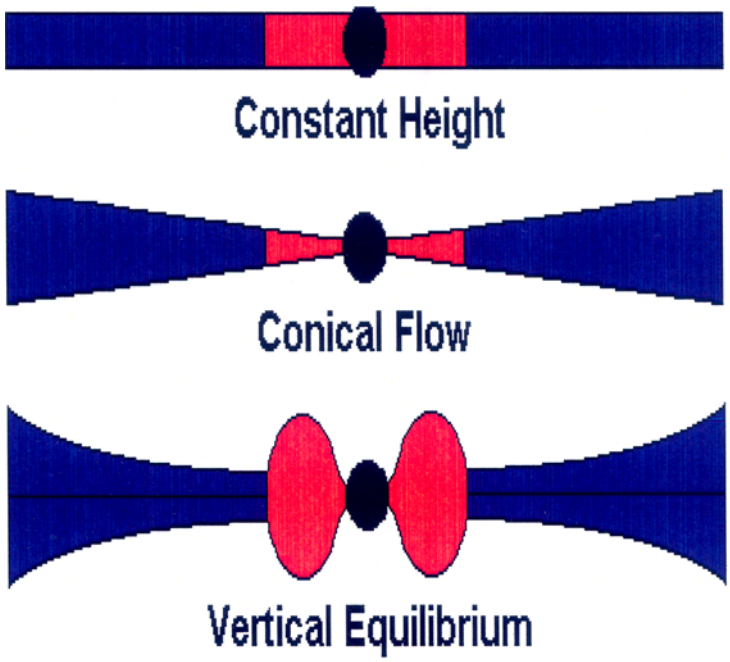

Figure 3.5: Cartoon diagram of three different models discussed in the text. In constant height flow (H) disk thickness is constant (upper). In a conical flow (C), the cross-section in the meridional plane is conical (middle). In a vertical equilibrium flow (V), matter is in locally in vertical equilibrium at every point of the disk (lower).

3.2.1 Model equations

In the present Section, we concern about three axisymmetric and inviscid models: (a) *Model H*: the flow has a constant height everywhere; (b) *Model C*: the flow cross-section in meridional plane is conical in shape and (c) *Model V*: the flow is in equilibrium in the transverse direction. Fig. 3.5 shows a cartoon diagram of these

three models. Filled circle at the centre corresponds to the black hole. Region of the disk shaded in light corresponds to the pre-shock flow while the region shaded in dark corresponds to the post-shock flow. We assume that flow variables are measured in the traditional dimensionless units described earlier.

In all the three models, the dimensionless energy conservation equation can be written as,

$$\mathcal{E} = \frac{\vartheta^2}{2} + \frac{a^2}{\gamma - 1} + \frac{\lambda^2}{2x^2} + g(x), \tag{3.20}$$

where, quantities denote their usual meanings as before. This energy equation is the integral from of the radial momentum balance equation.

The mass flux conservation equation, which comes directly from the continuity equation depends on specific geometry of the models. Apart from a geometric constant, the mass conservation equation (Chakrabarti & Das 2001) is given by,

$$\dot{M} = \vartheta \rho a^{\zeta} x^{\beta} (x-1)^{\delta}, \tag{3.21}$$

where, β, ζ and δ are constants. For Model V (Chakrabarti, 1989a), $\beta = 3/2$, $\zeta = 1$, $\delta = 1$. For Model C (Chakrabarti, 1990a), $\beta = 2, \zeta = 0, \delta = 0$. For Model H (Chakrabarti, 1992; Chakrabarti & Molteni, 1993), $\beta = 1, \zeta = 0, \delta = 0$. Note that since the local disc height $h(x)$ depends on sound speed $h(x) \sim ax^{1/2}(x-1)$, so a factor of a^{ζ} is applicable for this model.

Though it is customary to deal with the conserved mass accretion rate of the flow and since we incorporate shock formation where entropy is increased, it is more convenient to re-write the mass flux conservation equation in terms of ϑ and a in the following way (Chakrabarti & Das 2001),

$$\dot{\mathcal{M}} = \vartheta a^{\alpha} x^{\beta} (x-1)^{\delta} = \vartheta a^{\alpha} f(x), \tag{3.22}$$

where, $\alpha = 2n + \zeta$, $\alpha = 2n$ and $\alpha = 2n$ for Models V, C and H respectively and $f(x) = x^{\beta}(x-1)^{\delta}$. We shall use the phrase "entropy-accretion rate" for the quantity, $\dot{\mathcal{M}} = \dot{M} K^n \gamma^n$. In a flow without a shock, this quantity remains constant, but in presence of a shock it changes because of the generation of entropy.

3.2.2 Sonic point analysis and relation among the models

Since the flow is expected to be sub-sonic at a large distance and super-sonic on the horizon, the flow must pass through sonic points. At the sonic point a few conditions are to be satisfied. They can be derived using general procedure.

First, we differentiate the energy equation and the mass conservation equation and eliminate da/dx from them to obtain,

$$\frac{d\vartheta}{dx} = \left[\frac{2na^2}{\alpha}\left\{\frac{\beta' x - \beta}{x(x-1)}\right\} - \frac{dG}{dx}\right] \Big/ \left(\vartheta - \frac{2na^2}{\alpha\vartheta}\right) . \tag{3.23}$$

Here, $G(x) = \frac{\lambda^2}{2x^2} - \frac{1}{2(x-1)}$ is the effective potential and $\beta' = \beta + \delta$ (Chakrabarti & Das 2001). Since the flow is assumed to be smooth everywhere, if at any point of the flow denominator vanishes, the numerator must also vanish there. The vanishing of the denominator gives,

$$\vartheta_c^2(x_c) = \frac{2n}{\alpha} a_c^2(x_c). \tag{3.24a}$$

The vanishing of the numerator gives,

$$a_c^2(x_c) = \frac{\alpha(x_c - 1)}{2nx_c^2} \frac{[\lambda_K^2(x_c) - \lambda^2]}{[\beta' x_c - \beta]}. \tag{3.24b}$$

The subscript 'c' denotes quantities at the sonic points as before and λ_K represents the Keplerian angular momentum. It is to be noted that since square of the sound speed (Eq. 3.24b) is always positive, angular momentum at the sonic point must be sub-Keplerian. When the above expression for the velocity of sound is inserted in the expression for the specific energy, we get, for the *Vertical Equilibrium (V) Model*,

$$\mathcal{E}_{\rm V} = \frac{n_{\rm V}+1}{5} \frac{x_c}{(x_c - 3/5)(x_c - 1)} - \left[\frac{4(n_{\rm V}+1)}{5} \frac{(x_c-1)}{x_c - 3/5} - 1\right] \frac{\lambda^2}{2x_c^2} - \frac{1}{2(x_c-1)}, \tag{3.25a}$$

for *the Conical Flow (C) Model*,

$$\mathcal{E}_{\rm C} = \frac{2n_{\rm C}+1}{8} \frac{x_c}{(x_c-1)^2} - \frac{2n_{\rm C}-1}{2} \frac{\lambda^2}{2x_c^2} - \frac{1}{2(x_c-1)}, \tag{3.25b}$$

and *for Constant Height Flow (H) Model*,

$$\mathcal{E}_{\rm H} = \frac{2n_{\rm H}+1}{4} \frac{x_c}{(x_c-1)^2} - 2n_{\rm H} \frac{\lambda^2}{2x_c^2} - \frac{1}{2(x_c-1)}. \tag{3.25c}$$

Here, we have used the subscripts V, C and H under specific energy ($\mathcal{E}$) and polytropic index (n) to denote specific models. For a given angular momentum and at the same sonic point, the energy expression will be the same provided (Chakrabarti & Das 2001),

$$\frac{2n_{\rm C}+1}{8} = \frac{2n_{\rm H}+1}{4} = \frac{n_{\rm V}+1}{5}, \tag{3.26}$$

where, we have used

$$(x_c - 1)/(x_c - 3/5) \sim 1 \tag{3.26a}$$

for Model V.

The relations in Eq. (3.26) are very important. If these relations are satisfied, then transonic properties of Model C with polytropic index $n_{\rm C}$ would be identical to those of Model H with index $n_{\rm H}$ and those of Model V with index $n_{\rm V}$ respectively.

3.2.3 Shock invariants and locations in different models

In between two sonic points, the flow can undergo a standing shock transition, in general. For an inviscid flow, at the shock, a set of conditions are to be satisfied. These are known as the Rankine-Hugoniot conditions (Landau and Lifshitz, 1959). These conditions are different for different models (C89a, C90a). For Model V, the shock conditions are as follows:

(A) The energy flux conservation equation,

$$\mathcal{E}_+ = \mathcal{E}_-, \tag{27.a}$$

(B) The pressure balance condition,

$$W_+ + \Sigma_+ \vartheta_{e+}^2 = W_- + \Sigma_- \vartheta_{e-}^2. \tag{27.b}$$

(C) the baryon flux conservation equation,

$$\dot{M}_+ = \dot{M}_- \tag{27.c}$$

where, subscripts '$-$' and '$+$' refer, respectively, to quantities before and after the shock. Here, W and Σ denote the pressure and the density, integrated in the vertical direction (Matsumoto et al. 1984).

For Models C and H, energy flux conservation equation and the baryon number conservation equation for shock are exactly identical with the Model V but the pressure balance condition differs a bit from Model V which is given by,

$$P_+ + \rho_+ {\vartheta^2}_+ = P_- + \rho_- {\vartheta^2}_-. \tag{3.28}$$

Here, P and ρ denote the local pressure and the local density measured at the disk equatorial plane.

The expressions for the conserved quantities could be combined to obtain the so-called Mach number relation, which must be satisfied at the shock. For Model V, we obtain a useful equation relating the pre- and post-shock Mach number of the flow at the shock (C89a) which is given by,

$$C = \frac{[M_+(3\gamma-1)+(2/M_+)]^2}{2+(\gamma-1)M_+^2} = \frac{[M_-(3\gamma-1)+(2/M_-)]^2}{2+(\gamma-1)M_-^2}. \tag{3.29}$$

The constant C is invariant across the shock irrespective with the input parameters.

Similarly, one can obtain the Mach-number relations for the other two models, *i.e.*, Model C and H. The relation between the pre- and the post-shock Mach numbers

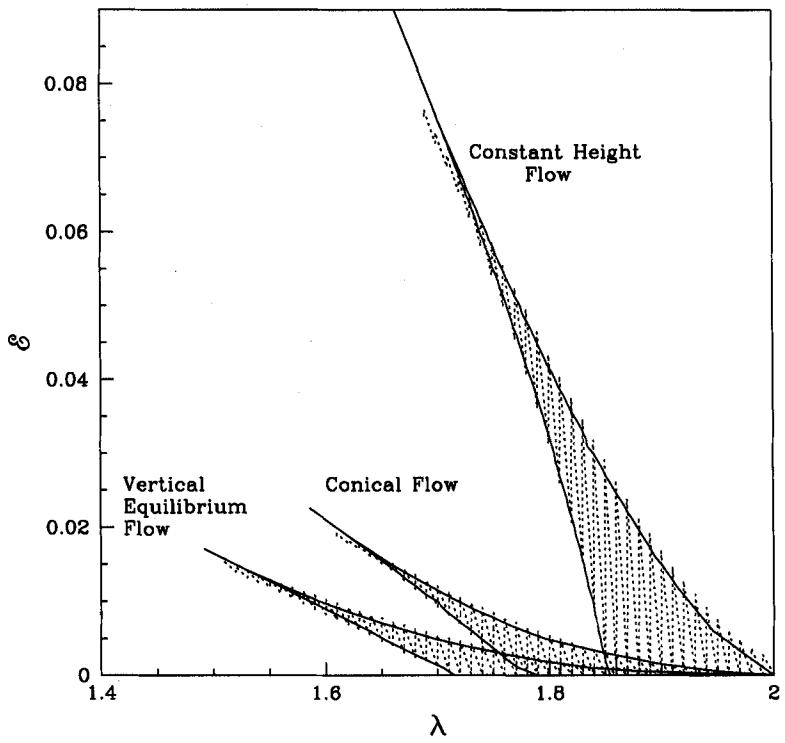

Figure 3.6: Comparison of the parameter space in three different models in which shocks form. $n_{\rm V} = n_{\rm H} = n_{\rm C} = 3$ is chosen throughout. Solid boundaries are obtained using numerical method and shaded regions are obtained using analytical method.

of the flow at the shock for Models C and H has identical expression and is given by,

$$C = \frac{[\gamma M_+ + (1/M_+)]^2}{2 + (\gamma - 1)M_+^2} = \frac{[\gamma M_- + (1/M_-)]^2}{2 + (\gamma - 1)M_-^2}. \tag{3.30}$$

So far, in the literature, analytical shock studies have been carried out in vertical equilibrium model (DCC01) by using the Mach invariant relation (Eq. 3.29) when two parameters, namely, the specific energy and the specific angular momentum are given. Presently we carry out the same analysis using Eq. 3.30 for Models H and C respectively and obtain shock locations and parameter space boundaries for all the three models.

Fig. 3.6 compares these results where plots of specific energy is given as function of specific angular momentum. Solid boundaries mark regions for which standing

shocks form in different models which is obtained numerically. Shaded regions are obtained from the analytical method (DCC01) and results of these two methods roughly agree. We note that constant height flows occupy much larger region than that of the Conical or vertical equilibrium model.

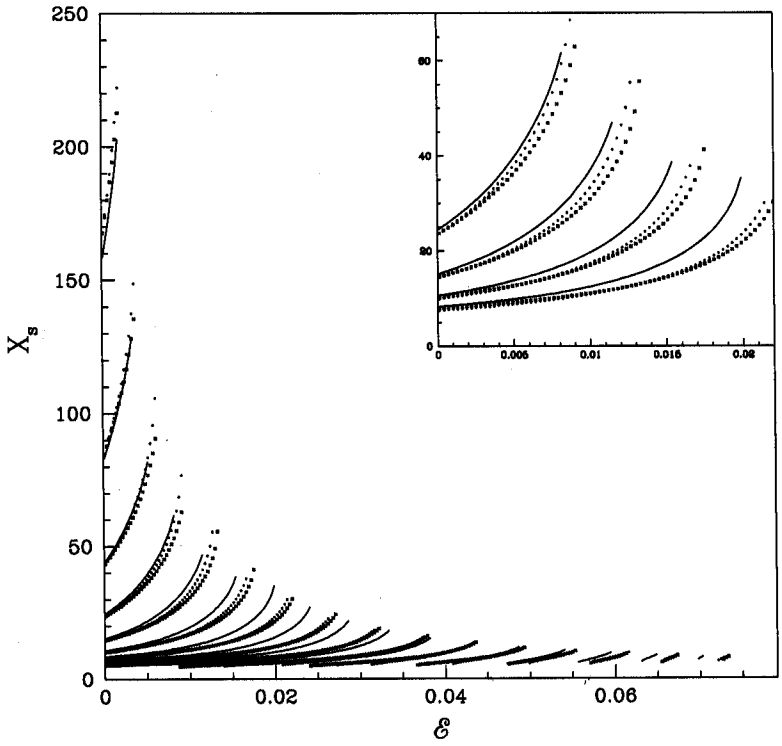

Figure 3.7: Variations of shock locations as function of the specific energy and angular momenta. The left most curve is drawn for $\lambda = 2$ and other curves are for decreasing angular momentum with an interval of $\delta\lambda = 0.02$. Solid curves, filled circles and crosses are drawn for Models V, H and C respectively with $n_{\rm V} = 31/4$, $n_{\rm C} = 13/2$ and $n_{\rm H} = 3$ which obey Eq. (3.26).

3.2.4 Results of mapping of one model to another

We have already noticed that one could use a relation (Eq. 3.26) which maps one model on to another, as far as the transonic properties are concerned. If, for instance, we choose $n_{\rm H} = 3$, we find from Eq. (3.26) that $n_{\rm V} = 31/4$ and $n_{\rm C} = 13/2$ respectively. This means that for a given energy and angular momentum a model H flow of polytropic index 3 would have sonic points exactly at the same place as a

Model V flow of polytropic index 31/4 and Model C flow of polytropic index 13/2 respectively. Corresponding polytropic exponents are $\gamma_H = 4/3$, $\gamma_V = 1.129$ and $\gamma_C = 1.15385$ respectively. In physical terms, a relativistic flow of constant height would have same properties as more or less isothermal flows in a conical flow and a flow in vertical equilibrium.

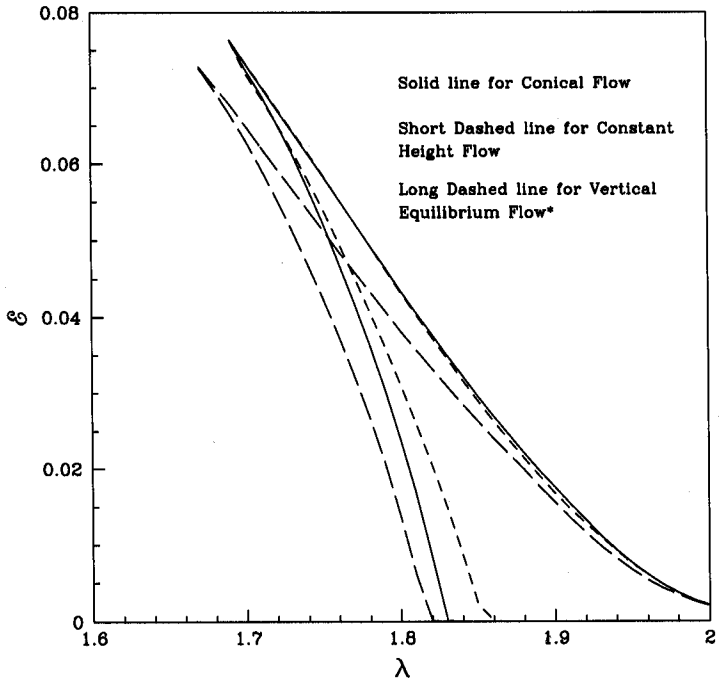

Figure 3.8: Nature of the boundary of the parameter space for the three models of the accretion flows. Solid, short-dashed, and long-dashed curves are drawn for Models C, H and V respectively with polytropic indices $n_V = 31/4$, $n_C = 13/2$ and $n_H = 3$ which obey Eq. (3.26). The roughly similar parameter space shows that the mapping of the indices based on the transonic properties remain roughly the same even when standing shocks are considered. The asterisk mark on 'Vertical Equilibrium Flow' indicates that condition Eq.(3.26a) has been utilized.

What about the shock locations? In Fig. 3.7, we compare the locations of the standing shocks around a black in these three models. Solid curves are for Model V, small circles are for Model H and crosses are for Model C respectively. The polytropic indices n_V, n_C and n_H are chosen as above. We note that though models are different, the shock locations are also remarkably close to one another. In Fig. 3.8, a comparison of the parameter space is shown once more (cf. Fig. 3.6) using the same polytropic indices mentioned above. Unlike disjoint regions in Fig. 3.6, we

find that the regions are almost completely over-lapping when Eq. (3.26) is used. This also shows that the Eq. (3.26) is valid even for the study of shock waves. We thus believe that generally speaking, the three models are identical when the Eq. (3.26) is taken into account.

What could be the possible applications of the pedagogical exercise we carried out? One could imagine that certain models are easier to study (say, using numerical simulations) than the others. For instance, Chakrabarti & Molteni (1993), Molteni, Gerardi & Chakrabarti (1994) and Chakrabarti & Molteni (1995) studied constant height disk using Smoothed Particle Hydrodynamics. This was done because a flow in vertical equilibrium cannot be forced on a time dependent study. However, one could question whether one can draw any conclusion about the behaviour of flows in vertical equilibrium using a simulation of constant height. Our present study shows that it does. Since three models are shown to be identical, running simulation for one model would give results for other models in a straight forward manner. Similarly, study of stability analysis of a model of constant height may be simpler and stability of one model would imply stability of others.

3.3 Computation of outflow rates from accretion disks around Black holes

In this Section, we self-consistently estimate the outflow rate from the accretion rate of a disk around a black hole in which both the Keplerian and the sub-Keplerian matter flows simultaneously. While Keplerian matter supplies soft-photons, hot sub-Keplerian matter supplies thermal electrons. The temperature of the hot electrons is decided by the degree of inverse Comptonization of the soft photons. If we consider only thermally-driven flows from the centrifugal pressure-supported boundary layer (CENBOL) around a black hole, we find that when the thermal electrons are cooled down, either because of the absence of the boundary layer (low compression ratio), or when the surface of the boundary layer is formed very far away, the outflow rate is negligible. For an intermediate size of this boundary layer the outflow rate is maximum. Since the temperature of the thermal electrons also decides the spectral state of a black hole, we predict that the outflow rate should be directly related to the spectral state.

Most of the galactic black hole candidates are known to undergo spectral state transitions (Tanaka & Lewin, 1985; CT95; Ebisawa et al. 1996). Two such common states are known as the hard state and the soft state. In the former, soft X-ray luminosity is low and the energy spectral index $\alpha \sim 0.5$ ($E_\nu \propto \nu^{-\alpha}$) in the 2-10keV range. In the latter state, the soft X-ray luminosity is very high, and hard X-ray intensity is negligible. There is also a weak power-law hard-tail component with an energy spectral slope $\alpha \sim 1.5$. In the two component advective flow (TCAF) model

(CT95), the viscous Keplerian disk resides in the equatorial plane, while the weakly viscous sub-Keplerian flow flanks the Keplerian component both above and below the equatorial plane. The two components merge into a single component when the Keplerian disk also becomes sub-Keplerian. It is suggested (C90a) that close to a black hole, at around $10 - 15\ r_g$, ($r_g = 2GM_{BH}/c^2$ is the Schwarzschild radius, M_{BH} and c are the mass of the black hole and the velocity of light respectively) the sub-Keplerian flow slows down due to the centrifugal barrier and becomes hotter. Chakrabarti (C99) showed that this centrifugal pressure-supported boundary layer region could be responsible for the generation of thermally-driven outflowing winds and jets and one could compute the ratio of the outflow to the inflow rate assuming a simple conical accretion disk model.

In the present study, we compute the *absolute* value of the outflow rate as a function of the rates of the two inflow components, namely, Keplerian and sub-Keplerian matter. This we do analytically following the similar procedure of obtaining shock locations described in §3.1.4 (DCC01). By dynamically mixing of these two components using solutions of the viscous transonic flows we obtain the specific energy and angular momentum of the sub-Keplerian region. We use these pair of parameters to locate shocks in the flow, compute the corresponding compression ratio and from this, the outflow rate. We note that as Keplerian matter is increased in the mixture, the shock compression ratio goes down, and the outflow rate decreases. This is also the case even from a radiative transfer point of view – when the Keplerian rate is high, the CENBOL region is completely cooled down and the shock compression ratio $R \sim 1$. Hence in the soft state, which is due to increase of the Keplerian rate, the outflow should be negligible.

3.3.1 Model equations

We consider matter accreting on the equatorial plane of a Schwarzschild black hole. As before, the space-time around the black hole is described by the Paczyński-Wiita pseudo-Newtonian potential $\phi = -\frac{GM_{BH}}{r-2GM_{BH}/c^2}$ (PW80), where M_{BH} is the mass of the black hole and G, c are the gravitational constant and velocity of light respectively. Here, r is the radial distance from the origin of the co-ordinate in which the black hole is treated at the centre. Here also, we use geometric unit ($M_{BH} = c = 1; G = 1/2$) to express flow variables in dimensionless manner and then Paczyński-Wiita pseudo-Newtonian potential reduces to the familiar form as $\phi = -1/\{2(x-1)\}$ where x represents the non-dimensional radial distance. In accretion or wind, we assume that the viscous stress is negligible so that matter moves with a constant specific angular momentum. Indeed, even if viscosity is not negligible, the transport of angular momentum is slow compared to the infall timescale. Hence, matter can have almost constant specific angular momentum.

Under this circumstances, the radial momentum equation (Eq. 3.1) and the corresponding conserved energy equation (Eq. 3.2) for a non-dissipative vertical equilibrium flow will take the identical form presented in §3.1.

In the steady state, the corresponding mass flux conservation equation in a flow which is in vertical equilibrium is given by,

$$\dot{M}_{in} = 4\pi\rho\vartheta x h(x) = \Theta_{in}\rho_s\vartheta_s x_s^2, \tag{3.31}$$

where $\Theta_{in}(=\sqrt{\frac{2n}{n+1}}4\pi a_s x_s^{1/2})$ is the solid angle subtended by the inflow at the CENBOL boundary (DCNC01). Subscript 's' denotes the quantities at shock (CENBOL boundary) and $h(x) = \sqrt{\frac{2}{\gamma}}ax^{1/2}(x-1)$ is the half-thickness of the disk at a radial distance x.

A sub-Keplerian flow with a positive energy will pass through the outer sonic point and depending on whether the Rankine-Hugoniot conditions are satisfied or not, a standing shock may form (C90a; C96a). If a standing shock forms, then the post-shock flow would become hot and would emit hard X-ray radiation. This post-shock (CENBOL) region behaves similarly to the boundary of a normal star and it would be expected to drive outflows. Using Eqs. (3.1 and 3.31), one can compute the shock locations (i.e., outer surface of the CENBOL) analytically following the formalism discussed in §3.1.4.

In the present study, since the outflow is expected to produce in the presence of shock, we consider only the region of the inflow parameter space ($\mathcal{E}$, λ) that is able to produce standing shocks. In the pre-shock region, matter is cooler and sub-Keplerian. Assuming $\mathcal{E} \sim 0$ (freely falling condition) and $a \sim 0$ (cool gas) in the presence of angular momentum, matter will fall with a velocity,

$$\vartheta(x) = \left[\frac{1}{x-1} - \frac{\lambda^2}{x^2}\right]^{1/2}. \tag{3.32}$$

Using Eq. (3.32) in Eq. (3.33) one can obtain the density distribution of the flow.

At the shock $x = x_s$, i.e., the boundary of the CENBOL, the compression ratio is given by,

$$R = \frac{\Sigma_+}{\Sigma_-} = \frac{h_+(x_s)\rho_+(x_s)}{h_-(x_s)\rho_-(x_s)} = \frac{\vartheta_-}{\vartheta_+}, \tag{3.33}$$

where subscripts '$-$' and '$+$' refer, respectively, to quantities before and after the shock. Here, Σ is the density of matter integrated vertically ($\Sigma \sim \rho h$) (Matsumoto et al. 1984) and the second '$=$' sign was written using the mass flux conservation equation given above (Eq. 3.31).

At the shock, the total pressure (thermal and ram pressure) must be balanced and we have,

$$W_-(x_s) + \Sigma_-(x_s)\vartheta_-^2(x_s) = W_+(x_s) + \Sigma_+(x_s)\vartheta_+^2(x_s), \tag{3.34}$$

where, W is the vertically integrated pressure of the flow (Matsumoto et al. 1984).

We assume that in the pre-shock region, the thermal pressure is small compared to the ram pressure. Therefore, we get

$$W_+(x_s) = \frac{R-1}{R}\Sigma_-(x_s)\vartheta_-^2(x_s). \tag{3.35}$$

Accordingly, the isothermal sound speed in the post-shock region is obtained as (DCNC01):

$$C_s^2 = \frac{W_+}{\Sigma_+} = \frac{R-1}{R^2}\vartheta_-^2 = \frac{1}{f_0}\left[\frac{x_s^2 - \lambda^2(x_s-1)}{x_s^2(x_s-1)}\right], \tag{3.36}$$

where, $f_0 = \frac{R^2}{R-1}$ has been used.

Up to the sonic point matter moves slowly and the density is higher. Since the outflow would take place in a sea of radiation, the momentum deposition is likely to be effective. With the electron number density $n_e \propto x^{-3/2}$, yet photon number density $n_\gamma \propto x^{-2}$, it is easier to deposit momentum only close to the black hole. In radiation driven outflows from the stellar surface, it is customary to assume flows to be isothermal until the sonic point. We first compute outflow rates making this assumption. Later we drop this assumption and show that the general behaviour remains similar. In addition, we assume that there is very little rotation in the outflow. There is no a priori reason to assume this, except that there is no observational support of rotation in the jet and it is possible that due to radiative viscosity most of the angular momentum is transported very close to the black hole. Furthermore, it has been observed that the effect of angular momentum in the outflow is to bring the sonic points closer to the black hole, especially away from the axis (Sakurai 1985; Chakrabarti 1986b). The general effect would produce a transverse structure in the jet which we ignore in the present solution. It was shown (Das & Chakrabarti 1999) that in presence of angular motion the conical outflow is to be replaced by an annular flow confined by the centrifugal barrier and the funnel wall. Generally speaking, the outflow surface varies as $x^{3/2}$. However, the inflow surface area is still proportional to x^2. Because of this asymmetry, the problem is no longer tractable analytically and is beyond the scope of the present study.

3.3.2 When the outflow is isothermal

The radial momentum balance equation in the outflow is given by

$$\vartheta\frac{d\vartheta}{dr} + \frac{1}{\rho}\frac{dP}{dr} + \frac{1}{2(r-1)^2} = 0, \tag{3.37}$$

where, ϑ and r are respectively the non-dimensional radial velocity and radial distance of the outflow. The so-called continuity equation in the steady state is given

by,

$$\frac{1}{r^2}\frac{d}{dr}(\rho\vartheta r^2) = 0. \tag{3.38}$$

Eliminating $d\rho/dr$ from above two equation we get

$$\frac{d\vartheta}{dr} = \frac{N}{D}, \tag{3.39}$$

where,

$$N = \frac{2C_s^2}{r} - \frac{1}{2(r-1)^2} \quad \text{and} \quad D = \vartheta - \frac{C_s^2}{\vartheta}.$$

To obtain the sonic point conditions, we put $N = 0$ and $D = 0$ and get, $\vartheta(r_c) = C_s$, and $r_c = \frac{1+8C_s^2 \pm \sqrt{1+16C_s^2}}{8C_s^2}$, where, the subscript 'c' denotes the quantities at the sonic point in the outflow.

Integrating the radial momentum equation (Eq. 3.37) and considering the sonic point conditions we have,

$$C_s^2 ln\rho_+ - \frac{1}{2(r_s-1)} = \frac{1}{2}C_s^2 + C_s^2 ln\rho_c - \frac{1}{2(r_c-1)}. \tag{3.40}$$

Here, we have ignored the radial velocity in the outflow at the boundary of the shock location (x_s) in the inflow. Using the notations $\rho(r_c) = \rho_c$ and $\rho(x_s) = \rho_+$, we obtain,

$$\rho_c = \rho_+ exp[-f], \tag{3.41}$$

where,

$$f = \frac{1}{2} - \frac{1}{2C_s^2}\frac{x_s - r_c}{(x_s-1)(r_c-1)}.$$

Indeed, the outflow rate is given by

$$\dot{M}_{out} = \Theta_{out}\rho_c\vartheta_c r_c^2, \tag{3.42}$$

where, Θ_{out} is the solid angle subtended by the outflow.

From Eq.(3.31) & Eq. (3.42) we get the ratio of the outflow rates to the inflow rates (DCNC01) as,

$$\frac{\dot{M}_{out}}{\dot{M}_{in}} = R_{\dot{m}} = \frac{\Theta_{out}}{\Theta_{in}}\left[\frac{x_s^2(x_s-1)}{x_s^2 - \lambda^2(x_s-1)}\right]^{-1/2}\frac{RC_s r_c^2}{x_s(x_s-1)}exp[-f]. \tag{3.43}$$

The above relation is very similar to that obtained in C99 when the effects of rotation in the inflow were ignored. However, there the ratio $R_{\dot{m}}$ was a function of R alone.

In the present analysis, R is computed self-consistently from the specific energy and the specific angular momentum of the flow and is obtained as

$$R = \frac{\Sigma_+}{\Sigma_-} = \frac{\vartheta_-}{\vartheta_+} = \left[\frac{\frac{1}{2}M_+^2 + n}{\frac{1}{2}M_-^2 + n}\right]^{1/2}, \tag{3.44}$$

where, pre-shock and post-shock Mach numbers $M_-(\mathcal{E}, \lambda)$ and $M_+(\mathcal{E}, \lambda)$ are computed analytically using the method presented in §3.1.4.

3.3.3 When the outflow is adiabatic

At the other extreme, when the energy of the outflow does not change, one can also obtain an analytical expression for the outflow rate assuming $x_s >> \lambda^2$. In this case, the entropy density of the flow in the post-shock region is same at the entropy density of the entire outflow and the specific energy is also conserved along the outflow. We assume that the turbulence generated at the CENBOL has effectively transported angular momentum away. Thus, the energy conservation equation gives

$$na_s^2 - \frac{1}{2r_s} = \frac{2n+1}{2}a_c^2 - \frac{1}{2r_c}, \tag{3.45}$$

where, the left hand side is the energy at the CENBOL ($x = x_s$) and the right hand side is at the sonic point ($r = r_c$) of the outflow where $u_c = a_c$ has been used. In a Bondi (in or out) flow, $a_c^2 = 1/2r_c$. At the CENBOL, $a_s^2 = \gamma C_s^2$, where C_s is the isothermal sound speed (Eq. 3.36). Using these, one obtains (assuming $x_s >> \lambda^2$)

$$\frac{r_c}{x_s} = \frac{2n-3}{4(\frac{2n\gamma}{f_0} - 1)}, \tag{3.46a}$$

and

$$\frac{a_c^2}{a_s^2} = \frac{f_0 x_s}{4\gamma r_c}. \tag{3.46b}$$

In an adiabatic flow with an equation of state $P = K\rho^\gamma$ (where K is a constant and a measure of entropy), one obtains, assuming, $K_c = K_s$,

$$\frac{\rho_c}{\rho_s} = \left(\frac{a_c^2}{a_s^2}\right)^n. \tag{3.47}$$

From these relations one obtains the ratio of the outflow to the inflow rate (DCNC01) as

$$R_{\dot{m}} = \frac{\Theta_o}{\Theta_i}\left(\frac{f_0}{4\gamma}\right)^3 \frac{R}{2}\left\{\frac{4}{3}\left[\frac{8(R-1)}{R^2} - 1\right]\right\}^{3/2}. \tag{3.48}$$

Here, we have used $n = 3$ for a relativistic flow. The nature of this function will be discussed latter.

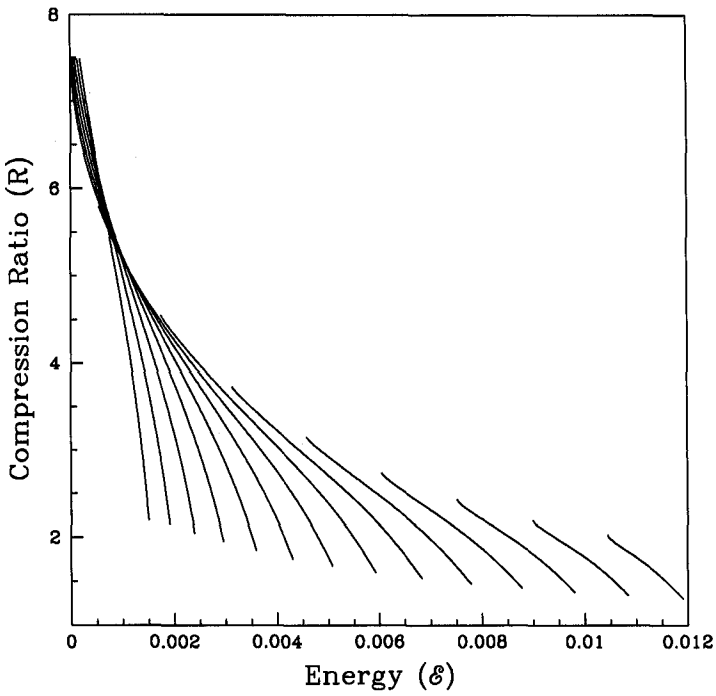

Figure 3.9: Variation of the compression ratio of the shocks as a function of specific energy $\mathcal{E}$ and angular momentum λ as obtained from the analytical solution. λ varies from 1.57 (right) to 1.79 (left). Curves are drawn at intervals of $d\lambda = 0.02$.

3.3.4 Outflow rates from inflow parameters

In Eq. (3.43), we presented the outflow-inflow rate ratio as a function of the compression ratio of the flow at shock. The compression ratio is obtained from the specific energy and angular momentum using Eq. (3.44). First, we employ analytical means to obtain this for a single component sub-Keplerian disk. Second, we use a two component Keplerian and sub-Keplerian disk to actually compute these parameters from more fundamental parameters such as accretion rates and viscosity.

3.3.5 Single component sub-Keplerian advective flows

In Fig. 3.9, we plot the analytical solution of the compression ratio R as a function of the inflow parameters such as the specific energy ($\mathcal{E}$) and the specific angular momentum (λ) (DCNC01). The shock strength generally increases when energy decreases and the angular momentum increases. This is because for low energy, the outer sonic point and the shock form very far away from the black hole and

the Mach number jumps from a very large number to a very small number. If the angular momentum is decreased, shock is produced only if the specific energy is high, i.e., if the sonic points and the shocks are formed very close to the black hole. Here, flow becomes sub-sonic before its Mach number could be very high.

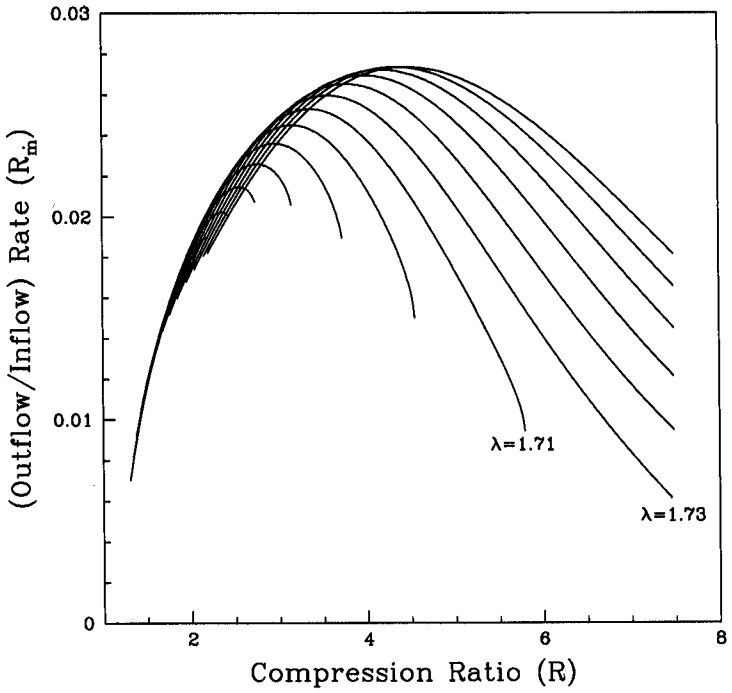

Figure 3.10: Variation of the ratio of outflow to inflow rates $R_{\dot{m}}$ as a function of compression ratio for various specific angular momenta ranging from $\lambda = 1.57$ (inner most) to 1.83 (outer most). Curves are drawn at intervals of $d\lambda = 0.02$. Outflow rate is maximum at some intermediate compression ratio.

Figure 3.10 shows the principle result of our work when only one sub-Keplerian accretion flow is chosen as inflow (DCNC01). We plot the ratio $R_{\dot{m}}$ for a large number of specific angular momenta of the flow ranging from 1.57 (innermost) to 1.83 (outermost) at intervals of $d\lambda = 0.02$. The curves are drawn for all ranges of specific energy ($\mathcal{E}$) for which shocks are formed. Along the X-axis the compression ratio R of these shocks are plotted. Here, to compute solid angles of the inflow and the outflow, we assume the half opening angle of the outflow to be 10^o. Therefore, $\Theta_{out} = \pi^3/162$. Θ_{in} is estimated from the discussion following Eq. (3.31). In Chakrabarti's (C99) work, the compression ratio R was assumed to be a parameter and no angular momentum was assumed a priori. Presently, we specifically show

the dependence of $R_{\dot{m}}$ on angular momentum. However, the general character, namely, that the outflow rate is negligible when the shock is weak ($R \sim 1$) and falls off gradually for strongest shock ($R \to 7$), remains the same as in Chakrabarti (1999). There is a peak at about $R_{\dot{m}} \sim 2.8\%$. Note that for a given R, $R_{\dot{m}}$ increases monotonically with specific angular momentum λ. This is because density of CENBOL rises with λ. The curves corresponding to $\lambda = 1.71$ and 1.73 are specially marked since there is a clear difference in tendency of the variation of $R_{\dot{m}}$. For instance, below $\lambda \sim 1.72$, very strong shocks are not possible at all and as a result the outflow rate has a lower limit. For $\lambda \gtrsim 1.72$ such a limit does not exist.

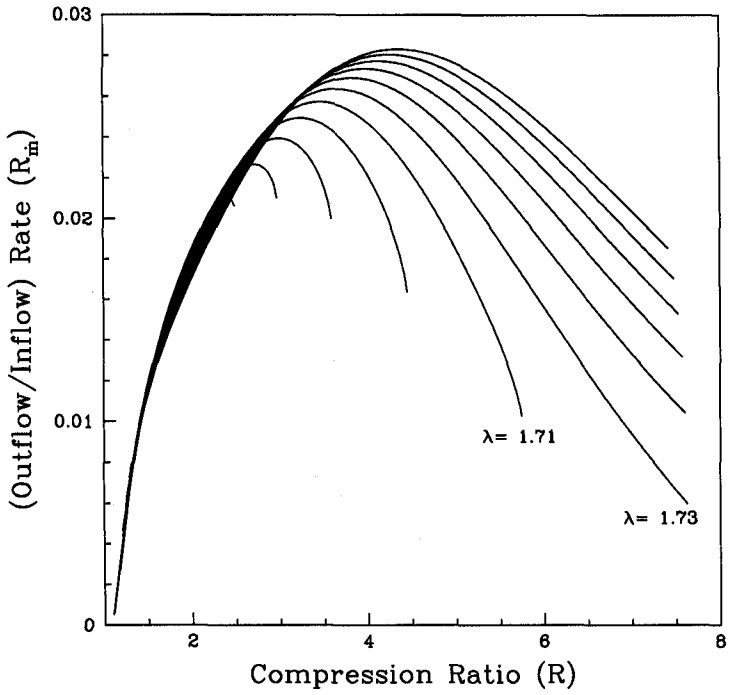

Figure 3.11: Same as Fig. 3.10 except that curves are drawn for the exact numerical solution.

The general behaviour of the outflow rate can be understood in the following way: when shocks are strong, they form very far out, and thus, even though the CENBOL area (which is basically the area of the base of the jet) increases, the net outflow rate is low. When the shock forms very close to the black hole, the temperature is high, and thus the outflow velocity is larger, but the CENBOL surface area goes down. Thus the product is low. For the intermediate cases the net effect is larger.

For comparison with the analytical work presented in Fig. 3.10, in Fig. 3.11

we present a similar diagram drawn using a numerical computation of the shock locations (C89a). Excellent agreement between these two figures implies that the approximations on which the analytical work was based are justified. All the features are reproduced well in Fig. 3.10, except that for the weakest shocks outflow rate is not as low as in the numerical calculation of Fig. 3.11.

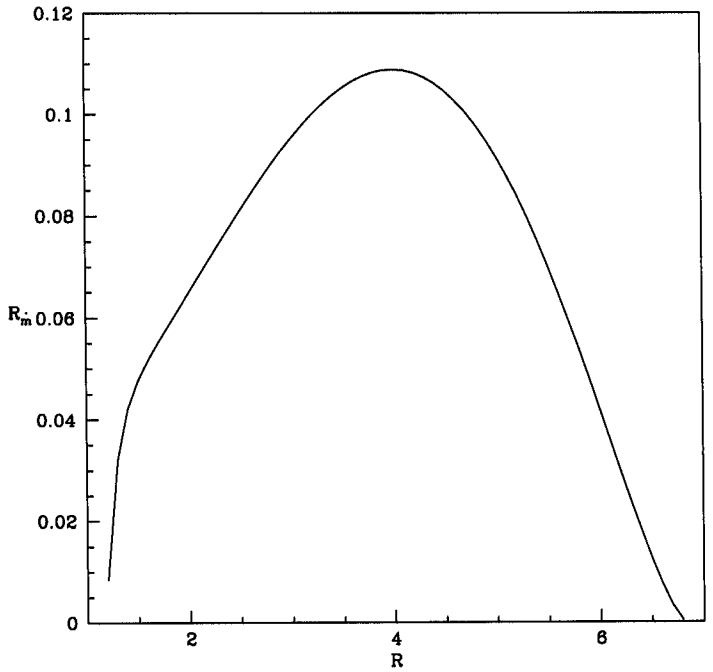

Figure 3.12: Ratio of the Outflow and the Inflow rates as a function of the compression ratio of the inflow when the outflow is adiabatic in nature. The general behavior of the function remains the same as that of the isothermal outflow.

We now present the nature of $R_{\dot{m}}$ when the outflow is also chosen to be adiabatic in Fig. 3.12 (DCNC01). We used $\Theta_o/\Theta_i \sim 0.1$ for reference. We observe that the peak is still located at around $R \cong 4$ and the outflow rate drops for very strong ($R \sim 7$) and very weak ($R \sim 1$) shocks. We, therefore, believe that our conclusion about the behaviour of $R_{\dot{m}}$ is generic.

3.3.6 Two component advective flows

Chakrabarti & Titarchuk (CT95) proposed that the spectral properties are better understood if the disk solutions of sub-Keplerian flows are included along with the Keplerian flows. Recently, Smith, Heindl and Swank (2001a), Smith et al. (2001b) and Miller et al. (2002) found conclusive evidence of these two components in many

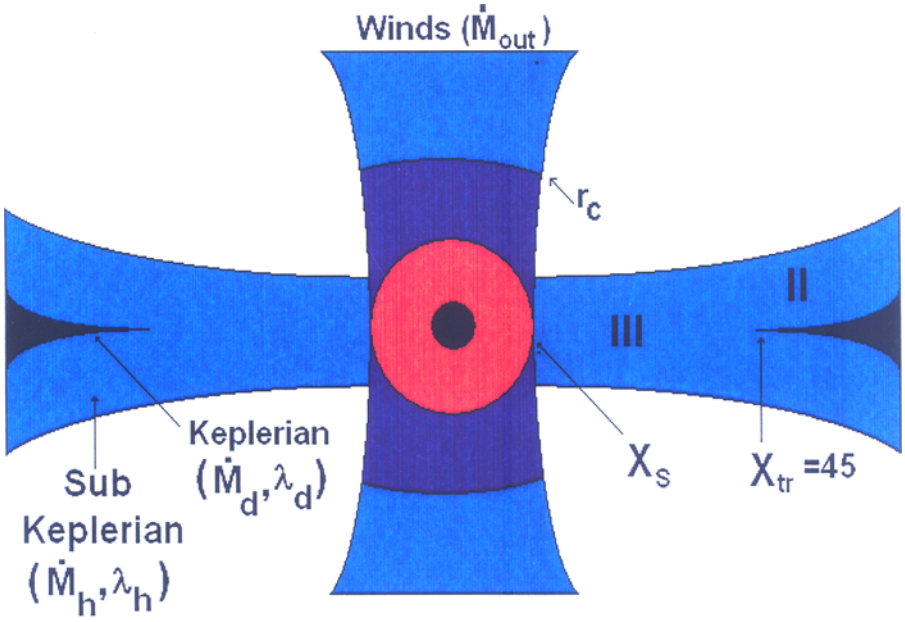

Figure 3.13: Schematic diagram of the meridional cross section of two-component accretion flow. Details of the figure are described inside the text.

of the black hole candidate accretion flows. While the matter with higher viscosity flows along the equatorial plane as a Keplerian disk (of rate $\dot{M}_K$), sub-Keplerian halo matter (of rate $\dot{M}_h$) with lower viscosity flanks the Keplerian disk above and below (Fig. 3.13). Since the inner boundary conditions on the black hole horizon force the flow to be sub-Keplerian, irrespective of their origin (C90a, C96a) matter mixes (at say, $r = r_{tr}$) from both the Keplerian and sub-Keplerian flows before entering into a black hole to form a single component sub-Keplerian with an average energy and angular momentum of $\mathcal{E}$ and λ respectively. In §3.1.5, we already discussed this issue briefly. Subsequently, the specific energy and angular momentum of the mixed flow is computed as (DCNC01):

$$\mathcal{E} = \frac{\dot{M}_K \mathcal{E}_K + \dot{M}_h \mathcal{E}_h}{\dot{M}_K + \dot{M}_h}, \tag{3.49}$$

and

$$\lambda = \frac{\dot{M}_K \lambda_K + \dot{M}_h \lambda_h}{\dot{M}_K + \dot{M}_h}, \tag{3.50}$$

where, $\mathcal{E}_K$, $\mathcal{E}_h$, λ_K and λ_h are the specific energies and specific angular momentum of the Keplerian and the sub-Keplerian components at $x = x_{tr}$ respectively.

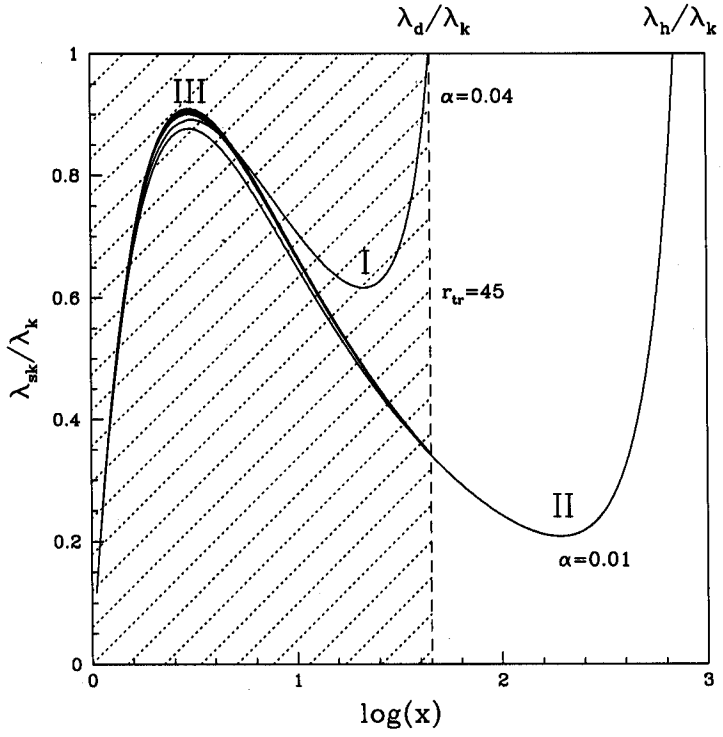

Figure 3.14: Solution of the two-component flow equations for two different viscosities. They are merged to form a single solution as depicted in Fig. 3.13.

Fig. 3.13 shows a schematic diagram of the cross-section of a two-component accretion flow. The transition radius ($x = x_{tr}$) where the Keplerian disk becomes sub-Keplerian, and the shock location $x = x_s$, are indicated in the Figure. Fig. 3.14 shows two solutions (marked I and II) of the equations governing a two-component flow (C96a) where λ_d/λ_K (Sub-Keplerian matter from the Keplerian disk) and λ_h/λ_K (Sub-Keplerian halo) are plotted as a function of the logarithmic radial distance (DCNC01). Viscosities chosen for these two components are $\alpha = 0.04$ and $\alpha = 0.01$ respectively. For $x < x_{tr} = 45$ (lightly shaded region) the two component flow, namely, Keplerian and sub-Keplerian flow mix to create a single component sub-Keplerian flow. For simplicity, we assume viscosity to be negligible in this region. Thus, the specific angular momentum and specific energy computed at $x = x_{tr}$ from Eqs. (3.49 & 3.50) remain constant for $x < x_{tr}$. Dark solid curve (marked III) shows the angular momentum distribution λ/λ_K of all possible mixtures of the two components which allows shock formation. We choose a case where $\dot{M}_d + \dot{M}_h = 2.0\dot{M}_{Edd}$ and vary the Keplerian component $\dot{M}_d$ where $\dot{M}_{Edd}$ is the

Eddington accretion rate.

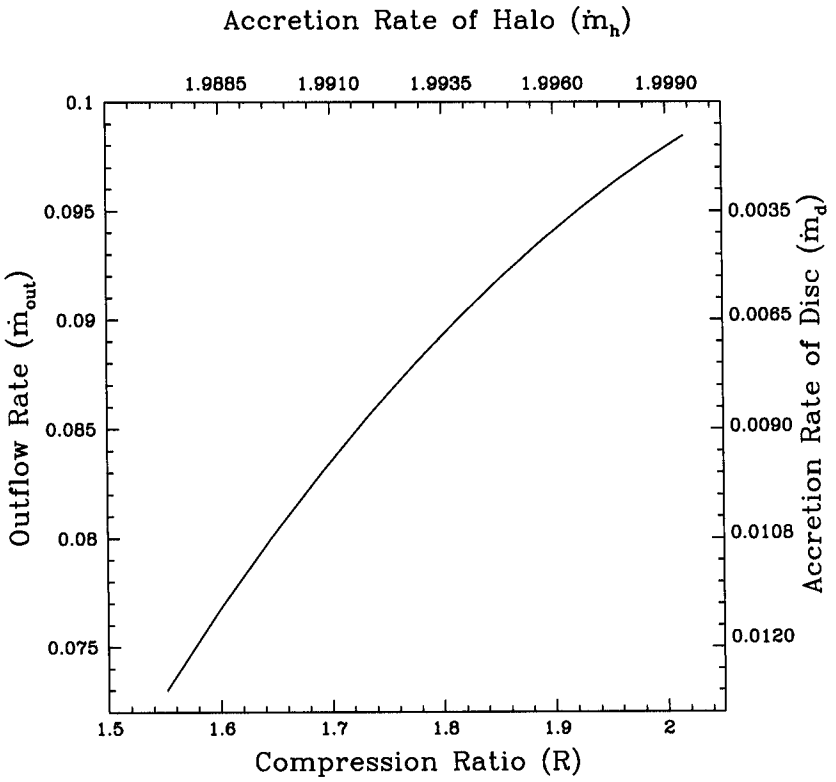

Figure 3.15: Variation of outflow rates (left axis) with compression ratio at shocks (lower axis). The upper axis gives the variation of sub-Keplerian accretion rate and right axis gives the same for Keplerian accretion rate.

In Fig. 3.15, the computed outflow rates are shown when the half opening angle of the outflow is 10^o. In this case, $\frac{\Theta_{out}}{\Theta_{in}} \sim \sqrt{\frac{n+1}{2n}} \frac{\pi^2}{648 a_s x_s^{1/2}}$. The left axis shows the rate of outflow $\dot{m}_{out} = \dot{M}_{out}/\dot{M}_{Edd}$ as a function of the Keplerian disk rate (right panel) ($\dot{m}_d = \dot{M}_d/\dot{M}_{Edd}$) and the halo rate (upper panel) ($\dot{m}_h = \dot{M}_h/\dot{M}_{Edd}$). The lower axis gives the compression ratio at the shock. The most important conclusion that can be drawn here is that the outflow rate steadily goes up as the Keplerian disk rate $\dot{m}_d$ decreases and the spectrum goes to a harder state. When the Keplerian rate is higher, the compression ratio is lower and the outflow rate is also lower. This conclusion, drawn completely from dynamical considerations, is also found to be true from the spectral studies (CT95) where it was shown that the post-shock region cools down and the shock disappears ($R \rightarrow 1$). Our work therefore hints that the outflow would be negligible in softer states.

3.4 Mechanism of ejection of matter in SS 433

So far, we discussed the propeties of accretion flows. Our next goal is to explain various observational features on the basis of these theoretical results. In this thesis, we shall discuss the possible mechanisms to produce clumpy jets (so called bullets) ejected from an enigmatic object called SS 433. Even 25 years after its discovery this object is yet not well understood in terms of whether the compact object is a black hole or a neutron star. However, it is believed that the companion is an OB-type star with an orbital period of 13.1 days which is losing mass at the rate of about $10^{-4}\ M_{\odot}\ \mathrm{yr}^{-1}$, corresponding to the extremely super-Eddington accretion rate. More surprisingly, the jets of SS 433 are apparently ejected as bullets with nearly constant radial velocity of about 26% of velocity of light. Interestingly, variable $H\alpha$ line emission demand the confirmation of presence of jets in SS 433 where the time variation of red- and blue-shifts of $H\alpha$ line from the jets occurs in a period of 162 days. Moreover, it is well known (C99 and Das & Chakrabarti 1999) that significant outflows are produced when the central source is in the low/hard state though it is difficult to remain in a low/hard state with $10^{-4}\ M_{\odot}\ \mathrm{yr}^{-1}$ accretion rate. The only possibility of sustaining such situation is that most of the incoming matter is expelled either by the centrifugal barrier (Chakrabarti et al. 2002) or by radiation force far outside the accretion disk and thus the compact object accrets only few times the Eddington rate ($\dot{M}_{Edd}$) which produces kinematic luminosity of the jet is around 10^{39} ergs sec^{-1} for a $10M_{\odot}$ compact object. In fact, numerical simulations (Molteni et al. 1994) suggested that about 15%-20% of matter could be ejected as an outflow for at most few $\dot{M}_{Edd}$ of accretion matter. Moreover, matter accreted around the compact object of SS 433 with the low angular momentum sub-Keplerian flow since it is supplied from the winds of companion star. In addition, the bullets of mass range $10^{19} - 10^{21}$ gm in the jets of SS 433 are expected to ejected in 50-1000 sec time intervals under normal circumstances. Along with this, some occasional flaring with an anti-correlation of radio and X-ray emission in jets of SS 433 is observed. Therefore, theoretical description must explain these essential features when attempting to produce bullets out of the accretion disk. Presently we briefly discuss several probable scenarios to understand the ejection mechanism of bullets in SS 433 system (Chakrabarti et al. 2002).

It is already established in the literature that the sub-sonic outflows are generated from the inner part of the accretion disk (C99 and Molteni et al. 1994) and immediately becomes super-sonic after passing through the sonic point. In fact, at the base of the jet density is high and optical depth is large enough ($\tau > 1$) to undergo Compton cooling. Therefore, the sub-sonic jet rapidly cools down due to interaction with soft photons supplied from the Keplerian disk and separates jet matter from the base of the jet as a blob. This mechanism, though attractive, does not work in our present context as SS 433 is a wind accreter which indicates the

absence of Keplerian disk for supplying the soft photon in the system.

Several authors (Langer, Chanmugam & Shaviv 1982; MSC96) already showed by numerical simulation that outflows may be ejected quasi-periodically when cooling time scale matches with the infall time scale inside the accretion disk. With this mechanism, outflow of similar order of the mass of the bullets observed in SS 433 may be ejected with the 50 sec oscillation period but such an oscillation requires very high specific angular momentum of the inflow compared to the marginally bound value ($\sim$ 30 times). Therefore, it is unlikely that this mechanism works in SS 433.

In order to have a standing shock in a sub-Keplerian flow there must be two X-type sonic points and in between these two sonic points Rankine-Hugoniot shock conditions are satisfied at some point (C89a). Indeed, there is a large region of parameter space where the flow has two X-type sonic points but shock conditions are not satisfied (C90a). In this situation, when the entropy of the inner sonic point is higher than the outer sonic point, the flow tries to make a shock transition but is unable to find the solution and then starts to oscillate (Ryu, Chakrabarti & molteni 1997). Therefore, periodic ejection of matter takes place in the form of outflow due to this non-steady shock oscillation. This mechanism has stronger possibility for blob ejection due to its generic nature as once the oscillation established could be sustained indefinitely.

In the recent development of accretion disk physics Nandi et al. (2001) showed that magnetic field from the companion star is first intercepted into the accretion disk in the form of a flux tube and then it is advected toward the inner edge of the disk. Subsequently, due to the shearing effect in the rotating flow, the magnetic field becomes toroidal and the acceleration due to magnetic tension becomes the dominant force in the post-shock region of the sub-Keplerian flow. Meanwhile, flux tubes catastrophically collapse and evacuate the inner part of the disk in the Alfvén time scale. Therefore, evacuation of the inner part of the disk is associated with flaring in the radio jets. Simultaneous observations in 2 GHz radio and 2-10 keV X-ray fluxes from SS 433 show clear dip in X-ray flux and at the same time strong radio flare is detected (Safi-Harb & Kotani 2002). Indeed, this mechanism could be another possibility for jet ejection in SS 433 in the form of bullets.

Chapter 4

Properties of Shock Waves in Dissipative Accretion Flow

In order to study the different properties of dissipative accretion flow around a black hole, we consider various heating and cooling processes that may impose significant contribution to the flow. Accordingly, we begin our study by incorporating viscosity as the heating process inside the accretion disk. For the shake of completeness, we further include different cooling mechanism, namely, bremsstrahlung and synchrotron cooling in succession.

4.1 Viscous accretion flow

In the standard theory of thin accretion flow around a black hole (SS73), viscosity transports angular momentum outwards and allows matter to sink into the black hole potential well. In this model, the flow angular momentum is assumed to be Keplerian and this is the standard notion about how matter is accreted. Meanwhile, Chakrabarti & Molteni (1995) and Lanzafame, Chakrabarti & Molteni (1998) showed by numerical simulation that the angular momentum distribution of accreted matter solely depends on the viscosity prescription and close to the black hole matter deviates from Keplerian to sub-Keplerian distribution since it has to be supersonic at the black hole horizon according to the inner boundary conditions. Presently we start with Chakrabarti's (C96a) modified viscosity prescription and ignore all the cooling effects. In the following Sections, we shall extensively carry out the sonic point analysis and study global solution topologies, shock properties and critical viscosity parameters.

4.1.1 Governing equations

We begin with a steady, thin, viscous, axisymmetric accretion flow on to a Schwarzschild black hole. The space-time geometry around a Schwarzschild black hole is dictated

by the pseudo-Newtonian potential introduced by Paczyński & Wiita (PW80) to avoid complexity. The expression for the pseudo-Newtonian potential given by,

$$g(r) = -\frac{GM_{BH}}{\left[r - \frac{2GM_{BH}}{c^2}\right]},$$

where, the quantities have their usual meanings as before.

In the steady state, the dimensionless hydrodynamic equations that govern the notion of infalling matter are the followings (C96a).

(a) Radial Momentum equation :

$$\vartheta\frac{d\vartheta}{dx} + \frac{1}{\rho}\frac{dP}{dx} - \frac{\lambda(x)^2}{x^3} + \frac{1}{2(x-1)^2} = 0, \tag{4.1a}$$

(b) Baryon number conservation equation :

$$\dot{M} = \Sigma\vartheta x, \tag{4.1b}$$

apart from a geometric constant.

(c) Angular momentum conservation equation :

$$\vartheta\frac{d\lambda(x)}{dx} + \frac{1}{\Sigma x}\frac{d}{dx}\left(x^2 W_{x\phi}\right) = 0, \tag{4.1c}$$

and finally,

(d) The entropy generation equation :

$$\Sigma\vartheta T\frac{ds}{dx} = Q^+ - Q^-, \tag{4.1d}$$

where, flow variables ϑ, ρ, P and $\lambda(x)$ in the above equations are the radial velocity, density, isotropic pressure and specific angular momentum of the flow respectively. Here Σ and $W_{x\phi}$ denote the vertically integrated density (Matsumoto et al. 1984) and the viscous stress, s is the entropy density of the flow, T is the local temperature. Q^+ and Q^- are the heat gained and lost by the flow (integrated in the vertical direction) respectively.

The present model is constructed in such a way that the disk is assumed to be in hydrostatic equilibrium in the vertical direction and therefore, local disk height is obtained as (§2.1, Eq. 2.3)

$$h = ax^{1/2}(x-1). \tag{4.2}$$

Here, a is the adiabatic sound speed defined as $a = \sqrt{\gamma P/\rho}$. We shall use the Chakrabarti's viscosity prescription (C96a) which is valid for flows with significant

radial motion. Since accretion flow possesses substantial amount of angular momentum, flow must be centrifugally supported and the knowledge of angular momentum distribution is important. We, therefore, explore the nature of shear stress which governs the transport of angular momentum. Indeed, the viscous stress is given by,

$$W_{x\phi} = -\alpha_{\Pi}\Pi, \tag{4.3}$$

where, Π $(= W + \Sigma\vartheta^2)$ is the total pressure of the flow. This special viscosity prescription will ensure that the viscous stress is continuous across the axisymmetric shock wave that we are studying here. It is to be noted that in SS73 prescription, $W_{x\phi}$ was not continuous across the shock. Therefore, the stress would transport angular momentum at different rates on both sides of the shock which would always move the shock one way or the other. This is unphysical, since in the absence of viscosity, a standing, axisymmetric shock is perfectly stable. It is impossible that an infinitesimal viscosity will destabilize the shock. However, this would have been the case if SS73 prescription were absolutely correct. Moreover, viscosity not only transport angular momentum, it heats the gas also. We include this effect in the present study.

4.1.2 Sonic point analysis

In Chapter 3, we mentioned the basic idea of the accretion procedure. Matter with almost negligible radial velocity at the outer edge of the accretion disk enters into the black hole with velocity of light c. Thus, during accretion, at some point, matter velocity should exactly match with the sound speed. This point is called a critical point or a sonic point and depending on the initial parameters a flow may have multiple sonic points (C89a, C89b, C90a and C90b). We carry out the sonic point analysis for dissipative accretion system by solving the governing equations [Eqs. (4.1a-4.1d)] using a general method similar to that used in C89b. The detailed discussions of sonic point analysis is presented in the following Sections.

Sonic point conditions

In the present analysis, we use the MISStress prescription (C96a) for computing Q^+ and obtain $W_{x\phi}$ from Eq. (4.1c). For the accretion flow, the entropy equation (Eq. 4.1d) can be simplified as,

$$\frac{\vartheta}{\gamma-1}\left[\frac{1}{\rho}\frac{dP}{dx} - \frac{\gamma P}{\rho^2}\frac{d\rho}{dx}\right] = \frac{Q^- - Q^+}{\rho h} = C - H, \tag{4.4}$$

and then $H(= Q^+/\rho h)$ takes the form,

$$H = Ax(ga^2 + \gamma\vartheta^2)\frac{d\Omega}{dx}, \tag{4.5}$$

where, γ is the adiabatic index, $A = -\alpha_\Pi I_n/\gamma$ and $g = I_{n+1}/I_n$. Here, Ω is the angular velocity of the accreting matter at the radial distance x, n is the polytropic index, I_n and I_{n+1} come from the definition of the vertically averaged density and pressure (Matsumoto et al. 1984) respectively.

In the present analysis, we use $Q_- = 0$, *i.e.*, the cooling effect is ignored. This would be strictly valid if the accretion rate is low, so that the loss of energy by bremsstrahlung and synchrotron cooling is insignificant compared to the rest mass energy.

After some simple algebra with the governing Eqs. (4.1a-4.1d) and Eq. (4.2) we get the following first order linear differential equation (Chakrabarti & Das 2004) as,

$$\frac{d\vartheta}{dx} = \frac{N}{D}, \tag{4.6}$$

where, the numerator N is,

$$N = -\frac{\alpha_\Pi A(a^2 g + \gamma\vartheta^2)^2}{\gamma x} - \left[\frac{\lambda^2}{x^3} - \frac{1}{2(x-1)^2}\right]\left[2\alpha_\Pi g A(a^2 g + \gamma\vartheta^2) + \frac{(\gamma+1)\vartheta^2}{(\gamma-1)}\right]$$

$$-\frac{\vartheta^2 a^2(5x-3)}{x(\gamma-1)(x-1)} - \frac{\alpha_\Pi g A a^2(5x-3)(a^2 g + \gamma\vartheta^2)}{\gamma x(x-1)} + \frac{2\lambda A\vartheta(a^2 g + \gamma\vartheta^2)}{x^2}, \tag{4.7}$$

and the denominator D is

$$D = \frac{2a^2\vartheta}{(\gamma-1)} - \frac{(\gamma+1)\vartheta^3}{(\gamma-1)} - A\alpha_\Pi\vartheta(a^2 g + \gamma\vartheta^2)\left[(2g-1) - \frac{a^2 g}{\gamma\vartheta^2}\right]. \tag{4.8}$$

Both N and D are algebraic equations which make this model easily tractable.

At the sonic point, both the numerator and the denominator must vanish simultaneously to keep the velocity gradient finite. For $D = 0$, one can get the expression for the Mach Number $M(x_c)$ at the sonic point and is given by,

$$M(x_c) = \sqrt{\frac{-m_b - \sqrt{m_b^2 - 4m_a m_c}}{2m_a}}, \tag{4.9}$$

where,

$$m_a = -A\alpha_\Pi\gamma^2(\gamma-1)(2g-1) - \gamma(\gamma+1),$$

$$m_b = 2\gamma - 2A\alpha_\pi g\gamma(\gamma-1)(g-1),$$

$$m_c = A\alpha_\pi g^2(\gamma-1).$$

In the weak viscosity limit, $\alpha_\Pi \to 0$, the Mach number at the sonic point is obtained as $M(x_c) \approx \sqrt{\frac{2}{\gamma+1}}$ which matches with the exact result obtained in C89b.

Setting $N = 0$, we get an algebraic equation for the sound speed at the sonic point which is given by,

$$F(\mathcal{E}_c, \lambda_c, x_c) = -\left[\frac{\alpha_\Pi A\{g+\gamma M^2\}^2}{\gamma x} + \frac{\alpha_\Pi A(5x-3)\{g+\gamma M^2\}}{\gamma x(x-1)} + \frac{M^2(5x-3)}{x(\gamma-1)(x-1)}\right]a^2$$

$$+\frac{2\lambda AM(g+\gamma M^2)}{x^2}a - \left[\frac{\lambda^2}{x^3} - \frac{1}{2(x-1)^2}\right]\left[2\alpha_\Pi gA(g+\gamma M^2) + \frac{(\gamma+1)M^2}{(\gamma-1)}\right] = 0. \tag{4.10}$$

We solve the above quadratic equation to obtain the sound speed at the sonic point. Das et al. 2001 (DCC01) suggested that depending on a given set of initial parameters accretion flow may have a maximum of four sonic points where one of the sonic points always lies inside the black hole horizon for non-dissipative accretion flow. In our present study, we also expect a similar result at least in the weak viscosity limit.

Nature of the sonic points

In Fig. 4.1, we show the variation of specific angular momentum (λ_c) as a function of the logarithmic sonic point location, $\log(x_c)$, for a given viscosity parameter ($\alpha_\Pi = 0.1$) (Chakrabarti & Das 2004). Here, different curves are drawn for a set of different specific energies at the sonic points. The energies, from the uppermost curve to the lowermost one, are given by $\mathcal{E}_c$ = 0.0007, 0.001, 0.003, 0.005, 0.007, 0.011, 0.015, 0.019, 0.023 and 0.027 respectively. The long-dashed curve at the top represents the Keplerian angular momentum distribution which is completely independent of the initial flow parameters and depends only on the flow geometry. Solid curves represent the saddle type sonic points, dotted curves represent the nodal type sonic points and the short-dashed curves are drawn for the spiral type sonic points. Fig. 4.1 indicates that sonic points always occur at angular momentum below the Keplerian value. Notice that for lower values of specific energy at the sonic point, an accretion flow contains all the three types of sonic points in a systematic order: saddle — nodal — spiral — nodal — saddle for monotonic increase of location of sonic point. With the increase of energy $\mathcal{E}_c$ the region of spiral type sonic points gradually decreases and finally replaced by the nodal type sonic points though multiple sonic points still exist. Shaded area separates the nodal type sonic point region in the $\lambda_c - \log(x_c)$ plane. With further increase of energy all the nodal type sonic points also disappear and are replaced by saddle type sonic points. In this case, the flow has only one sonic point for a given sub-Keplerian angular momentum. Thus, for a given angular momentum of the flow, there exists an energy range $\mathcal{E}_{min} < \mathcal{E}_c < \mathcal{E}_{max}$ such that the flow allows multiple sonic points. In the *inset*, we zoom a small portion of the curve

close the Keplerian value to highlight the fact that the angular momentum at the sonic point always remains sub-Keplerian when cooling process is ignored.

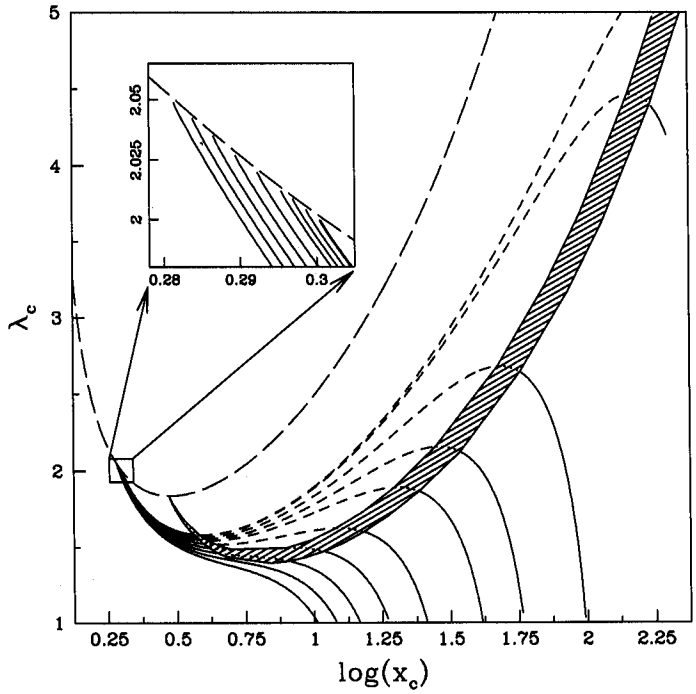

Figure 4.1: Variation of specific angular momentum (λ_c) as a function of the logarithmic sonic point location [$\log(x_c)$] for the viscosity parameter ($\alpha_\Pi = 0.1$). Long-dashed curve is the Keplerian angular momentum distribution. Solid curves represent the saddle type sonic points, dotted curves represent the nodal type sonic points and the short-dashed curves are for the spiral type sonic points. Shaded area represents the nodal type sonic point region.

A very important aspect of viscous transonic flow is shown in Fig. 4.2 where the angular momentum distribution at the sonic point is plotted as a function of logarithmic sonic point locations for a set of viscosity parameters, α_Π (Chakrabarti & Das 2004). The specific energy at the sonic point are kept fixed at $\mathcal{E}_{in} = 0.006$. In the absence of viscosity ($\alpha_\Pi = 0$, the uppermost curve), the flow has all the three types of sonic points. Similar to Fig. 4.1, here also we indicate the saddle, nodal and spiral type sonic points by the solid, dotted and short-dashed curves respectively. The uppermost long dashed curve represents the Keplerian angular momentum distribution. With the increase of α_Π, more and more inner saddle type sonic points are replaced by nodal type sonic points and similarly nodal type are also replaced by spiral type sonic points. The curves, from the topmost to the bottom one, are for $\alpha_\Pi = 0$, 0.2, 0.4, 0.6, and 0.7 respectively. Note that for $\alpha_\Pi = 0.7$, all

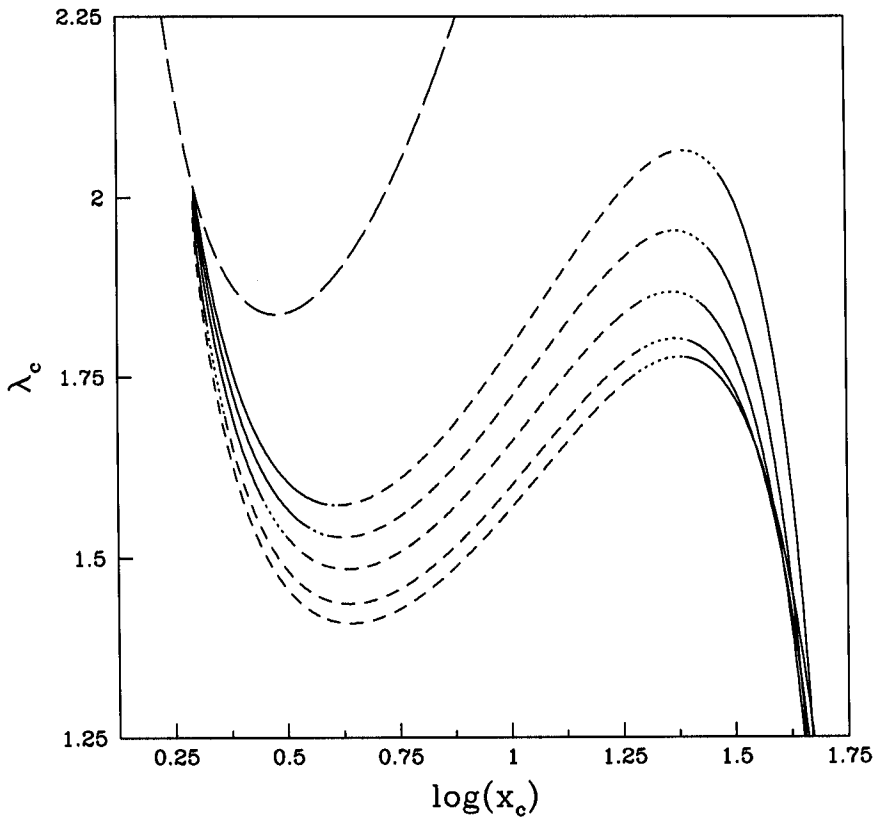

Figure 4.2: Variation of angular momentum at the sonic point as the viscosity parameter is varied. Specific energy at the inner sonic point is held fixed at 0.006. From top to the bottom curve: $\alpha_\Pi = 0, 0.2, 0.4, 0.6$ and 0.7 respectively. Other notations are the same as in Fig. 4.1.

the inner saddle type sonic points disappear and only the spiral type points remain. Therefore, there exists a critical viscosity parameter $\alpha_{\Pi(c,i)}$ at a given $\mathcal{E}_c$ for which all the inner saddle type sonic points are completely replaced by the spiral type ones. Under this situation, the flow has no choice but has to pass through the outer sonic point only. Existence of such critical viscosity gives an intuitive hints that the parameter space for the multiple transonic flow may shrink with the increase of viscosity.

In Fig. 4.3, we plot the variation of $\mathcal{E}_c$ with logarithmic sonic point $[\log(x_c)]$ for various α_Π while keeping the specific angular momentum at the inner sonic point to be fixed $\lambda_c = 1.65$. Values of α_Π are set as, from the uppermost to the lowermost curve, $\alpha_\Pi = 0$, 0.25, 0.35, 0.5, 0.6 and 0.7 respectively. Solid, dotted and short-dashed lines denote similar meaning as mentioned in the earlier figures. Long-dashed

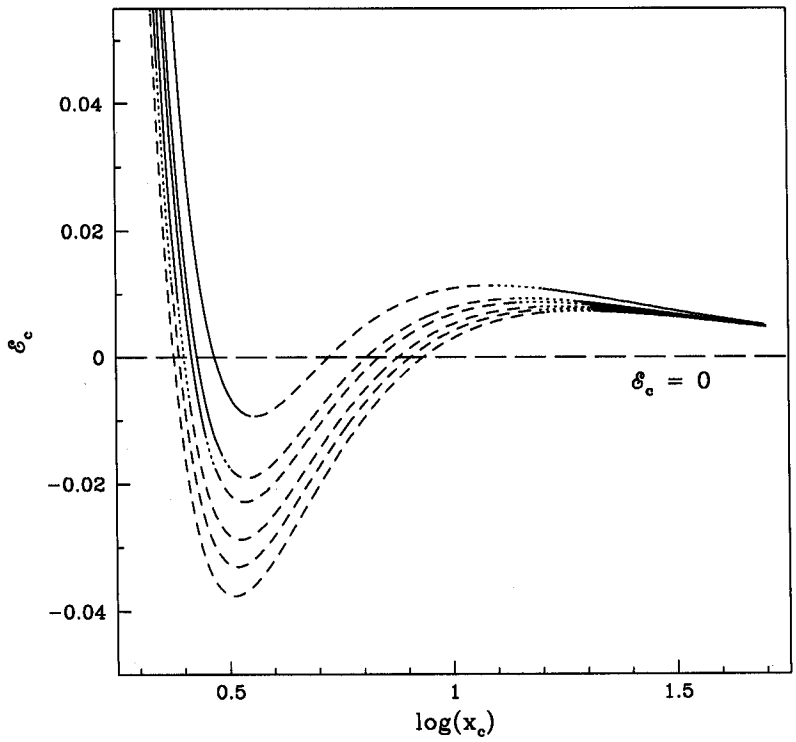

Figure 4.3: Variation of the specific energy at the inner sonic point as a function of the viscosity parameter α_Π. From the uppermost curve to the lowermost curve, $\alpha_\Pi = 0$, 0.25, 0.35, 0.5, 0.6 and 0.7 respectively. Other notations are the same as in Fig. 4.1.

line separates the positive and negative energy regions in the $\mathcal{E}_c - \log(x_c)$ plane. Notice that, for increasing α_Π, saddle type sonic points are gradually replaced by the nodal and spiral type sonic points: outer saddle type sonic points recede further away and the inner saddle sonic points proceed toward the black hole horizon. For $\alpha_\Pi = 0.7$, the inner saddle type sonic points completely disappear and become spiral type. This behaviour points to a critical value of viscosity parameter ($\alpha_{\Pi,c}$) which separates the accretion flow from the multiple sonic points regime to the single sonic point regime at a given λ_c. Fig. 4.3 also indicates that at the same sonic point, specific energy steadily decreases for increasing α_Π (Chakrabarti & Das 2004). The reason behind it is that when α_Π is increased, the accreting matter tends to become a Keplerian disk closer to the black hole and becomes more strongly bound with lower energy. More importantly, the energy at the outer sonic point remains always positive for all initial parameters.

For the shake of completeness of sonic point analysis, we chose the polytropic

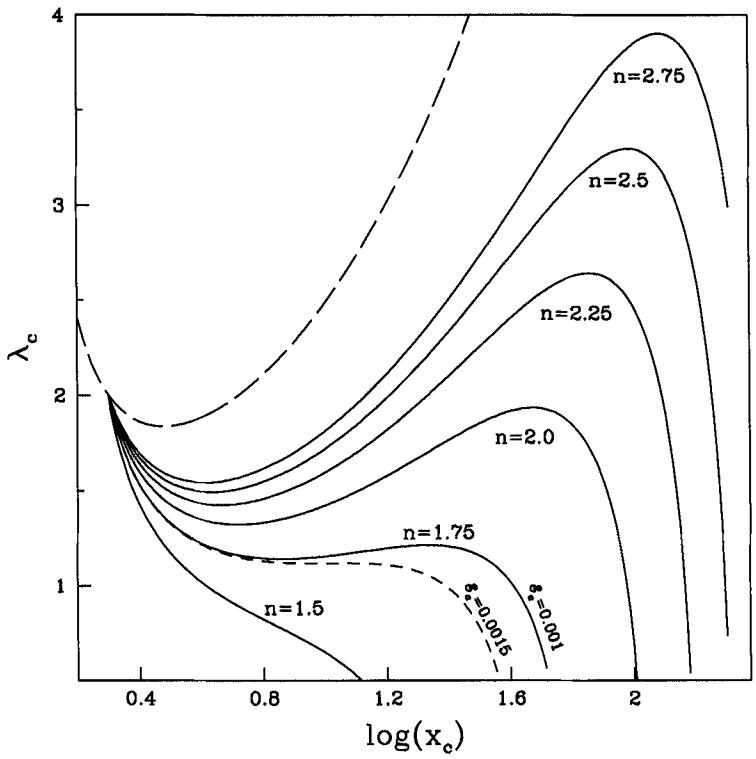

Figure 4.4: Variation of the specific angular momentum at the inner sonic point as a function of the polytropic index n (marked on each curve). Generally, the number of sonic points decreases with decreasing n. Specific energy has been kept fixed at 0.001 except for the dashed curve where it is 0.0015 to show that for a given polytropic index, number of sonic points increases with decreasing energy.

index (n) as a free parameter for further study. A mono-atomic, non-relativistic gas is identified with $n = 3/2$ while in the other extreme, *i.e.*, for very relativistic or a radiation dominated flow polytropic index is set at $n = 3$. In Fig. 4.4, we plot the variation of λ_c with logarithmic sonic point location, $\log(x_c)$, where specific energy at the sonic point is chosen as $\mathcal{E}_c = 0.001$ (Chakrabarti & Das 2004). The long-dashed curve is the Keplerian distribution as before. We note that with the increase of the adiabatic index γ, *i.e.*, decrease of the polytropic index n, the number of sonic points decreases from three to one. In this example, in the extreme non-relativistic regime ($n = 1.5$) the accretion flow has a single saddle type sonic point for any specific angular momentum. For the same energy, for $n = 1.75$, there are three sonic points, indicating that a standing or an oscillating shock in the flow may be possible. In this Figure, we also show that for a given n (such as for $n = 1.75$) if we increase energy at the sonic point ($\mathcal{E}_c = 0.0015$), multiple sonic points disappear

and a single sonic point forms. This indicates that there must be a critical value of $\mathcal{E}_c$ associated with each n above which multiple sonic points do not exist when all other parameters are kept fixed.

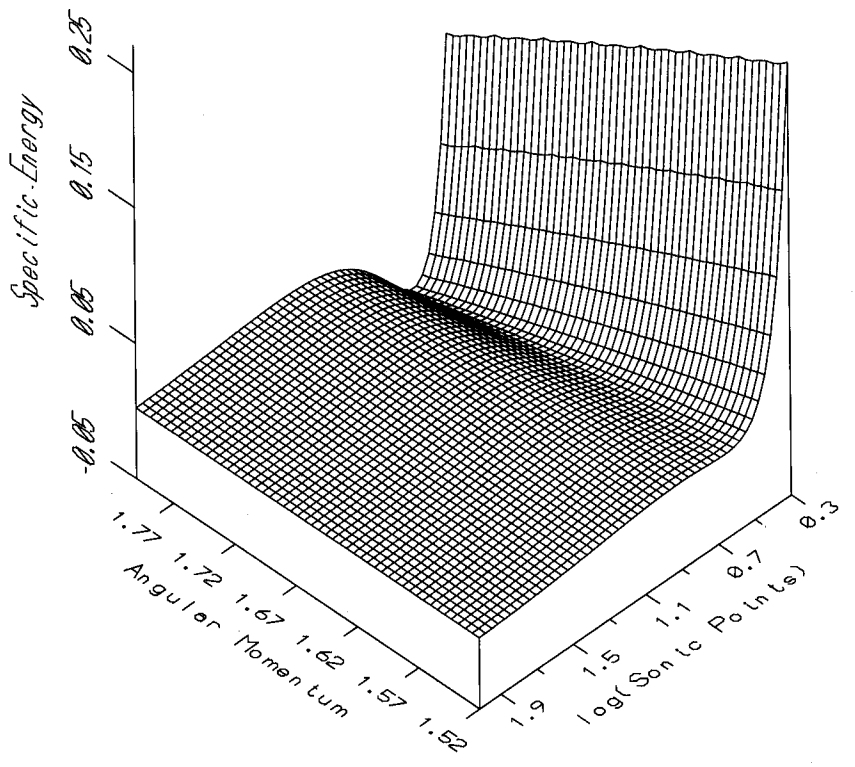

Figure 4.5: Gradual change in the number of physical sonic points is easily seen in this three-dimensional view of $F(\mathcal{E}_c, \lambda_c, x_c) = 0$ (Eq. 4.10) surface. At high angular momenta, there are three sonic points, but they merge to become one at lower angular momenta. $\alpha_\Pi = 0.01$ has been chosen.

The most general behaviour of the flow at the sonic point is best seen in Fig. 4.5, where we depict the surface $F(\mathcal{E}_c, \lambda_c, x_c) = 0$ (Eq. 4.10) for $\alpha_\Pi = 0.01$ (Chakrabarti & Das 2004). Sonic points x_c are plotted along X-axis in the logarithmic scale, λ_c is plotted along the Y-axis and $\mathcal{E}_c$ is plotted along the Z-axis. Note that, multiple sonic points appear at the relatively higher values of angular momentum whereas single sonic point solutions are obtained for lower angular momentum values. Therefore, below a critical value λ_{cri}, the flow does not have more than one sonic point.

4.1.3 Global solution topologies

In order to form shocks in an astrophysical system, flow must possess more than one X-type sonic points and flow solutions passing through these sonic points are connected by the discontinuous shock transition provided Rankine-Hugonoit relations are satisfied. In this Section we present a detail discussion about solution topologies which usually follow different pathways.

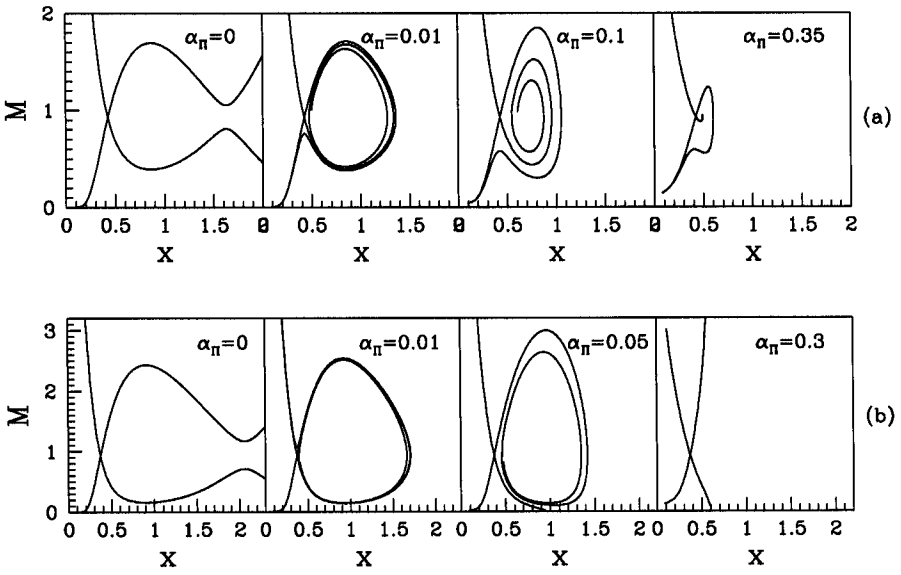

Figure 4.6: Variation of global solution topologies of the viscous accretion flow around black holes. In (a), drawn for $\lambda_{in}(x_{in} = 2.665) = 1.68$, four panels show how open topology at lower viscosity becomes closed at higher viscosity. In (b), drawn for $\lambda_{in}(x_{in} = 2.359) = 1.78$, closed topology opens up again.

Figure 4.6(a-b) shows the variation of flow topologies with the constant viscosity parameter α_Π and the specific angular momentum λ_{in} at the inner sonic point x_{in} (Chakrabarti & Das 2004). Indeed, different flow behaviours are distinctly highlighted in two separate panels for lower (Fig. 4.6a) and higher angular momentum regime (Fig. 4.6b). In fact, Fig. 4.6a is drawn for the inner sonic point at $x_{in} = 2.665$ and the specific angular momentum at this point is $\lambda_{in} = 1.68$. At low angular momentum and without viscosity (the box at extreme left in Fig. 4.6a) the sub-sonic flow enters into the black hole after passing through the inner sonic point. In the second box, viscosity is slightly higher and the topologies are closed for the same inner sonic point. So, for a given set of parameter, there must be a critical viscosity

parameter ($\alpha_{\Pi cri}$) for which open topologies become closed ones. Accretion with parameters causing this kind of topology never joins with any Keplerian disk unless a shock is formed. Moreover, when an accretion flow cannot make a shock transition, the flow directly passes through the outer sonic point before falling into the black hole. With the further increase of α_Π (next two boxes) closed topology shrinks gradually and finally disappears leaving behind only the outer sonic point (Bondi Type). This is directly analogous to the shrinking of the phase space of a simple harmonic oscillator in presence of damping (C90a). These solutions are basically the same as the $f = 1$ case of Fig. 2a of C96a.

Fig. 4.6b is drawn with a higher specific angular momentum at the inner sonic point ($x_{in} = 2.359$ and $\lambda_{in} = 1.78$) where the explanations of first and second box are similar to the earlier ones (Fig. 4.6a), but in the third box ($\alpha_\Pi = 0.05$), the accretion flow topology changes its spiraling direction and the flow can join with a Keplerian disk very close to a black hole. Interestingly, the basic differences between this two figures (Fig. 4.6a. and Fig. 4.6b) occur mainly due to the difference of specific angular momentum at the sonic point rather than the change of sonic point locations. In fact, a strong dependence of the accretion flow topologies on angular momentum at the sonic point will be presented in the subsequent Section (Fig. 4.18). For a higher α_Π (next two boxes) Keplerian disk comes even closer to the black hole and topologies passing through the inner sonic point become that of Bondi type. We suspect that two limits of viscosity parameters would cause an oscillation of the inner part of the Keplerian disk, but we cannot be certain about it without a time dependent numerical simulation. Details of this idea is beyond the scope of the present thesis.

To identify the new pathways of the solution topologies from the existing one (C96a) we have plotted in Fig. 4.7 the flow topologies passing through the outer sonic point. The input parameters are chosen as $x_{out} = 25$ and $\lambda(x_{out}) = 1.8$ for different viscosity parameters marked in the Figure (Chakrabarti & Das 2004). For a lower α_Π, the topologies are closed as in Fig. 4 of C96a and the flow having this topology cannot be transonic anyway. For gradual increase of α_Π closed topologies monotonically open up (unlike C96a where $x_{out} = 35$ was chosen and the opening of topologies did not occur) and if the shock condition is satisfied, the accretion flow passing through the outer sonic point jumps into the subsonic branch and go through the inner sonic point before entering into the black hole. For higher α_Π, the same outer sonic point no longer remains saddle type—first it becomes nodal type and then it reduces to spiral type (Fig. 4.1). This receding nature of sonic points for increasing viscosity parameter α_Π are not surprising as we already pointed this issue in the earlier Section. This, together with Fig. 4 of C96a show that there could be more than one way of reaching nodal topology.

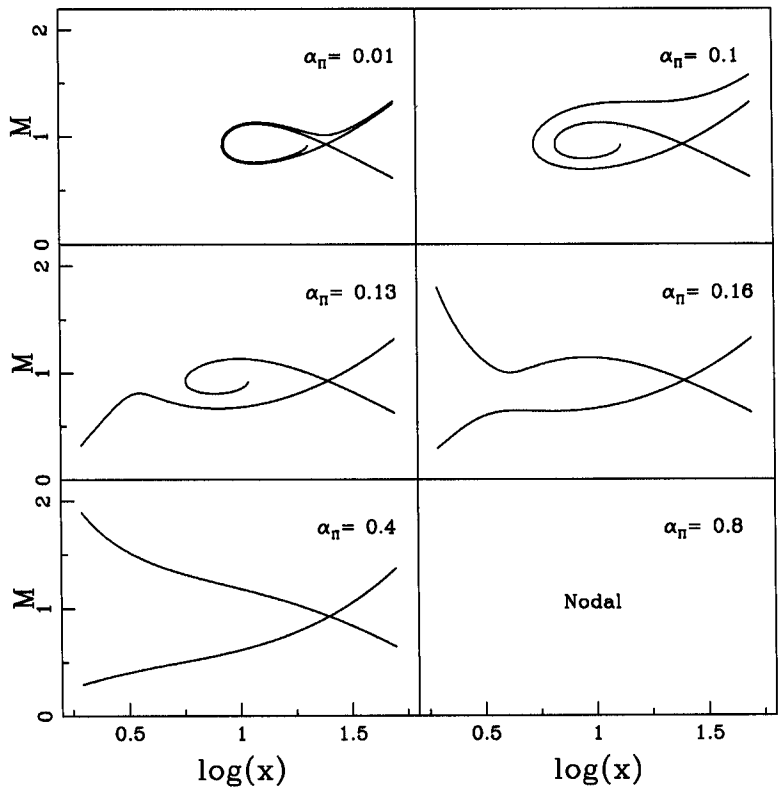

Figure 4.7: Variation of global solution topologies of the viscous accretion flow when the outer sonic point is kept fixed at $x_{out} = 30r_g$ while the viscosity parameter is varied. The closed topologies (with one saddle type and a spiral type at the center) at lower α_Π become open for higher α_Π. Eventually, the saddle type also disappears to produce a nodal type sonic point.

4.1.4 Classification of the parameter space

For details understanding of the viscous accretion flow it is important to classify the parameter space in terms of viscosity parameter. However, Fig. 4.8 separates the region of parameter space in an accretion flow for closed topologies passed through the inner sonic point (Chakrabarti & Das 2004). The parameter space is obtained by varying angular momentum at the inner sonic point (λ_{in}) along the X-axis and the corresponding specific energy at the inner sonic point ($\mathcal{E}_{in}$) along the Y-axis. The bounded region with a given curve contains parameters in which multiple saddle type sonic points exist. For instance, for $\alpha_\Pi = 0$, the region bounded by the solid curve is exactly identical to the region found by C89b. With the increase of α_Π, the region of multiple saddle type sonic points is reduced near high angular momentum side while it increases in the lower angular momentum side. It may be recalled (C89b

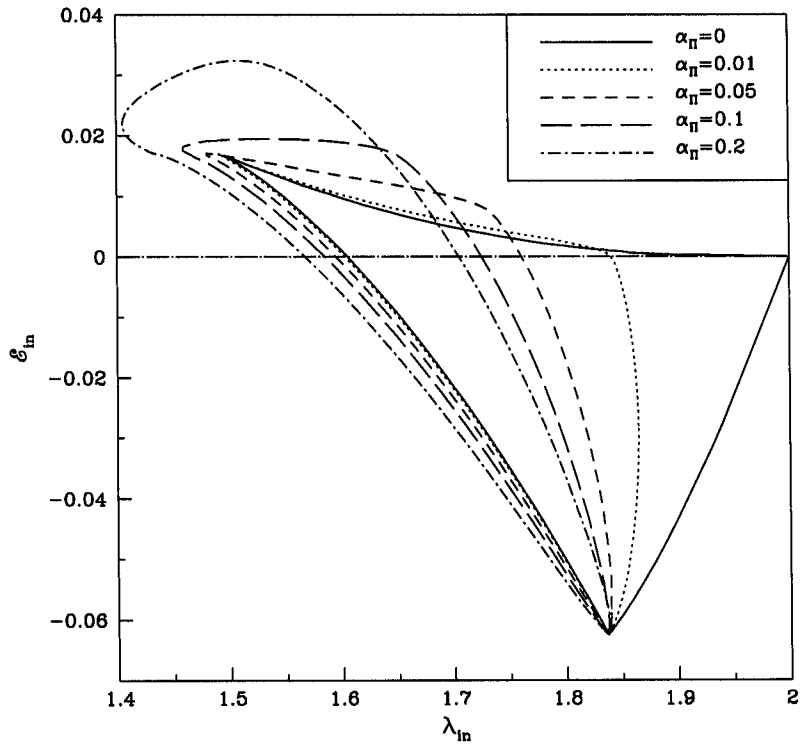

Figure 4.8: Classification of the parameter space spanned by the specific energy and the specific angular momentum of the flow at the inner sonic point. The bounded regions drawn for different viscosity parameters (marked at the inset) contain allowed solutions which may pass through the inner sonic point. As viscosity increases, the region shifts towards lower angular momentum and higher energy.

and Fig. 1a) that at low angular momentum, the number of sonic point is just one. With the rise of α_Π, the angular momentum at the sonic point is also increased which results the increase of number of sonic points. At a higher angular momentum, the situation is just the opposite. In this case, there are already multiple sonic points for $\alpha_\Pi \sim 0$ and for high enough α_Π, viscosity transports angular momentum very rapidly causing a steep rise in angular momentum itself. This, in turn, means that the flow can have only one saddle type sonic point in this case.

4.1.5 Standing shocks and further classification of the parameter space

It is widely believed that shocks are ubiquitous in the astrophysical system and most likely they are non-stationary. However, in an accretion flow, the shock properties, namely, the shock location, strength and it's various thermodynamic properties

could be quantified very accurately by using Rankine-Hugoniot conditions (RHCs). In the present context, this study is very similar to the study of shocks in solar winds (Holzer & Axford, 1970) and white-dwarf surfaces.

The shock conditions which we employ here are the usual RHCs presented in C89b (see also, Landau & Lifshitz 1959), *i.e.*, (a) the local energy flux is continuous across the shock; (b) the mass flux is continuous across the shock (c) the momentum balance condition is satisfied and finally, (d) angular momentum should be continuous across the axisymmetric shock.

Our consideration of satisfying RHCs at a given location holds only if the shock is thin, i.e., viscosity is low. Nevertheless, we continue to use this prescription at higher viscosities to have a first order guess of the shock location. Similarly, we assume that there is no excess source of torque at the shock itself, so that the angular momentum may be assumed to be continuous across it although this condition may be violated when magnetic fields are included. In the presence of large scale poloidal magnetic field, there could be magnetic torque which could make the flow angular momentum discontinuous. But at present, we are neglecting this issue.

Method of calculating the shock locations

Accretion flow originated at the outer edge of the disk with almost negligible radial velocity becomes super-sonic after passing through outer sonic point and makes a discontinuous jump (shock) into sub-sonic branch and again becomes super-sonic while crossing inner sonic point before entering into the black hole. In the present context, we begin numerical integration from inner sonic point and proceed towards the outer edge of the accretion disk to look for shock location (Chakrabarti & Das 2004). During integration along the sub-sonic branch, it is possible to calculate all the local flow variables (*i.e.*, ϑ, a, M, ρ) at the post-shock region in terms of the initial flow parameters. We calculate total pressure, local flow energy, specific angular momentum at the shock using these sub-sonic local variables. According to the Rankine-Hugoniot shock conditions at the shock, total pressure, local flow energy, mass accretion rate (one of the flow parameters) and specific angular momentum must be conserved. These conserved quantities at the shock give the other set of local variables for the super-sonic branch. This set of super-sonic local variables help to get outer sonic point uniquely for a accretion flow with fixed inner sonic point and other initial flow parameters when integration takes place towards the outer edge of the black hole. Thus, the accretion flow can be connected with both

the inner and outer saddle type sonic points through shock for dissipative system and this uniquely determines the standing shock location for a given set of initial flow parameters.

At the shock, super-sonic flow variables could be quantified as a function of sub-sonic local flow variables in the following way:

The model, of our interest, are constructed by considering the flow is to be in vertical equilibrium and total pressure of the accretion flow at any given radial distance is given by,

$$\Pi = W + \Sigma\vartheta^2, \tag{4.11}$$

where, W and Σ are the vertically averaged thermal pressure and density respectively (Matsumoto et at. 1984).

We use the mass flux conservation equation (Eq. 4.1b) in the Eq. (4.11) and calculate the sound speed a in terms of radial velocity (ϑ) at the shock (x_s) in the super-sonic branch which is given by,

$$a^2 = \mathcal{C}_1\mathcal{C}_2\vartheta - \mathcal{C}_2\vartheta^2, \tag{4.12}$$

where, $\mathcal{C}_1 = 4\pi\Pi x_s/(\dot{\mathrm{M}}I_n)$ and $\mathcal{C}_2 = \gamma/g$.

However, at the shock, radial velocity ϑ in the super-sonic branch is estimated by using Eq. 4.12 in the local flow energy equation and is given by,

$$\vartheta = \frac{-\vartheta_b + \sqrt{\vartheta_b^2 - 4\vartheta_a\vartheta_c}}{2\vartheta_a}, \tag{4.13}$$

where, $\vartheta_a = 2n\mathcal{C}_1\mathcal{C}_2$, $\vartheta_b = -2n\mathcal{C}_1\mathcal{C}_2$, $\vartheta_c = 2\mathcal{E} - [\lambda^2(x_s)/x_s^2] + [1/(x_s - 1)]$ and $\mathcal{E}$ is the local flow energy. In fact, total pressure and flow energy at the shock is calculated with the help of the sub-sonic flow variables. In this context, we consider only the '+' sign as we are interested to obtain the local flow variables in the super-sonic branch. This radial velocity is used to calculate the sound speed (Eq. 4.12) in the super-sonic branch of the flow. Under this circumstances, we use super-sonic flow variables (ϑ and a) to account the outer sonic point by numerical integration and a complete accretion flow solution with shock is obtained (Chakrabarti & Das 2004).

In a general shock solution, two different flow solutions, one with a lower entropy passing through the outer sonic point, and the other with a higher entropy passing through the inner sonic point are connected by the shock transition. A similar solution is presented in Fig. 4.9 (Chakrabarti & Das 2004). Two curves are drawn for two different energies (marked in the Figure). $\mathcal{E}_{in}$ and $\mathcal{E}_{out}$ are the energies at the inner and outer sonic points for a shocked accretion flow which has a standing shock. Due to viscous heating process, flow energy increased and the shock wave is formed when flow jump from the lower energy solution to higher energy solution. If we include cooling processes only, the situation would have been reversed. The

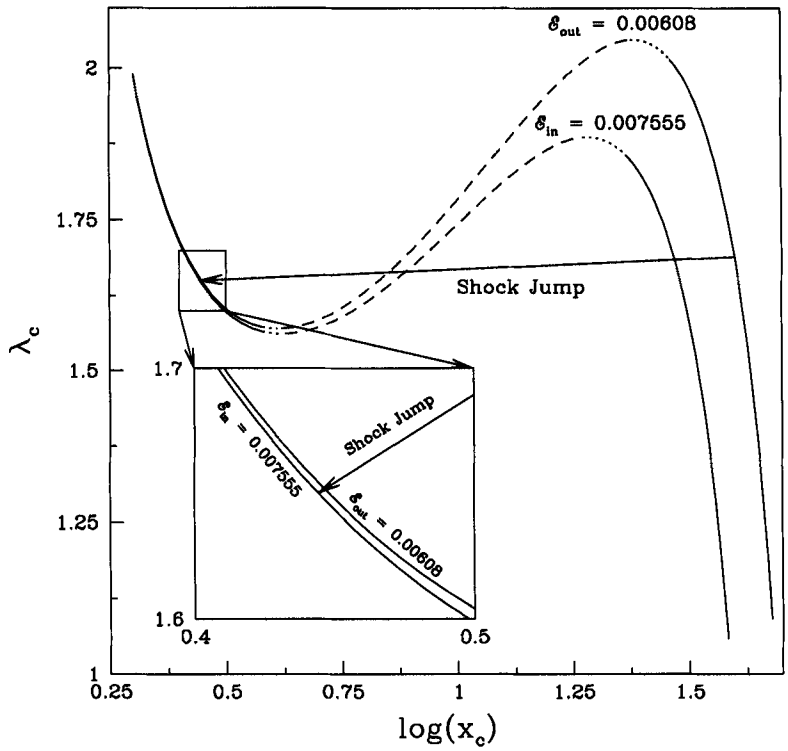

Figure 4.9: An example of how a standing shock might form in a viscous transonic flow is depicted here. Flow passing through the outer sonic point at $x_{out} = 39.7$ and energy $\mathcal{E}_{out} = 6.08 \times 10^{-3}$ has a shock and passes through the inner sonic point at $x_{in} = 2.78$ where its energy is $\mathcal{E}_{in} = 7.555 \times 10^{-3}$. Inset shows the details.

flow parameters are $x_{out} = 39.7$, $\lambda_{in} = 1.65$, $\alpha_\Pi = 0.05$ and $\gamma = 4/3$. The shock conditions uniquely determine the inner sonic point $x_{in} = 2.78$ and shock location $x_s = 18.2$ respectively. The end positions of the long arrow mark the locations of the sonic points. In the *inset*, we zoom a selected region in the $\lambda_c - \log(x_c)$ plane to show explicitly that the angular momentum is indeed decreased which is expected due to presence of viscosity.

Fig. 4.10 presents a complete solution of the flow which includes a standing shock in a viscous flow for the same set of parameters used in Fig. 4.9 (Chakrabarti & Das 2004). Arrows indicate the directions of the accreting flow. Sub-sonic accreting flow passes through the outer sonic point (O) and becomes super-sonic. At $x_s = 18.2$ (vertical dotted line), shock conditions are satisfied — the flow jumps from the super-sonic branch to the sub-sonic branch and subsequently pass through the inner sonic point (I).

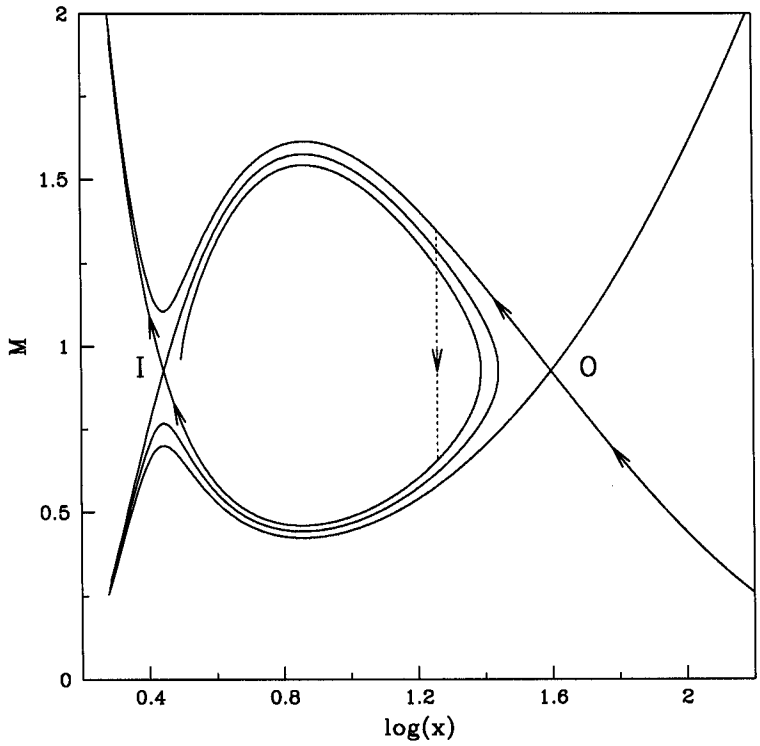

Figure 4.10: Actual solution topology for the case discussed in Fig. 4.9 is shown here which, along with the outer (O) and inner (I) sonic points, also showed the shock transition at $x_s = 18.2$ (vertical dotted line). The arrowed curve is followed by a flow while entering into the black hole.

Parameter space which allows standing shocks

In Fig. 4.8, we have already separated the region of the parameter space in terms of the number of sonic points present in the flow. Presently, in Fig. 4.11, we further classify the same parameter space on the region which allows only standing shocks in a viscous flow (Chakrabarti & Das 2004). The viscosity parameters are marked in the Figure. The region with $\alpha_\Pi = 0$ coincides with that in C89b and in Chakrabarti (C96b and Chakrabarti 1998) when appropriate models are considered. Compared to the inviscid case, the effective region of the parameter space shrinks in the high angular momentum side when the viscous effect is increased. However, exactly the opposite situation is observed at the lower angular momentum side. Notice that even at an angular momentum as low as $\lambda = 1.4$, standing shocks could be formed if the viscosity is high enough. Above a critical viscosity (which depends on other parameters as will be shown in Fig. 4.18 below), this region completely disappears.

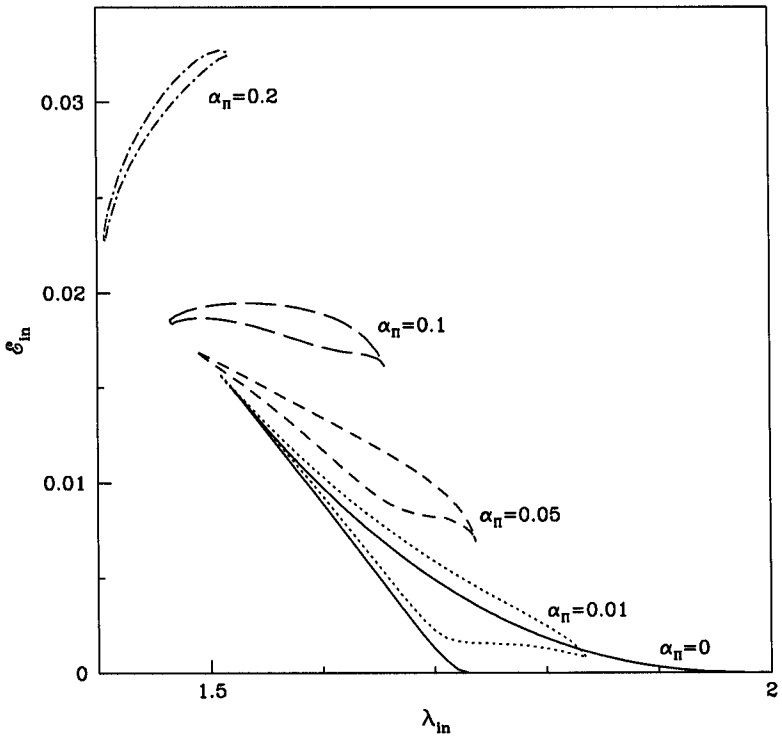

Figure 4.11: Variation of the region of the parameter space which forms a standing shock as a function of the viscosity parameter α_Π. The region shrinks with the increase of viscosity parameter.

We continue our study of the parameter space which may allow multiple sonic points as well as standing shocks. In Fig. 4.12, a curious feature is shown: the mapping between the post-shock parameters and the pre-shock parameters (Chakrabarti & Das 2004). We draw the region of the post-shock parameters at the inner sonic point $(\mathcal{E}_{in}, \lambda_{in})$ (bounded by the solid curve) and the region of the pre-shock parameters at the outer sonic point $(\mathcal{E}_{out}, \lambda_{out})$ (bounded by the long dashed-curve) for a shock which is determined through RHCs for $\alpha_\Pi = 0.01$. For each and every point in the pre-shock parameter space region, there exists a point in the post-shock parameter space region and therefore we have a complete solution. For definitiveness, we also show vertical dashed and dotted lines in the two different angular momentum range in the post-shock parameter space region in which λ_{in} is kept fixed but $\mathcal{E}_{in}$ is varied. The corresponding pre-shock parameters form a curve, indicating that both the angular momentum and the energy had to be adjusted to get the self-consistent solution. In a non-dissipative flow, there is no variation of energy and angular momentum in the accretion flow as both of these quantities are conserved

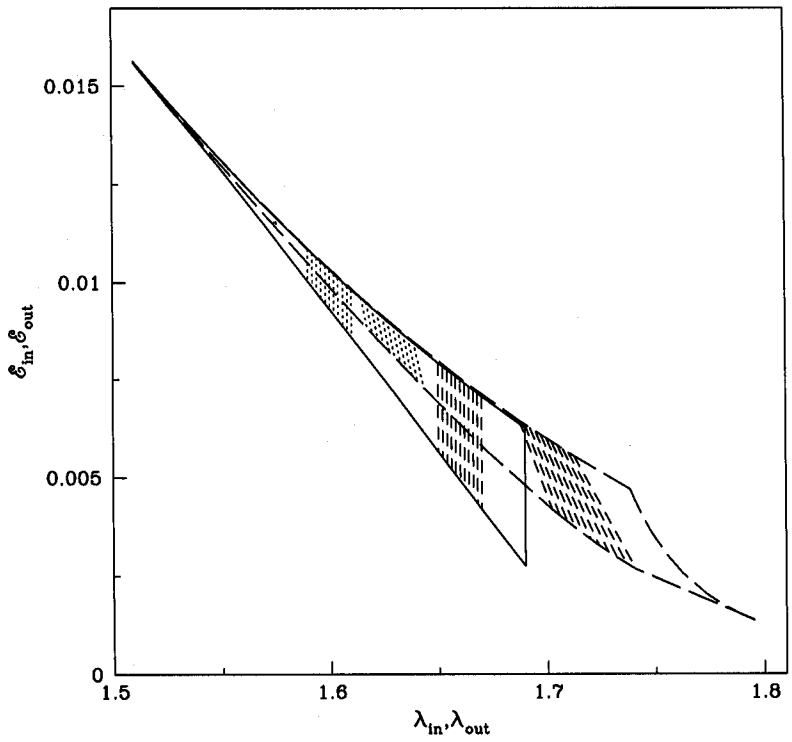

Figure 4.12: Mapping of the parameter space of the pre-shock region (solid boundary) spanned by $(\mathcal{E}_{in}, \lambda_{in})$ onto the parameter space in the post-shock region (dashed boundary) spanned by $(\mathcal{E}_{out}, \lambda_{out})$ in a viscous flow ($\alpha_\Pi = 0.01$).

all throughout. As a result, both the inner and the outer sonic point parameter spaces merge (C89b, Chakrabarti 1998) there.

Parameter space which may allow oscillating shocks

The remarkable feature of quasi-periodic variation of X-ray intensity originated from the vicinity of galactic black hole candidates is believed to be the outcome of oscillating shocks formed around the inner edge of the accretion disk. Such type of oscillating shock solutions are obtained for the flow parameters belonging to a large region of the parameter space for inviscid flow where the flow produces multiple sonic points but RHCs were not satisfied (Ryu, Chakrabarti & Molteni, 1997). However, the winds are also produced sporadically from the post-shock region. In presence of cooling, especially when the cooling time scale roughly agrees with the infall time-

scale, standing shocks may start to oscillate (Molteni, Sponholz and Chakrabarti, 1996). However, in a general flow, it is very difficult to divide the parameter space in terms of whether the shock will exist or not. This is because, when there is a shock, at least the RHCs allow us to map the pre-shock and the post-shock flow parameters (see, Fig. 4.12). But when there is no shock, it is not straight forward to map these two sets of parameters. Thus, one has to rely on global topological behaviour of the flow solutions and whether they allow multiple sonic points or not.

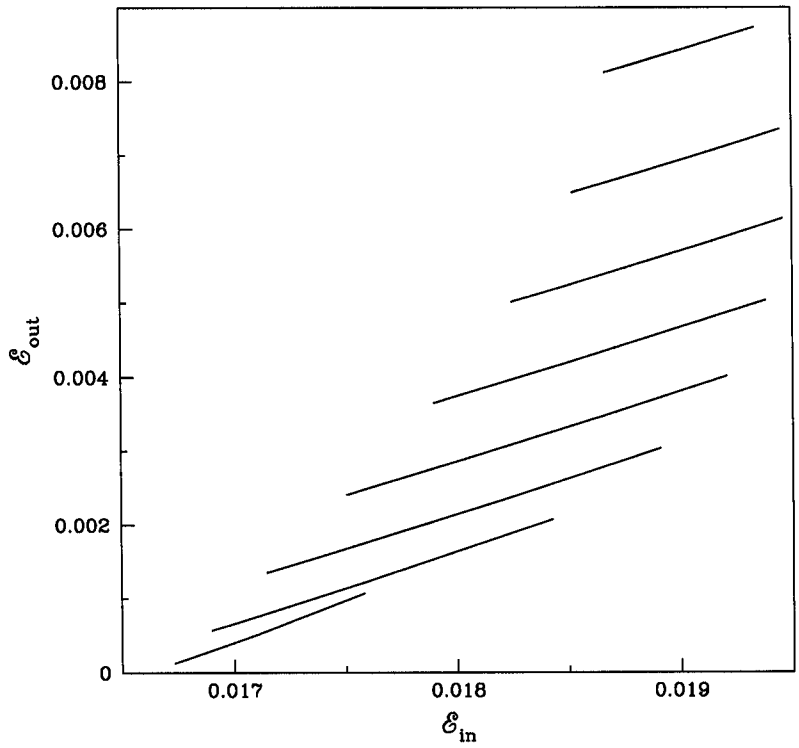

Figure 4.13: Example of variation of the outer sonic point energy $\mathcal{E}_{out}$ as a function of the inner sonic point energy $\mathcal{E}_{in}$ when the flow has a shock. $\alpha_{\Pi} = 0.1$ and $\lambda(x_{in}) = 1.50$ for the topmost curve. Curves have an increment of $\Delta\lambda(x_{in}) = 0.02$ while going towards the bottom.

In a viscous dissipative system, it is important to identify the parameter space that would allow one to have the inner sonic point energy to be larger compared with the outer sonic point energy. In Fig. 4.13, we plot inner sonic point energy ($\mathcal{E}_{in}$) along X-axis and the outer sonic point energy ($\mathcal{E}_{out}$) along the Y-axis for a set of inner sonic point angular momentum (λ_{in}) when accretion flow passes through

shock. Fig. 4.13 shows a linear variation of these two energies and the nature of this variation strongly depends on λ_{in} (Chakrabarti & Das 2004). It is not unwarranted to assume that a similar linear variation will continue for shock-free solutions also at least for the low viscosity limit. Therefore, we extrapolate this variation for the shock-free solution with the lower values of $\mathcal{E}_{in}$ till when $\mathcal{E}_{out} \sim 0$ for the same λ_{in} keeping in mind that the accretion flow topology passing through the inner sonic point must remain closed (Fig. 4.6a-b). Accordingly, we quantify the cut-off $\mathcal{E}_{in}$ for different λ_{in} following the similar procedure mentioned above and identify the region in the parameter space where the accretion flow does possess multiple saddle type sonic points.

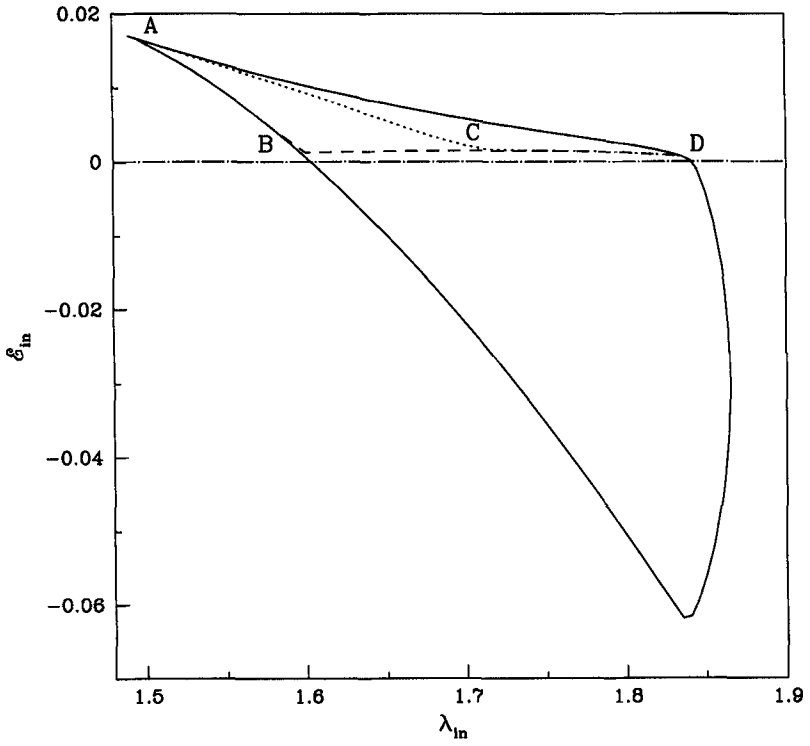

Figure 4.14: Division of the parameter space $(\mathcal{E}_{in}, \lambda_{in})$ for a viscosity parameter $(\alpha_\Pi = 0.01)$ on the basis of number of sonic points. Region separated by the dotted line has more than one X-type (saddle type) sonic points and flows in this region form standing shocks. The region surrounded by the dashed curve has more than one X-type sonic points but the Rankine-Hugoniot conditions are not satisfied here.

We proceed further to divide the parameter space $(\mathcal{E}_{in}, \lambda_{in})$ for the viscosity

parameter $\alpha_{\Pi} = 0.01$ on the basis of the number of sonic points. Such a plot is presented in Fig. 4.14 (Chakrabarti & Das 2004). A flow with initial parameters chosen from a region separated by the boundary ACD in the parameter space has multiple saddle type sonic points and also forms a shock as RHCs are satisfied there. A flow with parameters from the region ABC has more than one X-type sonic points but RHCs are not satisfied here. From our previous experience with non-dissipating flows, we predict that those solutions with multiple sonic points which do not form standing shocks must be responsible for producing oscillating shocks. This region becomes bigger when the viscosity parameter is reduced. Rest of the parameter space bounded by the solid curve gives solutions with closed topology passing through the inner sonic point.

4.1.6 Parameter space for all possible solutions

In Fig. 4.15, we present at a glance classification of the parameter space in the energy-angular momentum ($\mathcal{E}_{in}, \lambda_{in}$) plane in terms different accretion flow topologies (small box) for $\alpha_{\Pi} = 0.01$ (Chakrabarti & Das 2004). As before, solid boundary separates the region of the parameter space for the closed topology passing through the inner sonic point. Further classification is made depending on the nature of the solution topologies and is indicated by dotted, dashed and dot-dashed curves. Examples of solution topologies with initial parameters taken from different regions (marked) of the parameter space are plotted in seven small boxes (marked). All the small boxes depict Mach number variation as a function of the logarithmic radial distance. The box labeled S shows an accretion flow solution which passes through a shock. Dotted vertical line with an arrow indicates the location of the standing shock. The solution drawn in the box marked OS represents an accretion flow which has multiple sonic points but does not satisfy RHCs when the flow becomes supersonic. From our earlier experience with an inviscid flow, this topology is expected to give rise to an oscillating shock solution. The box marked OAC shows a new type of solution topology having multiple sonic points. One branch of the topology is closed and the other branch is open. This kind of solution is available in a small region of the parameter space shown in the inset on the upper-right corner. Solution inside the CI1 box has closed topology (inner spiral going anti-clockwise) having only one saddle type sonic point and this kind of solution belongs to a large region of the parameter space with relatively lower angular momentum region. The box CI2 shows a similar result as CI1 but here the nature of the topology is different (inner spiral going clockwise) and this type of solution exists at higher angular momentum region. The box labeled I* represents an accretion flow solution which passes through only the inner sonic point. This solution could be for an accretion or a wind and the initial parameters for this type of topology belongs to the region indicated by I* in the parameter space. Topology with parameters taken from O* region of the

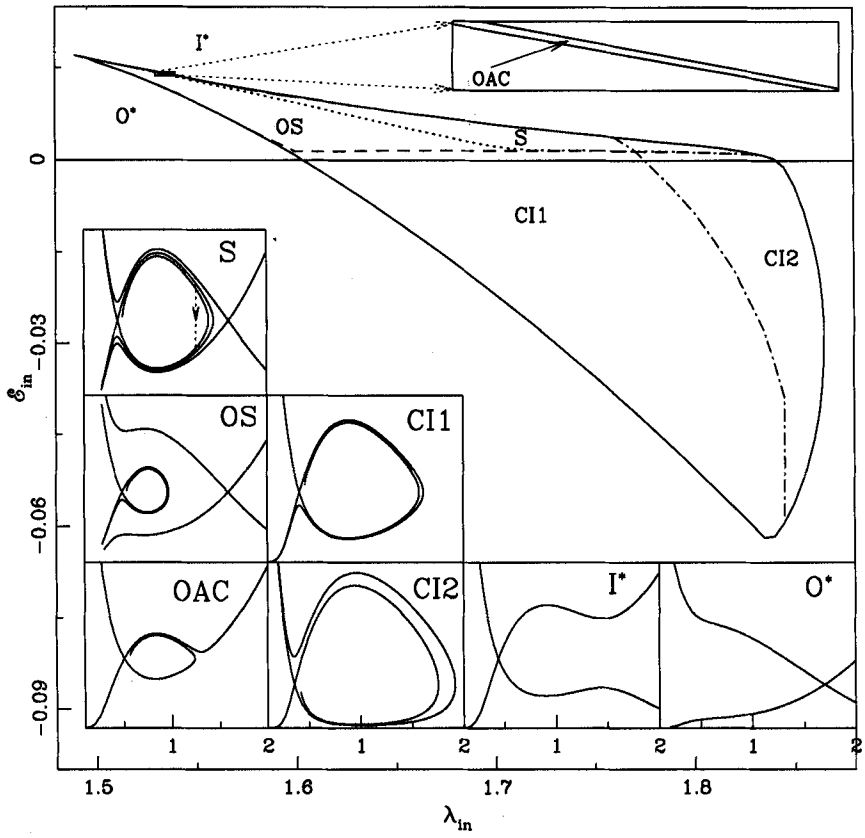

Figure 4.15: Division of the parameter space $(\mathcal{E}_{in}, \lambda_{in})$ (marked) for a viscosity parameter ($\alpha_\Pi = 0.01$) on the basis of solution topologies shown in boxes (marked). Details of the figure are described inside the text.

parameter space is also plotted in the box marked O^*. An accretion flow solution with these parameters passes only through the outer sonic point before falling onto the black hole (similar to a Bondi flow).

An important property of the shock wave is its strength which may be defined as the ratio of the post-shock Mach number to the pre-shock Mach number. In fact, shock strength determines the jump in temperature and density at the shock and thus it may be worthwhile to study the shock strength as well. For instance, in Fig. 4.16, we draw the variation of shock strength as a function of viscosity parameter α_Π for $x_{in} = 2.795$ and $\lambda_{in} = 1.65$ (Chakrabarti & Das 2004). At the lower viscosity limit, shock strength is relatively weak and it increases smoothly with the gradual increase of the viscosity parameter. Indeed, there is a cut off at a critical viscosity limit where the shock ceases to exist for the chosen set of initial flow parameters.

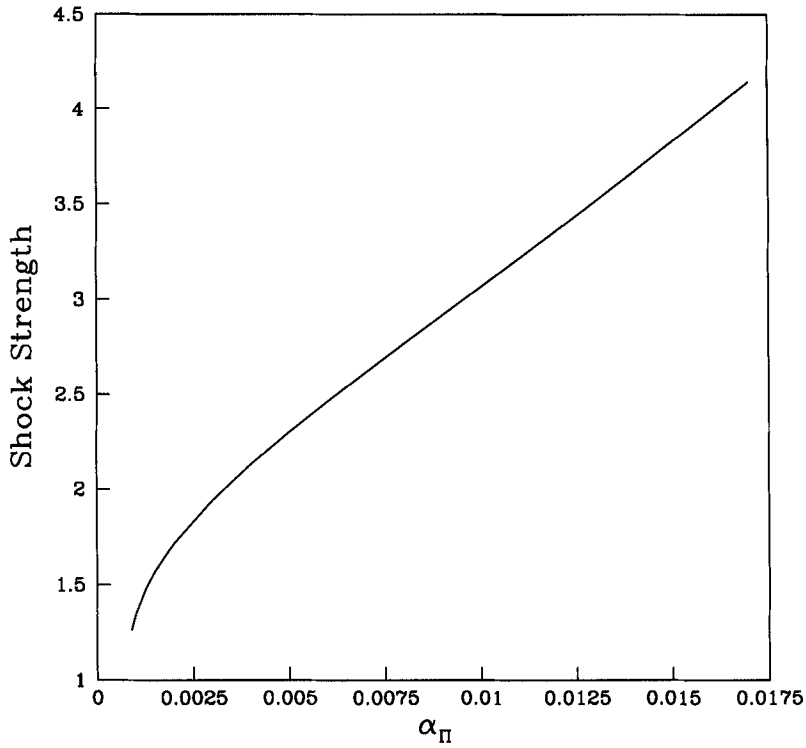

Figure 4.16: Variation of the ratio of the pre-shock to post-shock Mach numbers as a function of viscosity parameters for a fixed set of initial parameters ($x_{in} = 2.795$ and $\lambda_{in} = 1.65$). The shock disappears beyond the critical parameter $\alpha_\Pi \sim 0.017$.

4.1.7 Dependence of the critical viscosity parameter

We have already mentioned in our earlier discussion that there must be a critical viscosity parameter for which the flow topology must change its nature from an open topology to a closed one. In our present study, we compute the nature of this critical viscosity (Chakrabarti & Das 2004). Here, we find that there are in effect of two critical viscosity parameters: one at the boundary which separates the closed topology from the open topology while the other splits region of closed topology in terms of whether shocks can form or not. Not surprisingly, these are inflow parameter dependent, and thus do not have universal values. Nevertheless, these are useful, since they give us insights into the cases in which shocks may be possible.

In Fig. 4.17, we present the variation of the critical viscosity parameter as a

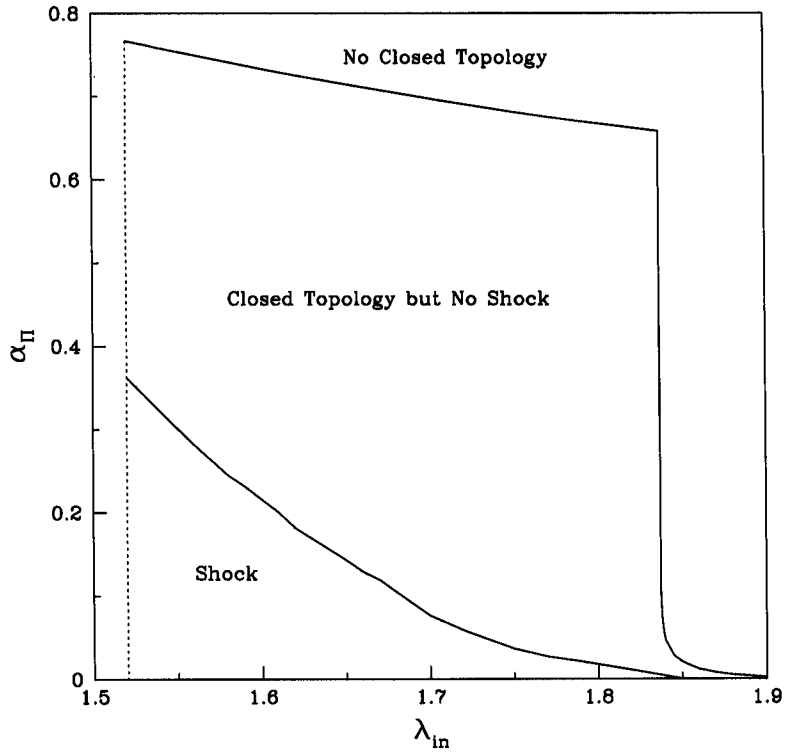

Figure 4.17: Critical viscosities separating standing from oscillating shocks and closed topologies from open topologies.

function of angular momentum at the inner sonic point. However, different regions of special interest are marked in the Figure. The vertical dotted line indicates the lower boundary of the angular momentum for the closed topology passing through the inner sonic point and notice that an universal lower boundary in angular momentum exist irrespective to the any values of viscosity parameter. Notice that shocks are formed even in the lower angular momentum domain for higher viscosity parameter (α_Π). This is not surprising according to our previous discussion (Fig. 4.3). Subsequently, shock disappears irrespective of any value of viscosity parameter at the higher angular momentum range.

4.1.8 Dependence of the shock location on viscosity parameter

We have already hinted that shock ceases to exist when viscosity is more than a critical value. For instance, in Fig. 4.18 (a-b), we show the dependence of shock

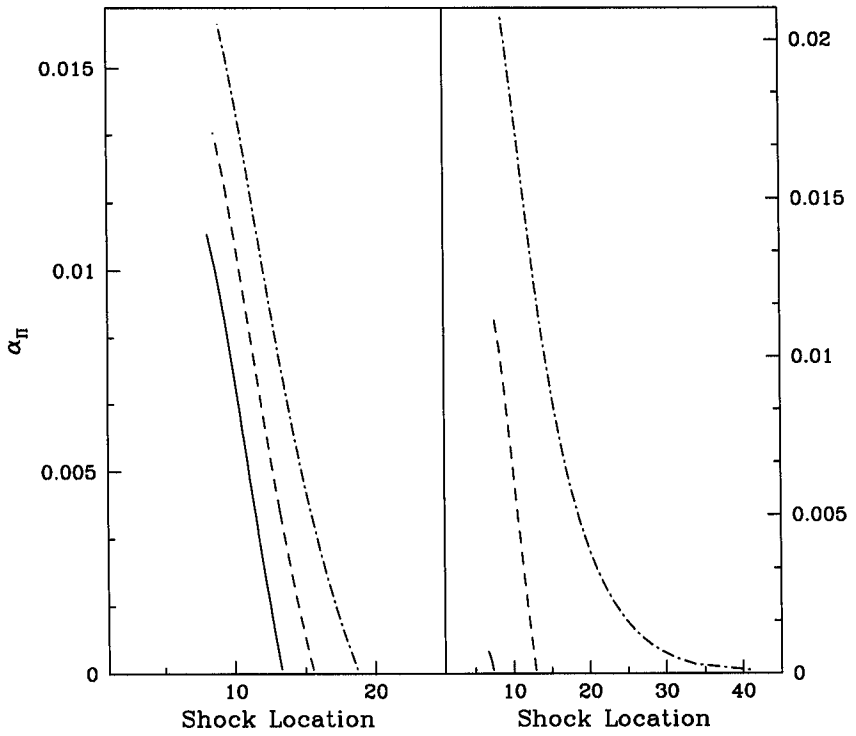

Figure 4.18: Variation of shock location with viscosity parameter and (a) inner sonic point and (b) specific angular momentum. Shock location always decreases with increase of viscosity till the critical viscosity parameter is reached beyond which the shock ceases to exist.

location on the viscosity parameter when the other two free parameters, i.e., the shock location (x_s) and angular momentum (λ_{in}) are kept fixed (Chakrabarti & Das 2004). In Fig. 4.18a, variation with the inner sonic point is presented when the angular momentum is kept fixed, while in Fig. 4.18b, the variation with the angular momentum is plotted keeping the inner sonic point fixed. In *all* the cases, the shock location is *reduced* with the increase in viscosity parameter till the critical viscosity parameter is reached beyond which the shocks disappear. This is significant because in an accretion flow, when viscosity is increased, the accretion rate is also increased and a black hole candidate goes from spectrally hard to spectrally soft state (CT95). Thus if the shock oscillation is indeed the cause of quasi-periodic oscillations (QPOs), then the frequency should increase with the accretion rate and finally as the shock ceases to exist, the QPOs also should disappear in softer states.

Observation of such features could be used to verify if the shock oscillations may be the prime cause of the QPOs in black hole candidates.

4.2 Effects of bremsstrahlung cooling on a viscous accretion flow

In §4.1, we have investigated the basic properties of viscous accretion flow around the black holes. In the present Section, we include both the viscous heating and bremsstrahlung cooling together as energy dissipative processes and carry on the similar study in a comprehensive way as presented in the earlier Section. Indeed, the study of the accretion flow problem in presence of heating and cooling processes, which usually give rise to opposite contributions to the total energy of the flow, present more realistic and sophisticated theoretical results that successfully explain the observational evidences. In fact, viscosity alone transports angular momentum and increases the possibility of shock formation at a larger distance from the black hole while cooling reduces the post-shock pressure and therefore, the possibility of shock formation becomes low. Moreover, various cooling processes will and should change the parameter space in which shocks form. In more recent years, it has become evident that the standing shocks may be very important in explaining the spectral properties of black hole candidates (CT95) as the post-shock region behaves as the boundary layer where accreting matter dissipates its thermal energy and generates hard X-ray by inverse Comptonization process. This region is also found to be responsible to produce relativistic outflows. Furthermore, numerical simulation indicates that the shocks may be oscillating at nearby regions of the parameter space in presence of cooling effects (MSC96) and the shock oscillations can also explain intricate properties of quasi-periodic oscillations (CM00).

4.2.1 Model equations

As far as the cooling processes are concerned, they could be due to various physical reasons, such as thermal and non-thermal bremsstrahlung, synchrotron, Comptonization etc. For simplicity, we assume that Comptonization enhances the injected photon intensity due to bremsstrahlung by a factor of ζ which can take any value from 1 to $\sim$ few $\times 100$ depending on the availability of soft photons (CT95). In other words, we use ζ as a parameter to represent the net cooling.

In order to study the effect of cooling mechanism in the accretion flow, we start with the same model as mentioned in §4.1 and add a cooling term in the entropy equation (Das & Chakrabarti 2004). The present work is done around a Schwarzschild black hole by using pseudo-Newtonian potential (PW80). We use a similar viscosity prescription as used in C96a. Thus, all the governing equations re-

main exactly identical as before except the entropy equation. The modified entropy generation equation is thus given by,

$$\Sigma\vartheta T\frac{ds}{dx} = Q^+ - Q^-, \tag{4.14}$$

where, s is the entropy density of the flow, T is the local temperature, Q^+ and Q^- represent the heat gained and lost by the flow respectively.

4.2.2 Sonic point analysis

We study the sonic point analysis for the dissipative accretion flow system following the general approach where gradient of radial velocity is expressed in terms of local flow variables.

For an accretion flow, entropy Eq. (4.14) can be simplified as (Das & Chakrabarti 2004),

$$\frac{\vartheta}{\gamma-1}\left[\frac{1}{\rho}\frac{dP}{dx} - \frac{\gamma P}{\rho^2}\frac{d\rho}{dx}\right] = \frac{Q^- - Q^+}{\rho h} = C - H, \tag{4.15}$$

and then $H(= Q^+/\rho h)$ takes the form,

$$H = Ax(ga^2 + \gamma\vartheta^2)\frac{d\Omega}{dx}, \tag{4.16}$$

where, the quantities have their usual meaning as mentioned in §4.1. In presence of viscous heating, we simultaneously use Comptonization of the bremsstrahlung radiation as the physical cooling process. Therefore, the non-dimensional cooling term $C = C_{br}(= Q^-/\rho h)$ may be written as,

$$C_{br} = \frac{\zeta B}{\vartheta x^{3/2}(x-1)}, \tag{4.17}$$

with

$$B = 1.4\times10^{-27}\left(\frac{\mu m_p}{2k}\right)^{1/2}\frac{\dot{M}}{2\pi m_p^2}\frac{1}{2GcM_{BH}}, \tag{4.18}$$

where, ζ is the cooling enhancement factor, μ is the mean molecular weight, m_p is the mass of the proton and k is the Boltzmann constant respectively (Das & Chakrabarti 2004).

Sonic point condition

We use the governing Eqs. 4.1(a-c) and Eq. 4.14 to obtain the sonic point conditions following the general procedure (C89a). Therefore, the gradient of radial velocity of the accreted matter may be obtained as,

$$\frac{d\vartheta}{dx} = \frac{N}{D}, \tag{4.19}$$

where the numerator N is

$$N = -\frac{\alpha_{\Pi} A(a^2 g + \gamma\vartheta^2)^2}{\gamma x} - \left[\frac{\lambda^2}{x^3} - \frac{1}{2(x-1)^2}\right]\left[2\alpha_{\Pi} g A(a^2 g + \gamma\vartheta^2) + \frac{(\gamma+1)\vartheta^2}{(\gamma-1)}\right]$$

$$-\frac{\vartheta^2 a^2(5x-3)}{x(\gamma-1)(x-1)} - \frac{\alpha_{\Pi} g A a^2(5x-3)(a^2 g + \gamma\vartheta^2)}{\gamma x(x-1)} + \frac{2\lambda A\vartheta(a^2 g + \gamma\vartheta^2)}{x^2} + \frac{B}{x^{3/2}(x-1)} \tag{4.20a}$$

and the denominator D is,

$$D = \frac{2a^2\vartheta}{(\gamma-1)} - \frac{(\gamma+1)\vartheta^3}{(\gamma-1)} - A\alpha_{\pi}\vartheta(a^2 g + \gamma\vartheta^2)\left[(2g-1) - \frac{a^2 g}{\gamma\vartheta^2}\right]. \tag{4.20b}$$

Note that, Eq. 4.20b is exactly identical with Eq. 4.8 as newly added cooling term does not change the radial velocity gradient in Eq. (4.19) as well (Das & Chakrabarti 2004).

Since accreted flow is smooth everywhere, both the numerator and the denominator must vanish simultaneously at the sonic point. Setting $D = 0$, one can obtain the expression for the Mach Number $M(x_c)$ at the sonic point which is exactly identical to Eq. 4.9 calculated in §4.1.3. In the weak viscosity limit it, Mach number at the sonic point reduces to the result obtained in C89a as,

$$M(x_c) = \sqrt{\frac{2}{\gamma+1}} \quad \text{for} \quad \alpha_{\Pi} \to 0. \tag{4.21}$$

Setting $N = 0$, we get an algebraic equation for sound speed at the sonic point which is given by,

$$F(\mathcal{E}_c, \lambda_c, x_c) = \mathcal{A}a^4(x) + \mathcal{B}a^3(x) + \mathcal{C}a^2(x) + \mathcal{D} = 0, \tag{4.22}$$

where,

$$\mathcal{A} = -\left[\frac{\alpha_{\Pi} A\{g+\gamma M^2\}^2}{\gamma x} + \frac{\alpha_{\Pi} A(5x-3)\{g+\gamma M^2\}}{\gamma x(x-1)} + \frac{M^2(5x-3)}{x(\gamma-1)(x-1)}\right], \tag{4.23a}$$

$$\mathcal{B} = \frac{2\lambda A M(g+\gamma M^2)}{x^2}, \tag{4.23b}$$

$$\mathcal{C} = -\left[\frac{\lambda^2}{x^3} - \frac{1}{2(x-1)^2}\right]\left[2\alpha_{\Pi} g A(g+\gamma M^2) + \frac{(\gamma+1)M^2}{(\gamma-1)}\right], \tag{4.23c}$$

and

$$\mathcal{D} = \frac{\zeta B}{x^{3/2}(x-1)}. \tag{4.23d}$$

We use sonic point condition (Eq. 4.21) in Eq. 4.22 to calculate the sound speed at the sonic point following the similar method described by DCC01 for the non-dissipative system and also expect the similar result if we restrict ourself only in the weak viscosity and weak cooling limit. Below, we study the nature of the sonic points in detail.

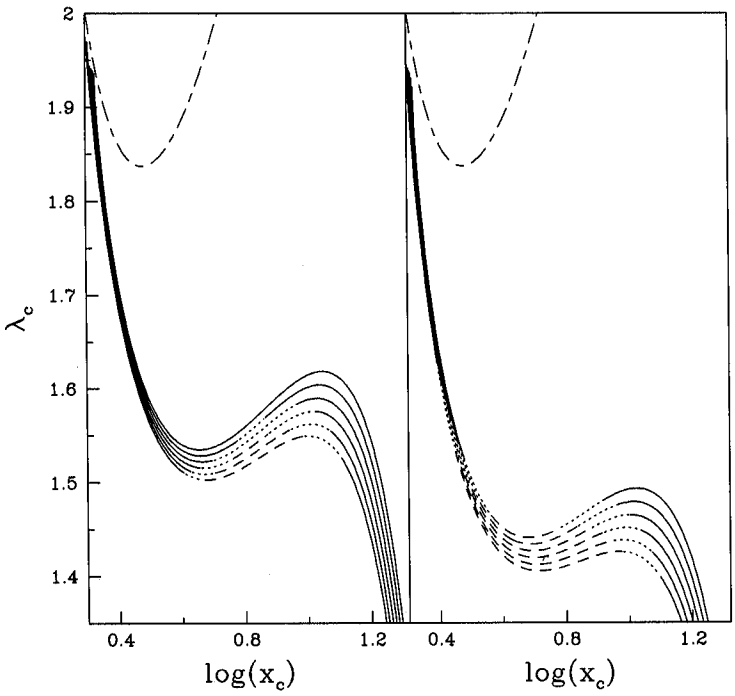

Figure 4.19: Variation of specific angular momentum (λ_c) as a function of the logarithmic sonic point location [$\log(x_c)$] for the viscosity parameter (a) $\alpha_\Pi = 0.1$ (left panel) and (b) $\alpha_\Pi = 0.5$ (right panel). Long-short dashed curve in the upper part represents the Keplerian angular momentum distribution. As before, solid curves represent the saddle type sonic points, dotted curves represent the nodal type sonic points and the short-dashed curves are for the spiral type sonic points.

Nature of the sonic points

In §4.1.4, we discussed in detail the nature of the sonic points for viscous transonic flows. In fact, the nature of sonic points mainly depends on the values of velocity gradients at the sonic points. Presently, we study the effect of bremsstrahlung

cooling on the nature of sonic points when viscosity is sufficiently effective into the flow (Das & Chakrabarti 2004).

In Fig. 4.19a, the variation of specific angular momentum (λ_c) as a function of the logarithmic sonic point location, $\log(x_c)$, is shown for a given viscosity parameter $\alpha_\Pi = 0.1$ and dimensionless accretion rate (made dimensionless by the Eddington rate) $\dot{m} = 1.0$ when specific energy at the sonic points is chosen as $\mathcal{E}_c = 0.013$ (Das & Chakrabarti 2004).. A set of ζ (Eq. 4.17) values are used while drawing the different curves. From the bottom curve to the top, $\zeta = 1$, 20, 40, 60, 80 and 100 respectively. In Fig. 4.19b, we plot the same curve for $\alpha_\Pi = 0.5$ when other parameters remain unchanged. The upper long-dashed curve corresponds to the Keplerian angular momentum distribution which is determined only by the flow geometry. Solid part of the curves are drawn for the saddle type sonic points while dotted curves represent the nodal type sonic points and the short-dashed curves are for the spiral type sonic points. Indeed, at a higher viscosity limit, the number of sonic points becomes three even with a very low angular momentum. For no Comptonization (lowermost curve), the viscous heating is so strong that only the outermost sonic point (solid part of the curve at large radius) exists. Only a large degree of cooling can compensate the viscous heating to bring back the innermost sonic point. Eventually, the matter becomes Keplerian passing through the inner sonic point. From Fig. 4.19(a-b), it is clear that the sonic point occurs at an angular momentum below Keplerian value, *i.e.*, flow angular momentum is always sub-Keplerian in nature. For lower degree of cooling (small ζ value) at the sonic point, an accretion flow contains all the three types of sonic points in a systematic order: saddle — nodal —spiral — nodal — saddle for monotonic increase of location of sonic points. With the increase of the value of ζ, the region of spiral type sonic points gradually decreases and finally it is replaced by the nodal type sonic points though multiple sonic points still exist. For further increase of ζ, all the nodal type sonic points also disappear and they are replaced by saddle type sonic points. More importantly, sonic points can form even for the super-Keplerian angular momentum when effect of cooling is sufficiently strong. We shall discuss this issue later.

In our further study, the transonic nature of the flow can be investigated from another point of view where a series of curves are plotted for a set of different specific energy ($\mathcal{E}_c$) (marked) at the sonic point. In Fig. 4.20, such a plot is presented where angular momentum (λ_c) at the sonic point is expressed as a function of logarithmic sonic point location (Das & Chakrabarti 2004). The long-short dashed curve is drawn for the Keplerian angular momentum distribution. Solid, dashed and dotted curves denote similar meaning as in Fig. 4.19. Note that, negative energies correspond to two sonic points where the inner one is saddle type and the furthest one represent the spiral type. For each energy, two curves are drawn. The thick curve is drawn when both the heating and cooling are included while the thin curve is drawn

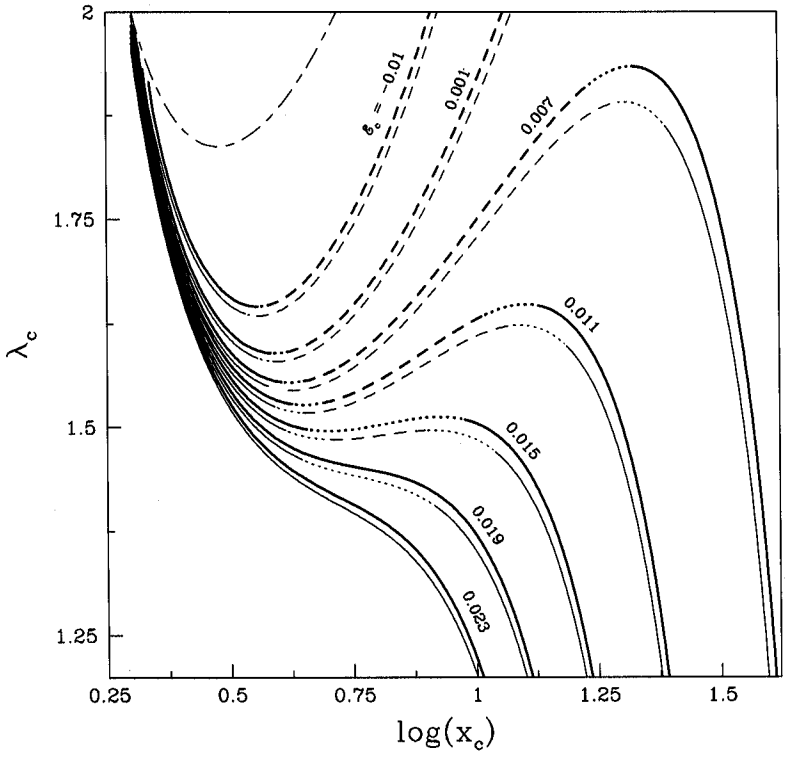

Figure 4.20: Variation of the specific angular momentum (λ_c) at the sonic point (x_c) as a function of the specific energy ($\mathcal{E}_c$) of the flow. For each energy, two curves are drawn. The thick curves are drawn for the cases when both the heating and cooling are included while the thin curves are drawn when only the heating is included. For negative energies, there are only two sonic points.

when cooling effect is ignored. An important point is that the character of solution can be changed by incorporating the cooling effect. For instance, as an example, the solution for $\mathcal{E}_c = 0.019$ with heating and cooling has no spiral or nodal sonic points. But when the cooling is turned off, the saddle type sonic point becomes nodal type.

We continue the study of nature of sonic points in Fig. 4.21(a-b) by plotting the specific energy at the sonic point ($\mathcal{E}_c$) as a function of location of sonic point (x_c) for a set of cooling factors (ζ) (Das & Chakrabarti 2004). In the left panel we present the results for low viscosity ($\alpha_\Pi = 0.1$) while in the right panel, high viscosity ($\alpha_\Pi = 0.5$) is used. In both the figures, the other parameters are: $\lambda_{in} = 1.65$ and $\dot{m} = 1$. The curves are drawn from bottom to the top for the cooling factors $\zeta = 1, 20, 40, 60, 80, 100$ and 120 respectively. Notice that three sonic points occur only when the specific energy is positive, *i.e.*, for sufficiently hot Keplerian disks or

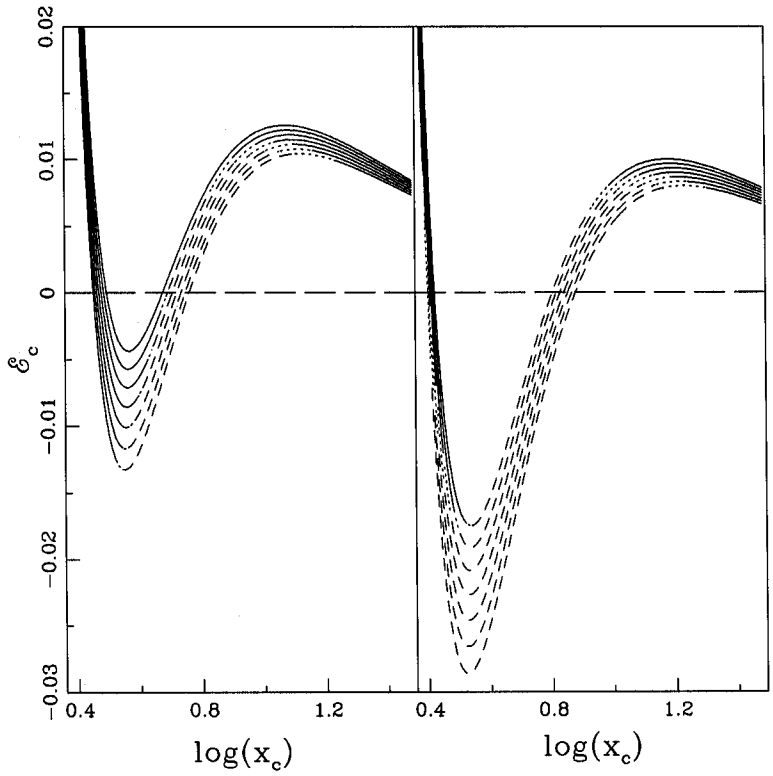

Figure 4.21: Variation of the specific energy ($\mathcal{E}_c$) at the sonic point (x_c) as a function of the cooling rate of the flow drawn for (a) $\alpha_\Pi = 0.1$ (left panel) and (b) $\alpha_\Pi = 0.5$ (right panel). For high viscosity, the outer sonic points almost disappear.

sub-Keplerian flows. However, outer sonic points almost disappear from the region close to the black hole at the high viscosity limit.

In Fig. 4.22, we show how the number of sonic points, reduced due to viscous heating process, is recovered back with the introduction of cooling (Das & Chakrabarti 2004). The curves are drawn, from the bottom to the top, for ζ = 1, 20, 60, 80 100 and 140 respectively while other parameters are marked in the inset. Solid and dotted curves represent saddle and nodal type sonic points respectively and short-long dashed curve corresponds to the Keplerian angular momentum distribution. The horizontal long dashed curve denotes the critical boundary of the angular momentum $\lambda_{cri} = 1.1733$ and cooling factor $\zeta = 4.2$ below which multiple sonic points do not exist, *i.e.*, shock is not formed in steady flows.

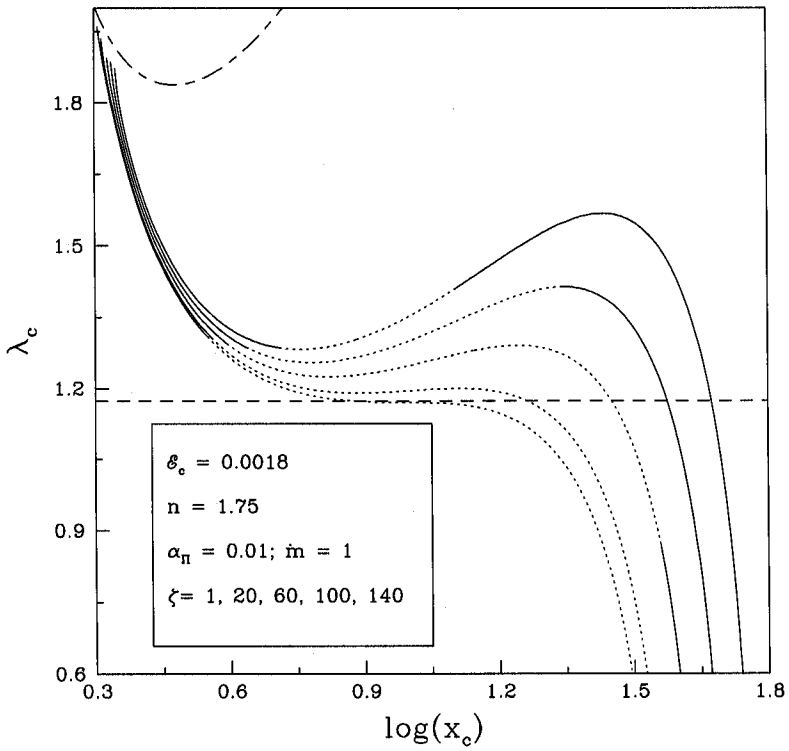

Figure 4.22: Recovery of outer sonic point points as cooling processes are introduced. Solid and dotted curves are for saddle and nodal type sonic points respectively. Parameters are marked on the plot. Long dashed curve at $\lambda_c = 1.1733$ gives a boundary below which there are no triple sonic points.

4.2.3 Global solution topology

The basic criteria for the study of the shock properties demands that flow has to be multi-transonic in nature. In fact, effect of viscous heating on the solution topology has already been presented in §4.1.5. In the following Section, we shall discuss the nature of solution topology in presence of both the of viscous heating and bremsstrahlung cooling together (Das & Chakrabarti 2004).

In Fig. 4.23(a-b), we investigate the modification of solution topology for different cooling factors. In Fig. 4.23a, Mach number is plotted as a function of the logarithmic radial distance for $\zeta = 1$, 10, 25 and 50 respectively while other parameters are considered as: $x_{in} = 2.71$, $\lambda_{in} = 1.68$, $\alpha_\Pi = 0.01$, $\dot{m} = 0.5$. Notice that topology opens up with the gradual increase of cooling factor to allow the flows to

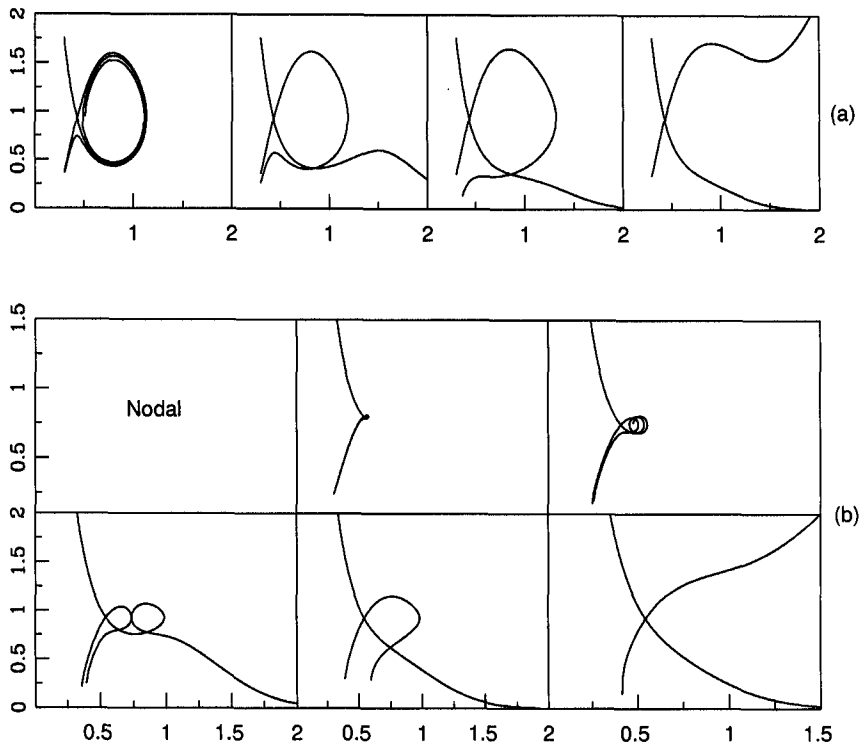

Figure 4.23: Solution topologies in presence of heating and cooling. In (a), the parameters are $\zeta = 1$, 10, 25 and 50 respectively. Other parameters are $x_{in} = 2.71$, $\lambda_{in} = 1.68$, $\alpha_{\Pi} = 0.01$, $\dot{m} = 0.5$. In (b), the parameters are $\zeta = 1$, 10, 25, 33.1, 50 and 70 respectively. Other parameters are; $x_{in} = 3.5$, $\lambda_{in} = 1.68$, $\alpha_{\Pi} = 0.01$, $\dot{m} = 2.0$.

enter into the black holes through the inner sonic point. In Fig. 4.23b, we present solution topology in six panels in which relatively higher accretion rate and higher inner sonic point locations are chosen. The cooling factors of our interest are considered as: $\zeta = 1$, 10, 25, 33.1, 50 and 70 respectively. Other parameters are: $x_{in} = 3.5$, $\lambda_{in} = 1.68$, $\alpha_{\Pi} = 0.01$, $\dot{m} = 0.2$. Important point is that, as the cooling is increased, the topologies open up similarly, but the route to opening up is different. For instance, the solution in the fourth panel, with $\zeta = 33.1$ is completely new and intriguing. In this case, the flow has the potential to join with a Keplerian disk far away (with low Mach number), while at the same time, it also passes through the inner sonic point. But it has multi-valued solution: there are two Mach numbers at a given radial distance in some region. We conjecture that this type of solution should be unstable and would cause non-steady accretion.

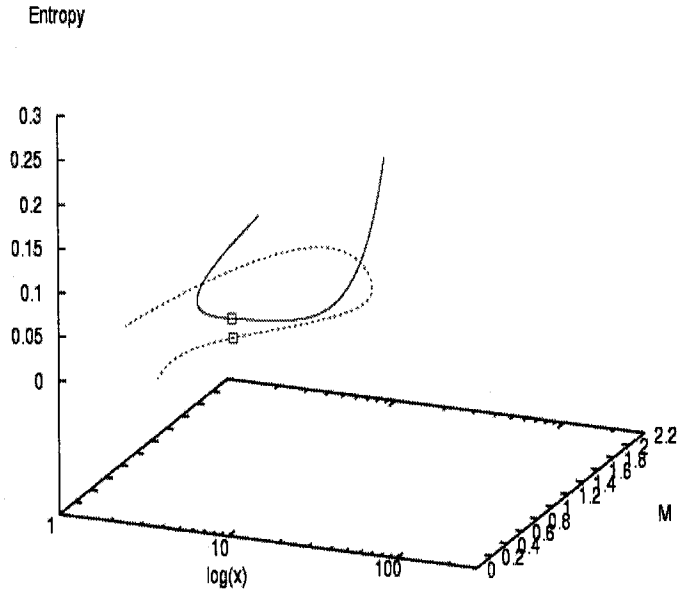

Figure 4.24: Three-dimensional plot of the second panel ($\zeta = 10$) of Fig. 5a in which the specific entropy is also plotted as it varies along the flow. The boxes represent the pseudo-intersection point of that panel at around $M \sim 0.5$. The two branches have different entropies.

In Fig. 4.23(a-b), all the closed topologies show 'multiple crossings' very similar to what was found in the study of spiral shocks (Chakrabarti 1990c). Actually, in dissipative system, since entropy is changing along the flow, the two dimensional plot of phase space diagram in Fig. 4.23(a-b) is slightly misleading. We resolve this illusion in Fig. 4.24 where we show a 3-dimensional plot of the second panel ($\zeta = 10$) of Fig. 4.23a in which the specific entropy is also plotted as it varies along the flow (Das & Chakrabarti 2004). More importantly, this diagram shows that at the true sonic point, the specific entropy is exactly identical in both the incoming (solid) and the outgoing (dotted) branches. But at the 'intersection' (at around $M \sim 0.5$) in 2-dimensional plot marked by two squares, the entropies are completely different. Thus, there is no 'sonic point' around $M \sim 0.5$.

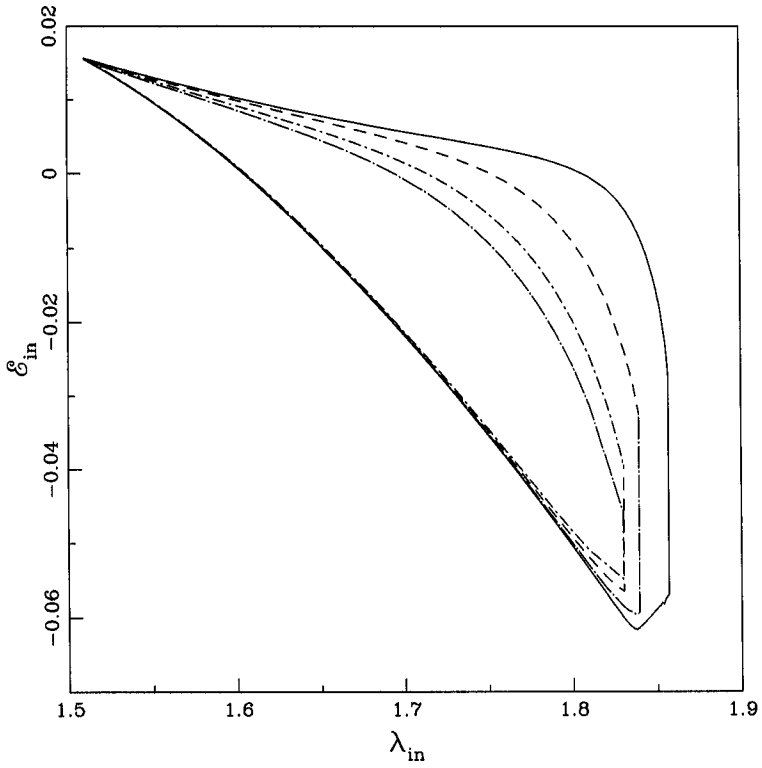

Figure 4.25: Region of the parameter space in which the solution passing through the inner sonic point contains a closed spiraling topology. The solid, dashed, dot-dashed and dot-long-dashed regions are plotted for cooling parameter 1, 10, 30, and 50 respectively. Other parameters are $\alpha_{\Pi} = 0.01$ and $\dot{m} = 0.1$.

4.2.4 Parameter space description

As before, we classify the region of parameter space spanned by the specific angular momentum (λ_{in}) and energy ($\mathcal{E}_{in}$) at the sonic point. In Fig. 4.25, such classifications of parameter space are presented for various cooling factors (Das & Chakrabarti 2004). For instance, the parameter space is separated for the solutions passing through the inner sonic point containing a closed spiraling topology as in panel 1 of Fig. 4.23a. In particular, such solutions indicate that a stationary or oscillatory shock may form depending on whether the Rankine-Hugoniot relation is satisfied (Landau & Lifshitz 1959) or not. The solid, dashed, dot-dashed and dot-long-dashed regions are for cooling parameter 1, 10, 30, and 50 respectively. In fact, with the increase of the cooling factor, the region shrinks and becomes smaller and smaller. This indicates that there exists a critical cooling parameter (ζ_{cri}), beyond which

a flow will cease to have multiple sonic points. Other parameters are chosen as $\alpha_\Pi = 0.01$ and $\dot{m} = 0.1$. When the viscosity and cooling are reduced to zero, this region merges exactly to the corresponding region in C89a.

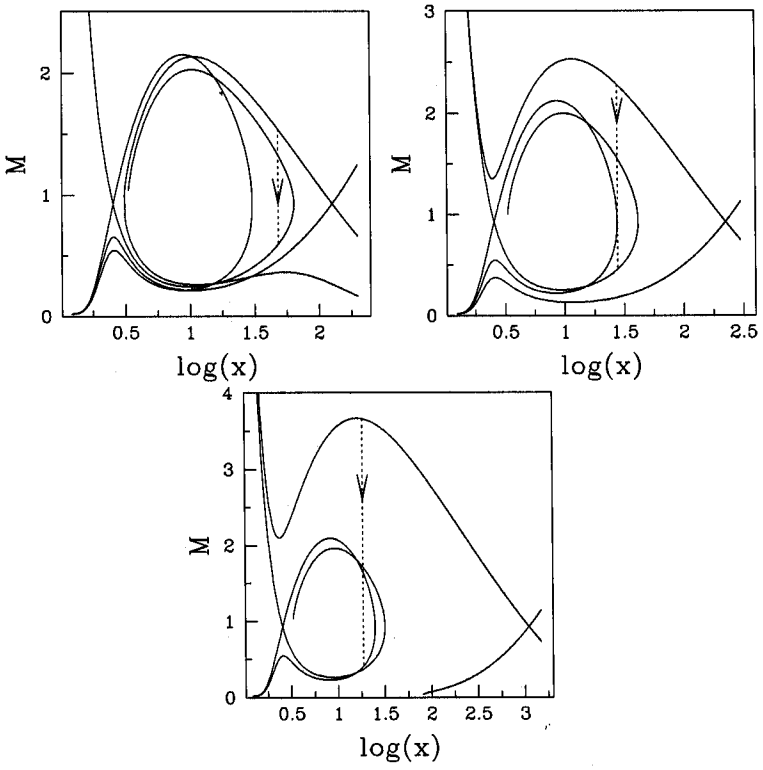

Figure 4.26: A few complete solutions which are drawn with the parameters at $\lambda_{in} = 1.7$, $\alpha_\Pi = 0.05$, $\dot{m} = 0.2$ and $\zeta = 5$ and only the inner sonic point is varied: (a) $x_{in} = 2.545$, (b) $x_{in} = 2.55$ and (c) $x_{in} = 2.555$. The corresponding shock locations are (a) $x_s = 48.199$, (b) $x_s = 27.8854$ and (c) $x_s = 18.6445$ respectively. Vertical dashed lines show the shock transitions.

It is customary to investigate a complete flow solution where shocks are inevitable. Accordingly, in Fig. 4.26(a-c), we present a few shock solutions which are drawn with the parameters at $\lambda_{in} = 1.7$, $\alpha_\Pi = 0.05$, $\dot{m} = 0.2$ and $\zeta = 5$ and only the inner sonic point is varied: (a) $x_{in} = 2.545$, (b) $x_{in} = 2.55$ and (c) $x_{in} = 2.555$ (Das & Chakrabarti 2004). The corresponding shock locations are obtained as (a) $x_s = 48.199$, (b) $x_s = 27.8854$ and (c) $x_s = 18.6445$ respectively. Vertical dotted arrows indicate the discontinuous shock transition which connects two solutions: one is passing through the inner sonic point and the other is passing through the outer sonic point. The spiral loop through the inner sonic point rapidly shrinks with the

increase in the sonic point location and shock location also comes closer. This shows that even though the shock location may change by orders of magnitude, the inner sonic point virtually remains at the same place.

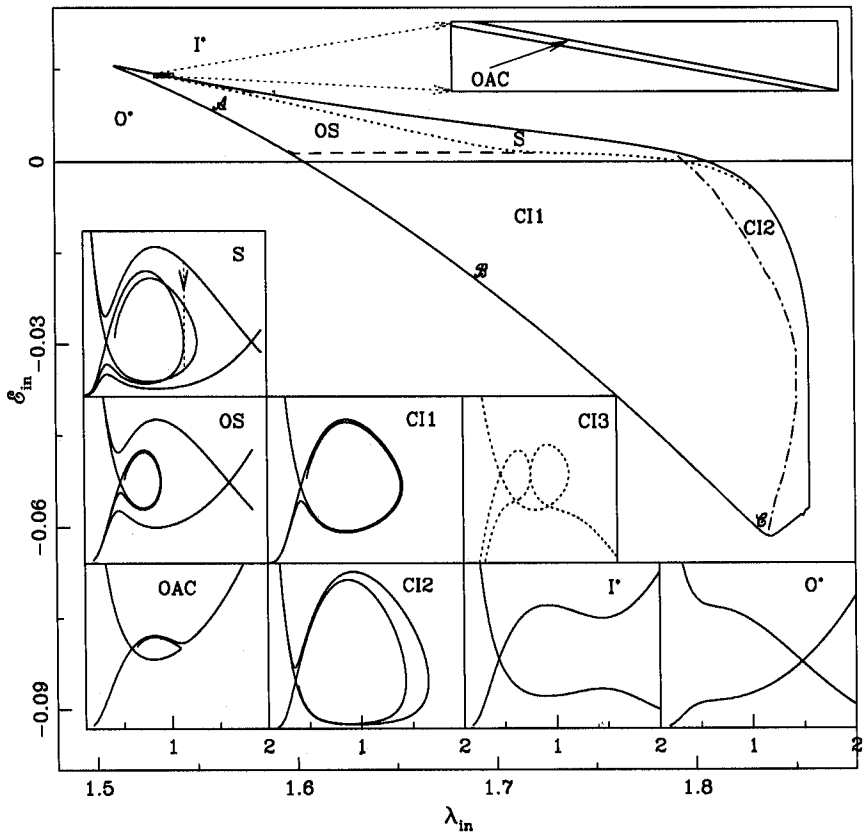

Figure 4.27: Division of the parameter space according to the solution topologies shown in the inset. Details of the figure are described inside the text.

In Fig. 4.27, we show the sub-division of the parameter space in terms of nature of solution topologies for a viscous flow once again where the cooling effect is included (Das & Chakrabarti 2004). A similar set of topologies seen in §4.1.6 are presented along with a new topology (Fig. 4.23b) which occurs when the cooling factor is especially strong. Indeed, the sub-divisions of the parameter space are labeled and the corresponding topologies are drawn in the bottom left. Meanwhile, for strong cooling effect, the curve $\mathcal{ABC}$ is further sub-divided and a new topology with parameters chosen from a region very close to the curve $\mathcal{ABC}$ occurs which is plotted in the box C13.

We continue our investigation to identify the possible modification of the pa-

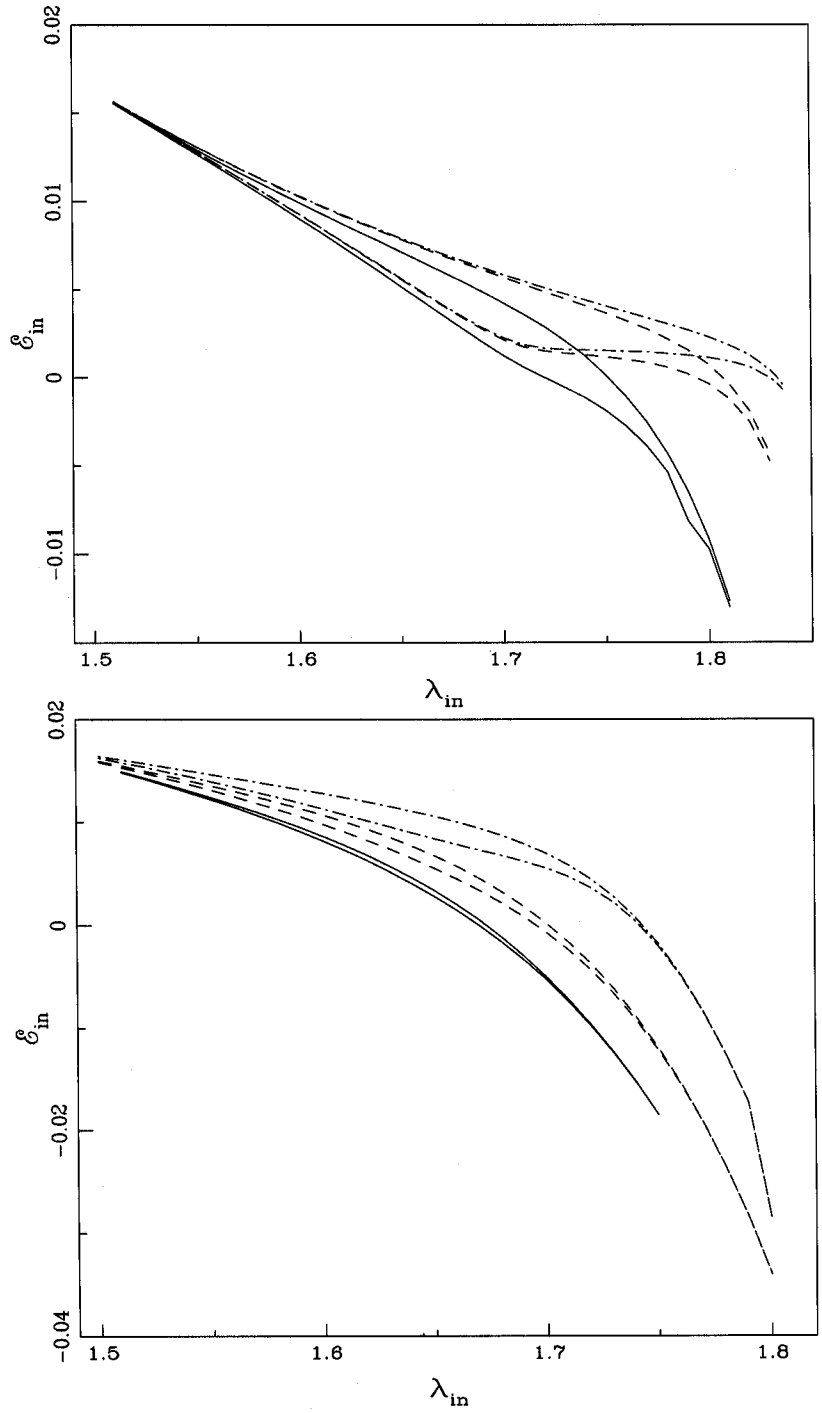

Figure 4.28: Modification of the parameter space for shock formation when cooling is varied. (a) $\alpha_\Pi = 0.01$ is chosen and $\zeta = 0.01$, (dot-dashed) 0.1 (long-dashed) and 1 (solid) (left panel). (b) $\alpha_\Pi = 0.05$ is chosen and $\zeta = 1$ (dot-dashed), 5 (long-dashed) and 10 (solid) (right panel).

rameter space for shock formation when cooling is enhanced. Accordingly, in Figs. 4.28(a-b), such a parameter space plot is presented. In Fig. 4.28a, $\alpha_\Pi = 0.01$ is chosen and the cooling factors are $\zeta = 0.01$ (dot-dashed), 0.1 (long-dashed) and 1 (solid) respectively (Das & Chakrabarti 2004). Note that, in particular, the region of the parameter space shifts to include negative energy regions as well due to the enhancement of cooling factor (for instance, for $\alpha_\Pi = 0$ and $\zeta = 0$, the parameter space contains only positive energy). However, in Fig. 4.28b, viscosity parameter is increased to $\alpha_\Pi = 0.05$ which causes a general shrinkage in the parameter space at its own coast. In this particular plot, the cooling parameters are chosen as $\zeta = 1$ (dot-dashed), 5 (long-dashed) and 10 (solid) respectively. Effectively the parameter space further shrinks drastically when cooling factor is enhanced.

4.2.5 Sonic points for super-Keplerian flows?

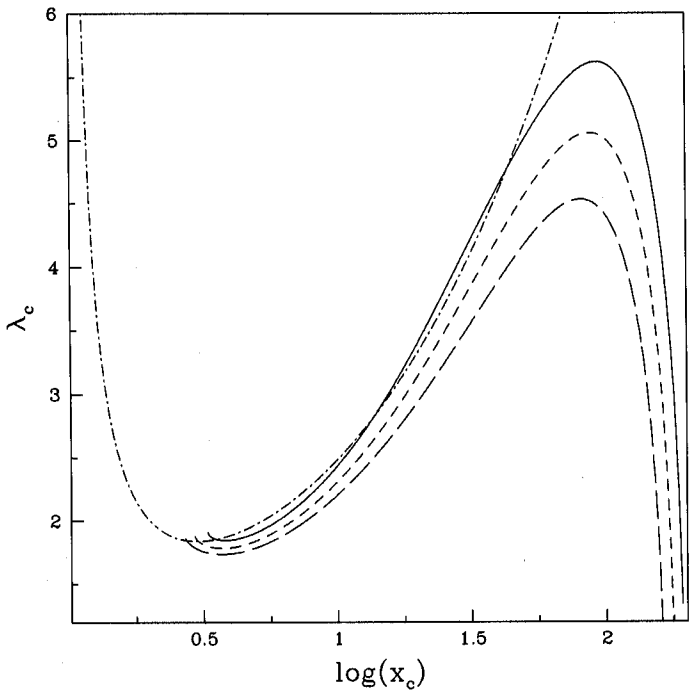

Figure 4.29: Example of parameters which produce transonic solutions with super-Keplerian angular momentum. The dot-dashed curve is the Keplerian distribution. Solid curves, from the bottom to the top, are for $\zeta = 400, 500$ and 600 respectively.

In the literature, it is generally believed that originally Keplerian matter at the outer edge of the disk becomes sub-Keplerian while crossing the sonic points before entering into the black hole horizon. However, this generic picture may be violated

when the cooling process is very efficient (Das & Chakrabarti 2004). In Fig. 4.29, we show that when ζ is very high, of the order of a few hundreds, the sonic point may have angular momentum *above* the Keplerian distribution (dotted curve). In particular, sonic point in super-Keplerian flow is formed when it is located closed to the black hole horizon. The implication of this is not obvious. Does it mean that very cold flow *can* be Keplerian or super-Keplerian throughout its journey? If so, can it spin up the black hole faster that what is presumed so far? The discussion about this issue is beyond the scope of this thesis.

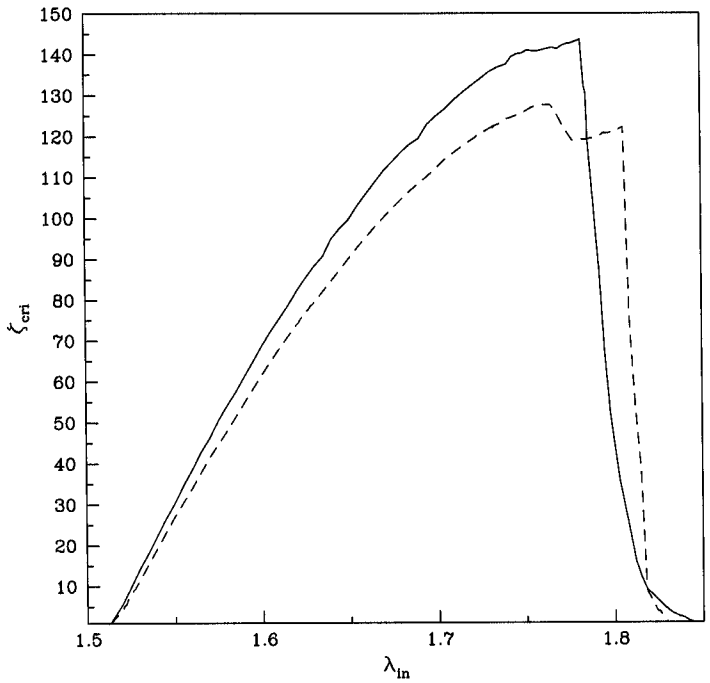

Figure 4.30: The variation of the critical cooling parameter as a function of the specific angular momentum at the inner sonic point for two different viscosity parameters. Solid curve is for $\alpha_{\Pi} = 0.01$ and the dashed curve is for $\alpha_{\Pi} = 0.05$. The region below the curve contains topologies which are closed and therefore standing or oscillating shocks could be possible while the region above the curve allows solutions with open topologies.

4.2.6 Critical cooling and sub-division of the parameter space

In the previous discussion, we have already pointed out that cooling and heating processes have opposite effects in deciding the solution topologies, but one can not

exactly compensate the other effect. When the cooling is enhanced for a given viscosity parameter, the possibility of shock formation is eventually reduced (Das & Chakrabarti 2004). This is shown in Fig. 4.30, where the critical cooling parameter $\zeta = \zeta_{cri}$ is plotted against the specific angular momentum for two different viscosity parameters. Solid curve is for $\alpha_\Pi = 0.01$ and the dashed curve is for $\alpha_\Pi = 0.05$. All possible inner sonic points are considered. The region below the curve contains topologies which are closed and therefore, standing or oscillating shocks could be possible while the region above the curve allows solutions with open topologies. Notice that for smaller λ_{in}, the critical cooling factor is smaller. This is expected since the possibility of shock formation is enhanced with larger λ_{in} in general. When α_Π is higher ζ_{cri} is lower. This indicates that general reduction of the parameter space due to higher viscosity (Chakrabarti & Das 2004) which is not totally compensated for by cooling effects.

4.3 Effects of synchrotron cooling on viscous accretion flow

Several attempts have been made for further development of the theory of accretion disk to emphasize the more realistic physical processes including angular momentum, heating and cooling effects. Unfortunately, no theoretical description of accretion flow including synchrotron cooling is presented in the literature so far. Similar to bremsstrahlung cooling, synchrotron cooling also has the same status on the basis of energy dissipation processes but technically the later one has stronger effect than the former one on the transonic accretion flow. In the following Section we briefly address this issue.

4.3.1 Basic equations and sonic point conditions

The effects of synchrotron cooling is well understood when it is considered as an isolated cooling process similar to bremsstrahlung cooling in a viscous transonic accretion flow. The magnetic field is obtained by equating the magnetic pressure to a certain percentage of the thermal pressure of the gas under consideration and is given by,

$$B_{mag} = \sqrt{\frac{8\pi\rho kT}{\mu m_p}}, \tag{4.24}$$

where, ρ is the density of the flow, k is the Boltzmann constant, T is the flow temperature, μ is the mean molecular weight and m_p is the mass of the proton respectively. Here, β is a non-dimensional constant factor. In an electron-proton plasma, we use the equipartition magnetic field (Eq. 4.24) to account for the non-dimensional synchrotron cooling effect which is obtained in a convenient form as (Shapiro & Teukolsky 1983):

$$C_{sy} = \frac{\beta S a^5}{\vartheta x^{3/2}(x-1)}, \tag{2.25a}$$

with

$$S = 7.542 \times \frac{\dot{M} m_p \mu^2 e^4}{m_e^4 \gamma^{5/2}} \frac{1}{2GM_{BH}c^3}, \tag{2.25b}$$

where, ϑ denotes the radial velocity, x is the radial distance and a is the flow sound speed. Here, $\dot{M}$, e and m_e represent the accretion rate, electronic charge and mass of the electron respectively. The factor β controls the cooling effect since certain percentage of equipartition is considered for computing the stray magnetic field inside the disk. Therefore, it is useful to treat β as an input parameter while

solving the present problem. Indeed, we incorporate the newly specified cooling process in the entropy equation while treating it at the same footing similar to other dissipation processes. Thus, the flow experiences combined cooling effects which come from the individual contribution of bremsstrahlung and synchrotron cooling processes ($C = C_{br} + C_{sy}$). However, following the standard sonic point analysis one can easily compute the sonic point conditions for a transonic flow where most of the major energy dissipative processes, namely, viscous heating, bremsstrahlung and synchrotron cooling are included. Since synchrotron cooling does not explicitly depends on the gradient of radial velocity ($d\vartheta/dx$), one of the sonic point conditions which usually obtained by vanishing the denominator of $d\vartheta/dx$ will be identical to Eq. (4.9). On the other extent, when numerator vanishes, we get an algebraic equation for the sound speed at the sonic point which is given by,

$$F(\mathcal{E}_c, \lambda_c, x_c) = \mathcal{A}a^5(x) + \mathcal{B}a^4(x) + \mathcal{C}a^3(x) + \mathcal{D}a^2(x) + \mathcal{G} = 0, \tag{4.26}$$

where,

$$\mathcal{A} = \frac{\beta S}{x^{3/2}(x-1)}, \tag{4.26a}$$

$$\mathcal{B} = -\left[\frac{\alpha_{\Pi} A\{g+\gamma M^2\}^2}{\gamma x} + \frac{\alpha_{\Pi} A(5x-3)\{g+\gamma M^2\}}{\gamma x(x-1)} + \frac{M^2(5x-3)}{x(\gamma-1)(x-1)}\right], \tag{4.26b}$$

$$\mathcal{C} = \frac{2\lambda A M(g+\gamma M^2)}{x^2}, \tag{4.26c}$$

$$\mathcal{D} = -\left[\frac{\lambda^2}{x^3} - \frac{1}{2(x-1)^2}\right]\left[2\alpha_{\Pi} g A(g+\gamma M^2) + \frac{(\gamma+1)M^2}{(\gamma-1)}\right], \tag{4.26d}$$

and

$$\mathcal{G} = \frac{\zeta B}{x^{3/2}(x-1)}. \tag{4.26e}$$

The nature of sonic points could be easily understood with the sonic point analysis. In fact, one can illustrate the detail properties of sonic point with the extensive study of Eqs. (4.26) when the flow parameters are known. A discussion of sonic point analysis have already been presented in the earlier Sections and thus will not be repeated here once again.

4.3.2 Shock solutions and its properties

In the last two decades, improvement of accretion disk physics advances rapidly. In the present thesis, this features repeatedly highlighted since we gradually include more realistic physical processes that are supposed to be effective inside the disk. The last but not the least, such process is the synchrotron cooling process, since magnetic filed is undoubtedly existed in the accretion disk though the nature of such magnetic field is still not well known. However, as a first step we are equating the magnetic energy density with the ideal gas pressure following the equipartition technique and incorporate the synchrotron cooling effect in the flow solution. Note that for the transonic property of the flow, a fraction of the ideal gas pressure is used at the equipartition and this is controlled by a non-dimensional factor β which is usually treated as an input parameter.

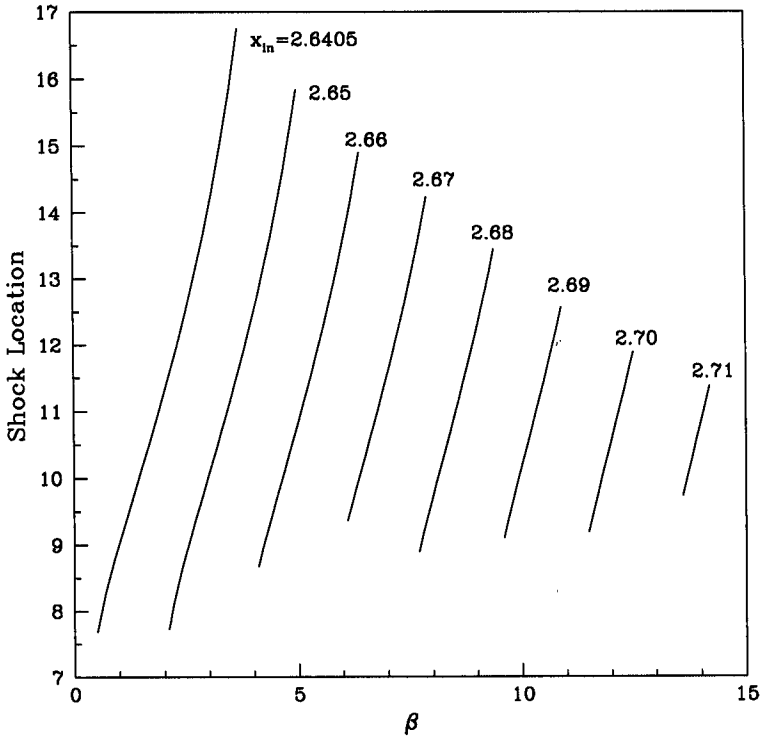

Figure 4.31: Plot of shock location against synchrotron cooling factor β for a set of inner sonic point locations for $\alpha_\Pi = 0.001$, $\dot{m} = 0.1$ and $\lambda_{in} = 1.70$.

In what follows, the outflows or jets, canonical spectrum, quasi-periodic oscillation of the X-ray etc. are successfully explained by the TCAF model and all these features strongly depend on the various properties of the shock wave. However, it

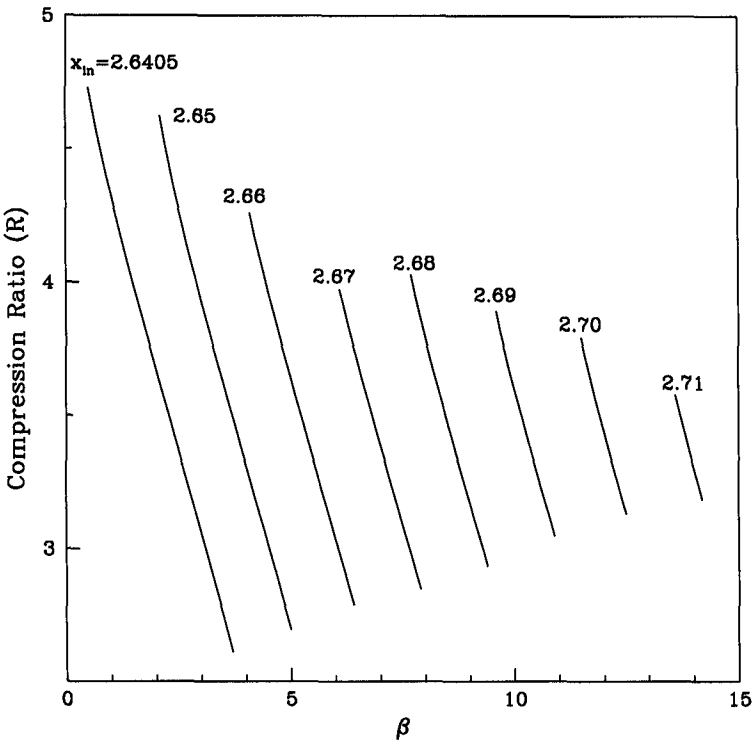

Figure 4.32: Plot of shock strength variation as a function of β for the same set of parameters used in Fig 4.31.

is necessary to understand the effect of synchrotron cooling on the shock properties in a viscous transonic flow, since the presence of magnetic field is inevitable inside the disk. In Fig. 4.31, we present the variation of shock locations with the synchrotron cooling parameter β for a given angular momentum at the inner sonic point $\lambda_{in} = 1.70$. Here, we set $\alpha_{\Pi} = 0.001$ and $\dot{m} = 0.1$ (measured in Eddington unit). The individual curve is drawn for fixed inner sonic point locations marked at the top of the line. Notice that at a given inner sonic point, shock forms only for a particular range of β and this range of β gradually decreases with the monotonic increase of sonic point location. It is clear from the figure that when the inner sonic point location increases, the flow suffers shock transition for relatively higher cooling factor β. In addition, the upper limit of the shock location decreases with the increase of the sonic point location whereas the lower limit of the shock location is generally insensitive with the inner sonic point location. This indicates that the cooling factor β has a critical value for shock and beyond this critical value the flow

ceases to have shock when the rest of the parameters are kept fixed.

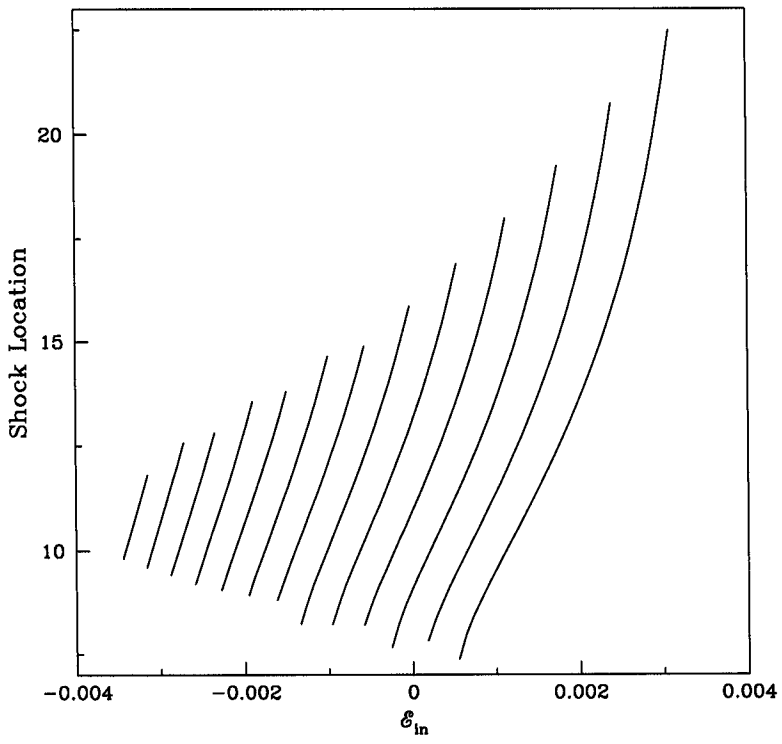

Figure 4.33: Variation of shock location as specific energy at the inner sonic point is changed for a set of β. The rest of the initial parameters are unchanged.

An important property of the shock waves is it's compression ratio that measures the strength of the shock. Compression ratio (R) is defined as the ratio of density at the pre-shock to post-shock flow. In Fig. 4.32, we plotted the variation of compression ratio with the cooling factor β for given set of inner sonic point locations. Same set of initial parameters as in Fig. 4.31 are used here. At the top of the curves, the locations of the inner sonic points are marked. The Figure shows that strong shocks ($R \sim 4$) are formed for a large region of the cooling factor β. Therefore, a significant amount of outflow and jet is expected to produce even when the synchrotron cooling is effective in the accretion system.

In Fig. 4.33, we show the variation of shock locations as a function of specific energy ($\mathcal{E}_{in}$) at the inner sonic point when the synchrotron cooling is turned on inside the flow. Separate lines are plotted for a fixed value of cooling factor starting from $\beta = 1.0 \times 10^{-07}$ (rightmost) to $\beta = 1.21 \times 10^{-05}$ (leftmost) with an interval

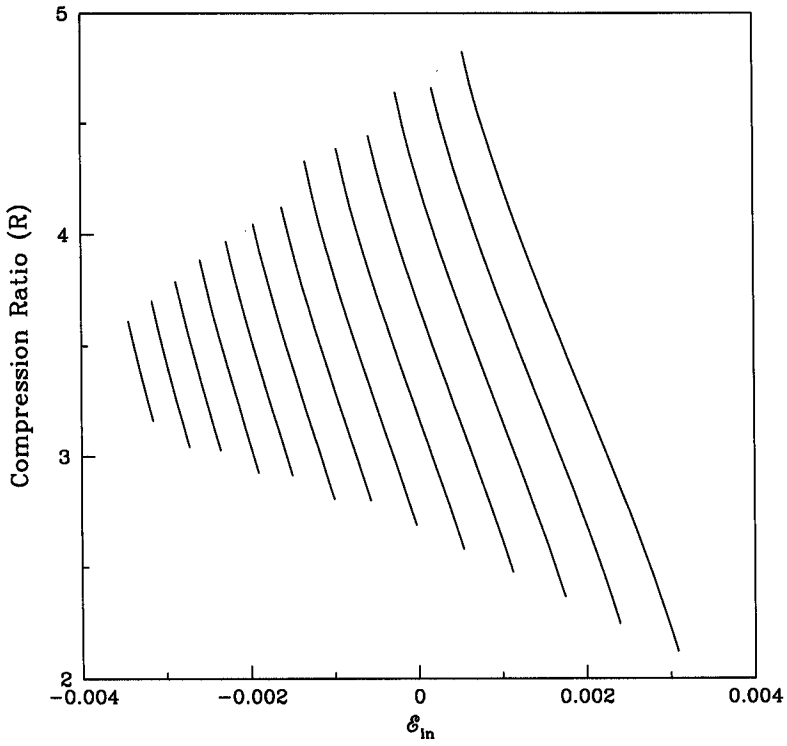

Figure 4.34: Variation of shock strength with specific energy at the inner sonic point for the same set of initial parameters used in Fig. 4.31.

of $\Delta\beta = 1.0 \times 10^{-06}$. With the gradual increase of cooling factor (β), upper limit of the shock location proceeds towards the black hole horizon and finally disappear when β exceeds its critical value. Shocks are formed even for negative energy at the inner sonic point (though a shocked flow is supposed to have a positive energy) indicates that due to the cooling, the flow looses significant amount of energy while falling towards the black hole.

In Fig. 4.34, we draw the variation of the compression ratio (R) as a function of specific energy ($\mathcal{E}_{in}$) at the inner sonic point for the same set of initial parameters used in Fig. 4.33. Different curves are drawn for different β ranging from $\beta = 1.0 \times 10^{-07}$ (rightmost) to $\beta = 1.21 \times 10^{-05}$ (leftmost) with an interval of $\Delta\beta = 1.0 \times 10^{-06}$. Fig. 4.34 clearly shows that the upper and lower limit of compression ratio monotonically decrease for the gradual increase of the synchrotron cooling factor (β) and finally compression ratio merges to the intermediate value ($R \sim 3.5$) upto a critical cooling factor beyond which shock disappear.

Chapter 5

Conclusions and Discussions

In the introduction, we have pointed out that the present thesis illustrates the development of accretion disk physics right from the beginning. We started with a brief introduction of 'compact objects' and also presented a simple classifications of such objects based on their mass limit. We mentioned the importance of accretion process around a compact object and pointed out that this process is believed to be the possible source of power supply for high luminous celestial objects like active galactic nuclei, quasars, micro-quasars etc. We identified the extreme limits of efficiency of accretion processes around a rotating and non-rotating black holes. We discussed the historical development of accretion process in §1.4. In this Section, first, we presented spherical accretion model in both the Newtonian and general relativistic approach. Second, to avoid complexity, we studied accretion processes in a strong gravitational field by considering pseudo-Newtonian potential which successfully mimics the space-time geometry of a Schwarzschild black hole. A discussion of this potential was presented in §1.4.4. We pointed out that black hole accretion is always transonic independent to the nature of central potential under consideration. We stressed that spherical accretion of interstellar gas gives minimal contribution of emitted radiation and can not be treated as a most general accretion disk model. In §1.5, we proceeded further for the improvement of the theory of accretion physics considering disk accretion. This Section started with a path breaking work of accretion process where a useful description of thin accretion disk model, commonly known as 'Keplerian disk' is presented. This model successfully explains the multi-colour black body component spectrum which is observed in the spectra of several accretion disk in the galactic and extra-galactic system but unable to produce power low emission at the higher energy limit shown by most of the black hole candidates. More importantly, in this model, accretion disk is terminated at the marginally stable orbit and the inner boundary conditions are not satisfied since the advection of flow was completely ignored. Therefore, the basic requirement of the accretion process around black hole, *i.e.*, the transonic property, is not satisfied in this model and we proceeded further for future development of this subject. In §1.5.2, we presented another disk model, known as the 'Thick disk' which have a

couple of interesting features such as the production of supercritical luminosity, explanation of rapid variability of sources, it's ability of jet collimation etc. However, the strong anisotropic nature of the emission properties of this model is a major disadvantage and this model is also dynamically as well as globally unstable due to non-axisymmetric perturbation. To avoid these difficulties, we launched a couple of advective accretion disk models which only differ from their geometrical shape. In §1.6, we discussed two such models—the first one is the conical flow model and the second is the flow of constant height. We explained the properties of the accretion disk using these models and showed that this flow properties strongly depends on the initial flow parameters.

Chapter 2 started by giving a description of most general non-dissipative accretion disk model where flow is supposed to be in hydrostatic equilibrium in the direction transverse to the radial motion. The results obtained from this model are the actual mathematical solutions of governing equations which depend, of course, on the flow parameters as well as model geometry. We showed that multiple sonic points are produced only for a particular range of initial flow parameters rather than their arbitrary values. We presented shock conditions in different limits and studied the nature of Rankine-Hugoniot shocks in this model for the accretion and the winds around a compact object. In §2.3, we mentioned that jets are originated only from the post shock region. In addition, we estimated the outflow rate as a function of compression ratio by considering a toy model. We also pointed out that outflows and jets are produced only in the hard state.

In an accretion flow, the study of standing and oscillatory shocks are of great importance. In Chapter 3, we showed that shocks could be studied completely analytically for a non-dissipative accretion flow system. We mentioned that shock locations strongly depend on the initial flow parameters and they form further from the black hole horizon when angular momentum is increased. This demands that shocks are mainly centrifugal pressure supported. We identified that post-shock locations are the ideal place for production of hard X-rays when the soft-photons are processed by the hot electron of the post-shock region through the inverse-Comptonization process. Accordingly, the spectral states and the time dependent behaviour of the hard X-rays are directly related to nature of this region. In fact, CT95 established the steady state spectra with the post-shock region as the source of hot Comptonizing electrons whereas CM00 showed that QPOs are due to the oscillation of this region, since only hard X-rays are seen to exhibit QPOs. Therefore, the above features demand that the shocks are essential ingredients of an accretion disk. Moreover, observationally, the present work has a great importance since the steady spectra, QPO frequencies, etc. are determined analytically from a few free physical parameters.

In §3.2, we identified a unique relation among the polytropic indices of three

different models of axisymmetric accretion flow which ensures identical transonic properties of these models for a set of given flow parameters. We further investigated the shock locations using the same unique relation of polytropic indices with fixed flow parameters and found that shocks are also formed roughly at the same place in three different models. We showed that disjoint parameter space for shock with same value of polytropic index in three different models exhibits considerable overlap when the same unique relation is used. This proves that the models are virtually identical in nature and various disk models belong to a single parameter family, namely, polytropic indices. It is well known that linear and non-linear stability analysis and time-dependent numerical simulations are easier to perform for a flow of constant disk height. Therefore, once certain properties are computed in one flow model, it would be valid for other models also, provided that the unique relations of polytropic index is maintained.

In §3.3, we analytically showed how the properties of centrifugal pressure supported boundary layer (CENBOL) control the observed spectral behaviour and the outflow rate of a black hole candidate. We computed that outflow rate is strongly dependent on the inflow parameters. We showed analytically that in the hard state when the shocks are strong, the outflow rate is small but significant while in the very soft state when the shocks disappear due to collapse of post-shock pressure, the outflow rate is negligible. Similar behaviour is obtained in both the adiabatic and isothermal flow. In the intermediate strength, the outflow rate is highest which monotonically increases for gradual increase of angular momentum. We also presented some interesting results obtained from a realistic two-component flow (TCAF) model. TCAF consisting of Keplerian and sub-Keplerian component produces a significant amount of outflow. We showed that as the Keplerian rate is raised, the outflow rate is decreased as the compression ratio approaches unity. When the Keplerian rate is increased the supply of soft-photon is also increased which immediately cools down the post-shock region by inverse Comptonisation process and shock disappears. This reduces the thermal pressure drive and the resulting outflow rate would be negligible.

In §3.4, we discussed various possible scenarios for the quasi-periodic ejection of massive bullets in SS 433 system. We mentioned that the shock oscillation due to inherent unsteady accretion solution may be one possible mechanism for bullet creation because of it's generic nature. However, intense magnetic tension of the toroidal flux tubes could be responsible for the occasional flaring events.

We demonstrated the dissipative polytropic accretion flow system in Chapter 4 where we included various independent energy dissipative processes (heating and cooling) in succession. Accordingly, in §4.1, we began with a very difficult yet more realistic case of viscous polytropic flow. We presented a detail study of the parameter space for shock formation in presence of viscosity. We showed that the

accretion flow possesses two critical viscosity parameters that separate the region of parameter space into three distinct domains—in the first domain, the flow is Bondi type, the flow belongs to the second domain has multiple sonic points but Rankine-Hugoniot relations are not satisfied and finally when Rankine-Hugoniot relations hold (shock forms). We found that these critical viscosity parameters are mainly inflow parameter dependent—when the specific angular momentum at the inner sonic point increases, critical viscosity parameters decrease gradually. We pointed out that shocks, standing or oscillating, may form even for very little angular momentum at the inner sonic point when the viscosity parameters is sufficiently high. We showed explicit dependence of shock properties on the flow parameters. We pointed out that shock location is reduced with enhancement of viscosity parameter for a given inner sonic point which implies the increase of QPO frequency. This result is consistent with the observational result since high frequency QPO is detected when the spectral slope becomes soften whose origin is believed to be due to an increase of viscosity and accretion rate (CM00).

In §4.2, we studied the viscous accretion flow in presence of bremsstrahlung cooling. We mentioned that the Mach number of the flow significantly reduces due to viscosity as it tends to heat the flow whereas cooling usually decrease the flow temperature enhances Mach number. Therefore, heating and cooling processes strongly affect the flow properties, namely, transonic property, shock formation and it's strength etc. We presented classification of parameter space in terms of presence of multiple sonic points and shock formation separately. We discovered a completely new multiple valued Mach number solution that connects matter from the outer edge of the disk to the black hole horizon. We showed that cooling can compensate the heating effect on the topological properties only to a certain extent. But, for high viscosity limit, no matter how much cooling is used, parameter space shrinks. We identified the critical cooling factor that separates the parameter space into closed region, one with a closed and the other with an open topology. It is believed that flow crossing through the sonic points are usually sub-Keplerian in nature. However, we found that super-Keplerian flow can even pass through the sonic point when the flow is strongly cooled.

In §4.3, we presented the solutions of viscous accretion flow when both bremsstrahlung and synchrotron cooling are effective into the flow. We mentioned that while estimating the stray magnetic field inside the disk one should equate the magnetic energy density with a few percentage of the gas pressure at equipartition for studying the transonic properties of the accreted flow. We found that shock forms in presence synchrotron cooling and it's location recedes away from the black hole horizon when synchrotron cooling is increased for a given inner sonic point. We also computed the strength of the shock and showed that it strongly depends on the synchrotron cooling factor.

Let us look into the works developed in this Thesis in proper perspective. First of all, it is abundantly clear that the Keplerian disk is unable to explain most of the observational facts. For instance, Smith et al. (2001a, 2001b) have concluded that they definitely required two components in the accretion flow to explain the observational features of a half a dozen of black holes. Therefore the study of the properties of the sub-Keplerian component becomes as essesntial, and perhaps more essential than the Keplerian component itself. Second, the Quasi-Periodic Oscillation (QPO) of the black hole candidates showed so much of power-modulation that simple models which involve vibrations of seismological activities inside the disk will not do. A Keplerian disk is never able to explain such QPO activities. The power in the variable component definitely require a dynamically oscillating component of the disk it self which we claim to the CENBOL. Thus the presence of CENBOL is required even to explain short-timescale variations. Third, before the development of the present picture, it was assumed that the whole disk was participating in forming jets and outflows. All types of self-similar models were developed to produce jets. However, observations showed that the jets are produced mostly if hard spectral states, and the jet activity is strongly related to the activities of the hard X-rays which are also produced at the CENBOL. So, it was natural to assume that CENBOL IS the origin of the jets and outflows and not the whole disk.

The work developed in the thesis thus addresses very important and relevant issues of modern day black hole astrophysics. In future this work is to be evolved by more self-consistent work including the magnetic fields and radiative transfer and perhaps some numerical simulations of such disks.

Chapter 6

APPENDIX

The procedure of obtaining an analytical solution of a quartic equation,

$$q^4 + b_1 q^3 + b_2 q^2 + b_3 q + b_4 = 0 \qquad A.1$$

is to first obtain a solution of the following cubic equation:

$$p^3 + a_1 p^2 + a_2 p + a_3 = 0, \qquad A.2$$

where,
$a_1 = -b_2$, $a_2 = b_1 b_3 - 4b_4$, and $a_3 = 4b_2 b_4 - b_3^2 - b_1^2 b_4$.
Let,

$Q = \frac{3a_2 - a_1^2}{9}$, $R = \frac{9a_1 a_2 - 27a_3 - 2a_1^3}{54}$,

$S = \sqrt[3]{R + \sqrt{Q^3 + R^2}}$, $T = \sqrt[3]{R - \sqrt{Q^3 + R^2}}$.

The *discriminant* is defined as

$$D = Q^3 + R^2. \qquad A.3$$

If $D > 0$, one root is real and two roots are complex conjugate. In this case, the real solution is,

$$p_1 = S + T - \frac{1}{3}a_1. \qquad A.4$$

If $D = 0$, all roots are real and at least two are equal.
If $D < 0$, all roots are real and unequal. They are:

$$p_1 = 2\sqrt{-Q}\cos(\frac{1}{3}\theta) - \frac{1}{3}a_1, \qquad A.5$$

$$p_2 = 2\sqrt{-Q}\cos(\frac{1}{3}\theta + 120^o) - \frac{1}{3}a_1, \qquad A.6$$

and,

$$p_3 = 2\sqrt{-Q}\cos(\frac{1}{3}\theta + 240^o) - \frac{1}{3}a_1, \qquad A.7$$

where, $\cos\theta = R/\sqrt{-Q}$.

One can now write a quadratic equation using any one of the real solutions of the cubic equation (see, Spiegel, 1968) as follows:

$$z^2 + \frac{1}{2}\{b_1 \pm \sqrt{b_1^2 - 4b_2 + 4p_1}\}z + \frac{1}{2}\{p_1 \mp \sqrt{p_1^2 - 4b_4}\} = 0. \qquad A.8$$

This is a quadratic equation which can be solved easily. Since we applied this procedure both of the sonic points and shocks, we denoted quantities like, D,Q and R by D_c,Q_c and R_c for sonic (critical) points and D_s,Q_s and R_s for shocks respectively.

Bibliography

Abramowitz M., and Stegun I. A., *Hand book of Mathematical Functions*, Dover Publications, INC., New York 1970.

Abramowicz, M. A., Czerny, B., Lasota, J. P., and Szuszkiewicz, E., *ApJ*, **332**, 646 (1988)

Bisnovatyi-Kogan, G. S. and Blinnikov, S. I., *Pisma Astron. Zh.*, **2**, 489 (1976)

Bisnovatyi-Kogan, G. S., *Observational Evidence for Black Holes in the Universe*, Ed. S. K. Chakrabarti (Kluwer Scientific Publ: Holland), 1 (1998)

Bondi, H., *MNRAS*, **112**, 195 (1952)

Balbus, S. A. and Hawley. J. F, *ApJ*, **376**, 214 (1991)

Chakrabarti, S. K., *ApJ*, **288**, 1 (1985)

Chakrabarti, S. K., *Accretion Processes in Astrophysics*, J. Audouze and J. Tran Thanh Van (Editions Frontieres, Paris, (1986a)

Chakrabarti, S. K., *ApJ*, **303**, 582 (1986b)

Chakrabarti, S. K. and Jin, L. and Arnett, W. D., *ApJ*, **313**, 674 (1987)

Chakrabarti, S. K., *Big bang, Active galactic Nuclei and Supernovae*, eds. S. Hayakawa and K. Sato (Universal Academy Press, Inc., Tokyo, (1988a) [C88a]

Chakrabarti, S. K., *ApJ*, **324**, 391 (1988b)[C88b]

Chakrabarti, S. K., *ApJ*, **347**, 365 (1989a) [C89a]

Chakrabarti, S. K., *MNRAS*, **240**, 7 (1989b)[C89b]

Chakrabarti, S. K., *Theory of Transonic Astrophysical Flows*, World Scientific: Singapore, (1990a) [C90a]

Chakrabarti, S. K., *MNRAS*, **243**, 610 (1990b)[C90b]

Chakrabarti, S. K., *ApJ*, **362**, 406 (1990c)

Chakrabarti, S. K., *MNRAS*, **259**, 410 (1992)

Chakrabarti, S. K. and Molteni, D., *ApJ*, **417**, 672 (1993)

Chakrabarti, S. K. and Molteni, D., *MNRAS*, **272**, 80 (1995)

Chakrabarti, S. K. and Titarchuk, L.G., *ApJ*, **455**, 623 (1995)[CT95]

Chakrabarti, S. K., *ApJ*, **464**, 664 (1996a)[C96a]

Chakrabarti, S. K., *MNRAS*, **283**, 325 (1996b)[C96b]

Chakrabarti, S., K., in *Observational Evidence for Black Holes in the Universe* Ed. S. K. Chakrabarti (Kluwer Scientific Publ: Holland), (1998)

Chakrabarti, S. K., *A&A*, **351**, 185 (1999) [C99]

Chakrabarti, S. K. and Manickam, S.G., *ApJ*, **531**, L41 (2000)[CM00]

Chakrabarti, S. K. and Das, S., *MNRAS*, **327**, 808 (2001)

Chakrabarti, S.K., Goldoni, P., Wiita, P. J., Nandi, A. and Das, S., *ApJ*, **576**,45L (2002)

Chakrabarti, S. K. and Das, S., *MNRAS*, **349**, 649 (2004)

Chandrasekhar, S. 'The stability of non-dissipative couette flow in hydromagnetics', *Proc. Nat. Acad. Sci. USA*, **46**, 253 (1960)

Das, T. and Chakrabarti, S. K., *Class. Quant. Grav.*, **16**, 3879 (1999)

Das, S., Chattopadhyay, I. and Chakrabarti, S. K., *ApJ*, **557**, 983 (2001) [DCC01]

Das, S., Chattopadhyay, I., Nandi, A. and Chakrabarti, S.K., *A&A*, **379**, 683 (2001)[DCNC01]

Das, S. and Chakrabarti, S. K., *IJMPD*, **13**, 1955 (2004)

Ebisawa, K., Titarchuk, L. and Chakrabarti, S. K., *PASJ*, **48**, 59 (1996)

Frank, J., King, A. R. and Raine, D. J., *Accretion power in astrophysics*, 3rd ed., Cambridge University Press, (2002)

Fricke, K. *A&A*, **1**, 388 (1969)

Hoyel, F. and Lyttleton, R. A., *Proc. Comp, Phil. Soc.*, **35**, 405 (1939)

Holzer, T. E. and Axford, W. I., *ARA & A*, **8**, 31 (1970)

Hjellming, R. and Johnston, S., *ApJ*, **246**, L141 (1981)

Jenison, R. C. and Dasgupta, M. K., *Nature*, **172**, 996 (1953)

Landau, L. D., and Lifshitz, E. D., *Fluid Mechanics* (New York : Pergamon) (1959)

Langer, S. H., Chanmugam, G., and Shaviv, G., *ApJ*, **258**, 289 (1982)

Lanzafame, G., Molteni, D. and Chakrabarti, S. K., *MNRAS*, **299**, 799 (1998)

Lanza, A., *MNRAS*, **299**, 799 (1992)

Lynden-Bell, D., *Phys. Scripta*, **17**, 185 (1978)

Lynden-Bell, D., *Nature*, **223**, 690 (1969)

Matsumoto, R., Kato, S., Fukue, J. and Okazaki, A. T., *PASJ*, **36**, 7 (1984)

Mirabel, I. F. and Rodriguez, L. F., *Nature*, **371**, 46 (1994)

Miller et al., *ApJ*, **566**, 358 (2002)

Molteni, D., Lanzafame and Chakrabarti, *ApJ*, **425**, 161 (1994)

Molteni, D., Sponholz, H. and Chakrabarti, S. K., *ApJ*, **457**, 805 (1996)[MSC96]

Molteni, D., Gerardi, G. and Chakrabarti, S. K., *ApJ*, **436**, 249 (1994)

Nandi, A., Chakrabarti, S. K., Vadawale, S., & Rao, A. R., *A&A*, **380**, 245 (2001)

Novikov, I. D. and Thorne, K. S., *Black Hole Astrophysics, in Black Holes* edited by Dewitt, C. and Dewitt, B., (Gordon and Breach New York, New York, 1973)

Paczyński, B. and Wiita, P. J., *A&A*, **88**, 23 (1980)[PW80]

Paczyński, B., *Astron. Gessels. Mitteilungen*, **57**, 27 (1982)

Prendergast, K. H. and Burbridge, G. R., *ApJ*, **151**, L83 (1968)

Pringle, J. E. and Rees, M. J., *Astron. Astrophys.*, **21**, 1 (1972)

Ryu, D., Chakrabarti and Molteni, D., *ApJ*, **474**, 378 (1997)

Sakurai, T., *A&A*, **152**, 121 (1985)

Schalinski, C. J., Johnston, K. J., Witzel, A., Spencer, R. E., Fiedler, R., Waltman, E., Pooley, G. G., Hjellming, R. and Molnar, L. A., *ApJ*, **447**, 752 (1995)

Smith, D. M., Heindl, W. A., Markwardt, C. B. and Swank, J. H., *ApJ*, **554**, L41 (2001b)

Shapiro, S. L. and Teukolsky, S. A., *Black Holes, White Dwarfs and Neutron Stars: The Physics of Compact Objects*, (A Wiley-Interscience Publication, New York, 1983)

Shapiro, S.L., *ApJ*, **185**, 69S (1973)

Shakura, N. I. and Sunyaev, R. A., *A&A*, **24**, 337 (1973)[SS73]

Shakura, N. I., *Astron. Zhur.*, **49**, 921 (1972)

Safi-Harb, S., and Kotani, T. in Proc. *4th Microquasar Workshop*, eds. Ph. Dourouchaux, Y. Fuchs, and J. Rodriguez (Kolkata: CSP), 279 (2002)

Smith, D. M., Heindl, W. A. and Swank, J. H., *ApJ*, **569**, 362 (2001a)

Tanaka, Y. and Lewin, W. H. G., in *X-ray Binaries*, eds. Lewin., W. H. G., Jan Van Paradijs, and van den Heuvel, **Cambridge University Press**, 166 (1985)

Velikhov, E. P., *Stability of an ideally conducting liquid flowing between cylinders rotating in a magnetic field, Sov. Phys. JETP.*, **338**, 957 (1959)

Watson, M. G., Stewart, G. C., Brinkmann, W. and King, A. R., *MNRAS*, **222**, 261 (1986)

Wiita, P., *ApJ*, **256**, 666 (1982)

THE ASTROPHYSICAL JOURNAL, 557:983–989, 2001 August 20

STANDING SHOCKS AROUND BLACK HOLES: AN ANALYTICAL STUDY

SANTABRATA DAS, INDRANIL CHATTOPADHYAY, AND SANDIP K. CHAKRABARTI[1]
S. N. Bose National Centre for Basic Sciences, JD Block, Salt Lake City, Calcutta 700098, India; sbdas@boson.bose.res.in, indra@boson.bose.res.in, chakraba@boson.bose.res.in
Received 2001 February 6; accepted 2001 April 25

ABSTRACT

We compute locations of sonic points and standing shock waves in a thin, axisymmetric, adiabatic flow around a Schwarzschild black hole. We use a completely analytical method to achieve our goal. Our results are compared with those obtained numerically, and good agreement is seen. Our results prove the existence of shocks in centrifugal pressure–dominated flows. We indicate how our results can be used to obtain spectral properties and frequencies of shock oscillations, which may be directly related to the quasi-periodic oscillations of hard X-rays.

Subject headings: accretion, accretion disks — black hole physics — hydrodynamics — shock waves

1. INTRODUCTION

In recent years, the study of standing and oscillating shocks in accretion flows has become very important, since it is recognized that the spectral states of black holes, as well as quasi-periodic oscillations (QPOs) observed in light curves of black hole candidates, are directly related to the radiative transfer properties of a compact Comptonizing region close to a black hole (e.g., Chakrabarti & Titarchuk 1995, hereafter CT95; Ling et al. 1997; Chakrabarti & Manickam 2000; Muno, Morgan, & Remillard 1999; Feroci et al. 1999; Homan et al. 2001). These shocks have been studied very extensively in the literature (Chakrabarti 1989, hereafter C89; Chakrabarti 1990), and their properties have been verified by several independent groups of workers (Yang & Kafatos 1995; Nobuta & Hanawa 1994; Lu & Yuan 1997). If the standing shocks exist analytically for a given set of initial parameters, numerical simulations do find them (Chakrabarti & Molteni 1993; Molteni, Lanzafame, & Chakrabarti 1994; Ryu et al. 1995; Molteni, Ryu, & Chakrabarti 1996); otherwise, the shock would be oscillating (Molteni, Sponholz, & Chakrabarti 1996; Ryu, Chakrabarti, & Molteni 1997), causing QPOs in the X-rays emitted from the postshock region. Furthermore, it has been observed that in at least some of the black hole candidates, such as GRS 1915+105, outflows are produced from the same region that emits the Comptonized photons (Fender et al. 2000; Dhawan, Mirabel, & Rodriguez 2000), i.e., the postshock region or the centrifugal barrier–dominated region, according to our present understanding of the flow solutions.

It is therefore pertinent to ask whether the properties of the shocks, such as location, strength, compression ratio, and so on, could be understood solely analytically. The solutions obtained thus far by Chakrabarti and collaborators and other groups have always resorted to numerical means. Roughly, the method has been as follows: For a given set of parameters (such as the specific energy and specific angular momentum), it is first determined whether the flow allows more than one X-type sonic point (C89). This is because, at the horizon, matter must have a velocity equal to the velocity of light and, from causality arguments, the flow must be supersonic. Thus, once the flow becomes supersonic through the outermost sonic point and forms a shock (i.e., jumps to a subsonic branch), it must pass through the inner sonic point to become supersonic at the horizon. The next question is whether the specific entropy at the inner sonic point is higher compared with that at the outer sonic point. This is because, at the shock, entropy must be generated and the postshock flow that passes through the inner sonic must have higher entropy. The final and most important question is whether all the Rankine-Hugoniot conditions (also known as the shock conditions) are satisfied somewhere between the two X-type sonic points. The three Rankine-Hugoniot conditions could be combined to obtain a combination of Mach numbers (shock invariant). C89 obtained this expression, which is continuous across the shock, and used it to obtain the shock location via an iterative technique.

In the present paper we follow the same philosophy but obtain the shock locations analytically. There were two motivations for this. First, from the theoretical point of view it is challenging to find solutions of a large number of nonlinear equations that must satisfy the number of conditions mentioned above. Second, from the observer's point of view, any observation that could require standing shock waves could be explained using more fundamental parameters, such as specific energy and angular momentum or, even better, accretion rates of Keplerian and sub-Keplerian flows, as in the two-component flow solution of CT95. Analytical work also provides insight into why the shocks form in the first place. The boundary of the parameter space for shock formation is also obtained by analytical means. These findings are important, as they can tell us when QPOs may or may not be seen. These details will be discussed in a future paper.

In the next section, we present the model equations and shock conditions. In § 3, we present the sonic point analysis and include the expression for the shock invariant (C89) for the sake of completeness. In § 4, we present the analytical expressions for the sonic points and discuss how the parameter space is divided into regions of one or three sonic points. In § 5, we present the expression for the shock locations and again divide the parameter space into regions that may or may not have shocks. We also compare our solu-

[1] Honorary Scientist, Centre for Space Physics, 114/v/1A Raja S. C. Mullick Road, Calcutta 700047, India.

tions with numerical work. In § 6, we discuss some of the astrophysical implications of our solutions, and finally, in § 7 we make concluding remarks.

2. MODEL EQUATIONS AND SHOCK CONDITIONS

We start with a thin, axisymmetric, inviscid steady flow that is in equilibrium in a direction transverse to the flow. The model equations that govern the motion of matter accreting onto a black hole are as follows (C89).

1. The radial momentum equation:

$$\mathcal{V}\frac{d\mathcal{V}}{dx}+\frac{1}{\rho}\frac{dP}{dx}+\frac{\lambda^2}{x^3}+\frac{1}{2(x-1)^2}=0\,. \tag{1}$$

In a nonviscous flow, integration of this equation leads to the energy conservation equation:

$$\mathscr{E}=\frac{\mathcal{V}_e^2}{2}+\frac{a_e^2}{\gamma-1}+\frac{\lambda^2}{2x^2}+g(x)\,, \tag{2}$$

where $g(x)$ is the pseudo-Newtonian potential introduced by Paczyński & Wiita (1980), which is given by $g(x)=-\frac{1}{2}(x-1)^{-1}$. Here ρ is the mass density, P is the isotropic pressure, $\mathcal{V}_e$ and a_e are the nondimensional radial and sound velocities measured in units of the velocity of light c, x is the nondimensional radial distance measured in units of the Schwarzschild radius $r_g=2GM/c^2$ with M the mass of the black hole and G the gravitational constant, γ is the adiabatic index of the flow, and $P=K\rho^\gamma$ is assumed to be the equation of state. K is the measure of the specific entropy, which is constant except at the shock location, where local turbulence generates some entropy, enabling the flow to pass through the inner sonic point. The subscript e refers to the quantities measured on the equatorial plane.

2. The continuity equation,

$$\frac{d}{dx(\mathcal{V}_e\rho xh)}=0\,, \tag{3}$$

is integrated to obtain the mass conservation equation:

$$\dot{M}=\mathcal{V}_e\rho xh\,, \tag{4}$$

where h is the half-thickness of the flow at radial coordinate x. Here $\dot{M}$ is the mass accretion rate apart from a geometric constant. If we assume that the flow is in hydrostatic equilibrium in the transverse direction, then the vertical component of gravitational force balances the pressure gradient force. Hence, the expression for the half-thickness of the disk is given by (C89),

$$h(x)=a_e x^{1/2}(x-1)\,. \tag{5}$$

We write the mass flux conservation equation in terms of $\mathcal{V}_e$, and the sound speed on the equatorial plane, $a_e=(\gamma P/\rho)^{1/2}$, in the following way:

$$\dot{\mathscr{M}}=\mathcal{V}_e a_e^q x^{3/2}(x-1)=\mathcal{V}_e a_e^q f(x)\,, \tag{4a}$$

where $q=\gamma+1/\gamma-1$ and $f(x)=x^{3/2}(x-1)$. The shock conditions we employ here are (C89)

The continuity of energy flux across the shock,

$$\mathscr{E}_+=\mathscr{E}_-\,. \tag{6}$$

The continuity of mass flux across the shock,

$$\dot{M}_+=\dot{M}_-\,; \tag{7}$$

and finally, the momentum balance condition,

$$W_+ + \Sigma_+ \mathcal{V}_{e+}^2 = W_- + \Sigma_- \mathcal{V}_{e-}^2\,. \tag{8}$$

Here subscripts " $-$ " and " $+$ " refer, respectively, to quantities before and after the shock. A shock satisfying these conditions is termed a Rankine-Hugoniot shock (Landau & Lifshitz 1959). Here, W and Σ denote the pressure and the density integrated in the vertical direction (see, e.g., Matsumoto et al. 1984); that is,

$$\Sigma=\int_{-h}^{h}\rho\,dz=2\rho_e I_n h,\quad W=\int_{-h}^{h}P\,dz=2P_e I_{n+1}h\,, \tag{9}$$

where $I_n=(2^n n!)^2/(2n+1)!$ and n is the polytropic index defined previously. In the subsequent analysis, we drop the subscript e if no confusion arises in doing so.

3. SONIC POINT ANALYSIS AND SHOCK INVARIANTS

In order to have a shock, the flow must be supersonic, i.e., the stationary flow must pass from a subsonic flow to a supersonic flow. Discussions in this section are based on earlier works (see C89, Chakrabarti 1990).

3.1. *Sonic Point Conditions*

From the radial momentum and continuity equations (eqs. [1] and [3]), we derive the sonic point condition (or critical point condition) in the usual way (C89). The first derivative of the radial velocity with respect to radial distance is given by

$$\frac{d\mathcal{V}}{dx}=\frac{2a^2}{\gamma+1}\frac{d\ln f}{dx}-\frac{dG}{dx}\Big/\left[\mathcal{V}-\frac{2a^2}{(\gamma+1)\mathcal{V}}\right]. \tag{10}$$

Here $G(x)=\frac{1}{2}\lambda^2/x^2-\frac{1}{2}(x-1)^{-1}$ is the effective potential. Since the denominator must vanish at the sonic points, if the flow is assumed to be smooth everywhere, the numerator must vanish simultaneously. The vanishing of the denominator gives

$$\mathcal{V}_c^2(x_c)=2(\gamma+1)^{-1}a_c^2(x_c)\,. \tag{11}$$

The factor (which is unity only in isothermal flows) in front of $a_c^2(x_c)$ arises because the flow is assumed to be in vertical equilibrium. The vanishing of the numerator gives

$$a_c^2(x_c)=\frac{(\gamma+1)(x_c-1)}{x_c^2}\,\frac{[\lambda_K^2(x_c)-\lambda^2]}{5x_c-3}\,. \tag{12}$$

The subscript c denotes quantities at the critical points. Here λ_K is the Keplerian angular momentum, defined as $\lambda_K^2=\frac{1}{2}x_c^3/(x_c-1)^2$. It is to be noted that since the left-hand side of this equation is always positive, angular momentum at the sonic point must be sub-Keplerian, that is, $\lambda(x_c)<\lambda_K$ (see, e.g., Chakrabarti 1990 and references therein).

3.2. *Mach Number Relation at the Shock*

From the equations given in § 2, we now seek an invariant relation that must be satisfied at the shock (C89). We rewrite the condition of energy flux continuity (eq. [6]) and the pressure balance condition (eq. [8]) in terms of the Mach number $M=\mathcal{V}/a$ of the flow,

$$\frac{1}{2}M_+^2 a_+^2+\frac{a_+^2}{\gamma-1}=\frac{1}{2}M_-^2 a_-^2+\frac{a_-^2}{\gamma-1}\,, \tag{13}$$

$$\dot{\mathscr{M}}_+ = M_+ a^{\nu'}_+ f(x_s), \quad \dot{\mathscr{M}}_- = M_- a^{\nu'}_- f(x_s), \quad (14)$$

where $\nu' = 2\gamma/(\gamma - 1)$, and

$$\frac{a^{\nu}_+}{\dot{\mathscr{M}}_+}\left(\frac{2}{3\gamma - 1} + M^2_+\right) = \frac{a^{\nu}_-}{\dot{\mathscr{M}}_-}\left(\frac{2}{3\gamma - 1} + M^2_-\right), \quad (15)$$

where $\nu = (3\gamma - 1)/(\gamma - 1)$ and x_s is the location of the shock. From equations (13) through (15), one obtains the following equation relating the pre- and postshock Mach numbers of the flow at the shock (C89):

$$C = \frac{[M_+(3\gamma - 1) + (2/M_+)]^2}{2 + (\gamma - 1)M^2_+} = \frac{[M_-(3\gamma - 1) + (2/M_-)]^2}{2 + (\gamma - 1)M^2_-}. \quad (16)$$

The constant C is invariant across the shock. The Mach number of the flow just before and after the shock can be written in terms of C as

$$M^2_{\mp} = \frac{2(3\gamma - 1) - C \pm \sqrt{C^2 - 8C\gamma}}{(\gamma - 1)C - (3\gamma - 1)^2}. \quad (17)$$

The product of the Mach number is given by

$$M_+ M_- = -2/\sqrt{(3\gamma - 1)^2 - (\gamma - 1)C}. \quad (18)$$

4. ANALYTICAL EXPRESSION OF SONIC POINTS AND BEHAVIOR IN PARAMETER SPACE

To obtain shock locations, we first need to obtain the locations of the sonic points and ensure that at least two of them are X type (Chakrabarti 1990). In § 3.1 we presented the sonic point conditions. Using the definition $M = \vartheta/a$ of the Mach number and substituting $a^2_c(x_c)$ from equation (12) into equation (2), we obtain the following algebraic equation for x_c:

$$\mathscr{N}x^4_c - \mathscr{O}x^3_c + \mathscr{P}x^2_c - \mathscr{Q}x_c + \mathscr{R} = 0, \quad (19)$$

where $\mathscr{N} = 10\mathscr{E}$, $\mathscr{O} = 16\mathscr{E} + 2n - 3$, $\mathscr{P} = 6\mathscr{E} + \lambda^2(4n - 1) - 3$, $\mathscr{Q} = 8n\lambda^2$, $\mathscr{R} = (1 + 4n)\lambda^2$, and $n = (\gamma - 1)^{-1}$ is the polytropic index.

We solve this equation analytically (Abramowitz & Stegun 1970) and obtain the location of the sonic points. Details are given in the Appendix. For the purpose of critical or sonic points, D of the Appendix is denoted as D_c. The equation has four roots, and equation (A6) can be used to check whether all of them are complex (a pair of complex conjugates). At least two are real and two are complex, or all four are real. A necessary condition to form a shock wave is to have four real roots. Of course, only one would be inside the black hole, and the other three would be outside; out of these, for topological reasons, only two would be X type or saddle type, and the one in between must be either O or center type. This is determined by computing the derivative $d\vartheta/dx$ at the sonic point by using l'Hôpital's rule and checking whether they are real. For our purpose, two derivatives at each sonic point must be real and of opposite signs in order for the sonic point to be of X type or saddle type.

Figure 1 shows the division of the parameter space. Denoting the discriminant D (of the Appendix) by D_c, we find that the condition $D_c < 0$ is a necessary condition for having three sonic points. The boundary $D_c = 0$ separates this region, on which two sonic points merge and the third remains separate. Outside the region $D_c > 0$, only one sonic point is possible, and the other two roots are the complex conjugates of one another. The dashed curve in the middle represents the condition

$$\dot{\mathscr{M}}_o = \dot{\mathscr{M}}_i,$$

where $\dot{\mathscr{M}}_i$ and $\dot{\mathscr{M}}_o$ are the entropy accretion rates at the inner and outer sonic points, respectively. The region above it contains parameters with $\dot{\mathscr{M}}_i < \dot{\mathscr{M}}_o$, and the region below contains parameters with $\dot{\mathscr{M}}_i > \dot{\mathscr{M}}_o$. This latter region is suitable for shock formation in accretion flows.

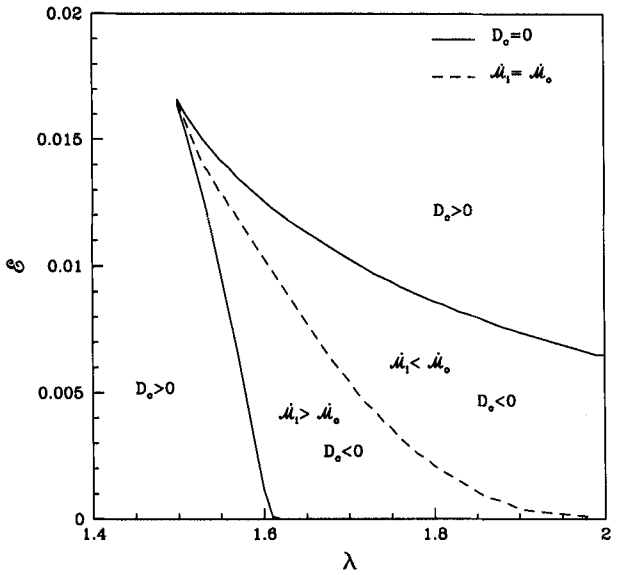

FIG. 1.—Division of the parameter space as spanned by the pair $(\mathscr{E}, \lambda)$ according to the number of sonic points. The solid curve represents $D_c = 0$, which divides the region into a $D_c > 0$ (one sonic point) and $D_c < 0$ (three sonic points) region. The plot is for $\gamma = 4/3$. For $\gamma \gtrsim 1.5$, D_c is always positive, suggesting that no shocks are possible in a flow with vertical equilibrium. The dashed curve further divides the region into two regions where the entropy accretion rate $\dot{\mathscr{M}}$ at the two saddle-type sonic points behave differently (the inner point is denoted by i and the outer point by o).

In passing, we wish to point out that from equation (10) one can easily show that locations where $dM/dx = 0$ exactly coincide with the sonic points of the flow. Thus, the number of extrema of $M = M(x)$ is the same as that of the sonic points. Hence, the division in Figure 1 could give an idea about the behavior of $M = M(x)$ as well.

5. ANALYTICAL EXPRESSION FOR SHOCK LOCATION AND BEHAVIOR IN PARAMETER SPACE

A black hole accretion flow, being transonic, must satisfy two sonic point conditions at the cost of one extra unknown, namely, the sonic point. Because of this extra condition, out of the three constants of the motion, namely, $\mathscr{E}$, $\dot{M}$, and λ, only two are to be supplied as free parameters. We used past experience derived from numerical methods to compute shock locations where we found that only one of the shocks, x_{s3} (C89 notation), is stable. Accordingly, our procedure as delineated below attempts to compute only this location.

The flow will have a shock only at the point where the shock-invariant condition is satisfied. Simplifying the

shock-invariant relation (eq. [16]), we obtain

$$2(\gamma-1)(M_+^2+M_-^2)-[(3\gamma-1)^2-2(3\gamma-1)\times(\gamma-1)]M_+^2M_-^2+4=0\,. \quad (20)$$

We consider a relativistic flow with $\gamma=4/3$, so that the polytropic index $n=3$. Then, from equation (20), we obtain

$$2(M_+^2+M_-^2)-21M_+^2M_-^2+12=0\,. \quad (21)$$

We now expand the postshock Mach number M_+^2 by a polynomial that must satisfy the following conditions:

1. The derivative dM/dx is zero at the central O-type sonic point. This is a general property of the flow (see discussion at the end of the previous section).
2. The Mach number M_+ at the location of the middle sonic point matches that derived from the approximate analytical solution obtained using the energy equation (eqs. [2] and [A4]).
3. The solution passes through the position where $dM/dx=\infty$ and a good guess for this location (say, from the location of the sonic points) is known.

Similarly, we expand M_-^2 by a polynomial that must satisfy the following conditions:

1. The derivative dM/dx is zero at the outer sonic point (the location of which has already been determined above). This is a general condition (see discussion at the end of the previous section).
2. The Mach number at the outer sonic point matches the analytical value obtained from the sonic point condition (eq. [11]).
3. The Mach number M_- at the location of the middle sonic point matches the analytical value derived from the approximate analytical solution obtained using the energy equation (eqs. [2] and [A4]).

Keeping in mind that an algebraic equation that is beyond quartic cannot be solved analytically (see Abramowitz & Stegun 1970), we expand $M_\pm^2$ as a quadratic equation so that equation (21) may become quartic. We will show, a posteriori, that such an assumption introduces a very small and tolerable error in our computation.

If x_s denotes the shock location, we assume

$$M_\pm^2=\sum_{q=0}^{2}A_{[q,\pm]}x_s^q\,, \quad (22)$$

where the $A_{[q,\pm]}$ are constant coefficients to be determined from the conditions mentioned above. We find them to be

$$A_{[2,+]}=\frac{1-(M_+^2)_{\rm mid}}{(x_{\rm inf}-x_{\rm mid})^2}\,,\quad A_{[2,-]}=\frac{(M_-^2)_{\rm mid}-1}{(x_{\rm out}-x_{\rm mid})^2}\,,$$

$$A_{[1,+]}=-2x_{\rm mid}A_{[2,+]},\quad A_{[1,-]}=-2x_{\rm mid}A_{[2,-]},$$

$$A_{[0,+]}=1+(2x_{\rm mid}x_{\rm inf}-x_{\rm inf}^2)A_{[2,+]}\,,$$

$$A_{[0,-]}=1+x_{\rm out}^2A_{[2,-]}\,,$$

where $x_{\rm mid}$, $x_{\rm inf}$, and $x_{\rm out}$ are, respectively, the middle (O-type) sonic point, the position where the first derivative of the Mach number is infinity, and the outer sonic point.

We now substitute the above expression (eq. [22]) for the Mach number in the Mach invariant relation (eq. [21]) to obtain the following algebraic equation:

$$\mathscr{A}x_s^4+\mathscr{B}x_s^3+\mathscr{C}x_s^2+\mathscr{D}x_s+\mathscr{F}=0\,, \quad (23)$$

where

$$\mathscr{Y}=(3\gamma-1)(\gamma+1)\,,$$

$$\mathscr{Z}=2(\gamma-1)\,,$$

$$\mathscr{A}=\mathscr{Y}A_{[2,+]}A_{[2,-]}\,,$$

$$\mathscr{B}=\mathscr{Y}(A_{[1,+]}A_{[2,-]}+A_{[2,+]}A_{[1,-]})\,,$$

$$\mathscr{C}=\mathscr{Y}(A_{[0,+]}A_{[2,-]}+A_{[1,+]}A_{[1,-]}+A_{[2,+]}A_{[0,-]})-\mathscr{Z}(A_{[2,+]}+A_{[2,-]})\,,$$

$$\mathscr{D}=\mathscr{Y}(A_{[0,+]}A_{[1,-]}+A_{[1,+]}A_{[0,-]})-\mathscr{Z}(A_{[1,+]}+A_{[1,-]})\,,$$

$$\mathscr{F}=\mathscr{Y}A_{[0,+]}A_{[0,-]}-\mathscr{Z}(A_{[0,+]}+A_{[0,-]})-4\,.$$

We solve for x_s analytically using the same procedure as in § 4 (details are described in the Appendix). We denote the discriminant D by D_s, and Q- and R-values as Q_s and R_s, respectively, for our discussion of the parameter-space behavior of shocks.

In Figure 2 we redraw the parameter space as in Figure 1 but consider the formation of shocks alone. We find that $Q_s>0$ produces no shock from above, and $Q_s=0$ with $R_s\neq 0$ gives the boundary of the weakest shock (shocks with unit compression ratio). This boundary, although obtained using our approximate analytical method, generally coincides with the dashed curve of Figure 1. The edge of the boundary is obtained with an extra condition $R_s=0$. Thus, R_s progressively decreases toward the edge along the dashed curve. This edge (denoted by $D_s=R_s=0$) ought to have coincided with the cusp of the $D_c=0$ curve drawn for the sonic point (see also Fig. 1), had the analytical method been exact. A small shift is the evidence that a small error is present at this corner of the parameter space. We also provide the region of the oscillating shocks ($Q_s<0$ and $D_s<0$). Here the shock location is imaginary, and therefore the shock continuously oscillates back and forth, causing a

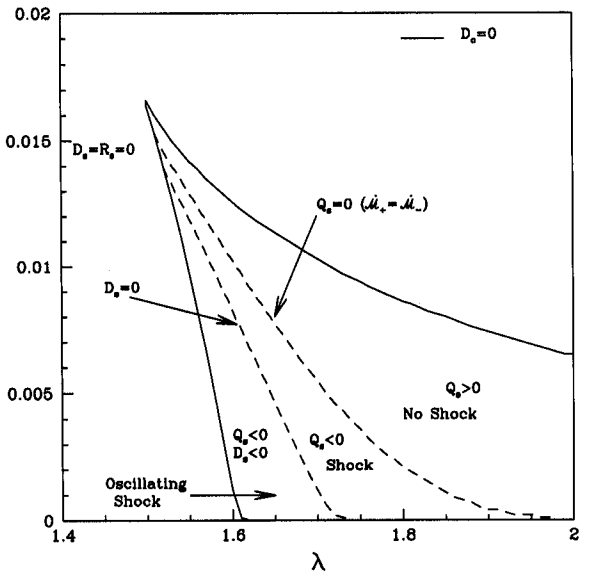

FIG. 2.—Division of the parameter space as spanned by the pair $(\mathscr{E},\lambda)$ according to whether shocks can form or not. The solid curve represents $D_c=0$, as in Fig. 1. The dashed curve ($D_s=0$) surrounds the region with shocks in accretion. When $D_s<0$ and yet there are three sonic points, the shocks are oscillatory, giving rise to quasi-periodically varying hard X-rays.

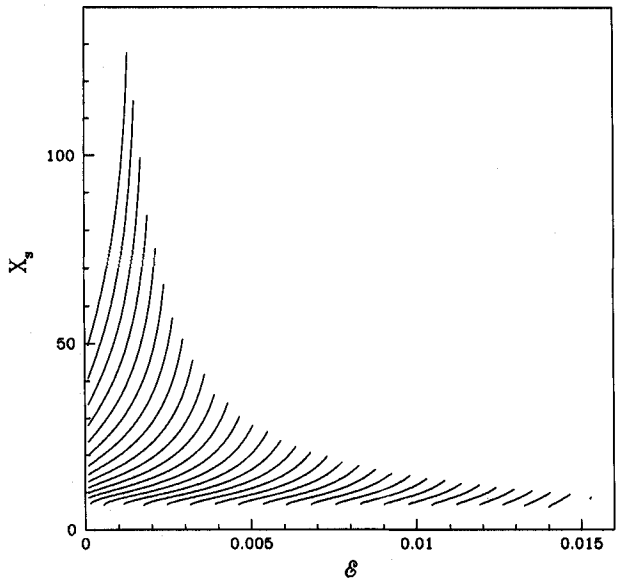

FIG. 3.—Variation of shock location (x_s along the y-axis) with specific energy ($\mathscr{E}$ along the x-axis) of the flow. Each curve is drawn for a specific angular momentum λ. From right to left, curves are drawn for $\lambda = 1.51$, 1.52, 1.53, ..., until 1.84. For a given specific energy $\mathscr{E}$, shock location increases with increasing centrifugal force (through λ). Similarly, for a given λ, shock location increases with energy.

very interesting astrophysical effect known as quasi-periodic oscillations, which are discussed in the next section. The boundary between the shock and the no-shock region from below is denoted by the dashed curve marked $D_s = 0$. Below the no-shock region, where the energy and angular momentum of the flow are very low, the flow has only one sonic point.

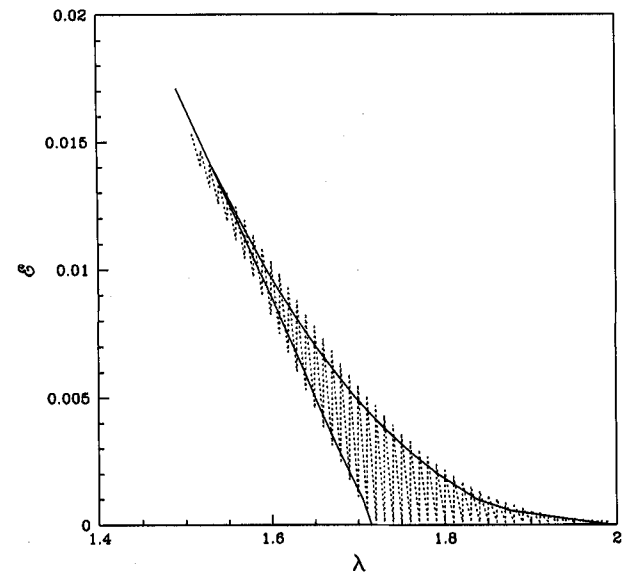

FIG. 4.—Comparison of the boundary of the parameter space in the ($\mathscr{E}$, λ)-plane using numerical and analytical methods. Except for the region near the cusp (*upper left*), the agreement is very strong.

In Figure 3, we draw shock location x_s (along the y-axis) as a function of energy (along the x-axis). Different curves are drawn for different specific angular momenta of the flow. The rightmost curve is for $\lambda = 1.51$ and the leftmost is for $\lambda = 1.84$, with the remainder drawn at intervals of $\lambda = 0.01$. As the angular momentum increases, the shock is located farther from the black hole. Comparing the locations from those obtained analytically, one may note that the same location is obtained for a specific angular momentum slightly more ($\sim 3\%$) than that used in the numerical method. We therefore believe that the results obtained are very reliable.

In Figure 4, we present a comparison of the boundary of the parameter space for which standing shocks may form as obtained from our analytical solution (*dotted region*) and by the numerical means (*solid curve*) existing in the literature (C89). The agreement is very good aside from a region near the cusp (as also noted while discussing Fig. 2, previously). Since very little parameter space is involved at this edge, we think that this small mismatch is tolerable.

6. ASTROPHYSICAL APPLICATIONS

Even though a black hole has no hard surface, it is remarkable that matter forms standing shocks around it in the same way a shock is formed when a supersonic flow encounters a hard boundary. Shock waves heat a gas and puff it up. This postshock region intercepts soft photons from the preshock matter, particularly from the Keplerian disk located on the equatorial plane (CT95). In this scenario, the nature of the Comptonized radiation depends on the amount of matter in the sub-Keplerian and Keplerian flow: if the intensity of soft photons is very low, they cannot cool the postshock region by an inverse Compton process, and the spectrum remains very hot. On the other hand, if the intensity of soft photons is very high (i.e., the Keplerian rate is large), they cool down the postshock region to the extent that the shock cannot be sustained (the pressure balance condition breaks down). This produces a soft-state spectrum with a hard tail due to bulk motion Comptonization (CT95). There are several models in the literature that perhaps explain the soft and hard states. However, no model other than that of CT95 explains the power-law hard tail in the soft state. Similarly, regarding the question of quasi-periodic oscillations, the shock oscillation model turns out to be a sufficiently satisfactory one (Chakrabarti & Manickam 2000).

When the parameters fall in the "no-shock" region of Figure 2, the shock location becomes imaginary. However, three sonic points are still present, and the entropy of the flow at the inner sonic point continues to be higher compared with that at the outer sonic point. In this case, the shock starts oscillating with a time period T_s comparable to the infall time from the postshock region (Ryu et al. 1997). Even when shocks form, if the infall timescale turns out to be comparable to the cooling time, then the resonance condition is satisfied (Molteni et al. 1996; Chakrabarti & Manickam 2000) and shocks oscillate on timescales of

$$T_s \sim x_s/v_s ,$$

where $v_s \sim 1/R\sqrt{x_s}$ is the infall velocity and R is the compression ratio at the shock (easily obtained analytically from our equations). Observed QPO frequencies are comparable to $1/T_s$.

When a mixture of Keplerian and sub-Keplerian matter is accreted, it is easy to obtain the parameters λ and $\mathscr{E}$ in terms of the Keplerian ($\dot{M}_d$) and sub-Keplerian ($\dot{M}_h$) accretion rates. Suppose the viscosity parameter is such that the flow deviates from a Keplerian disk at $x = x_K$, where its energy and angular momentum are $\mathscr{E}_d$ and λ_K, respectively. Further suppose that the sub-Keplerian halo has a constant energy $\mathscr{E} \sim 0 \sim \mathscr{E}_h$ and constant angular momentum λ_h; then the average angular momentum and energy of the transonic flow would be

$$\mathscr{E} = \frac{\dot{M}_d \mathscr{E}_d + \dot{M}_h \mathscr{E}_h}{\dot{M}_d + \dot{M}_h}, \quad \lambda = \frac{\dot{M}_d \lambda_d + \dot{M}_h \lambda_h}{\dot{M}_d + \dot{M}_h}.$$

It is easy to compute the shock location of the resultant flow using our formalism given above.

It should be noted from Figure 3 that shock solutions are allowed only if the specific energy is positive. In other words, if a flow deviates from a cool Keplerian disk on the equatorial plane, the flow cannot have shocks, since the specific energy in such a flow would be negative unless the flow is mixed with a substantial amount of sub-Keplerian matter with a positive energy. Typically, $\dot{M} \gg {}_h\dot{M}_d$, and even with a small energy, the specific energy of the mixture becomes positive, giving rise to shocks and (unbound) winds. In the case that magnetic dissipation is present, flow energy could increase to a positive value, and a solution with a shock would be allowed. The prospect of magnetic energy dissipation has been discussed several times in the literature (Shapiro 1973; Bisnovatyi-Kogan & Blinnikov 1976; Bisnovatyi-Kogan 1998). Briefly, since the magnetic field rises as $B_r \propto r^{-2}$ and, therefore, magnetic pressure rises as $P_{\rm mag} \propto r^{-4}$, while the gas pressure in the sub-Keplerian matter varies as $P_{\rm gas} \propto r^{-5/2}$, any magnetic field in excess of the equipartition value will escape from the disk buoyantly and may dissipate at the atmosphere, as in the case of the Sun. If the flow has specific energy $\mathscr{E}_h$ at, say, $r = 100r_g$, where the flow is in equipartition, then at the shock the energy will be at least 2^4 times larger if *all* the magnetic energy is dissipated into the flow. Thus, a basically free fall of matter of $\mathscr{E} \sim 10^{-4}$ would have an energy $\sim 10^{-3}$ and a shock at a few tens of Schwarzschild radii would be expected.

An accreting flow can intercept hard X-rays emitted at the inner edge. This preheating effect need not be negligible. For instance, a flow emitting isotropically with 6% efficiency will definitely intercept a fraction $\theta \sim \Theta_{\rm in}/4\pi$ of the radiation in between the shocked region and the Keplerian disk. Assuming $\theta \sim 0.1$, the energy deposition due to preheating is 0.6%, which is significant. This would energize Keplerian matter as well, and shocks in the sub-Keplerian flow would be expected.

7. CONCLUDING REMARKS

Thus far in the astrophysical literature, the existence of shocks in accretion flows has been indicated by steady and time-dependent numerical simulations. Study of these standing and oscillatory shocks in accretion flows has been shown to be of great importance. Here we have shown that the shocks can be studied completely analytically, at least in the case of thin, axisymmetric, inviscid flows with positive energy. We note that shock locations vary with flow parameters in a simple way—they form farther from a black hole when angular momentum is increased. This proves that they are mainly supported by centrifugal pressure.

Given that the shocks, especially the standing shocks, are ideal locations for a flow to be heated up, hard X-rays are produced from the postshock region after the soft photons are processed by the flow by an inverse Comptonization process. Thus, the spectral states and time-dependent behavior of the hard X-rays are directly related to the behavior of this region. For instance, CT95 computed steady state spectra using postshock regions as the source of hot Comptonizing electrons. Chakrabarti & Manickam (2000) have established that QPOs are a result of oscillations of this region, since only hard X-rays are seen to exhibit QPOs. We therefore believe that shocks should be an important ingredient in an accreting system. However, if the disk is cool and Keplerian far in its periphery, the specific energy must be negative. Therefore, the problem is not whether shocks should exist, but how to energize Keplerian matter as it becomes sub-Keplerian by, for example, magnetic energy dissipation or preheating. This work is in progress and will be reported separately.

From the observer's point of view, our work could also be useful because the steady spectra, QPO frequencies, and so on are, in principle, determined analytically from a few free physical parameters. In the future, we will focus our efforts on obtaining spectral properties and QPO behaviors more quantitatively.

This work was partly supported by grant SP/S2/K-14/98, funded by the Department of Science and Technology, India.

APPENDIX

METHOD FOR THE ANALYTICAL SOLUTION

The procedure for obtaining an analytical solution of a quartic equation,

$$q^4 + b_1 q^3 + b_2 q^2 + b_3 q + b_4 = 0, \tag{A1}$$

is to first obtain a solution of the following cubic equation:

$$p^3 + a_1 p^2 + a_2 p + a_3 = 0, \tag{A2}$$

where $a_1 = -b_2$, $a_2 = b_1 b_3 - 4b_4$, and $a_3 = 4b_2 b_4 - b_3^2 - b_1^2 b_4$.

Let

$$Q = \frac{3a_2 - a_1^2}{9}, \quad R = \frac{9a_1 a_2 - 27a_3 - 2a_1^3}{54}, \quad S = (R + \sqrt[3]{Q^3 + R^2})^{1/2}, \quad T = (R - \sqrt[3]{Q^3 + R^2})^{1/2}.$$

The discriminant is defined as

$$D = Q^3 + R^2 . \tag{A3}$$

If $D > 0$, one root is real and two roots are complex conjugates. In this case, the real solution is

$$p_1 = S + T - \tfrac{1}{3}a_1 . \tag{A4}$$

If $D = 0$, all roots are real and at least two are equal. If $D < 0$, all roots are real and unequal. They are

$$p_1 = 2\sqrt{-Q}\cos(\tfrac{1}{3}\theta) - \tfrac{1}{3}a_1, \qquad p_2 = 2\sqrt{-Q}\cos(\tfrac{1}{3}\theta + 120) - \tfrac{1}{3}a_1, \qquad p_3 = 2\sqrt{-Q}\cos(\tfrac{1}{3}\theta + 240) - \tfrac{1}{3}a_1 , \tag{A5}$$

where $\cos\theta = R/\sqrt{-Q}$.

One can now write a quadratic equation using any one of the real solutions of the cubic equation (see Abramowitz & Stegun 1970) as follows:

$$z^2 + \tfrac{1}{2}(b_1 \pm \sqrt{b_1^2 - 4b_2 + 4p_1})z + \tfrac{1}{2}(p_1 \mp \sqrt{p_1^2 - 4b_4}) = 0 . \tag{A6}$$

This quadratic equation can be solved easily. Since we applied this procedure to both the sonic points and shocks, we denoted quantities such as D, Q, and R by D_c, Q_c, and R_c for sonic (critical) points and D_s, Q_s, and R_s for shocks, respectively.

REFERENCES

Abramowitz, M., & Stegun, I. A. 1970, Handbook of Mathematical Functions (New York: Dover)
Bisnovatyi-Kogan, G. S. 1998 in Observational Evidence for Black Holes in the Universe, ed. S. K. Chakrabarti (Dordrecht: Kluwer), 1
Bisnovatyi-Kogan, G. S., & Blinnikov, S. I. 1976, AZh Pisma, 2, 489
Chakrabarti, S. K. 1989, ApJ, 347, 365 (C89)
———. 1990, Theory of Transonic Astrophysical Flows (Singapore: World Sci.)
Chakrabarti, S. K., & Manickam, S. G. 2000, ApJ, 531, L41
Chakrabarti, S. K., & Molteni, D. 1993, ApJ, 417, 671
Chakrabarti, S. K., & Titarchuk, L. G. 1995, ApJ, 455, 623 (CT95)
Dhawan, V., Mirabel, I. F., & Rodríguez, L. F. 2000, ApJ, 543, 373
Fender, R. P., et al. 2000, MNRAS, 312, 853
Feroci, M., et al. 1999, A&A, 351, 985
Homan, J., Wijnands, R., van der Klis, M., Belloni, T., van Paradijs, J., Klein-Wolt, M., Fender, R., & Méndez, M. 2001, ApJS, 132, 377
Landau, L. D., & Lifshitz, E. D. 1959, Fluid Mechanics (New York: Pergamon)
Ling, J. C., et al. 1997, ApJ, 484, 375
Lu, J. F., & Yuan, F. 1997, PASJ, 49, 525
Matsumoto, R., Kato, S., Fukue, J., & Okazaki, A. T. 1984, PASJ, 36, 71
Molteni, D., Lanzafame, G., & Chakrabarti, S. K. 1994, ApJ, 425, 161
Molteni, D., Ryu, D., & Chakrabarti, S. K. 1996, ApJ, 470, 460
Molteni, D., Sponholz, H., & Chakrabarti, S. K. 1996, ApJ, 457, 805
Muno, M. P., Morgan, E. H., & Remillard, R. A. 1999, ApJ, 527, 321
Nobuta, K., & Hanawa, T. 1994, PASJ, 46, 257
Paczyński, B., & Wiita, P. J. 1980, A&A, 88, 23
Ryu, D., Brown, G. L., Ostriker, J. P., & Loeb, A. 1995, ApJ, 452, 364
Ryu, D., Chakrabarti, S. K., & Molteni, D. 1997, ApJ, 474, 378
Shapiro, S. L. 1973, ApJ, 185, 69
Yang, R., & Kafatos, M. 1995, A&A, 295, 238

Mon. Not. R. Astron. Soc. 327, 808–812 (2001)

Model dependence of transonic properties of accretion flows around black holes

Sandip K. Chakrabarti[1]★† and Santabrata Das[1]★
[1]S. N. Bose National Centre for Basic Sciences, JD-Block, Sector III, Salt Lake, Kolkata 700098, India

Accepted 2001 June 14. Received 2001 June 14; in original form 2001 February 21

ABSTRACT

We analytically study how the behaviour of accretion flows changes when the flow model is varied. We study the transonic properties of the conical flow, a flow of constant height and a flow in vertical equilibrium, and show that all these models are basically identical, provided that the polytropic constant is suitably changed from one model to another. We show that this behaviour is extendible even when standing shocks are produced in the flow. The parameter space where shocks are produced remains roughly identical in all these models when the same transformation among the polytropic indices is used. We present applications of these findings.

Key words: accretion, accretion discs – black hole physics – hydrodynamics – shock waves.

1 INTRODUCTION

Fully self-consistent study of any astrophysical system is generally prohibitive. Very often, for simplicity, it is necessary to construct models which have all the salient features of the original problem. However, these models need not be unique. In the present paper we make a pedagogical review of three different models of rotating accretion flows, and show that even though they are based on fundamentally different assumptions, they have identical physical properties. What is more, results of one model could be obtained from the other by changing a *physical* parameter, namely the polytropic constant. In other words, all these models are *identical*.

Accretion disc physics has undergone major changes in the last 50 years. Bondi (1952) studied spherical accretion and found the existence of only one saddle-type sonic point in an adiabatic flow. Later, for the Keplerian disc model of Shakura & Sunyaev (1973) and the thick disc model of Paczyński & Wiita (1980) the disc solutions became more realistic, although none of them was transonic, i.e., none was passing through any sonic point. Meanwhile, Liang & Thompson (1980) generalized this work for a flow which included angular momentum, and discovered that there could be three sonic points. Matsumoto et al. (1984) tried to let the flow pass through the inner sonic point only, and found that the flow could pass through nodal type sonic points.

Chakrabarti (1989, 1990, hereafter C89 and C90 respectively) studied transonic properties of accretion flows which are conical in shape in the meridional plane ('Wedge-shaped Flow'), and also flows which are in vertical equilibrium. Subsequently, Chakrabarti & Molteni (1993) studied flows of constant height, and also verified by time-dependent numerical simulations that the flow indeed allows standing shocks in it. In a Bondi (1952) flow, to specify a solution one requires exactly one parameter, namely the specific energy $\mathcal{E}$ of the flow. This is in turn determined by the temperature of the flow at a large distance. In an inviscid, rotating axisymmetric accretion flow, one requires two parameters, namely specific energy $\mathcal{E}$ and specific angular momentum λ. Once they are specified, all the crucial properties of the flow, namely the locations of the sonic points, the shocks, as well as the complete global solution, are determined. C89 numerically studied the properties of the parameter space rather extensively, and divided the parameter space in terms of whether standing shocks can form or not. In the present paper we compare these models completely analytically and show, very interestingly, that one could easily 'map' one model on to another by suitably changing the polytropic index of the flow. In other words, we show that these models are roughly identical to one another as far as the transonic properties go.

In the next section we present a set of equations which govern the steady state flow in all the three models. In Section 3, we present the sonic point analysis, and provide the expressions for the energy of the flow in terms of the sonic points. We observe that these expressions are identical, provided that there is a unique relation among the polytropic indices of these model flows. In Section 4 we compare shock locations in all the three models. We also compare the parameter space which allows shock formation in these models with the regions obtained using purely numerical methods. In Section 5 we show that in fact if the relations between the polytropic indices are used, the shock locations in all these models are also roughly identical. Consequently, the apparently disjoint parameter spaces drawn with the same polytropic index overlap almost completely when the above-mentioned relations among polytropic indices is used. This remarkable behaviour

★E-mail: chakraba@boson.bose.res.in (SKC); sbdas@boson.bose.res.in (SD)

†Honorary scientist at the Centre for Space Physics, 114/v/1A Raja S.C. Mullick Road, Kolkata 700047, India.

shows an underlying unity in these apparently diverse models. Finally, in Section 6 we draw our conclusions.

2 MODEL EQUATIONS

As discussed in the introduction, we shall be concerned with three axisymmetric and inviscid models: (a) *Model H*: the flow has a constant height everywhere; (b) *Model C*: the flow cross-section in meridional plane is conical in shape, and (c) *Model V*: the flow is in equilibrium in the transverse direction. Fig. 1 shows a cartoon diagram of these three models. The filled circle at the centre corresponds to the black hole. The lightly shaded region of the disc corresponds to the pre-shock flow, while the heavily shaded region corresponds to the post-shock flow. We also assume that the distances are measured in units of $r_S = 2GM_{BH}/c^2$, where G is the gravitational constant, c is the velocity of light, and M_{BH} is the mass of the black hole. Velocities and angular momenta are measured in units of c and $cr_S = 2GM_{BH}/c$ respectively. In all the three models, the dimensionless energy conservation law can be written as

$$\mathcal{E} = \frac{\vartheta_e^2}{2} + \frac{a_e^2}{\gamma - 1} + \frac{\lambda^2}{2x^2} + g(x), \tag{1}$$

where $g(x)$ is the pseudo-Newtonian potential introduced by Paczyński & Wiita (1980) and is given by $g(x) = -\frac{1}{2(x-1)}$. Here ϑ_e and $a_e = \sqrt{\gamma p/\rho}$ are the non-dimensional radial and the sound velocities respectively, x is the non-dimensional radial distance, and the subscript e refers to the quantities measured on the equatorial plane. The flow has been chosen to be adiabatic with equation of state, $P = K\rho^\gamma$, where K is a constant which measures the entropy of the flow, and γ is the polytropic exponent. The energy equation is the integral form of the radial momentum balance equation.

The mass flux conservation equation, which comes directly from the continuity equation, depends on specific geometry of the models. Apart from a geometric constant, the conservation equation is given by,

$$\dot{M} = \vartheta_e \rho a^\zeta x^\beta (x-1)^\delta, \tag{2}$$

where β, ζ and δ are constants. For Model V (see C89), $\beta = 3/2$, $\zeta = 1$, $\delta = 1$. For Model C (see C90), $\beta = 2$, $\zeta = 0$, $\delta = 0$. For Model H (Chakrabarti 1992; Chakrabarti & Molteni 1993), $\beta = 1$, $\zeta = 0$, $\delta = 0$. Note that since the local disc height $h(x)$ depends on sound speed, $h(x) \sim a_e x^{1/2}(x-1)$, and so a factor of a_e^ζ is applicable for this model.

Figure 1. Cartoon diagram of three different models discussed in the text. In a constant-height flow (H), the disc thickness is constant (top). In a conical flow (C), the cross-section in the meridional plane is conical (middle). In a vertical equilibrium flow (V), matter is locally in vertical equilibrium at every point of the disc (bottom).

Although it is customary to deal with the conserved mass accretion rate of the flow, since we incorporate shock formation where entropy is increased, it is more convenient to rewrite the mass flux conservation equation in terms of ϑ_e and a_e in the following way:

$$\dot{\mathcal{M}} = \vartheta_e a_e^\alpha x^\beta (x-1)^\delta = \vartheta_e a_e^\alpha f(x), \tag{3}$$

where $\alpha = 2n + \zeta$, $\alpha = 2n$ and $\alpha = 2n$ for Models V, C and H respectively, and $f(x) = x^\beta (x-1)^\delta$. We shall use the phrase 'entropy-accretion rate' for the quantity $\dot{\mathcal{M}} = \dot{M}K^n\gamma^n$. In a flow without a shock this quantity remains constant, but in the presence of a shock it changes because of the generation of entropy.

3 SONIC POINT ANALYSIS AND RELATION BETWEEN MODELS

Since the flow is expected to be subsonic at a long distance and supersonic on the horizon, the flow must pass through sonic points. At the sonic point a few conditions are to be satisfied. They can be derived in the following way.

First, we differentiate the energy equation and the mass conservation equation, and eliminate da/dx from them to obtain

$$\frac{d\vartheta}{dx} = \frac{\frac{2na^2}{\alpha}\left[\frac{\beta' x - \beta}{x(x-1)}\right] - \frac{dG}{dx}}{\left(\vartheta - \frac{2na^2}{\alpha\vartheta}\right)}. \tag{4}$$

Here, $G(x) = \frac{\lambda^2}{2x^2} - \frac{1}{2(x-1)}$ is the effective potential and $\beta' = \beta + \delta$. Since the flow is assumed to be smooth everywhere if at any point of the flow denominator vanishes, the numerator must also vanish there. The vanishing of the denominator gives

$$\vartheta_c^2(x_c) = \frac{2n}{\alpha} a_c^2(x_c). \tag{5}$$

The vanishing of the numerator gives

$$a_c^2(x_c) = \frac{\alpha(x_c - 1)}{2nx_c^2} \frac{[\lambda_K^2(x_c) - \lambda^2]}{(\beta' x_c - \beta)}. \tag{6}$$

The subscript c denotes quantities at the critical points. Here, λ_K is the Keplerian angular momentum defined as $\lambda_K^2 = x_c^3/[2(x_c-1)^2]$. It is to be noted that since the square of the sound speed (equation 6) is always positive, the angular momentum at the sonic point must be sub-Keplerian, i.e., $\lambda < \lambda_K$. When the above expression for the velocity of sound is inserted in the expression for the specific energy, we get, for the *Vertical Equilibrium (V) Model*,

$$\mathcal{E}_V = \frac{n_V + 1}{5} \frac{x_c}{(x_c - 3/5)(x_c - 1)} - \left[\frac{4(n_V+1)}{5}\frac{(x_c-1)}{x_c - 3/5} - 1\right]\frac{\lambda^2}{2x_c^2} - \frac{1}{2(x_c-1)}; \tag{7a}$$

for *the Conical Flow (C) Model*,

$$\mathcal{E}_C = \frac{2n_C + 1}{8}\frac{x_c}{(x_c-1)^2} - \frac{2n_C - 1}{2}\frac{\lambda^2}{2x_c^2} - \frac{1}{2(x_c-1)}, \tag{7b}$$

and *for Constant Height Flow (H) Model*,

$$\mathcal{E}_H = \frac{2n_H + 1}{4}\frac{x_c}{(x_c-1)^2} - 2n_H\frac{\lambda^2}{2x_c^2} - \frac{1}{2(x_c-1)}. \tag{7c}$$

Here, we have used the subscripts V, C and H under specific energy

and polytropic index n to denote specific models. For a given angular momentum and at the same sonic point, the energy expression will be the same, provided that

$$\frac{2n_C+1}{8}=\frac{2n_H+1}{4}=\frac{n_V+1}{5}, \tag{8}$$

where we have used

$$(x_c-1)/(x_c-3/5)\sim 1 \tag{8a}$$

for Model V.

The relations in equation (8) are very important. If these relations are satisfied, then transonic properties of Model C with polytropic index n_C would be identical to those of Model H with index n_H and those of Model V with index n_V respectively.

4 SHOCK INVARIANTS AND LOCATIONS IN DIFFERENT MODELS

In between two sonic points, the flow can undergo a standing shock transition. For an inviscid flow, at the shock, a set of conditions are to be satisfied. These are known as the Rankine–Hugoniot conditions (Landau & Lifshitz 1959). These conditions are different for different models (C89; C90). For Model V, the shock conditions are as follows: the energy flux conservation equation,

$$\mathcal{E}_+=\mathcal{E}_-, \tag{9a}$$

the pressure balance condition,

$$W_+ + \Sigma_+ \vartheta_{e+}^2 = W_- + \Sigma_- \vartheta_{e-}^2, \tag{9b}$$

and the baryon flux conservation equation,

$$\dot{M}_+=\dot{M}_-, \tag{9c}$$

where subscripts '−' and '+' refer, respectively, to quantities before and after the shock. Here, W and Σ denote the pressure and the density, integrated in the vertical direction (see, e.g., Matsumoto et al. 1984), i.e.,

$$\Sigma=\int_{-h}^{h}\rho\,dz=2\rho_e I_n h, \tag{10a}$$

and

$$W=\int_{-h}^{h}P\,dz=2P_e I_{n+1}h, \tag{10b}$$

where, $I_n=\frac{(2^n n!)^2}{(2n+1)!}$, n being the polytropic index as defined previously.

For Models C and H, the shock conditions are as follows: the energy flux conservation equation,

$$\mathcal{E}_+=\mathcal{E}_-, \tag{11a}$$

the pressure balance condition,

$$P_+ + \rho_+ \vartheta_{e+}^2 = P_- + \rho_- \vartheta_{e-}^2, \tag{11b}$$

and the baryon number conservation equation,

$$\dot{M}_+=\dot{M}_-. \tag{11c}$$

The subscripts '−' and '+' have the same interpretation as before. Here, P and ρ denote the local pressure and the local density. In the subsequent analysis we drop the subscript e if no confusion arises in doing so.

The expressions for the conserved quantities could be combined to obtain the so-called Mach number relation, which must be satisfied at the shock. For Model V, we obtain this relation as follows. We rewrite the energy conservation equation (9a) and the pressure balance equation (9b) in terms of the Mach number $M=\vartheta/a$ of the flow:

$$\frac{1}{2}M_+^2a_+^2+\frac{a_+^2}{\gamma-1}=\frac{1}{2}M_-^2a_-^2+\frac{a_-^2}{\gamma-1}, \tag{12a}$$

$$\dot{\mathcal{M}}_+=M_+a_+^{\nu'}f(x_s), \tag{12b}$$

$$\dot{\mathcal{M}}_-=M_-a_-^{\nu'}f(x_s), \tag{12c}$$

where $\nu'=\frac{2\gamma}{\gamma-1}$, and

$$\frac{a_+^{\nu}}{\dot{\mathcal{M}}_+}\left(\frac{2}{3\gamma-1}+M_+^2\right)=\frac{a_-^{\nu}}{\dot{\mathcal{M}}_-}\left(\frac{2}{3\gamma-1}+M_-^2\right), \tag{12d}$$

where, $\nu=\frac{3\gamma-1}{\gamma-1}$, and x_s is the location of the shock. $f(x_s)=x_s^{3/2}(x_s-1)$ is the term in accretion rate which is explicitly a function of x and is the same both before and after the shock. From equations 12(a)–(d) one obtains the following equation relating the pre- and post-shock Mach numbers of the flow of Model V at the shock (C89a):

$$C=\frac{[M_+(3\gamma-1)+(2/M_+)]^2}{2+(\gamma-1)M_+^2}=\frac{[M_-(3\gamma-1)+(2/M_-)]^2}{2+(\gamma-1)M_-^2}. \tag{13}$$

The constant C is invariant across the shock. The Mach number of the flow just before and after the shock can be written down in terms of C as

$$M_\mp^2=\frac{2(3\gamma-1)-C\pm\sqrt{C^2-8C\gamma}}{(\gamma-1)C-(3\gamma-1)^2}. \tag{14}$$

The product of the Mach number is given by

$$M_+M_-=-\frac{2}{[(3\gamma-1)^2-(\gamma-1)C]^{1/2}}. \tag{15}$$

Similarly, one can obtain the Mach-number relations and the expression for Mach numbers for the other two models. The relation between the pre- and the post-shock Mach numbers of the flow at the shock for Models C and H are given by,

$$C=\frac{[\gamma M_+ + (1/M_+)]^2}{2+(\gamma-1)M_+^2}=\frac{[\gamma M_- + (1/M_-)]^2}{2+(\gamma-1)M_-^2}. \tag{16}$$

So far, in the literature, analytical shock studies have been carried out in models of vertical equilibrium (Das, Chattopadhyay & Chakrabarti 2001) by using the Mach-invariant relations (equation 13) when two parameters, namely the specific energy and the specific angular momentum, are given. We carried out the same analysis using equation (16) for Models H and C respectively, and obtained shock locations and parameter space boundaries for all the three models. Fig. 2 compares these results where plots of specific energy (y-axis) is given as function of specific angular momentum (x-axis). Solid boundaries mark regions for which standing shocks form in different models. Shaded regions are obtained from the analytical method (Das et al. 2001), and the results of these two methods roughly agree. We note that constant height flows occupy much a larger region than that of the conical or vertical equilibrium.

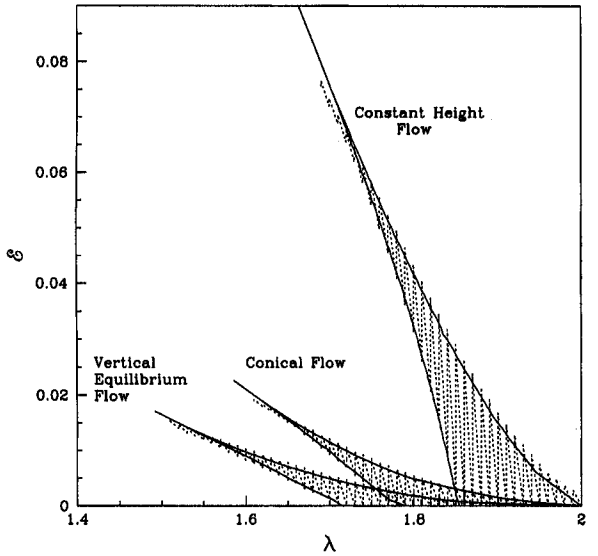

Figure 2. Comparison of the parameter space in three different models in which shocks form. $n_V = n_H = n_C = 3$ is chosen throughout. Solid boundaries are obtained using the numerical method, and shaded regions are obtained using the analytical method.

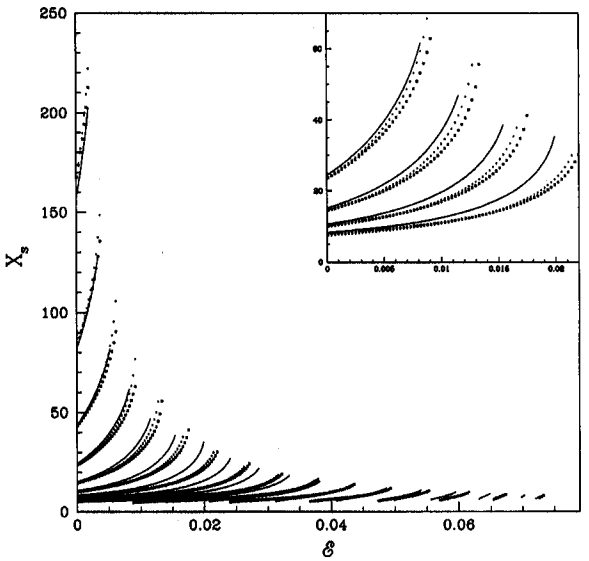

Figure 3. Variations of shock locations (y-axis) as functions of the specific energy (x-axis) and angular momenta. The leftmost curve is drawn for $\lambda = 2$, and other curves are for decreasing angular momentum with an interval of $\delta\lambda = 0.02$. Solid curves, filled circles and crosses are drawn for Models V, H and C respectively with $n_V = 31/4$, $n_C = 13/2$ and $n_H = 3$, which obey equation (8).

5 RESULTS OF MAPPING OF ONE MODEL TO ANOTHER

We have already noticed that one could use a relation (equation 8) which maps one model on to another, as far as the transonic properties go. If, for instance, we choose $n_H = 3$, we find that $n_V = 31/4$ and $n_C = 13/2$ respectively. This means that for a given energy and angular momentum a model H flow of polytropic index 3 would have sonic points exactly at the same place as a Model V flow of polytropic index 31/4 and Model C flow of polytropic index 13/2 respectively. Corresponding polytropic exponents are $\gamma_H = 4/3$, $\gamma_V = 1.129$ and $\gamma_C = 1.15385$ respectively. In physical terms, a relativistic flow of constant height would have same properties as more or less isothermal flows in a conical flow and a flow in vertical equilibrium.

What about the shock locations? In Fig. 3 we compare the locations of the standing shocks around a black hole in these three models. Solid curves are for Model V, small circles are for Model H, and crosses are for Model C. The polytropic indices n_V, n_C and n_H are as above. We note that although the models are different, the shock locations are also remarkably close to one another. In Fig. 4 a comparison of the parameter space is shown once more (cf. Fig. 2). However, the polytropic indices are chosen as above. Unlike disjoint regions in Fig. 2, we find that the regions are almost completely overlapping when equation (8) was used. This also shows that the equation (8) is valid even for the study of shock waves. We thus believe that, generally speaking, the three models are identical when the equation (8) is taken into account.

What could be possible applications of the pedagogical exercise we carried out? One could imagine that certain models are easier to study (say, using numerical simulations) than the others. For instance, Chakrabarti & Molteni (1993), Molteni, Gerardi & Chakrabarti (1994) and Chakrabarti & Molteni (1995) studied constant-height discs using smoothed particle hydrodynamics. This was done because a flow in vertical equilibrium cannot be forced on a time-dependent study. However, one could question

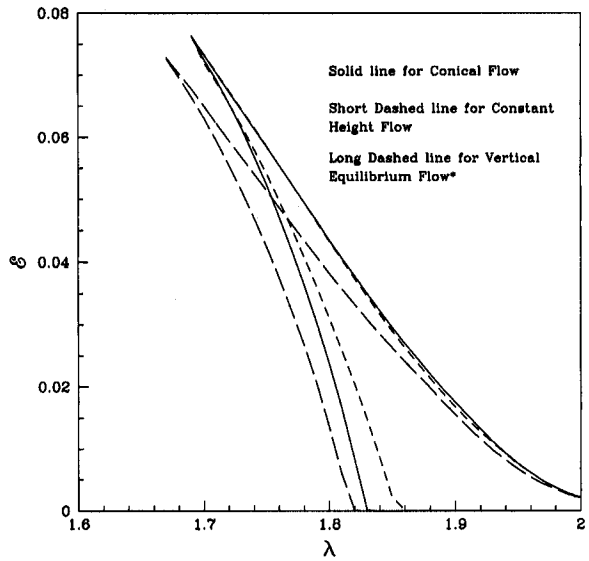

Figure 4. Nature of the boundary of the parameter space for the three models of the accretion flows. Solid, short-dashed, and long-dashed curves are drawn for Models C, H and V respectively with polytropic indices $n_V = 31/4$, $n_C = 13/2$ and $n_H = 3$ which obey equation (8). The roughly similar parameter space shows that the mapping of the indices based on the transonic properties remain roughly the same even when standing shocks are considered. The asterisk mark on 'Vertical Equilibrium Flow' indicates that condition (8a) has been utilized.

whether one can draw any conclusion about the behaviour of flows in vertical equilibrium using a simulation of constant height. Our present study shows that it does. Since the three models are shown to be identical, running a simulation for one model would give results for other models in a straightforward manner. Similarly, a

study of the stability of a model of constant height may be simpler, and stability of one model would imply stability of others.

6 CONCLUDING REMARKS

In this paper we discovered a unique relation among the polytropic indices of three different models of the axisymmetric accretion flows which ensures identical transonic properties in the sense that if all these models have the same conserved energies and angular momenta, then the sonic points also form exactly at the same place. When we proceeded further to compute the shock locations, we found that even the shocks form roughly at the same places. Apparently, disjoint parameter spaces for shock formation with the same value of polytropic index in three different models exhibit considerable overlap when the same unique relation (equation 8) was used. This shows that the models are virtually identical in properties, and various disc models belong to a one-parameter family. Our finding has given some insight into the relation between the nature of a flow with its equation of state. It seems that the relativistic equation of state in a flow in vertical equilibrium behaves similarly to a roughly isothermal flow in a disc of constant height or in a conical flow. It is possible that in the latter models (Models C and H) the geometric compression is smaller, and hence it is easier to keep them roughly isothermal while conserving energy as well.

Although our work has been mainly pedagogical, we believe that it could have several applications. For instance, linear and non-linear stability analysis and time-dependent calculations (numerical simulations) are easier to perform when the disc is of constant thickness. Our work indicates that once certain properties regarding stability are established in one flow model, they would remain valid in other models also, provided that the relation among the polytropic indices is incorporated.

ACKNOWLEDGMENTS

The authors gratefully acknowledge financial support from Department of Science and Technology through a Grant (No. SP/S2/K-14/98) with SKC.

REFERENCES

Bondi H., 1952, MNRAS, 112, 195
Chakrabarti S. K., 1989, ApJ, 347, 365 (C89)
Chakrabarti S. K., 1990, Theory of Transonic Astrophysical Flows. World Scientific, Singapore (C90)
Chakrabarti S. K., 1992, MNRAS, 259, 410
Chakrabarti S. K., Molteni D., 1993, ApJ, 417, 672
Chakrabarti S. K., Molteni D., 1995, MNRAS, 272, 80
Das S., Chattopadhyay I., Chakrabarti S. K., 2001, ApJ, 557, 983
Landau L. D., Lifshitz F. D., 1959, Fluid Mechanics. Pergamon Press, New York
Liang E. P. T., Thompson K. A., 1980, ApJ, 240, 271
Matsumoto R., Kato S., Fukue J., Okazaki A. T., 1984, PASJ, 36, 7
Molteni D., Gerardi G., Chakrabarti S. K., 1994, ApJ, 436, 249
Paczyński B., Wiita P. J., 1980, A&A, 88, 23
Shakura N. I., Sunyaev R. A., 1973, A&A, 24, 337

This paper has been typeset from a TEX/LATEX file prepared by the author.

A&A 379, 683–689 (2001)
DOI: 10.1051/0004-6361:20011307

Astronomy & Astrophysics

Computation of outflow rates from accretion disks around black holes

S. Das, I. Chattopadhyay, A. Nandi, and S. K. Chakrabarti*

S. N. Bose National Centre for Basic Sciences, Salt Lake, Kolkata 700098, India

Received 15 May 2001 / Accepted 30 August 2001

Abstract. We self-consistently estimate the outflow rate from the accretion rates of an accretion disk around a black hole in which both the Keplerian and the sub-Keplerian matter flows simultaneously. While Keplerian matter supplies soft-photons, hot sub-Keplerian matter supplies thermal electrons. The temperature of the hot electrons is decided by the degree of inverse Comptonization of the soft photons. If we consider only thermally-driven flows from the centrifugal pressure-supported boundary layer around a black hole, we find that when the thermal electrons are cooled down, either because of the absence of the boundary layer (low compression ratio), or when the surface of the boundary layer is formed very far away, the outflow rate is negligible. For an intermediate size of this boundary layer the outflow rate is maximal. Since the temperature of the thermal electrons also decides the spectral state of a black hole, we predict that the outflow rate should be directly related to the spectral state.

Key words. X-rays: stars – stars: winds, outflows – black hole physics

1. Introduction

Most of the galactic black hole candidates are known to undergo spectral state transitions (Tanaka & Lewin 1995; Chakrabarti & Titarchuk 1995, hereafter CT95; Ebisawa et al. 1996). Two common states are the so-called hard state and the soft state. In the former, soft-X-ray luminosity is low and the energy spectral index $\alpha \sim 0.5$ ($E_\nu \propto \nu^{-\alpha}$) in the 2–10 keV range. In the latter state, the soft-X-ray luminosity is very high, and hard-X-ray intensity is negligible. There is also a weak power-law hard-tail component with an energy spectral slope $\alpha \sim 1.5$. In the two component advective flow (TCAF) model (CT95), the viscous Keplerian disk resides in the equatorial plane, while the weakly viscous sub-Keplerian flow flanks the Keplerian component both above and below the equatorial plane. The two components merge into a single component when the Keplerian disk also become sub-Keplerian. It is suggested (Chakrabarti 1990) that close to a black hole, at around 10–15 r_g, ($r_g = 2GM_{BH}/c^2$ is the Schwarzschild radius, M_{BH} and c are the mass of the black hole and the velocity of light respectively) the sub-Keplerian flow slows down due to the centrifugal barrier and becomes hotter. Chakrabarti (1999, hereafter Paper I) shows that this centrifugal pressure-supported boundary layer (CENBOL for short) region could be responsible for the generation of thermally-driven outflowing winds and jets and computed the ratio of the outflow to the inflow rate assuming a simple conical accretion disk model.

In the present paper, we compute the *absolute* value of the outflow rate as a function of the rates of the two inflow components, Keplerian and sub-Keplerian. This we do analytically following the recently developed procedure of obtaining shock locations (Das et al. 2001). By dynamically mixing these two components using solutions of the viscous transonic flows we obtain the specific energy and angular momentum of the sub-Keplerian region. We use these pair of parameters to locate shocks in the flow, compute the compression ratio and from this, the outflow rate. We note that as Keplerian matter is increased in the mixture, the shock compression ratio goes down, and the outflow rate decreases. This is also the case even from a radiative transfer point of view – when the Keplerian rate is high, the CENBOL region is completely cooled and the shock compression ratio $R \sim 1$. Hence in the soft state, which is due to increase of the Keplerian rate, outflow should be negligible.

In the next section, we present the governing equations to compute the outflow rates using a purely analytical method. We compute results for both the isothermal and adiabatic outflows. In Sect. 3, we present our results for a single component sub-Keplerian flow. We also produce examples of realistic disks with Keplerian and sub-Keplerian components and obtain outflow rates as functions of the

Send offprint requests to: S. K. Chakrabarti,
e-mail: chakraba@boson.bose.res.in

* *Honorary Scientist,* Centre for Space Physics, 114/v/1A Raja S.C. Mullick Rd., Kolkata 700047.

inflow parameters. In Sect. 4, we discuss our results and draw conclusions.

2. Model equations

We consider matter accreting on the equatorial plane of a Schwarzschild black hole. Spacetime around the black hole is described by the Paczyński-Wiita pseudo-Newtonian potential $\phi = \frac{GM_{\rm BH}}{r-2GM_{\rm BH}/c^2}$ (Paczyński & Wiita 1980) where $M_{\rm BH}$ is the mass of the black hole and G, c are the gravitational constant and velocity of light respectively. Here, r is the radial distance from the origin of the coordinate in which the black hole is treated at the centre. We use geometric units in which all the length, time and velocity scales are measured in units of $2GM_{\rm BH}/c^2$, $2GM_{\rm BH}/c^3$ and c respectively. In future, we use r to denote non-dimensional distance, ϑ and a to denote the non-dimensional radial velocity and adiabatic speed of sound respectively. In accretion or outflow, we assume that the viscous stress is negligible so that matter moves with a constant specific angular momentum. Indeed, even if viscosity is not negligible, the transport of angular momentum is slow compared to the infall timescale. Hence, matter can have almost constant specific angular momentum.

In this case, the radial momentum equation for a non-dissipative flow in vertical equilibrium is given by (Chakrabarti 1989),

$$\vartheta\frac{{\rm d}\vartheta}{{\rm d}r} + \frac{1}{\rho}\frac{{\rm d}P}{{\rm d}r} - \frac{\lambda^2}{r^3} + \frac{1}{2(r-1)^2} = 0. \quad (1)$$

Integrating this, we obtain the conserved specific energy of the flow,

$$\mathcal{E}_v = \frac{1}{2}\vartheta^2 + na^2 + \frac{\lambda^2}{2r^2} - \frac{1}{2(r-1)}, \quad (2)$$

where n is the polytropic index of the inflow and λ is the specific angular momentum. In Eq. (1), P and ρ are thermal pressure and density respectively, v is the infall velocity and $a = \sqrt{(\gamma P/\rho)}$ is the adiabatic sound speed.

The mass flux conservation equation in a flow which is in vertical equilibrium is given by,

$$\dot{M}_{\rm in} = 4\pi\rho\vartheta r h(r) = \Theta_{\rm in}\rho_{\rm s}\vartheta_{\rm s}r_{\rm s}^2, \quad (3)$$

where $\Theta_{\rm in}(=\sqrt{\frac{2n}{n+1}}4\pi a_{\rm s}r_{\rm s}^{1/2})$ is the solid angle subtended by the inflow at the CENBOL boundary. Subscripts "s" denote the quantities at shock (CENBOL boundary) and $h(r) = \sqrt{\frac{2}{\gamma}}ar^{1/2}(r-1)$ is the half-thickness of the disk in vertical equilibrium at a radial distance r.

A sub-Keplerian flow with a positive energy will pass through the outer sonic point and depending on whether the Rankine-Hugoniot condition is satisfied or not, a standing shock may form (Chakrabarti 1990; Chakrabarti 1996). If a standing shock forms, then the post-shock flow would become hotter and would emit hard X-ray radiation. This CENBOL region behaves similarly to the boundary of a normal star; it would be expected to drive outflows. Using Eqs. (2) and (3), it is easy to obtain shock locations (i.e., outer surface of the CENBOL) analytically. Briefly, the procedure to obtain shocks involves the following steps:

(a) For a given pair of specific energy $\mathcal{E}_v$ and angular momentum λ, one obtains a quartic equation for the sonic point and solves it for the three sonic points located outside the horizon. Two of them are saddle type or "X" type sonic points and one is a centre type or "O" type sonic point.

(b) From the inner and the outer "X" type points. Mach numbers are expressed as polynomials of radial distance r. These Mach number expressions satisfy constraints that they must have appropriate values at the sonic points.

(c) In addition, it is enforced that the Mach number invariants at the shock location are also satisfied ($r_{\rm s}$).

(d) The resulting equation becomes quartic in $r_{\rm s}$ and the shock locations are obtained from its solution.

Details are discussed in Das et al. (2001). We consider only the region of the inflow parameter space ($\mathcal{E}_v$, λ) that is able to produce standing shocks.

In the pre-shock region, matter is cooler and is sub-Keplerian. Assuming $\mathcal{E}_v \sim 0$ (freely falling condition) and $a \sim 0$ (cool gas) in presence of angular momentum, matter will fall with a velocity,

$$\vartheta(r) = \left[\frac{1}{r-1} - \frac{\lambda^2}{r^2}\right]^{1/2}. \quad (4)$$

Using this, from Eq. (3) the density distribution can be obtained.

At the shock $r = r_{\rm s}$, i.e., the boundary of the CENBOL, the compression ratio is given by,

$$R = \frac{\Sigma_+}{\Sigma_-} = \frac{h_+(r_{\rm s})\rho_+(r_{\rm s})}{h_-(r_{\rm s})\rho_-(r_{\rm s})} = \frac{\vartheta_-}{\vartheta_+}, \quad (5)$$

where subscripts "$-$" and "+" refer, respectively, to quantities before and after the shock. Here, Σ is the density of matter integrated vertically ($\Sigma \sim \rho h$) and the second "=" sign was written using the mass flux conservation equation given above (Eq. (3)).

At the shock, the total pressure (thermal and ram pressure) is balanced:

$$W_-(r_{\rm s}) + \Sigma_-(r_{\rm s})\vartheta_-^2(r_{\rm s}) = W_+(r_{\rm s}) + \Sigma_+(r_{\rm s})\vartheta_+^2(r_{\rm s}), \quad (6)$$

where W is the pressure of the gas integrated vertically.

We assume that in the pre-shock region, the thermal pressure is small in comparison to the ram pressure,

$$W_+(r_{\rm s}) = \frac{R-1}{R}\Sigma_-(r_{\rm s})\vartheta_-^2(r_{\rm s}). \quad (7)$$

The isothermal sound speed in the post-shock region is obtained from:

$$C_{\rm s}^2 = \frac{W_+}{\Sigma_+} = \frac{R-1}{R^2}\vartheta_-^2 = \frac{1}{f_0}\left[\frac{r_{\rm s}^2 - \lambda^2(r_{\rm s}-1)}{r_{\rm s}^2(r_{\rm s}-1)}\right], \quad (8)$$

where, $f_0 = \dfrac{R^2}{R-1}$.

Up to the sonic point matter moves slowly and the density is higher. Since the outflow would take place in a sea of radiation, the momentum deposition is likely to be effective. With the electron number density $n_e \propto r^{-3/2}$, yet photon number density $n_\gamma \propto r^{-2}$, it is easier to deposit momentum only close to the black hole. In radiation driven outflows from the stellar surface, it is customary to assume flows to be isothermal until the sonic point. We first compute outflow rates making this assumption. Later we drop this assumption and show that the general behaviour remains similar. In addition, we assume that there is very little rotation in the outflow. There is no a priori reason to assume this, except that there is no observational support of rotation in the jet and it is possible that due to radiative viscosity most of the angular momentum is transported very close to the black hole. Furthermore, it has been observed that the effect of angular momentum in the outflow is to bring the sonic points closer to the black hole, especially away from the axis (Sakurai 1985; Chakrabarti 1986). The general effect would produce a transverse structure in the jet which we ignore in the present solution. It was shown (Das & Chakrabarti 1999) that in presence of angular motion the conical outflow is to be replaced by an annular flow confined by the centrifugal barrier and the funnel wall. Generally speaking, the outflow surface varies as $r^{3/2}$. However, the inflow surface area is still proportional to r^2. Because of this asymmetry, the problem is no longer tractable analytically and is beyond the scope of the present paper.

2.1. When the outflow is isothermal

The radial momentum balance equation in the outflow is given by

$$\vartheta\frac{\mathrm{d}\vartheta}{\mathrm{d}r}+\frac{1}{\rho}\frac{\mathrm{d}P}{\mathrm{d}r}+\frac{1}{2(r-1)^2}=0, \tag{9}$$

and the continuity equation is given by

$$\frac{1}{r^2}\frac{\mathrm{d}}{\mathrm{d}r}(\rho\vartheta r^2)=0. \tag{10}$$

From above equations we get

$$\frac{\mathrm{d}\vartheta}{\mathrm{d}r}=\frac{N}{D}, \tag{11}$$

where

$$N=\frac{2C_s^2}{r}-\frac{1}{2(r-1)^2}\quad\text{and}\quad D=\vartheta-\frac{C_s^2}{\vartheta}. \tag{12}$$

To obtain the sonic point condition, we put $N=0$ and $D=0$ and get, $\vartheta(r_c)=C_s$, and $r_c=\frac{1+8C_s^2\pm\sqrt{1+16C_s^2}}{8C_s^2}$, where the subscript c denotes the quantities at the sonic point in the outflow.

Integrating the radial momentum equation, considering the sonic point condition, we have,

$$C_s^2\ln\rho_+-\frac{1}{2(r_s-1)}=\frac{1}{2}C_s^2+C_s^2\ln\rho_c-\frac{1}{2(r_c-1)}. \tag{13}$$

Here, we have ignored the radial velocity in the outflow at the boundary of the shock. Using the notations $\rho(r_c)=\rho_c$ and $\rho(r_s)=\rho_+$, we obtain,

$$\rho_c=\rho_+\exp[-f], \tag{14}$$

where $f=\frac{1}{2}-\frac{1}{2C_s^2}\frac{r_s-r_c}{(r_s-1)(r_c-1)}$.

The outflow rate is given by

$$\dot{M}_{out}=\Theta_{out}\rho_c\vartheta_c r_c^2, \tag{15}$$

where Θ_{out} is the solid angle subtended by the outflow.

From Eqs. (2) and (15) we get,

$$\frac{\dot{M}_{out}}{\dot{M}_{in}}=R_{\dot{m}}=\frac{\Theta_{out}}{\Theta_{in}}\left[\frac{r_s^2(r_s-1)}{r_s^2-\lambda^2(r_s-1)}\right]^{-1/2}\frac{RC_s r_c^2}{r_s(r_s-1)}\times\exp[-f]. \tag{16}$$

The above relation is very similar to that obtained in Paper I when the effects of rotation in the inflow were ignored. However, there the ratio $R_{\dot{m}}$ was a function of R alone. In the present analysis, R is computed self-consistently from the specific energy and the specific angular momentum of the flow:

$$R=\frac{\Sigma_+}{\Sigma_-}=\frac{\vartheta_-}{\vartheta_+}=\left[\frac{\frac{1}{2}M_+^2+n}{\frac{1}{2}M_-^2+n}\right]^{1/2}, \tag{17}$$

where pre-shock and post-shock Mach numbers $M_-(\mathcal{E},\lambda)$ and $M_+(\mathcal{E},\lambda)$ are computed analytically from Das et al. (2001).

2.2. When the outflow is adiabatic

At the other extreme, when the energy of the outflow does not change, one can also obtain an analytical expression for the outflow rate assuming the $r_s >> \lambda^2$. In this case, the entropy density of the flow in the post-shock region is the same at the entropy density of the entire outflow and the specific energy is also conserved along the outflow. We assume that the turbulence generated at the CENBOL has effectively transported angular momentum away. Thus, the energy conservation equation gives

$$na_s^2-\frac{1}{2r_s}=\frac{2n+1}{2}a_c^2-\frac{1}{2r_c}, \tag{18}$$

where the left hand side is the energy at the CENBOL ($r=r_s$) and the right hand side is at the sonic point ($r=r_c$) of the outflow where $u_c=a_c$ has been used. $n=\frac{1}{\gamma-1}$ is the polytropic constant. In a Bondi (in or out) flow, $a_c^2=1/4r_c$. At the CENBOL, $a_s^2=\gamma C_s^2$, where C_s is the isothermal sound speed (Eq. (8)). Using these, one obtains (assuming $r_s >> \lambda^2$)

$$\frac{r_c}{r_s}=\frac{2n-3}{4(\frac{2n\gamma}{f_0}-1)}, \tag{19a}$$

and

$$\frac{a_c^2}{a_s^2}=\frac{f_0 r_s}{4\gamma r_c}. \tag{19b}$$

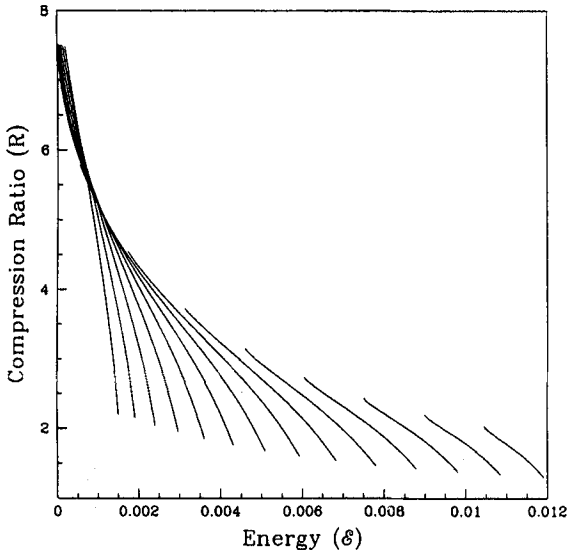

Fig. 1. Variation of the compression ratio of the shocks as a function of specific energy $\mathcal{E}$ and angular momentum λ as obtained from the analytical solution. λ varies from 1.57 (right) to 1.79 (left). Curves are drawn at intervals of $d\lambda = 0.02$.

In an adiabatic flow with an equation of state $P = K\rho^{\gamma}$ (where K is a constant and a measure of entropy), one obtains, assuming, $K_c = K_s$,

$$\frac{\rho_c}{\rho_s} = \left(\frac{a_c^2}{a_s^2}\right)^n . \tag{20}$$

From these relations one obtains the ratio of the outflow to the inflow rate as

$$R_{\dot{m}} = \frac{\Theta_o}{\Theta_i}\left(\frac{f_0}{4\gamma}\right)^3 \frac{R}{2}\left\{\frac{4}{3}\left[\frac{8(R-1)}{R^2} - 1\right]\right\}^{3/2} . \tag{21}$$

Here, we have used $n = 3$ for a relativistic flow. The nature of this function will be discussed below.

3. Outflow rates from inflow parameters

In Eq. (16), we presented the outflow/inflow rate ratio as a function of the compression ratio of the flow at the shock. The compression ratio is obtained from the specific energy and angular momentum using Eq. (17). First, we employ analytical means to obtain this for a single component sub-Keplerian disk. Second, we use a two component Keplerian/sub-Keplerian disk to actually compute these parameters from more fundamental parameters such as accretion rates and viscosity.

3.1. Single component sub-Keplerian flows

In Fig. 1, we plot the analytical solution of the compression ratio R as a function of the flow parameters: specific energy $\mathcal{E}$ and the specific angular momentum λ. The shock strength generally increases when energy decreases and the angular momentum increases. This is because for low energy, the outer sonic point and the shock form very far away and the Mach number jumps from a very large number to a very small number. If the angular momentum is decreased, shock is produced only if the specific energy is high, i.e., if the sonic points and the shocks are very close to the black hole. Here, flow becomes subsonic before its Mach number could be very high.

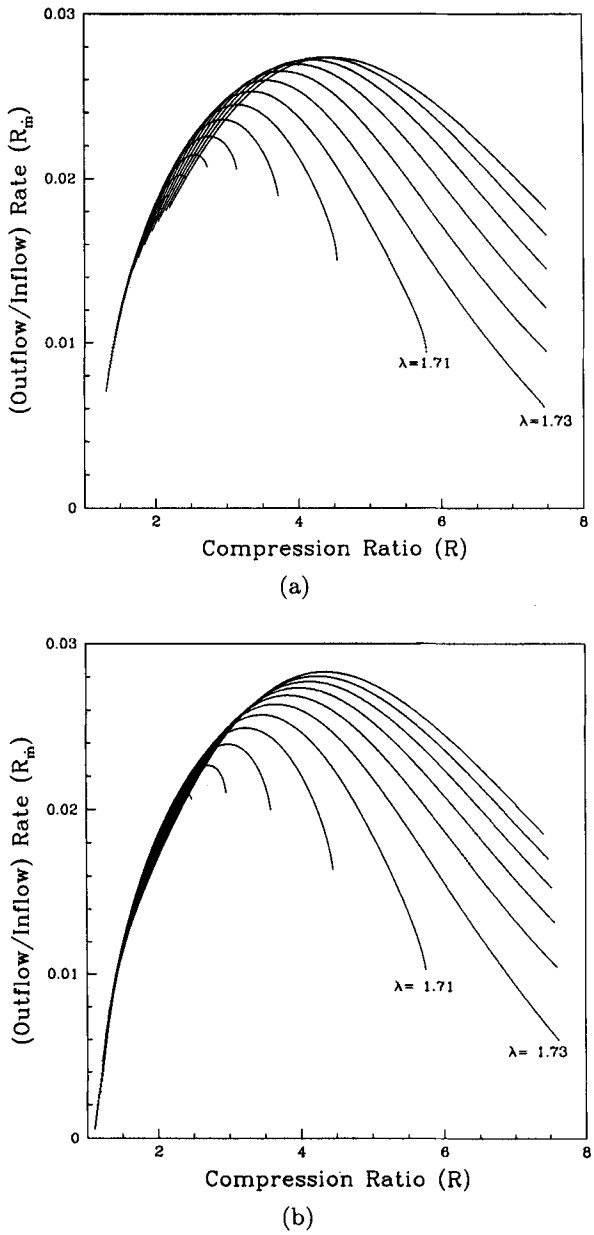

Fig. 2. a) Variation of the ratio of outflow to inflow rates $R_{\dot{m}}$ as a function of compression ratio for various specific angular momenta. $\lambda = 1.57$ (inner most) to 1.83 (outer most). Curves are drawn at intervals of $d\lambda = 0.02$. Outflow rate is maximum at some intermediate compression ratio; **b)** Same as Fig. 2a except that curves are drawn for the exact numerical solution.

Figure 2a shows the principle result of our work when only one sub-Keplerian accretion is chosen as the inflow. We plot the ratio $R_{\dot{m}}$ for a large number of specific angular momenta of the flow ranging from 1.57 (innermost) to 1.83 (outermost) at intervals of $d\lambda = 0.02$. The curves are

drawn for all ranges of specific energy $\mathcal{E}$ for which shocks are formed. Along the X-axis the compression ratio R of these shocks is written. Here to compute solid angles of the inflow and the outflow, we assume the half opening angle of the outflow to be 10°. Therefore, $\Theta_{\rm out} = \pi^3/162$. $\Theta_{\rm in}$ is given in the discussion following Eq. (2). In Paper I, the compression ratio R was assumed to be a parameter and no angular momentum was assumed a priori. Presently, we show the dependence on angular momentum. The general character, namely, that the outflow rate is negligible when the shock is weak ($R \sim 1$) and falls off gradually for strongest shock ($R \to 7$), remains the same as in Paper I, however. There is a peak at about $R_{\dot{m}} \sim 2.8\%$. Note that for a given R, $R_{\dot{m}}$ increases monotonically with specific angular momentum λ. This is because density of CENBOL rises with λ. The curves corresponding to $\lambda = 1.71$ and 1.73 are specially marked since there is a clear difference in tendency of the variation of $R_{\dot{m}}$. For instance, below $\lambda \sim 1.72$, very strong shocks are not possible at all and as a result the outflow rate has a lower limit. For $\lambda \gtrsim 1.72$ such a limit does not exist.

The general behaviour of the outflow rate can be understood in the following way: when shocks are strong, they form very far out, and thus, even though the CENBOL area (which is basically the area of the base of the jet) increases, the net outflow rate is low. When the shock forms very close to the black hole, the temperature is high, and thus the outflow velocity is larger, but the CENBOL surface area goes down. Thus the product is low. For the intermediate cases the net effect is larger.

For comparison with the analytical work presented in Fig. 2a, in Fig. 2b we present a similar diagram drawn using a numerical computation of the shock locations (Chakrabarti 1989). Excellent agreement between these two figures implies that the approximations on which the analytical work was based are justified. All the features are reproduced well in Fig. 2a, except that for the weakest shocks outflow rate is not as low as in the numerical calculation of Fig. 2b.

We now present the nature of $R_{\dot{m}}$ when the outflow is also chosen to be adiabatic in Fig. 3. We used $\Theta_{\rm o}/\Theta_{\rm i} \sim 0.1$ for reference. We observe that the peak is still located at around $R =\sim 4$ and the outflow rate drops for very strong ($R \sim 7$) and very weak ($R \sim 1$) shocks. We therefore believe that our conclusion about the behaviour of $R_{\dot{m}}$ is generic.

3.2. Two component advective flows

Chakrabarti & Titarchuk (1995) proposed that the spectral properties are better understood if the disk solutions of sub-Keplerian flows are included along with the Keplerian flows. Recently, Smith et al. (2001a), Smith et al. (2001b), Miller et al. (2001) found conclusive evidence of these two components in many of the black hole candidate accretion flows. While the matter with higher viscosity flows along the equatorial plane as a Keplerian

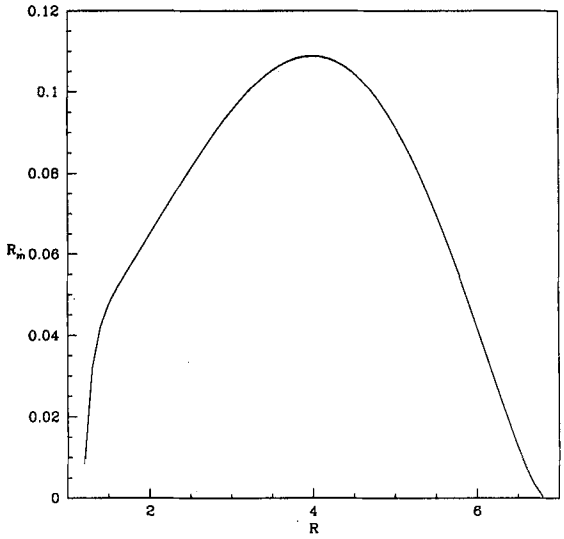

Fig. 3. Ratio of the outflow and the inflow rates as a function of the compression ratio of the inflow when the outflow is adiabatic. The general nature of the function remains the same as that of the isothermal outflow.

disk (of rate $\dot{M}_{\rm K}$), sub-Keplerian halo matter (of rate $\dot{M}_{\rm h}$) with lower viscosity flanks the Keplerian disk above and below (Fig. 4a). Since the inner boundary condition on the horizon forces the flow to be sub-Keplerian, irrespective of their origin (Chakrabarti 1990, 1996) matter mixes (at say, $r = r_{\rm tr}$) from both the Keplerian and sub-Keplerian flows before entering a black hole to form a single component sub-Keplerian with an average energy and angular momentum of $\mathcal{E}$ and λ respectively. The specific energy and angular momentum of the mixed flow is computed from:

$$\mathcal{E} = \frac{\dot{M}_{\rm K}\mathcal{E}_{\rm K} + \dot{M}_{\rm h}\mathcal{E}_{\rm h}}{\dot{M}_{\rm K} + \dot{M}_{\rm h}}, \tag{22}$$

and

$$\lambda = \frac{\dot{M}_{\rm K}\lambda_{\rm K} + \dot{M}_{\rm h}\lambda_{\rm h}}{\dot{M}_{\rm K} + \dot{M}_{\rm h}}. \tag{23}$$

Here, $\mathcal{E}_{\rm K}$, $\mathcal{E}_{\rm h}$, $\lambda_{\rm K}$ and $\lambda_{\rm h}$ are the specific energies and specific angular momentum of the Keplerian and the sub-Keplerian components at $r = r_{\rm tr}$ respectively.

Figure 4a shows a schematic diagram of the cross-section of a two-component accretion flow. The transition radius ($r = r_{\rm tr}$) where the Keplerian disk becomes sub-Keplerian, and the shock location $r = r_{\rm s}$, are indicated. Figure 4b shows two solutions (marked I and II) of the equations governing a two-component flow (Chakrabarti 1996) where $\lambda_{\rm d}/\lambda_{\rm K}$ (Sub-Keplerian matter from the Keplerian disk) and $\lambda_{\rm h}/\lambda_{\rm K}$ (Sub-Keplerian halo) are plotted as a function of the logarithmic radial distance. Viscosities chosen for these two components are $\alpha = 0.04$ and $\alpha = 0.01$ respectively. For $r < r_{\rm tr} = 45$ (lightly shaded region) the two sub-Keplerian flows mix to create a single component. For simplicity, we assume viscosity to be negligible in this region. Thus, the specific angular momentum and specific energy computed at

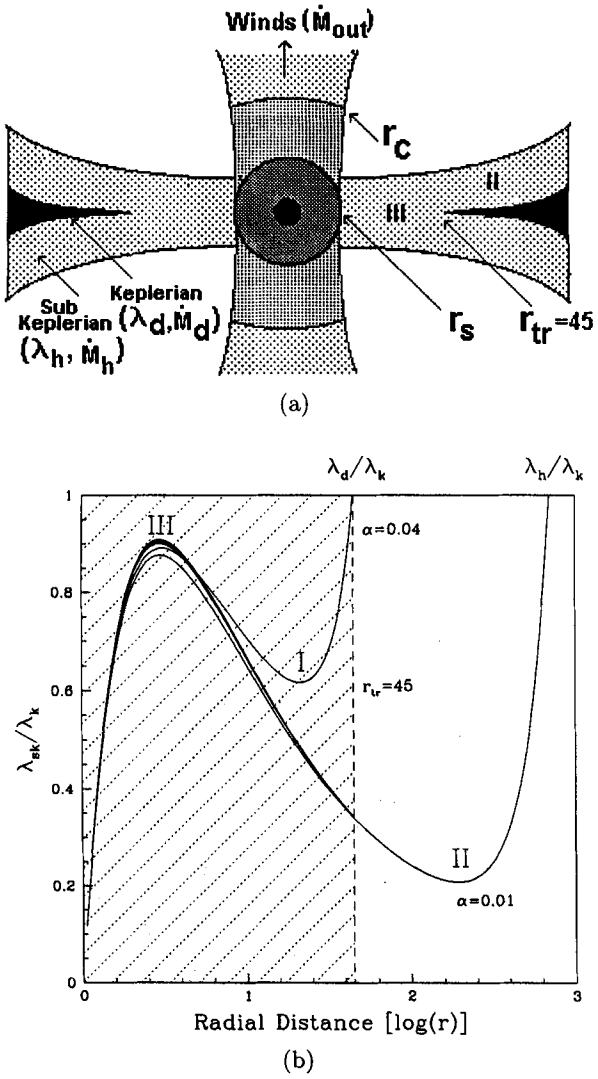

Fig. 4. **a)** Schematic diagram of the cross section of two-component accretion flow. See text for details; **b)** Solution of the two-component flow equations for two different viscosities. They are merged to form a single solution as depicted in Fig. 4a.

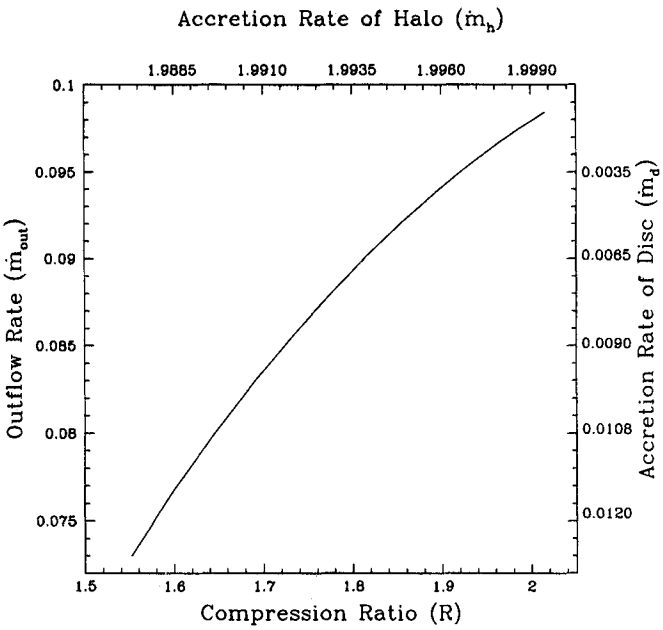

Fig. 5. Variation of outflow rates (left axis) with compression ratio at shocks (lower axis). The upper axis gives the variation of sub-Keplerian accretion rate and right axis gives the same for Keplerian accretion rate.

$r = r_{tr}$ from Eqs. (22) and (23) remain constant (λ) for $r < r_{tr}$. Dark solid curve (marked III) shows the angular momentum distribution λ/λ_K of all possible mixtures of the two components which allow shock formation. We chose a case where $\dot{M}_d + \dot{M}_h = 2.0\dot{M}_{Edd}$ and vary the Keplerian component $\dot{M}_d$ where $\dot{M}_{Edd}$ is the Eddington accretion rate.

In Fig. 5, the computed outflow rates are shown when the half opening angle of the outflow is 10°. In this case, $\frac{\Theta_{out}}{\Theta_{in}} \sim \sqrt{\frac{n+1}{2n}} \frac{\pi^2}{648 a_s r_s^{1/2}}$. The left axis shows the rate of outflow $\dot{m}_{out} = \dot{M}_{out}/\dot{M}_{Edd}$ as a function of the Keplerian disk rate (right panel) ($\dot{m}_d = \dot{M}_d/\dot{M}_{Edd}$) and the halo rate (upper panel) ($\dot{m}_h = \dot{M}_h/\dot{M}_{Edd}$). The lower axis gives the compression ratio at the shock. The most important conclusion that can be drawn here is that the outflow rate steadily goes up as the Keplerian disk rate $\dot{m}_d$ decreases and the spectrum goes to a harder state. When the Keplerian rate is higher, the compression ratio is lower and the outflow rate is also lower. This conclusion, drawn completely from dynamical considerations, is also found to be true from the spectral studies (CT95) where it was shown that the post-shock region cools down and the shock disappears ($R \rightarrow 1$). Our work therefore hints that the outflow would be negligible in softer states.

4. Discussion and concluding remarks

CT95 pointed out that the centrifugal pressure-supported boundary layer (CENBOL) of a black hole accretion flow is responsible for the spectral properties of a black hole candidate. In this Paper, we present analytical results to show that this CENBOL is also responsible for the production of the outflows, and the outflow rate is strongly dependent on the inflow parameters, such as specific energy and angular momentum. We showed that in general, the outflow rate is negligible when the shock is absent and very small when the shock is very strong. In intermediate strength, the outflow rate is the highest. As the specific angular momentum is increased, the outflow rate is also increased. This conclusion is valid when the flow is either isothermal or adiabatic.

We also demonstrated how a realistic two-component flow (TCAF) consisting of Keplerian and sub-Keplerian components produces a significant amount of outflow. Since matter close to a black hole is sub-Keplerian by nature, the two components must mix to form a single sub-Keplerian flow which has positive specific energy and almost constant specific angular momentum. We showed

that as the Keplerian rate of the disk is increased, the outflow rate is decreased as the shock compression ratio approaches unity. This conclusion, drawn from a dynamical point of view, is also corroborated by the spectral behavior as well – as the Keplerian rate is raised, the post-shock region is cooled due to inverse Comptonization and the shock disappears. This reduces the thermal pressure drive and the resulting outflow rate is reduced.

Acknowledgements. This work is partly supported by a project (Grant No. SP/S2/K-14/98) funded by Department of Science and Technology (DST), Govt. of India.

References

Chakrabarti, S. K. 1986, ApJ, 303, 582
Chakrabarti, S. K. 1989, ApJ, 347, 365 (C89)
Chakrabarti, S. K. 1990, Theory of Transonic Astrophysical Flows (Singapore: World Sci.) (C90)
Chakrabarti, S. K., & Titarchuk, L. G. 1995, ApJ, 455, 623
Chakrabarti, S. K. 1996, ApJ, 464, 664
Chakrabarti, S. K. 1999, A&A, 351, 185 (Paper I)
Das, T. K., & Chakrabarti, S. K. 1999, Class Quant. Grav, 16, 3879
Das, S., Chattopadhayay, I., & Chakrabarti, S. K. 2001, ApJ, 557, 983
Ebisawa, K., Titarchuk, L. & Chakarbarti, S. K. 1996, PASJ, 48, 59
Miller, J. M., et al. 2001, ApJ, submitted [astro-ph/0107514]
Paczyński, B., & Wiita, P. J. 1980, A&A, 88, 23
Sakurai, T. 1985, Astron. Astrophys., 152, 121
Smith, D. M., Heindl, W. A., & Swank, J. H. 2001a, ApJ, submitted [astro-ph/0103304]
Smith, D. M., Heindl, W. A., Markwardt, C., & Swank, J. H. 2001b, ApJ, 554, L41
Tanaka, Y., & Lewin, W. H. G. 1985, in X-ray Binaries, ed. W. H. G. Lewin, J. van Paradijs, & E. P. I. van den Heuvel (Cambridge University Press), 166

THE ASTROPHYSICAL JOURNAL, 576:L45–L48, 2002 September 1

ON THE EJECTION MECHANISM OF BULLETS IN SS 433

SANDIP K. CHAKRABARTI,[1,2] P. GOLDONI,[3] PAUL J. WIITA,[4] A. NANDI,[1] AND S. DAS[1]
Received 2002 July 4; accepted 2002 July 24; published 2002 August 2

ABSTRACT

We discuss plausible mechanisms to produce bulletlike ejecta from the precessing disk in the SS 433 system. We show that nonsteady shocks in the sub-Keplerian accretion flow can provide the basic timescale of the ejection interval while the magnetic rubber-band effect of the toroidal flux tubes in this disk can yield flaring events.

Subject headings: accretion, accretion disks — hydrodynamics — instabilities — shock waves — stars: individual (SS 433) — stars: mass loss

1. INTRODUCTION

SS 433 remains one of the most enigmatic objects in the sky. Even 25 years after its first appearance in the catalog of Stephanson & Sanduleak (1977), it is not clear whether the compact object is a black hole or a neutron star. However, there is ample evidence that the companion is an OB-type star with an orbital period of 13.1 days, which is losing mass at the rate of about $10^{-4}\ M_\odot\ \mathrm{yr}^{-1}$ (van den Heuvel 1981), corresponding to extremely super-Eddington accretion regardless of the mass of the compact object.

One of the most curious properties of the jets of SS 433, which first made their presence distinctly felt through the emission of variable Hα lines, is that they are apparently ejected as bullets (e.g., Borisov & Fabrika 1987; Vermeulen et al. 1993; Paragi et al. 1999, 2002; Gies et al. 2002), with a surprisingly nearly constant radial velocity of about $0.26c$. The absence of a significant intrinsic rotational velocity (i.e., v_ϕ) component is clear from the fact that the kinematic model (e.g., Abell & Margon 1979), which assumes only radial injection, quite accurately explains the time variation of the red- and blueshifts of the Hα emission from the jets with a period of 162 days, which is attributed to the precession of the accretion disk about the compact object. The radial velocity is less than the maximum allowed sound speed of $c/\sqrt{3}$, and thus hydrodynamic acceleration could, in principle, explain it. Therefore one may not require a magnetic or electrodynamic acceleration process (e.g., Belcher & MacGregor 1976; Lovelace 1976). However, the rather good collimation (Margon 1984; Paragi et al. 1999) supports the hypothesis that a substantial degree of confinement produced by toroidal flux tubes may be present. Gies et al. (2002) showed that the ratios of the Hα emission equivalent widths from the approaching and receding jets as a function of precessional phase could be fitted nicely only if these emission components are bulletlike. Indeed, the recent *Chandra X-Ray Observatory* discovery of X-rays at a distance of about 10^{17} cm from the center may result from the collision of such bullets (S. Migliari, R. P. Fender, & M. R. Mendez 2002, in preparation).

SS 433 poses another interesting problem: it was pointed out by Chakrabarti (1999) and Das & Chakrabarti (1999) that significant outflows are produced only when the accretion rate is such that the X-ray source is in a low/hard state, and all the observational indications in other microquasars also suggest that the jets are indeed produced in low/hard states (Corbel et al. 2001; Klein-Wolt et al. 2001). However, it is difficult to imagine how SS 433 manages to remain in the low/hard state with $10^{-4}\ M_\odot\ \mathrm{yr}^{-1}$ of wind matter ejected from its companion. The answer to this quandary probably lies in the recent results of Paragi et al. (1999) and Blundell et al. (2000), whose high-resolution radio maps show that there is a large region of roughly 50 AU in radius that is filled with enough gas and dust to obscure the accretion disk and the base of the jets. They also found an equatorial outflow. Gies et al. (2002) present additional evidence from observations of the "stationary" Hα and He I lines for an extended "disk wind." So it is distinctly possible that most of the matter from the donor is rejected either by centrifugal force (Chakrabarti 2002) or by radiation force far outside the central accretion disk, and thus the compact object receives only a few times the Eddington rate ($\dot{M}_{\mathrm{Edd}}$) of its companion's wind matter to accrete. This consideration finds further support from the fact that the kinematic luminosity of the jet itself is around 10^{39} ergs s^{-1} (Margon 1984), which corresponds to about 1 Eddington rate for a 10 $M_\odot$ compact object.

In numerical simulations of supercritical winds by Eggum, Coroniti, & Katz (1985) designed to model SS 433, it was shown that only a fraction of a percent of the infalling matter is ejected from a radiation pressure–supported Keplerian disk, which indicates that the accretion rate must be at least $100\dot{M}_{\mathrm{Edd}}$ if the accretion takes place through a Keplerian disk. On the other hand, numerical simulations of a sub-Keplerian disk by Molteni, Lanzafame, & Chakrabarti (1994) suggest that about 15%–20% of matter is ejected as an outflow, indicating that the accretion rate onto the compact object in SS 433 need be at most a few $\dot{M}_{\mathrm{Edd}}$. Similar simulations with different parameters yield situations where no steady shocks can form, even though two saddle-type sonic points are present (Ryu, Chakrabarti, & Molteni 1997, hereafter RCM); under these conditions, large-scale shock oscillations produce intermittent outflows instead of continuous outflows. Since the compact object is a wind accretor, a low angular momentum, sub-Keplerian flow is the most likely description of the accretion flow. Indeed, the presence of sub-Keplerian flows in several other high-mass X-ray binaries has now been verified (Smith, Heindl, & Swank 2002).

In this Letter, we present a few scenarios leading to ejection of matter as bullets in SS 433. We discuss four possible ways

[1] S. N. Bose National Center for Basic Sciences, JD-Block, Salt Lake, Kolkata 700098, India; chakraba@bose.res.in, anuj@boson.bose.res.in, sbdas@bose.res.in.
[2] Also at Centre for Space Physics, P-61 Southend Gardens, Kolkata 700084, India.
[3] Service d'Astrophysique, CEA/Saclay, 91191 Gif-sur-Yvette Cedex, France; paolo@discovery.saclay.cea.fr.
[4] Department of Physics and Astronomy, Georgia State University, Atlanta, GA 30303; wiita@chara.gsu.edu.

to create blobs of matter emerging from the disk and conclude that periodic ejection of the blobs by the large-scale oscillation of an accretion shock (something like a piston) may be the fundamental production mechanism of the "normal" bullets. The irregularly observed rapid flaring (Vermeulen et al. 1993) could be understood in terms of the catastrophic collapse of toroidal magnetic flux tubes, very similar to what has been argued to be occurring in GRS 1915+105 (Vadawale et al. 2001; Nandi et al. 2001). In the next section, we discuss these processes and their suitability or unsuitability for SS 433. In § 3, we present concluding remarks.

2. MECHANISMS TO PRODUCE BULLET-LIKE EJECTA FROM ACCRETION FLOWS

In both the works of Eggum et al. (1985) and Molteni et al. (1994), continuous ejection was reported when a radiation pressure–dominated Keplerian disk, or a sub-Keplerian disk capable of producing a steady shock, was considered. However, in SS 433 the basic ejection is bulletlike, and since the size of the X-ray–emitting region is smaller than $l_X \sim 10^{12}$ cm within which the material in the jets is already accelerated to $v_{jet} \sim 0.26c$ (Watson et al. 1986; Stewart et al. 1987), the bullets are not expected to be delayed by more than $l_X/v_{jet} \sim 100$ s. Indeed, recent *Rossi X-Ray Timing Experiment* (*RXTE*) observations of hard X-rays from SS 433 indicated variability on timescales of 50–1000 s (Safi-Harb & Kotani 2002), roughly corroborating this picture. In fact, a simultaneous measurement of a flare at 2 GHz in the radio (Kotani & Trushkin 2001) and in hard X-rays (Safi-Harb & Kotani 2002) indicated a strong anticorrelation of radio and X-ray fluxes, similar to what is observed in GRS 1915+105 (Mirabel & Rodriguez 1994). Moreover, the X-ray luminosity is very low ($\sim 10^{36}$ ergs s^{-1}) and is believed to come from the base of the jets (Watson et al. 1986). It is believed to have a thermal origin, and *EXOSAT* (Watson et al. 1986) and *Ginga* (Yuan et al. 1995) observations were adequately fitted with a thermal bremsstrahlung model with $kT \gtrsim 30$ keV. The overall spectral shape suggests that the source has always been in a standard low/hard state, and so far no quasi-thermal emission expected from a "Keplerian disk" has been detected. From the interaction of the jet with the supernovae remnant W50, the lower limit of kinematic luminosity is found to be at least 10^{39} ergs s^{-1} (Biretta et al. 1983; Davidson & McCray 1980). This means that the mean mass outflow rate is around 10^{18} g s^{-1}, and if most of it is in the form of bullets ejected at 50–1000 s intervals, the mass accumulated in each bullet should be in the range of 10^{19}–10^{21} g.

The above data imply that the essential features that one must explain when attempting to produce bullets out of the accretion disks are (*a*) the disk should be a sub-Keplerian flow, (*b*) the object (black hole or a neutron star) and its surroundings should be in a low/hard state, (*c*) bullets should be ejected in 50–1000 s timescales under normal circumstances, (*d*) the mass of each bullet should be around 10^{19}–10^{21} g, and, finally, (*e*) there should be occasional flaring with an anticorrelation of radio and X-ray emission. We now discuss several scenarios and present what we believe to be the most probable picture of what is going on in SS 433. The four processes are schematically shown in Figures 1*a*–1*d*.

2.1. *Cooling of the Jet Base by Comptonization and Separation of Blobs*

It was shown by several numerical simulations that significant outflows are produced from regions very close to the inner edge of the accretion flow, possibly from the centrifugal pressure–dominated region (Molteni et al. 1994, 2001). These jets are launched subsonically but quickly pass through the inner sonic point to become supersonic. In the subsonic region while the matter moves slowly, the density is high and the optical depth could be large enough ($\tau > 1$) to undergo Compton cooling (Fig. 1*a*) *provided there is a Keplerian disk underneath to supply soft photons*. A part of the outflow, which was subsonic previously, becomes supersonic because of this rapid cooling and separates from the base of the jet. This separation of blobs is expected to occur at the sonic surface r_c which is $\sim(2$–$3)r_s$, where r_s is the size of the centrifugal barrier (see Chakrabarti 1999)

This possibility, though attractive, and in fact likely to be a major mechanism for rapid state change in objects like GRS 1915+105 (Chakrabarti & Manickam 2000), is untenable in SS 433 because the latter is a wind accretor: thus no significant Keplerian disk is expected in this system to supply the soft photons, and indeed none has been detected so far (Watson et al. 1986; Yuan et al. 1995).

2.2. *Resonance Oscillation of Accretion Shocks in the Presence of Bremsstrahlung Cooling*

Numerical simulations of accretion flow show that in cases where the cooling timescale nearly matches the infall timescale, a shock forms, but it then starts oscillating and ejects matter quasi-periodically (Langer, Chanmugam, & Shaviv 1983; Molteni, Sponholz, & Chakrabarti 1996, hereafter MSC; see Fig. 1*b*). In order to have an oscillation period of around 50 s, the shock must be located at the large distance of $r_{s,\mathrm{MSC}} \approx 6400 r_g$ for a black hole of mass $M = 10\ M_\odot$, where $r_g = 2GM/c^2$. The mass of the postshock region is computed by equating the bremsstrahlung (which we assume to be the major cooling mechanism) cooling time and the infall time in the postshock region (MSC):

$$T_{\mathrm{MSC}} \simeq \frac{\mathcal{E}}{\dot{\mathcal{E}}} \simeq \frac{r_{s,\mathrm{MSC}}}{v_f} \simeq \left(\frac{R r_{s,\mathrm{MSC}}}{r_g}\right)^{3/2} \frac{r_g}{c}, \tag{1}$$

where $\mathcal{E}$ is the specific thermal energy, v_f is the infall velocity, and $R = (\gamma + 1)/(\gamma - 1) \simeq 4$–$7$ (these limits are for a strong shock with $\gamma = 5/3$ and $\gamma = 4/3$, respectively) is the compression ratio at the shock. Assuming the gas density (n) and temperature (T) scale as $n \sim r^{-3/2}$ and $T \sim r^{-1}$, respectively, the mass of the sub-Keplerian region of $r < r_s$ turns out to be 7×10^{19} g (with $M = 10\ M_\odot$, $\gamma = 5/3$). This is indeed of the same order as the mass of the bullets observed in SS 433. However, one has to have both the angular momentum and energy of the injected material comparable to the marginally bound values determined by the central object in order to achieve such an oscillation. On the other hand, if the mass expulsion from the system takes place at the similar radius of $r_{ex} \sim 10^4 r_g = 2 \times 10^9 M/M_\odot$ cm due to the centrifugal force, the specific angular momentum of the flow is approximately $[r_{ex}/(2r_g)]^{1/2} r_g c \sim 70 r_g c$, which is very large compared to the marginally bound value of $2r_g c$. So it is unlikely that this mechanism works in SS 433.

2.3. *Nonsteady and Nonlinear Shock Oscillation*

A standing shock can form in a sub-Keplerian flow only if there are two saddle-type sonic points and the Rankine-Hugoniot relation is satisfied at least at one point in between these two sonic points. However, Chakrabarti (1990) showed that there is a large region of the parameter space where there are two

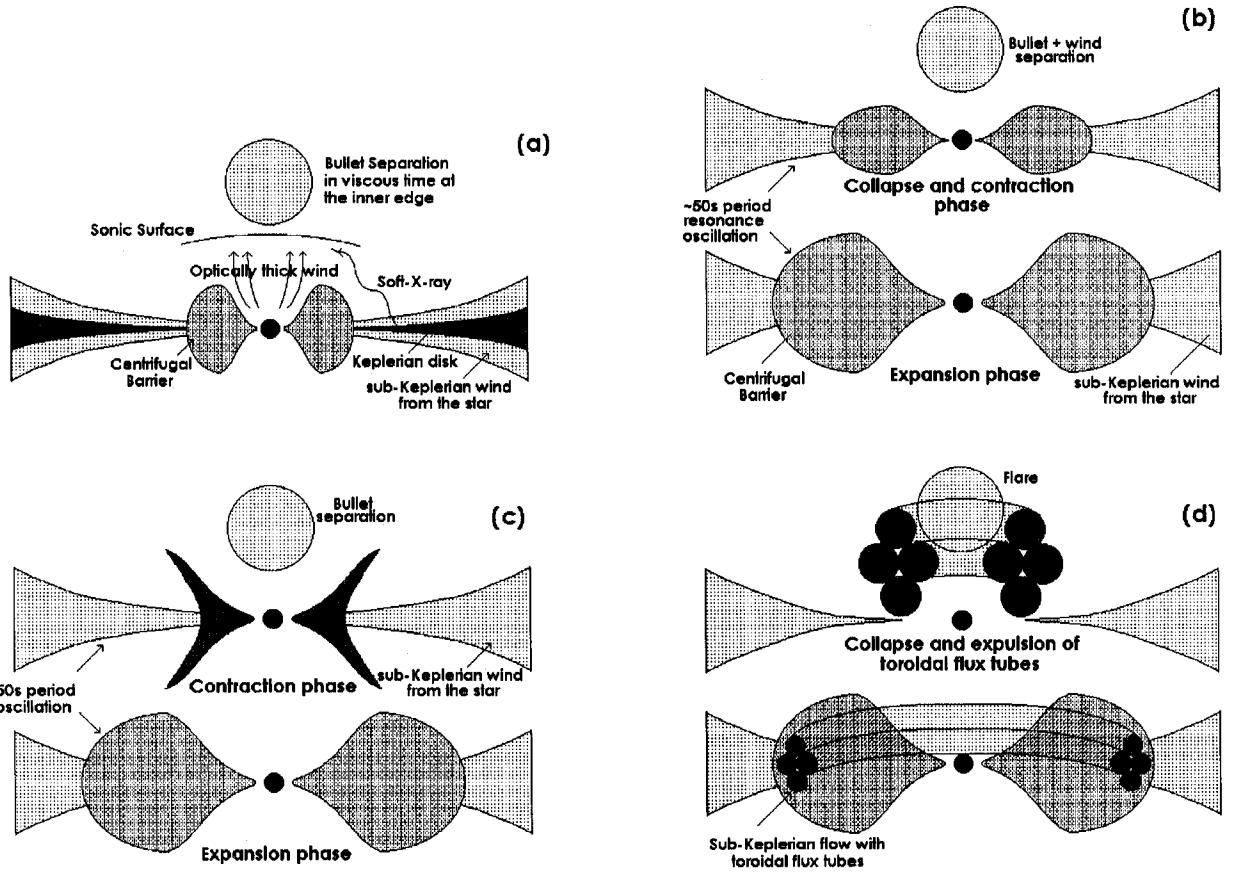

FIG. 1.—Four scenarios of bullet separation in SS 433 are schematically shown. (*a*) The base of the jet is cooled down by soft photons from a Keplerian disk and detaches when it becomes supersonic. (*b*) Resonance oscillation of the sub-Keplerian region due to the near matching of the infall time with the cooling time produces discrete ejecta during the phase when the centrifugal barrier contracts. (*c*) Nonsteady motion of the centrifugal barrier due to the inability of the flow to find a steady shock solution. (*d*) Magnetic tension from toroidal flux tubes (shown as shaded narrow tori) causes them to collapse catastrophically in a hot ambient medium in rapid succession, which evacuates the centrifugal barrier. The recurrence time of (*a*) is the viscous timescale in the inner part of the disk, ~10 s; (*b–c*) is ~50 s; and (*d*) is random and dictated by the enhanced magnetic activity.

saddle-type sonic points but the shock conditions are not satisfied. Even an initially supersonic accretion (such as the wind from the companion) can fall into this category.

What will happen to such a realistic flow, especially when the specific entropy at the inner sonic point is greater than that at the outer sonic point? RCM discovered that a flow injected with these parameters exhibits yet another type of shock oscillation (Fig. 1*c*). Here the shock searches for a stable location and oscillates without finding it. In the first half of the cycle, the shock recedes far away, the postshock region fills up, but the accretion is essentially completely blocked. In the second half of the cycle, the shock pushes the matter into the black hole, thereby evacuating the postshock region. In a realistic simulation, RCM find that while the ratio of actually accreted matter to the amount available from the companion, $R_{ai} \equiv \dot{M}_{acc}/\dot{M}_{inj}$, would be around 0.2 during the first half-cycle, $R_{ai} \sim 1.3$ in the second half-cycle. The outflow was also found to be very large. The timescale of oscillation was found to be $T_{RCM} \sim (4000\text{–}6000) r_g/c$ for a $r_s \simeq 20 r_g$ whose infall time is only about $T_{MSC} \simeq (R r_s/r_g)^{3/2}(r_g/c) \sim (350\text{–}400) r_g/c$. Thus, this type of oscillation takes about a factor of $R_T = T_{RCM}/T_{MSC} \sim 15$ times longer than the resonance oscillation discussed in § 2.2. For a 50 s oscillation, the location of the shock should be obtained from $(r_{s,RCM}/r_g)^{3/2} \simeq (1/R)(50\text{ s}/R_T)(c/r_g) \sim 10^4$, which gives $r_{s,RCM} \sim 450 r_g$ for a 10 $M_\odot$ black hole, a more physically reasonable value. Even though the size of the oscillating region goes down by a factor of 10 or so, compared with that involved in the resonance oscillation, the ejected mass need not go down (even for the same accretion rate as in the earlier case). This is because nearly all of the accretion flow is accumulated in half the cycle (~25 s in this case) before being ejected (see Fig. 2 of RCM).

Another advantage of this type of nonsteady shock oscillation is that it is driven by centrifugal force and not by thermal cooling. Hence the result is generally independent of the accretion rate. Thus, as long as the viscosity remains low, equivalent to having the Shakura-Sunyaev (1973) parameter $\alpha \leq \alpha_c \simeq 0.015$ (Chakrabarti 1990), and $\dot{M}_{inj}$ remains fairly constant, this oscillation, once established, could be sustained indefinitely.

2.4. *Magnetic Rubber-Band Effect*

In the event of increase in magnetic activity of the disk, as could happen for instance when the accretion disk bends toward the binary companion during its precessional motion, it is not unlikely that a strong magnetic field will be first intercepted, and then advected, toward the inner edge of the disk. In this

case the field will preferentially become toroidal due to shear in the rotating flow. Then, as has already been pointed out (Chakrabarti & D'Silva 1994; Nandi et al. 2001), the acceleration due to magnetic tension,

$$a_T = -\frac{B_\phi^2}{4\pi r(\rho_e + \rho_i)} \sim -\frac{B_\phi^2}{4\pi r \rho_e}, \quad (2)$$

would be the dominant force in the postshock region of the sub-Keplerian flow (Fig. 1*d*). Here r is the major radius of the toroidal flux tube and ρ_i and ρ_e are the densities of the medium internal and external to the flux tube, respectively. The last step in equation (2) is written because $\rho_i \ll \rho_e$ for a strong flux tube. Since $B_\phi \propto 1/r$ and $\rho_e \propto r^{-3/2}$, we get

$$a_T \propto r^{-3/2}, \quad (3)$$

thus increasing rapidly as the tube comes closer to the black hole, and even surpassing the magnetic buoyancy,

$$a_{MB} = \frac{1 - X}{1 + X}\left(\frac{\lambda_{Kep}^2 - \lambda^2}{r^3}\right) \simeq \frac{\lambda_{Kep}^2 - \lambda^2}{r^3}, \quad (4)$$

where $X = \rho_i/\rho_e \rightarrow 0$ and λ_{Kep} and λ are, respectively, the specific angular momenta of a Keplerian disk and the disk under consideration. The accelerations in equations (3) and (4) do cross over, since at a location very close to a black hole, $\lambda \rightarrow \lambda_{Kep}$ for a sub-Keplerian flow.

The effect of magnetic tension is dramatic, and the inner part of the disk is evacuated in the Alfvén timescale: $r/v_A \sim (r/a_T)^{1/2} \lesssim 0.1$ s, for a 10 $M_\odot$ black hole with a realistic Alfvén speed, $v_A \simeq 0.1c$ (Nandi et al. 2001). The enhanced plasma ejection along the axis presumably causes sporadic magnetic flare events that would be observable as radio outbursts, at the same time reducing the X-ray emission from the disk that forms the base of the jet. Recently, such effects may have been seen (Safi-Harb & Kotani 2002) where simultaneous observations of 2 GHz radio and 2–20 keV X-ray fluxes from SS 433 have been made, and a clear dip in X-ray flux is seen at the same time a strong radio flare is observed. It is worth noting that similar anticorrelated variations are common during flares in GRS 1915+105 (Feroci et al. 1999; Naik et al. 2001), and we suggest that the flares in SS 433 originate in the same way.

3. CONCLUDING REMARKS

In this Letter, we have studied various competing processes for the creation of bullets which move ballistically in the jet of SS 433. We showed that blobs may be separated by (1) Comptonization, (2) shock oscillations due to resonance, (3) oscillations due to inherent unsteady accretion solutions, and (4) intense magnetic tension of the toroidal flux tubes. We reject the first possibility because it requires a large Keplerian disk, which is unlikely. We are unable to distinguish at this stage which type of shock oscillation is more capable of producing bullet formation in SS 433, but we prefer the third possibility owing to its impulsive and generic nature and smaller involved region. We believe that the fourth possibility of the inner disk evacuation should produce flaring events but will occur rather rarely, perhaps only once in a single precession period, when the magnetic field of the companion is preferentially tilted toward the accretion disk during precessional motion. This fourth mechanism gives rise to an anticorrelation between radio and X-rays, perhaps already observed in SS 433 (Safi-Harb & Kotani 2002).

S. K. C., A. N., and S. D. acknowledge a grant from the Department of Science and Technology, India, and financial support from CEA/Saclay, where part of this work was performed. P. J. W. is grateful for hospitality at the Department of Astrophysical Sciences, Princeton University, and for support from the Research Program Enhancement program at Georgia State University.

REFERENCES

Abell, G. O., & Margon, B. 1979, Nature, 279, 701
Belcher, J. W., & MacGregor, K. B. 1976, ApJ, 210, 498
Biretta, J. A., Cohen, M. H., Unwin, S. C., & Pauliny-Toth, I. I. K., 1983, Nature, 306, 42
Blundell, K. M., Mioduszewski, A. J., Muxlow, T. W. B., Podsiadlowski, P., & Rupen, M. P. 2001, ApJ, 562, L79
Borisov, N. V., & Fabrika, S. N. 1987, Soviet Astron. Lett., 13, 200
Chakrabarti, S. K. 1990, Theory of Transonic Astrophysical Flows (Singapore: World Scientific)
———. 1999, A&A, 351, 185
———. 2002, in IAU Colloq. 187, Exotic Stars as Challenges to Evolution, ed. W. Vanhamme & C. Tout, in press
Chakrabarti, S. K., & D'Silva, S. 1994, ApJ, 424, 138
Chakrabarti, S. K., & Manickam, S. G. 2000, ApJ, 531, L41
Corbel, S. et al. 2001, ApJ, 554, 43
Das, T., & Chakrabarti, S. K. 1999, Classical Quantum Gravity, 16, 3879
Davidson, K., & McCray, R. 1980, ApJ, 241, 1082
Eggum, G. E., Coroniti, F. V., & Katz, J. I. 1985, ApJ, 298, L41
Feroci, M., Matt, G., Pooley, G., Costa, E., Tavani, M., & Belloni, T. 1999, A&A, 351, 985
Gies, D. R., McSwain, M. V., Riddle, R. L., Wang, Z., Wiita, P. J., & Wingert, D. W. 2002, ApJ, 566, 1069
Klein-Wolt, M., Fender, R. P., Pooley, G. G., Belloni, T., Migliari, S., Morgan, E. H., & van der Klis, M. 2001, Ap&SS Suppl., 276, 291
Kotani, T., & Trushkin, S. 2001, IAU Circ. 7747
Langer, S. H., Chanmugam, G., & Shaviv, G. 1982, ApJ, 258, 289
Lovelace, R. V. E. 1976, Nature, 262, 649
Margon, B. 1984, ARA&A, 22, 507
Mirabel, I. F., & Rodriguez, L. F. 1994, Nature, 371, 46
Molteni, D., Acharya, K., Kuznetsov, O., Bisikalo, D., & Chakrabarti, S. K. 2001, ApJ, 563, L57
Molteni, D., Lanzafame, G., & Chakrabarti, S. K. 1994, ApJ, 425, 161
Molteni, D., Sponholz, H., & Chakrabarti, S. K. 1996, ApJ, 457, 805 (MSC)
Naik, S., Agrawal, P. C., Rao, A. R., Paul, B., Seetha, S., & Kasturirangan, K. 2001, ApJ, 546, 1075
Nandi, A., Chakrabarti, S. K., Vadawale, S., & Rao, A. R. 2001, A&A, 380, 245
Paragi, Z., Fejes, I., Vermeulen, R. C., Schilizzi, R. T., Spencer, R. E., & Stirling, A. M. 2002 in Proc. 6th European VLBI Network Symposium, ed. R. W. Porcas, A. P. Lobanov, & J. A. Zensus (Bonn: MPIfR), 263
Paragi, Z., et al. 1999, A&A, 348, 910
Ryu, D., Chakrabarti, S. K., & Molteni, D. 1997, ApJ, 474, 378 (RCM)
Safi-Harb, S., & Kotani, T. 2002, in Proc. 4th Microquasar Workshop, ed. Ph. Dourouchaux, Y. Fuchs, & J. Rodriguez (Kolkata: CSP), in press
Shakura, N. I., & Sunyaev, R. A. 1973, A&A, 24, 337
Smith, D. M., Heindl, W. A., & Swank, J. H., 2002, ApJ, 569, 362
Stephenson, C. B., & Sanduleak, N. 1977, ApJS, 33, 459
Stewart, G. C., et al. 1987, MNRAS, 228, 293
Vadawale, S. V., Rao, A. R., Nandi, A., & Chakrabarti, S. K. 2001, A&A, 370, L17
van den Heuvel, E. P. J. 1981, Vistas Astron., 25, 95
Vermeulen, R. C., et al. 1993, A&A, 270, 189
Watson, M. G., Stewart, G. C., Brinkmann, W., & King, A. R. 1986, MNRAS, 222, 261
Yuan, W., Kawai, N., Brinkmann, W., & Matsuoka, M. 1995, A&A, 297, 451

Mon. Not. R. Astron. Soc. 349, 649–664 (2004) doi:10.1111/j.1365-2966.2004.07536.x

Properties of accretion shock waves in viscous flows around black holes

Sandip K. Chakrabarti[1,2★] and Santabrata Das[1]

S.N. Bose National Centre for Basic Sciences, JD-Block, Sector III, Salt Lake, Kolkata 700098, India
Centre for Space Physics, Chalantika 43, Garia Station Road, Garia, Kolkata 700084, India

Accepted 2003 December 9. Received 2003 December 8; in original form 2003 October 14

ABSTRACT

Accretion flows having low angular momentum and low viscosity can have standing shock waves. These shocks arise because of the presence of multiple sonic points in the flow. We study the region of the parameter space in which multiple sonic points occur in viscous flows in the absence of cooling. We also separate the parameter space into regions allowing steady shocks and oscillating shocks. We quantify the nature of two critical viscosities which separate the flow topologies. The post-shock region being hotter, it emits harder X-rays and oscillating shocks cause oscillating X-ray intensities giving rise to quasi-periodic oscillations. We show that with the increase in viscosity parameter, the shock always moves closer to the black hole. This implies an enhancement of the quasi-periodic oscillation frequency as viscosity is increased.

Key words: accretion, accretion discs – black hole physics – shock waves.

1 INTRODUCTION

In the standard theory of thin accretion flows around black holes (Shakura & Sunyaev 1973, hereafter referred to as SS73) viscosity plays a major role. Viscosity transports angular momentum outwards and allows matter to sink into the potential well formed by the central compact object. In this model, the flow angular momentum is assumed to be Keplerian and this is the standard notion about how matter is accreted. However, Chakrabarti & Molteni (1995, hereafter referred to as Paper I), and Lanzafame, Molteni & Chakrabarti (1998, hereafter referred to as Paper II), through extensive numerical simulations showed that the angular momentum distribution depends strictly on the viscosity parameter and the way the viscous stress is defined. They showed that close to a black hole, the disc does not have a Keplerian distribution. This is because the flow must be supersonic on the horizon (Chakrabarti 1990a) whereas a Keplerian disc is always subsonic (SS73). In Papers I and II, it was shown that for a large region of the parameter space, shocks may form in accretion flows and when viscosity is increased beyond a critical value (Chakrabarti 1990a,b, 1996a, hereafter C96a), the shocks disappear.

Paper I also improved the concept of the viscosity parameter α (SS73): it argued that in a generalized flow with significant radial velocity ϑ, the viscous stress $w_{\phi r}$ should not be equated to $-\alpha P$ as in SS73, where P is the total pressure, but to $-\alpha_\Pi(P + \rho\vartheta^2)$ (actually, its vertically integrated value using a thin-disc approximation) where ρ is the density and the subscript Π is given to α to distinguish it from the Shakura–Sunyaev viscosity parameter. The latter prescription naturally goes over to the original prescription when radial velocity is unimportant as in the case of a standard Keplerian disc model (SS73); however, when the radial velocity is important as in the transonic flow solutions (Chakrabarti 1990a), the latter definition preserves the angular momentum even across axisymmetric discontinuities, such as accretion shocks. The reason is that, according to the Rankine–Hugoniot conditions (Landau & Lifshitz 1959), in a steady flow, the sum of the thermal pressure and ram pressure, i.e. $P + \rho\vartheta^2$ is continuous across discontinuities. This makes the viscous stress $w_{r\phi}$ continuous across axisymmetric discontinuities as well.

In an earlier study, Chakrabarti (1989a, hereafter C89a) considered the transonic properties of isothermal accretion flows and showed that for a large region of the parameter space spanned by the specific angular momentum and the temperature of the flow, an accretion disc can have standing shock waves. The specific angular momentum of the disc was smaller than that of a Keplerian disc everywhere. This flow comes about especially when the matter is accreted from the winds of a binary companion. Subsequently, Chakrabarti (1990b, hereafter C90b) showed that inclusion of viscosity reduces the region of the parameter space in that, at a sufficiently high viscosity, the Rankine–Hugoniot conditions which must be satisfied at a steady shock are not satisfied anywhere in the flow. The existence of standing shocks in sub-Keplerian inviscid accretion discs has been tested independently by several groups since then (Nobuta & Hanawa 1994; Yang & Kafatos 1995; Lu & Yuan 1997). Numerical simulations have also been carried out with several independent codes such as smoothed particle hydrodynamics (SPH) and

★E-mail: chakraba@bose.res.in

total variation diminishing (TVD) and distinct standing shocks were found exactly at the predicted locations (Chakrabarti & Molteni 1993; Molteni, Ryu & Chakrabarti 1996b).

In more recent years, it has become evident that the standing shocks may be very important in explaining the spectral properties of black hole candidates (Chakrabarti & Titarchuk 1995, hereafter CT95) as the post-shock region behaves as the boundary layer where accreting matter dissipates its thermal energy and generates hard X-rays by inverse Comptonization. C96a considered the unification of solutions of winds and accretion around compact objects. However, the cooling was treated in terms of a parameter and no parameter space was studied. The post-shock region is also found to be responsible for producing relativistic outflows (Chakrabarti 1999; Chattopadhyay & Chakrabarti 2002). Furthermore, numerical simulations indicated that the shocks may be oscillating at nearby regions of the parameter space in the presence of cooling effects (Molteni, Sponholz & Chakrabarti 1996a) and the shock oscillations correctly explain intricate properties of quasi-periodic oscillations (Chakrabarti & Manickam 2000). Recent observations support the presence of sub-Keplerian flows in accretion discs (Smith et al. 2001; Smith, Heindl & Swank 2002).

In view of the importance of the sub-Keplerian flows we plan to reinvestigate the work done on isothermal flow by C89a and C90b by extending them to the study of *polytropic flows* to check the properties of shock waves in viscous flows. What is more, unlike C89a and C90b, we investigate the behaviour of the solutions in the entire parameter space spanned by the specific energy, angular momentum and viscosity. Some work was done in C96a, but the parameter space was not explored. We find very important results: even when the viscosity parameter is very high, the flow continues to have three sonic points, a prime condition to have a standing or oscillating shock wave. However, the parameter space for standing shock waves is gradually reduced with the increase of viscosity. On the other hand, we discover that the shock location itself is reduced with the increase in viscosity parameter.

We wish to emphasize that the problem at hand is by no means a trivial extension of previous work. In an accretion flow, where the flow is subsonic at a large distance and is necessarily supersonic on the horizon, the flow has first to become supersonic at a sonic point and then, after the shock transition where it becomes subsonic, the flow must again pass through the inner sonic point before entering the black hole. In studying flows with constant energy (Chakrabarti 1989b, hereafter C89b) or isothermal flows (C89a), both the sonic points were known when the so-called 'eigenvalues', namely, the specific energy (for polytropic flow) or temperature (for isothermal flow) and the specific angular momentum are supplied. In the present situation, neither of these two quantities is constant in the flow since the viscosity will heat up the gas, increase the thermal energy and at the same time reduce the specific angular momentum as the flow proceeds towards the black hole. Thus, the inner sonic point, through which the flow will pass after the shock, is not known before the entire problem is actually solved. We have devised a novel way to solve the entire problem by iterating the location of the inner sonic point till the shock condition is satisfied. We have identified the topologies which are essential for shock formation. We have also identified the parameter space which will have solutions with three sonic points but need not have standing shocks. These solutions generally produce oscillating shocks as shown by Ryu, Chakrabarti & Molteni (1997). In C96a, some effects of viscous heating were studied and the cooling effect was chosen to be proportional to the heating effect for simplicity. No parameter space study was made. In the present paper, we ignore cooling completely. The exact effects of various cooling processes and their influence on the parameter space will be discussed elsewhere (Das & Chakrabarti 2004).

The plan of the present paper is the following: in the next section, we present the model equations. In Section 3, we present the sonic-point analysis. In Section 4, we study the global solution topology. In Section 5, we classify the parameter space in terms of whether a global solution has triple sonic points or not. In Section 6, we classify the region with triple sonic points further to indicate which region may allow standing shocks and which region may allow oscillating shocks in the presence of viscosity. We show in particular that matter with very low angular momentum may allow shocks even when the viscosity parameter is very high. In C96a it was shown that topologies are changed with viscosity and there exists two critical viscosity parameters at which such changes take place. In Section 7, we quantify these critical viscosity parameters. Finally, in Section 8 we discuss the relevance of shocks in the context of quasi-periodic oscillations and make concluding remarks.

2 MODEL EQUATIONS

We consider a steady, thin, viscous, axisymmetric accretion flow on to a Schwarzschild black hole. The space-time geometry around a Schwarzschild black hole is described by the pseudo-Newtonian potential introduced by Paczynski & Wiita (1980). Here, one uses the pseudo-Newtonian potential given by

$$g(r) = -\frac{GM}{r - 2GM_{\rm BH}/c^2}.$$

We consider the units of velocity, distance and time to be c, $r_g = 2GM_{BH}/c^2$ and $2GM_{\rm BH}/c^3$, respectively, where c is the velocity of light, and G and $M_{\rm BH}$ are the gravitational constant and the mass of the black hole, respectively. In these units, defining $x = r/r_g$, we get the potential as $g(x) = -[2(x-1)]^{-1}$. We assume the disc to be in *hydrostatic* equilibrium in the vertical direction.

In the steady state, the dimensionless hydrodynamic equations that govern the infalling matter are the following (C96a):

(i) radial momentum equation,

$$\vartheta\frac{{\rm d}\vartheta}{{\rm d}x} + \frac{1}{\rho}\frac{{\rm d}P}{{\rm d}x} - \frac{\lambda(x)^2}{x^3} + \frac{1}{2(x-1)^2} = 0; \qquad \text{(1a)}$$

(ii) baryon number conservation equation,

$$\dot{M} = \Sigma \vartheta x, \tag{1b}$$

apart from a geometric constant;

(iii) angular momentum conservation equation,

$$\vartheta \frac{d\lambda(x)}{dx} + \frac{1}{\Sigma x}\frac{d}{dx}\left(x^2 W_{x\phi}\right) = 0; \tag{1c}$$

and finally

(iv) entropy generation equation,

$$\Sigma \vartheta T \frac{ds}{dx} = Q^+ - Q^-. \tag{1d}$$

The local variables ϑ, ρ, P and $\lambda(x)$ in the above equations are the radial velocity, density, isotropic pressure and specific angular momentum of the flow, respectively. Here Σ and $W_{x\phi}$ are the vertically integrated density (Matsumoto et al. 1984) and the viscous stress, s is the entropy density of the flow, and T is the local temperature. Q^+ and Q^- are the heat gained and lost by the flow (integrated in the vertical direction), respectively.

In our model of the disc which is assumed to be in hydrostatic equilibrium in the vertical direction, the local disc height is obtained by equating the pressure gradient force in the vertical direction with the component of the gravitational force in that direction. The half-thickness of the disc is obtained as:

$$h = ax^{1/2}(x-1). \tag{2}$$

Here, a is the adiabatic sound speed defined as $a = \sqrt{\gamma P/\rho}$. As discussed in the introduction, we shall use the viscosity prescription of Paper I valid rigorously for flows with significant radial motion. Thus the viscous stress is:

$$W_{x\phi} = -\alpha_\Pi \Pi, \tag{3}$$

where $\Pi = W + \Sigma\vartheta^2$. As mentioned before, this will ensure that the viscous stress is continuous across the axisymmetric shock wave that we are studying here. It is to be noted that in the SS73 prescription, $W_{x\phi}$ is not continuous across the shock. Thus, the stress would transport angular momentum at different rates on two sides of the shock which would always move the shock one way or the other. This is unphysical, since in the absence of viscosity, a standing, axisymmetric shock is perfectly stable. It is impossible that an infinitesimal viscosity should destabilize the shock. However, this would have been the case if the SS73 prescription were rigorously correct.

3 SONIC-POINT ANALYSIS

At the outer edge of the accretion disc, matter has almost zero radial velocity even though it enters the black hole with the velocity of light c. Thus, during accretion, at some point, the velocity of matter should exactly match the sound speed. This point is called a critical point or a sonic point. When matter crosses a sonic point, it becomes transonic. As Chakrabarti (C89ab, C90ab) pointed out, depending on the initial parameters, a flow may have multiple sonic points and therefore, depending on whether the shock conditions are satisfied or not, a flow may or may not have a standing shock.

For the sake of completeness, we carry out the sonic-point analysis by solving the above equations (1)–(3) using a method similar to that used in C89b.

3.1 Sonic-point conditions

In the present analysis, we use the MISStress prescription (C96a) for computing Q^+, and $W_{x\phi}$ is obtained from equation (3). For the accretion flow, the entropy equation (equation 4) can be simplified as

$$\frac{\vartheta}{\gamma-1}\left[\frac{1}{\rho}\frac{dP}{dx} - \frac{\gamma P}{\rho^2}\frac{d\rho}{dx}\right] = \frac{Q^- - Q^+}{\rho h} = C - H, \tag{4}$$

and then $H(= Q^+/\rho h)$ takes the form

$$H = Ax(ga^2 + \gamma\vartheta^2)\frac{d\Omega}{dx}, \tag{5}$$

where γ is the adiabatic index, $A = -\alpha_\Pi I_n/\gamma$ and $g = I_{n+1}/I_n$. Here, $\Omega(x)$ is the angular velocity of the accreting matter at the radial distance x, n is the polytropic index ($n = (\gamma-1)^{-1}$), and I_n and I_{n+1} come from the definition of the vertically averaged density and pressure (Matsumoto et al. 1984).

In the present analysis, we use $Q_- = 0$, i.e. the cooling is ignored. This would be strictly valid if the accretion rate is low, so that the loss of energy by bremsstrahlung cooling is insignificant compared to the rest-mass energy.

After some simple algebra and eliminating da/dr, etc. we get from the governing equations 1(a-c) and equation (2) the following first-order linear differential equation:

$$\frac{d\vartheta}{dx} = \frac{N}{D}, \tag{6}$$

where the numerator N is

$$N = -\frac{\alpha_\Pi A(a^2 g+\gamma\vartheta^2)^2}{\gamma x} - \left[\frac{\lambda^2}{x^3}-\frac{1}{2(x-1)^2}\right]\left[2\alpha_\Pi g A(a^2 g+\gamma\vartheta^2)+\frac{(\gamma+1)\vartheta^2}{(\gamma-1)}\right]$$
$$-\frac{\vartheta^2 a^2(5x-3)}{x(\gamma-1)(x-1)} - \frac{\alpha_\Pi g A a^2(5x-3)(a^2 g+\gamma\vartheta^2)}{\gamma x(x-1)} + \frac{2\lambda A\vartheta(a^2 g+\gamma\vartheta^2)}{x^2} \quad (7)$$

and the denominator D is

$$D = \frac{2a^2\vartheta}{(\gamma-1)} - \frac{(\gamma+1)\vartheta^3}{(\gamma-1)} - A\alpha_\Pi\vartheta(a^2 g+\gamma\vartheta^2)\left[(2g-1)-\frac{a^2 g}{\gamma\vartheta^2}\right] \quad (8)$$

Both N and D are algebraic equations which makes this model easily tractable.

At the sonic point, both the numerator and the denominator must vanish simultaneously. For $D = 0$, one can get the expression for the Mach number, $M(x_c)$, at the sonic point and it is given by

$$M(x_c) = \sqrt{\frac{-m_b - \sqrt{m_b^2 - 4m_a m_c}}{2m_a}} \quad (9)$$

where

$$m_a = -A\alpha_\Pi\gamma^2(\gamma-1)(2g-1) - \gamma(\gamma+1),$$

$$m_b = 2\gamma - 2A\alpha_\pi g\gamma(\gamma-1)(g-1)$$

$$m_c = A\alpha_\Pi g^2(\gamma-1).$$

In the weak viscosity limit, $\alpha_\Pi \to 0$ and the Mach number at the sonic point is

$$M(x_c) \approx \sqrt{\frac{2}{\gamma+1}}$$

for $\alpha_\Pi \to 0$, a result obtained in C89b.

Setting $N = 0$, we get an algebraic equation for the sound speed at the sonic point, which is given by

$$F(\mathcal{E}_c, \lambda_c, x_c) = -\left[\frac{\alpha_\Pi A\{g+\gamma M^2\}^2}{\gamma x} + \frac{\alpha_\Pi A(5x-3)\{g+\gamma M^2\}}{\gamma x(x-1)} + \frac{M^2(5x-3)}{x(\gamma-1)(x-1)}\right]a^2$$
$$+\frac{2\lambda A M(g+\gamma M^2)}{x^2}a - \left[\frac{\lambda^2}{x^3}-\frac{1}{2(x-1)^2}\right]\left[2\alpha_\Pi g A(g+\gamma M^2)+\frac{(\gamma+1)M^2}{(\gamma-1)}\right] = 0. \quad (10)$$

We solve the above quadratic equation to obtain the sound speed at the sonic point. Das et al. (2001) suggested that, depending on a given set of initial parameters, the accretion flow may have a maximum of four sonic points where one of the sonic points always lies inside the black hole horizon for non-dissipative accretion flow. In our present study, we also expect a similar result.

3.2 Nature of the sonic points

A black hole accretion is always transonic. Thus the originally subsonic matter definitely has to pass through the sonic point to become supersonic before entering the black hole. Depending on the initial parameters, a flow may have multiple sonic points. The nature of the sonic point depends on the value of the velocity gradients at the sonic point. It is easy to show that $d\vartheta/dx$ assumes two values at the sonic point. One of them is valid for the accretion flow and the other is valid for the wind. If both the derivatives are real and of opposite signs, the sonic point is saddle type. When the derivatives are real and of the same sign, the sonic point is nodal type. When the derivative is complex, the sonic point is spiral type (or O-type, for non-dissipative flow). See C90b for details of the classifications. In order to form a standing shock, the flow must have more than one saddle-type sonic point.

In Fig. 1(a) we plot the variation of specific angular momentum (λ_c) as a function of the logarithmic sonic-point location (x_c) for a given viscosity parameter ($\alpha_\Pi = 0.1$). Here different curves are drawn for different specific energies at the sonic points. The energies, from the top curve to the bottom, are given by: $\mathcal{E}_c = 0.0007$, 0.001, 0.003, 0.005, 0.007, 0.011, 0.015, 0.019, 0.023 and 0.027, respectively. The long-dashed curve at the top represents the Keplerian angular momentum distribution which is completely independent of the initial flow parameters and depends only on the geometry. The solid part of the curves represents the saddle-type sonic points, the dotted part of the curves represents the nodal-type sonic points and the short-dashed part of the curves are for the spiral-type sonic points. First notice that the sonic points always occur at angular momentum below the Keplerian value. Notice that for lower values of the specific energy at the sonic point, an accretion flow contains all three types of sonic points in a systematic order: saddle–nodal–spiral–nodal–saddle for a monotonic increase of the location of the sonic points. With the increase of energy $\mathcal{E}_c$ the region of spiral-type sonic points gradually decreases and is finally replaced by the nodal-type sonic points, though multiple sonic points still exist. The shaded area separates the nodal-type sonic-point region in the λ_c–x_c plane. With further increase of energy all the nodal-type sonic points also disappear and are replaced by saddle-type sonic points. In this case, the flow has only one sonic point for a given sub-Keplerian angular momentum. Thus, for a given angular momentum of the flow, there exists

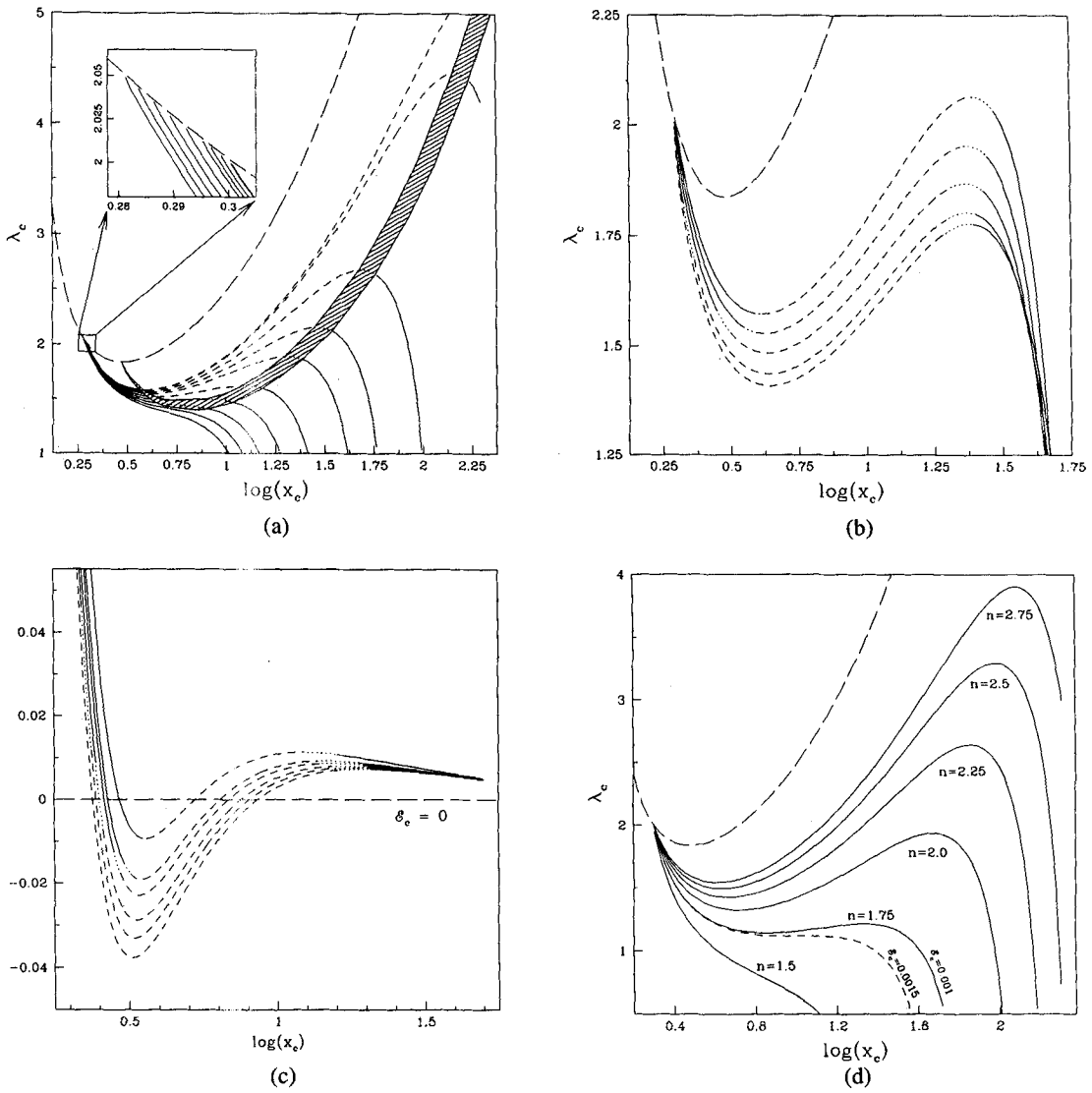

Figure 1. (a) Variation of specific angular momentum (λ_c) as a function of the logarithmic sonic-point location (x_c) for the viscosity parameter ($\alpha_\Pi = 0.1$). The long-dashed curve is the Keplerian angular-momentum distribution. The solid curves represent the saddle-type sonic points, dotted curves represent the nodal-type sonic points and the short-dashed curves are for the spiral-type sonic points. The shaded area is the nodal-type sonic-point region. (b) Variation of angular momentum at the sonic point as the viscosity parameter is varied. The specific energy at the inner sonic point is held fixed at 0.006. From the uppermost to the lowermost curve: $\alpha_\Pi = 0$, 0.2, 0.4, 0.6 and 0.7, respectively. Other notation is the same as in (a). (c) Variation of the specific energy at the inner sonic point as a function of the viscosity parameter α_Π. From the uppermost curve to the lowermost curve, $\alpha_\Pi = 0$, 0.25, 0.35, 0.5, 0.6 and 0.7, respectively. Other notation is the same as in (a). (d) Variation of the specific angular momentum at the inner sonic point as a function of the polytropic index n (marked on each curve). Generally, the number of sonic points decreases by decreasing n. The specific energy has been kept fixed at 0.001 except for the dashed curve where it is 0.0015, to show that for a given polytropic index, the number of sonic points increases with decreasing energy.

a range of energy $\mathcal{E}_{\rm min} < \mathcal{E}_c < \mathcal{E}_{\rm max}$ such that the flow has multiple sonic points. In the inset, we zoom in on a small portion of the curve close the Keplerian value to highlight the fact that the angular momentum at the sonic point always remains sub-Keplerian when the cooling process is ignored. In the future (Das & Chakrabarti, 2004), we shall show that a flow can also be super-Keplerian when cooling is added.

In Fig. 1(b) we show a very important aspect of viscous transonic flow. Here we show how the angular momentum at the sonic point varies when the viscosity parameter α_Π is increased. We hold the energy at the sonic point fixed at $\mathcal{E}_c = 0.006$. In the absence of viscosity ($\alpha_\Pi = 0$, the uppermost curve), the flow has all three types of sonic points. Similar to Fig. 1(a), here we also indicate the saddle-, nodal- and spiral-type sonic points by the solid, dotted and short-dashed curves, respectively. The uppermost long-dashed curve represents the Keplerian angular momentum distribution. With the increase of α_Π, more and more inner saddle-type sonic points are replaced by nodal-type sonic points and similarly nodal-type sonic points are also replaced by spiral-type sonic points. The curves, from the uppermost to the lowermost, are for $\alpha_\Pi = 0$, 0.2, 0.4, 0.6, 0.7, respectively. For $\alpha_\Pi = 0.7$, all the inner saddle-type sonic points disappear and only the spiral-type points remain. Thus there exists a critical viscosity parameter $\alpha_{\Pi(c,i)}$ at a given $\mathcal{E}_{\rm in}$ for which all the inner saddle-type sonic points are completely converted into spiral-type points. In this case, the flow has no choice but to pass through the outer sonic point only. The existence of such

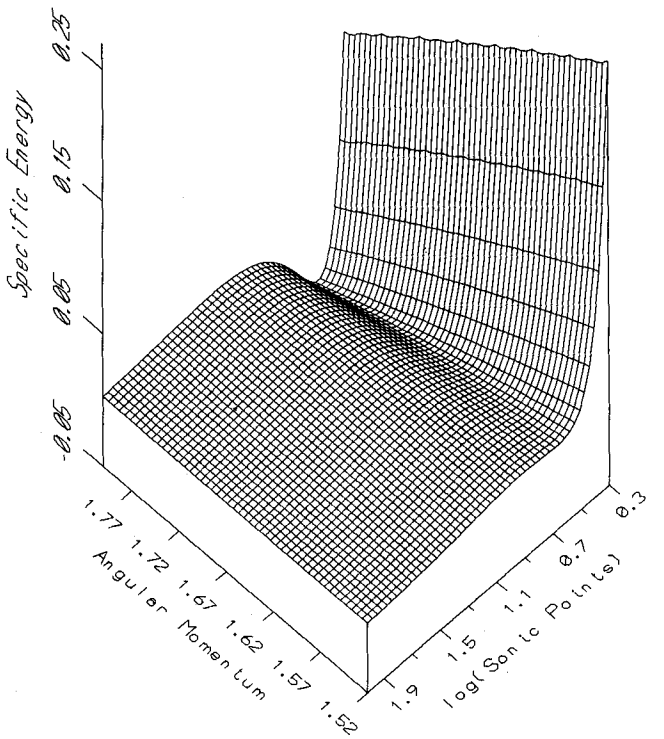

Figure 2. A gradual change in the number of physical sonic points is easily seen in this three-dimensional view of $F(E_c, \lambda_c, x_c) = 0$ (equation 9) surface. At high angular momenta there are three sonic points, but they merge to become one at lower angular momenta. $\alpha_\Pi = 0.01$ has been chosen.

critical viscosities has been predicted in C90ab and C96a – below we compute their values exactly as a function of the inflow parameters. This behaviour also hints at the conclusion that the parameter space for the existence of a transonic flow may shrink with increase of viscosity.

We continue our investigation of the transonic nature of the flow and have replotted in Fig. 1(c) a figure similar to Fig. 1(a) but we increase α_Π gradually while keeping the specific angular momentum at the sonic point fixed ($\lambda_c = 1.65$). Values of α_Π are, from the top to the bottom curve, $\alpha_\Pi = 0$, 0.25, 0.35, 0.5, 0.6 and 0.7, respectively. Solid, dotted and short-dashed lines represent the saddle-type, nodal-type and spiral-type sonic points, respectively. The long-dashed line separates the positive and negative energy regions in the $\mathcal{E}_c$–x_c plane. Notice that, for increasing α_Π, saddle-type sonic points are gradually replaced by the nodal- and spiral-type sonic points: outer saddle-type sonic points recede further away and the inner saddle sonic points proceed toward the black hole horizon. For $\alpha_\Pi = 0.7$, the inner saddle-type sonic points completely disappear and become spiral type. This behaviour points to a critical value of the viscosity parameter ($\alpha_{\Pi,c}$) which separates the accretion flow from the multiple sonic-point regime to the single sonic-point regime at a given λ_c. It is also clear that at the same sonic point, the specific energy steadily decreases for increasing α_Π. This is because, when α_Π is increased, the accreting matter tends to become a Keplerian disc closer to the black hole and becomes more strongly bound with lower energy. Note that the energy at the outer sonic point always remains positive for all initial parameters.

In our final study of the nature of the sonic points, we chose n, the polytropic index, to be our free parameter. For a highly relativistic flow, or a radiation-dominated flow, $n = 3$, but for a monatomic, non-relativistic gas, $n = 3/2$. In Fig. 1(d) we show the variation of λ_c with sonic-point location x_c. We keep the specific energy at the sonic point to be 0.001. The long-dashed curve is the Keplerian distribution as before. We note that with the increase of the adiabatic index γ, i.e. decrease of the polytropic index n, the number of sonic points decreases from three to one. In this example, in the extreme non-relativistic regime ($n = 1.5$) the accretion flow has a single saddle-type sonic point for any specific angular momentum. For the same energy, for $n = 1.75$ there are three sonic points, indicating that a standing or an oscillating shock in the flow may be possible. In this figure, we also show that for a given n (such as for $n = 1.75$) if we increase the energy at the sonic point ($\mathcal{E}_c = 0.0015$), multiple sonic points disappear and a single sonic point forms. This indicates that there must be a critical value of $\mathcal{E}_c = \mathcal{E}_{\rm cri}$ associated with each n above which multiple sonic points do not exist when all other parameters are kept fixed.

The general behaviour of the flow at the sonic point is best seen in Fig. 2, where we depict the surface $F(\mathcal{E}_c, \lambda_c, x_c) = 0$ (equation 9) for $\alpha_\Pi = 0.01$. Sonic points x_c are plotted along the X-axis in the logarithmic scale, λ_c is plotted along the Y-axis and $\mathcal{E}_c$ is plotted along the Z-axis. At high angular momenta, there are three sonic points, but they merge to become one at lower angular momenta. Below a critical value $\lambda_{\rm cri}$, the flow does not have more than one sonic point.

4 GLOBAL SOLUTION TOPOLOGY

A basic criterion for studying shock properties is that the accretion flow must have multiple saddle-type sonic points and the shock should join two solutions – one passing through the outer sonic point and the other passing through the inner sonic point. The solution topologies

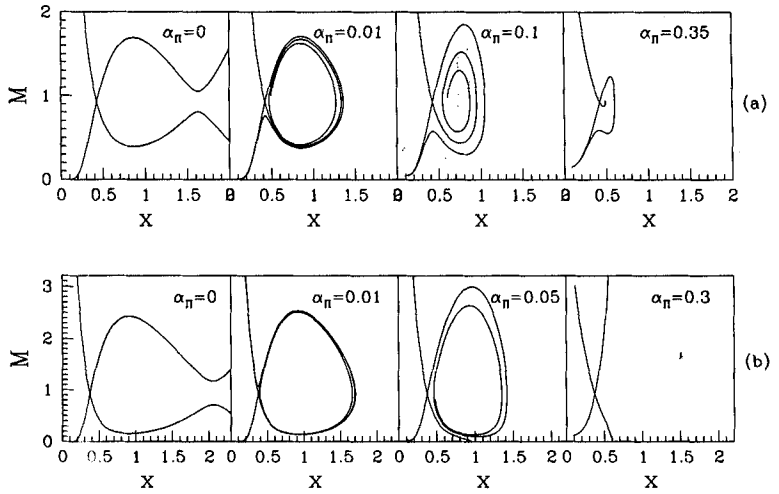

Figure 3. Variation of global solution topologies of the viscous accretion flow around black holes. In (a), drawn for $\lambda(x_{in} = 2.665) = 1.68$, the four panels show how the open topology at lower viscosity becomes closed at higher viscosity. In (b), drawn for $\lambda(x_{in} = 2.359) = 1.78$, the closed topology opens up again.

have already been discussed in C96a. The current paper studies in greater detail the topologies associated with $f = 1$ of C96a. In particular, we show below new pathways through which topologies may vary.

In Figs 3(a)–(b) we have shown how the flow topologies change with the viscosity parameter α_Π and the specific angular momentum λ_{in} at the inner sonic point x_{in}. Two distinct types of behaviour have been highlighted here: one at a low angular-momentum regime (Fig. 3a) and the other at a high angular-momentum regime (Fig. 3b). In Fig. 3(a) we keep the inner sonic point fixed at $x_{in} = 2.665$ and the specific angular momentum at this point is $\lambda_{in} = 1.68$. At low angular momentum and without viscosity (the box at the extreme left in Fig. 3a) the subsonic flow enters the black hole after passing through the inner sonic point. In the second box, the viscosity is slightly higher and topologies are closed for the same inner sonic point. So, for a given set of parameters, there must be a critical viscosity parameter ($\alpha_{\Pi c}$) for which open topologies become closed topologies. We will discuss critical viscosity rigorously in Section 7. Accretion with parameters causing this kind of topology never joins with any Keplerian disc unless a shock is formed (this will be shown below). When a standing shock formation is not possible, an accretion flow passes through the outer sonic point directly before falling into the black hole. For a further increase of α_Π (next two boxes) the closed topology shrinks gradually and finally disappears leaving behind only the outer sonic point (Bondi type). This is directly analogous to the shrinking of the phase space of a simple harmonic oscillator in the presence of damping (C90a). These solutions are basically the same as the $f = 1$ case of fig. 2(a) of C96a.

In Fig. 3(b), where solutions are plotted with a higher specific angular momentum at the inner sonic point ($x_{in} = 2.359$ and $\lambda_{in} = 1.78$), the explanations of the first and second boxes is similar to the earlier ones (Fig. 3a), but in the third box ($\alpha_\Pi = 0.05$) the accretion flow topology reverses its direction of spiraling and the flow can join with a Keplerian disc very close to a black hole. All the differences between these two figures (Figs 3a and b) are mainly due to the difference of specific angular momentum at the sonic point rather than the change of sonic-point locations. In Fig. 11 (below), we will show that the nature of the accretion flow topologies have a strong dependence on the angular momentum at the sonic point. For a higher α_Π (next two boxes) the Keplerian disc comes even closer to the black hole and topologies passing through the inner sonic point becomes Bondi type. We suspect that two limits of viscosity parameters would cause an oscillation of the inner part of the Keplerian disc, but we cannot be certain about it without a time-dependent numerical simulation.

In order to show that flow topologies often can take new pathways than what was already known (C96a), in Fig. 4 we have plotted solution topologies passing through the outer sonic point chosen at $x_{out} = 25r_g$ and the specific angular momentum $\lambda(x_{out})$ is 1.8. The viscosity parameter is varied (marked on each box). For a lower α_Π, the topologies are closed as in fig. 4 of C96a and a flow having this topology cannot be transonic anyway. When α_Π is increased, closed topologies gradually open up (unlike C96a where $x_{out} = 35$ was chosen and the opening of the topologies did not occur) and if the shock condition is satisfied, the accretion flow passing through the outer sonic point jumps into the subsonic branch and goes through the inner sonic point before entering the black hole. For higher α_Π, the same outer sonic point no longer remains saddle type. First it becomes nodal type and then it becomes spiral type (Fig. 1a). Considering that the outer sonic point recedes farther away with the increase of α_Π, this behaviour is not surprising. This, together with fig. 4 of C96a, shows that there could be more than one way of reaching a nodal topology.

5 CLASSIFICATION OF THE PARAMETER SPACE

An important part of understanding a viscous flow is to classify the parameter space as a function of the viscosity parameter. In Fig. 5 we have separated the parameter space for the accretion flow which can pass through the inner sonic point. The angular momentum at this sonic point (λ_{in}) is varied along the X-axis and the corresponding specific energy at the inner sonic point ($\mathcal{E}_{in}$) is plotted along the Y-axis. The

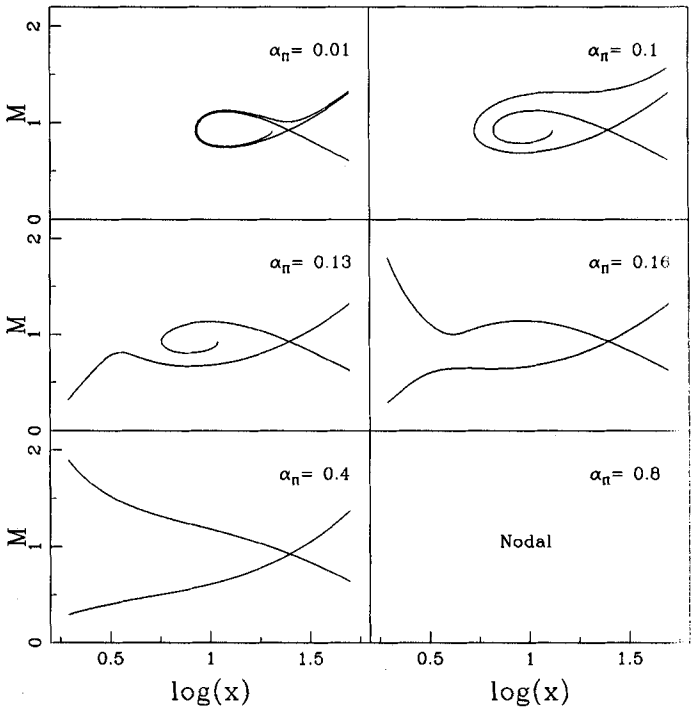

Figure 4. Variation of global solution topologies of the viscous accretion flows when the outer sonic point is kept fixed at $x_{out} = 30r_g$ while the viscosity parameter is varied. The closed topologies (with one saddle type and a spiral type at the centre) at lower α_Π become open. Eventually, the saddle type also disappears to produce a nodal-type sonic point.

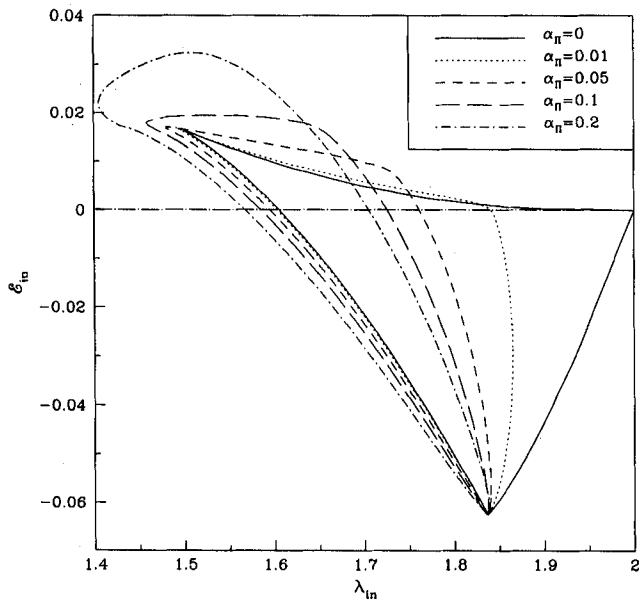

Figure 5. Classification of the parameter space spanned by the specific energy and the specific angular momentum of the flow at the inner sonic point. The bounded regions drawn for different viscosity parameters (marked in the inset) contain allowed solutions which may pass through the inner sonic point. As the viscosity increases, the region shifts towards lower angular momentum and higher energy.

region bounded by a given curve contains a parameter space in which multiple sonic points are possible. For instance, for $\alpha_\Pi = 0$, the region bounded by the solid curve is identical to the region found by C89b. For increasing α_Π, the region of multiple saddle-type sonic points is reduced near the high angular-momentum side, while it increases in the lower angular-momentum side. It may be recalled (C89b and Fig. 1a) that at low angular momentum, the number of sonic points is just one. With the rise of α_Π, the angular momentum at the sonic point is increased, increasing the number of sonic points. At a higher angular momentum, the situation is just the opposite. In this case, there are already multiple sonic points for $\alpha_\Pi \sim 0$ and for high enough α_Π, viscosity transports angular momentum very rapidly causing a steep rise in angular momentum itself. This, in turn, means that the flow can have only one saddle-type sonic point in this case.

6 STANDING SHOCKS AND FURTHER CLASSIFICATION OF THE PARAMETER SPACE

Although, in general astrophysical contexts, shocks are ubiquitous and possibly non-stationary, in an accretion flow, the location, strength and thermodynamic quantities may be quantified very exactly by using the Rankine–Hugoniot conditions (RHCs). The study is similar to the study of shocks in solar winds (e.g. Holzer & Axford 1970) and white-dwarf surfaces.

The shock conditions which we employ here are the usual RHCs presented in C89b, i.e. (a) the local energy flux is continuous across the shock; (b) the mass flux is continuous across the shock; (c) the momentum balance condition is satisfied; and finally (d) angular momentum should be continuous across the axisymmetric shock.

The way an accretion flow moves around a black hole, as seen from the local rotating frame, is as follows. First the flow, subsonic at a very large distance, passes through the outer sonic point and becomes supersonic. The RHCs then decide whether a shock will be formed or not. Of course, our consideration of satisfying the RHCs at a given location holds only if the shock is thin, i.e. viscosity is low. Nevertheless, we continue to use this prescription at higher viscosities to have a first-order guess of the shock location. Similarly, we assume that there is no excess source of torque at the shock itself, so that the angular momentum may be assumed to be continuous across it. This condition may be violated when magnetic fields are present. In the presence of large-scale poloidal magnetic fields, there could be magnetic torques which could make the flow angular momentum discontinuous.

6.1 Method of calculating the shock locations

Accretion flow first passes through the outer sonic point and becomes supersonic. It then jumps to the subsonic branch through a shock. This subsequently passes through the inner sonic point before disappearing into the black hole. In our present study we begin a numerical integration from the inner sonic point and proceed towards the outer edge of the accretion disc to look for the shock location. During integration along the subsonic branch, it is possible to calculate all the local variables (i.e. ϑ, a, M, ρ) at the post-shock region, in terms of the initial flow parameters. We calculate the total pressure, local flow energy, and specific angular momentum at the shock using these subsonic local variables. At the shock, the total pressure, local flow energy, mass accretion rate (one of the flow parameters) and specific angular momentum are conserved. These conserved quantities at the shock give the other set of supersonic local variables for the supersonic branch. This supersonic set of local variables helps us to find the outer sonic point uniquely for an accretion flow with fixed inner sonic point and other initial flow parameters when integration takes place towards the outer edge of the black hole. Thus, the accretion flow can be connected with both saddle-type sonic points through the shock for a dissipative system and this determines the standing shock location for a given set of initial parameters.

We compute the supersonic local flow variables in terms of the subsonic local flow variables in the following way.

Our model accretion flow is in vertical equilibrium and the total pressure of the accretion flow at any given point is given by

$$\Pi = W + \Sigma\vartheta^2, \tag{11}$$

where W and Σ are the vertically averaged thermal pressure and density, respectively.

We use the mass conservation equation (equation 1b) in equation (10) and calculate the sound speed a in terms of the radial velocity (ϑ) at the shock, x_s, in the supersonic branch, which is given by

$$a^2 = C_1C_2\vartheta - C_2\vartheta^2, \tag{12}$$

where

$$C_1 = \frac{4\pi\Pi x_s}{\dot{M}I_n}$$

and $C_2 = \gamma/g$.

From the local flow energy equation, the radial velocity ϑ at the shock in the supersonic branch can be calculated using equation (11) and is given by

$$\vartheta = \frac{-\vartheta_b + \sqrt{\vartheta_b^2 - 4\vartheta_a\vartheta_c}}{2\vartheta_a}, \tag{13}$$

where $\vartheta_a = 2nC_1C_2$, $\vartheta_b = -2nC_1C_2$,

$$\vartheta_c = 2\mathcal{E} - \frac{\lambda^2(x_s)}{x_s^2} + \frac{1}{(x_s - 1)}$$

and $\mathcal{E}$ is the local flow energy.

Here, the total pressure and flow energy at the shock are calculated with the help of the subsonic flow variables. We consider only the '+' sign as we are interested in finding the local flow variables in the supersonic branch. This radial velocity is used to get the sound speed (equation 12) in the supersonic branch of the flow. This is used to obtain the outer sonic point by using numerical integration. We thus have a complete solution with a standing shock in a viscous flow.

In Fig. 6(a) we have shown how a shock may be formed by joining two solutions, one with a lower entropy passing through the outer sonic point, and the other with a higher entropy passing through the inner sonic point. Two curves are drawn for two different energies (marked). $\mathcal{E}_{in}$ and $\mathcal{E}_{out}$ are the energies at the inner and outer sonic points for a shocked accretion flow which has a standing shock. Due to viscous heating processes, energy is increased and the shock wave is formed when the flow jumps from the lower-energy solution to the higher-energy solution. If we included only the cooling process, the situation would have been reversed. The flow parameters are $x_{out} = 39.7$, $\lambda_{in} = 1.65$,

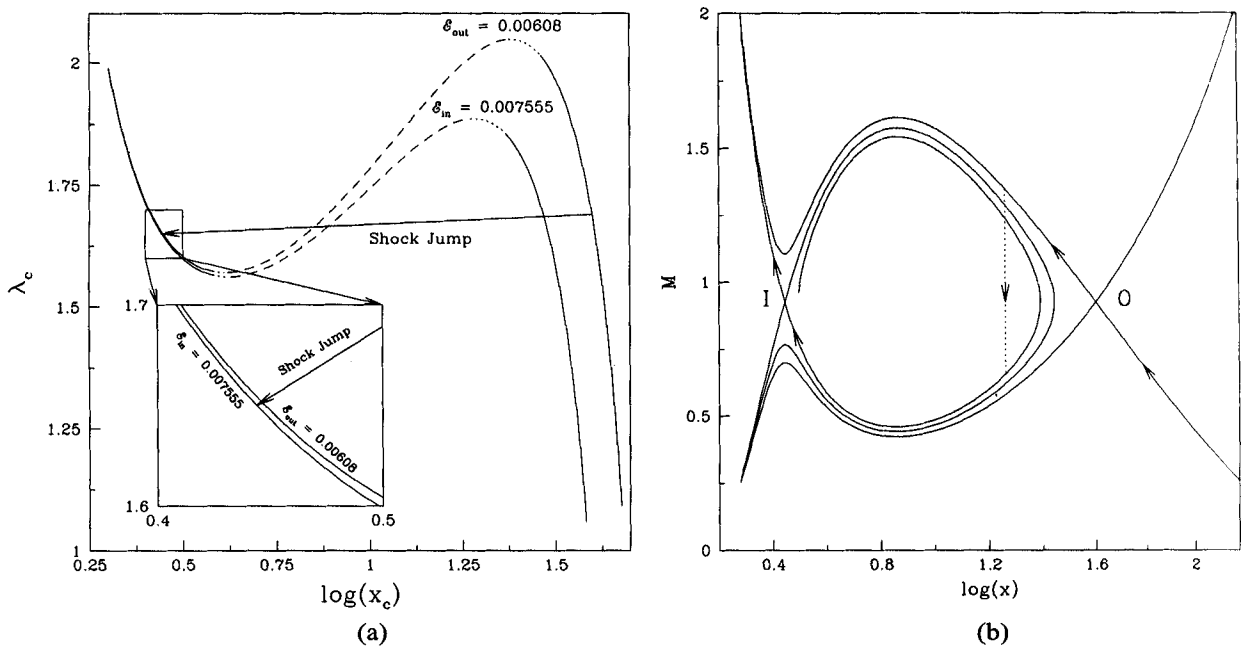

Figure 6. (a) An example of how a standing shock might form in viscous transonic flows is depicted here. Flow passing through the outer sonic point at x_{out} = 39.7 and energy $\mathcal{E}_{out}$ = 0.00608 has a shock and passes through the inner sonic point at x_{in} = 2.78 where its energy is $\mathcal{E}_{in}$ = 0.007555. The inset shows the details. (b) The actual solution topology for the case discussed in (a) is shown here which, along with the outer (O) and inner (I) sonic points, also shows the shock transition at x_s = 18.2 (vertical dotted line). The arrowed curve is followed by a flow while entering the black hole.

$\alpha_\Pi = 0.05$ and $\gamma = 4/3$. The shock condition uniquely determines the inner sonic point, which is at $x_{in} = 2.78$. The end positions of the long arrow mark the locations of the sonic points. In the inset, we zoom in on a selected region in the λ_c–x_c plane to show explicitly that the angular momentum is indeed decreased.

In Fig. 6(b) we present the complete solution of the flow which includes a standing shock in a viscous flow for the same set of parameters used to draw Fig. 6(a). The arrows indicate the direction of the accreting flow. Subsonic accreting flow passes through the outer sonic point (O) and becomes supersonic. At x_s, the shock conditions are satisfied – the flow jumps from the supersonic branch to the subsonic branch and subsequently passes through the inner sonic point (I). In this particular case, the shock conditions are satisfied at $x_s = 18.2$ and the shock is denoted by the dotted vertical line.

6.2 Parameter space which allows standing shocks

In Fig. 5 we have already classified the parameter space in terms of the number of sonic points in the flow. Here, in Fig. 7, we concentrate on the region which allows only standing shocks in a viscous flow. The viscosity parameters are marked. The region marked α_Π = 0 coincides with that in C89b and in Chakrabarti (1996b, 1998, hereafter C96b and C98, respectively) when appropriate models are considered. Compared to the inviscid case, the effective region of the parameter space shrinks in the high angular-momentum side when the viscosity is increased. The situation is exactly the opposite at the lower angular-momentum side. We observe that even at angular momentum as low as 1.4, standing shocks could be formed if the viscosity is high enough. Above a critical viscosity (which depends on other parameters as will be shown in Fig. 13 below), this region disappears completely.

We continue our study of the parameter space which may allow multiple sonic points. In Fig. 8 we show a curious feature: the mapping between the post-shock parameters and the pre-shock parameters. We plot the region of the post-shock parameters at the inner sonic point ($\mathcal{E}_{in}$, λ_{in}) (bounded by the solid curve) and the region of the pre-shock parameters at the outer sonic point ($\mathcal{E}_{out}$, λ_{out}) (bounded by the long-dashed curve) for a shock which is determined through the RHCs for $\alpha_\Pi = 0.01$. For each and every point in the pre-shock parameter space region, there exists a point in the post-shock parameter space region and therefore we have a complete solution. For definiteness, we also show vertical dashed and dotted lines in the two different angular-momentum ranges in the post-shock parameter space region in which λ_{in} is kept fixed but $\mathcal{E}_{in}$ is varied. The corresponding pre-shock parameters form a curve, indicating that both the angular momentum and the energy had to be adjusted to get the self-consistent solution. In a non-dissipative flow, there is no variation of energy and angular momentum in the accretion flow. As a result, both the inner and outer sonic-point parameter spaces merge (C89b; C98).

6.3 Parameter space which may allow oscillating shocks

An important role that is played by oscillating shocks is to produce the so-called quasi-periodic variations of the X-ray intensity from galactic black hole candidates. In inviscid flow, the region of the parameter space which produced multiple sonic points, but where the RHCs were

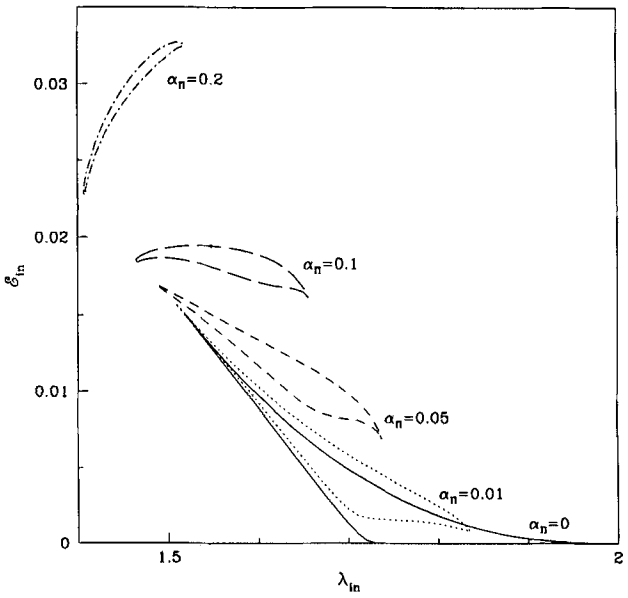

Figure 7. Variation of the region of the parameter space which forms a standing shock as a function of the viscosity parameter α_Π. The region shrinks with the increase of viscosity parameter.

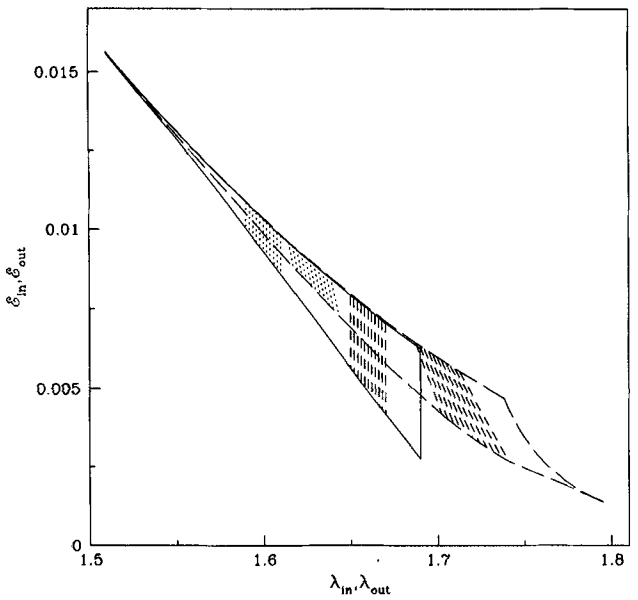

Figure 8. Mapping of the parameter space of the pre-shock region (solid boundary) spanned by ($\mathcal{E}_{in}$, λ_{in}) onto the parameter space in the post-shock region (dashed boundary) spanned by ($\mathcal{E}_{out}$, λ_{out}) in a viscous flow ($\alpha_\Pi = 0.01$).

not satisfied, was important for this type of oscillating shocks (Ryu et al. 1997). Here, winds are also produced sporadic from the post-shock region. In the presence of cooling, especially when the cooling time-scale roughly agrees with the infall time-scale, a new phenomenon occurs. Here, a steady shock may exhibit oscillations when time-dependent simulation is carried out.

It is to be noted that it is, in a general flow, very difficult to divide the parameter space in terms of whether the shock will exist or not. This is because, when there are shocks, at least the RHCs allow us to map the pre-shock and the post-shock flow parameters (see Fig. 8). When there are no shocks, however, it is not straightforward to map these two sets of parameters. Thus, one has to rely on global topological behaviour of the flow solutions and whether they allow multiple sonic points.

One of the criteria to use is to check which parameter space allows one to have the inner sonic-point energy larger than the outer sonic-point energy. For instance, in Fig. 9(a) we plotted the inner sonic-point energy ($\mathcal{E}_{in}$) along the X-axis and the outer sonic-point energy ($\mathcal{E}_{out}$) along the Y-axis for a set of inner sonic-point angular momentum (λ_{in}) when accretion flows pass through shocks. It is clear that $\mathcal{E}_{out}$ varies almost linearly with $\mathcal{E}_{in}$ and the nature of this variation depends only on λ_{in}. It is not unwarranted to assume that a similar linear variation

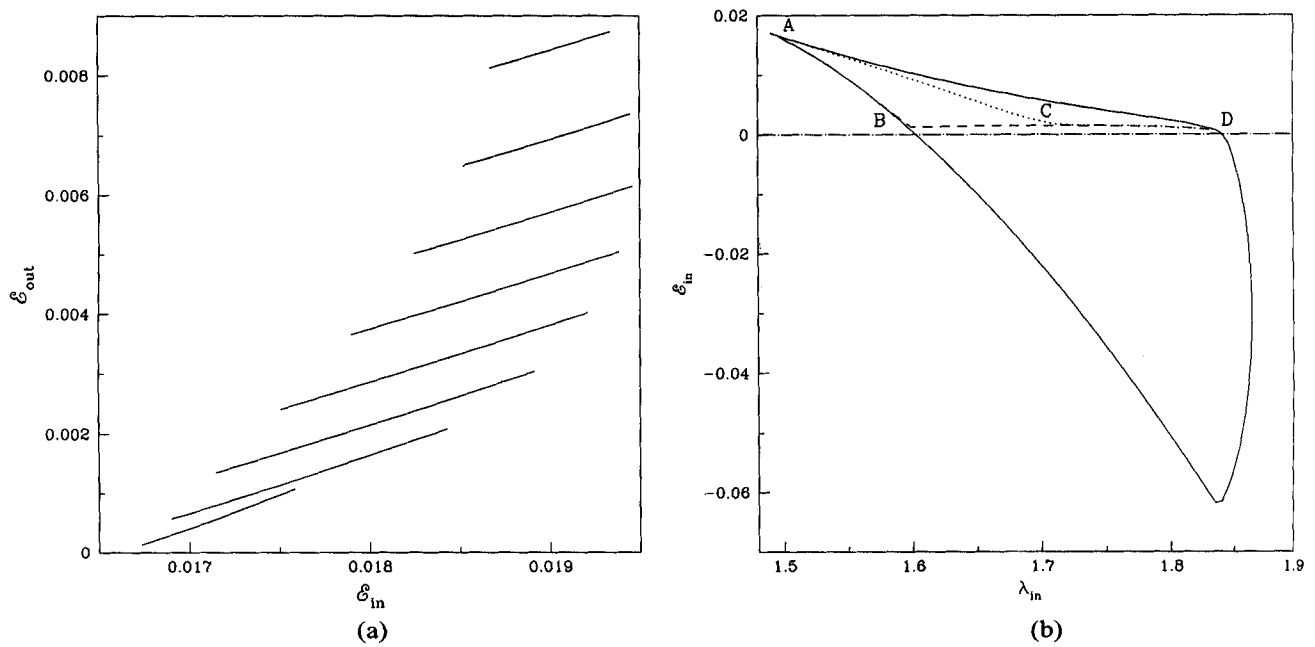

Figure 9. (a) Example of variation of the outer sonic-point energy $\mathcal{E}_{out}$ as a function of the inner sonic-point energy $\mathcal{E}_{in}$ when the flow has a shock. $\alpha_\Pi = 0.1$ and $\lambda(x_{in}) = 1.50$ for the topmost curve. Curves have an increment of $\Delta\lambda(x_{in}) = 0.02$ while going towards the bottom. (b) Division of the parameter space $(\mathcal{E}_{in}, \lambda_{in})$ for a viscosity parameter ($\alpha_\Pi = 0.01$) on the basis of the number of sonic points. The region separated by the dotted line has more than one X-type (saddle-type) sonic point and flows in this region form standing shocks. The region surrounded by the dashed curve has more than one X-type sonic point but the Rankine–Hugoniot conditions are not satisfied here.

will continue for shock-free solutions also at least if the viscosity is low. Assuming this, we extrapolate this variation in shock-free solutions towards lower values of $\mathcal{E}_{in}$ till $\mathcal{E}_{out} \sim 0$, keeping λ_{in} constant. In doing so, we ensured that the accretion flow topology which passes through the inner sonic point must remain closed (Figs 3a–b). We follow this procedure to estimate the cut-off $\mathcal{E}_{in}$ for different λ_{in} and obtain the region in the parameter space where the accretion flow has more than one X-type sonic point.

In Fig. 9(b) we show the division of the parameter space $(\mathcal{E}_{in}, \lambda_{in})$ for the viscosity parameter $\alpha_\Pi = 0.01$ on the basis of the number of sonic points. Flows with parameters from the region ACD have more than one X-type (saddle-type) sonic point and the RHCs are also satisfied. Flows with parameters from the region ABC have more than one X-type sonic point but the RHCs are not satisfied here. From our previous experience with non-dissipating flows, we predict that those solutions with multiple sonic points which do not produce standing shocks must be producing oscillating shocks. This region becomes bigger when the viscosity parameter is reduced. The rest of the parameter space gives solutions with a closed topology passing through the inner sonic point.

6.4 Parameter space for all possible solutions

Fig. 10 shows the classification of the parameter space in the energy–angular momentum $(\mathcal{E}_{in}, \lambda_{in})$ plane in terms of different accretion flow topologies (small box) for $\alpha_\Pi = 0.01$. The solid boundary separates the region in the parameter space for closed topologies passing through the inner sonic point in general. Further subclasses are indicated by the dotted, dashed and dot-dashed curves which classified the solution topologies depending on their behaviour. Examples of solution topologies with initial parameters taken from different regions (marked) of the parameter space are plotted in seven small boxes (marked). All the small boxes depict Mach number variation as a function of the logarithmic radial distance. The box labelled S shows an accretion flow solution which passes through a shock. The dotted vertical line with an arrow indicates the location of the standing shock. The solution drawn in the box marked OS is an accretion flow which has multiple sonic points but does not satisfy the RHCs after the flow becomes supersonic. From our earlier experience with an inviscid flow, this topology is expected to give rise to an oscillating shock solution. The box marked OAC shows a new type of solution topology having multiple sonic points. One branch of the topology is closed and the other branch is open. This kind of solution is available in a small region of the parameter space shown in the inset on the upper-right corner. Solutions inside the CI1 box have closed topology (inner spiral going anticlockwise) having only one saddle-type sonic point and this kind of solution belongs to a large region of the parameter space with a relatively lower angular-momentum region. The box CI2 shows a similar result as CI1 but here the nature of the topology is different (inner spiral going clockwise) and this type of solution exists in a higher angular-momentum region. The box labelled I* represents an accretion flow solution which only passes through the inner sonic point. This solution could be for an accretion or wind and the initial parameters for this type of topology belong to the region indicated by I* in the parameter space. The topology with parameters taken from the O* region of the parameter space is also plotted in the

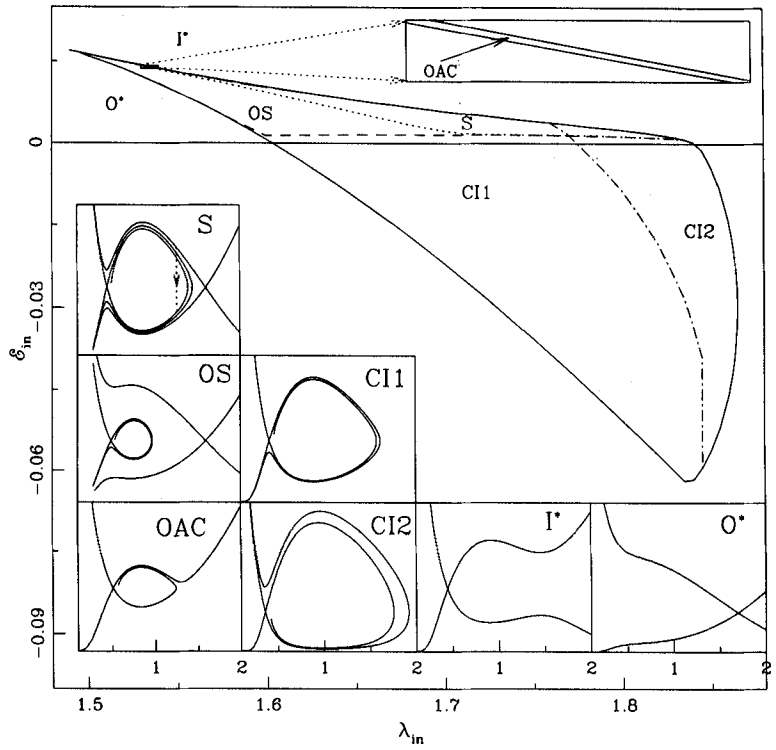

Figure 10. Division of the parameter space $\mathcal{E}_{in}$, λ_{in} (marked) for a viscosity parameter ($\alpha_{\Pi} = 0.01$) on the basis of the solution topologies shown in the boxes (marked). See text for details.

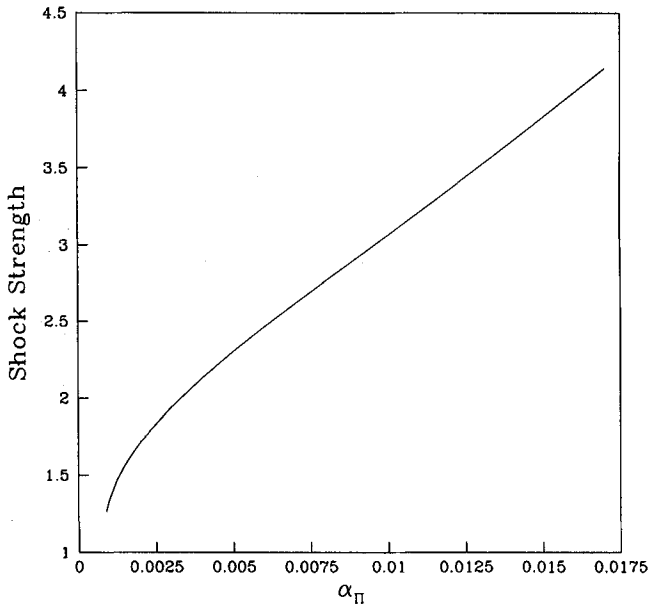

Figure 11. Variation of the ratio of the pre-shock to post-shock Mach numbers as a function of viscosity parameters for a fixed set of initial conditions ($x_{in} = 2.795$ and $\lambda_{in} = 1.65$). The shock disappears beyond the critical parameter $\alpha_{\Pi} \sim 0.017$.

box marked O*. An accretion flow solution with these parameters passes only through the outer sonic point before falling into the black hole (similar to a Bondi flow).

Since the strength of the shock determines the jump in temperature and density, it may be worthwhile to study the shock strength. We define this as the ratio of the pre-shock Mach number to the post-shock Mach number. As an example, in Fig. 11 we show the variation of the shock strength as a function of viscosity parameter α_{Π}. This figure is drawn for $x_{in} = 2.795$ and $\lambda_{in} = 1.65$. For the lower viscosity limit, the strength of the shock is weak. It increases smoothly with the gradual increase of viscosity and there is a cut-off at a critical viscosity limit where the shock disappears.

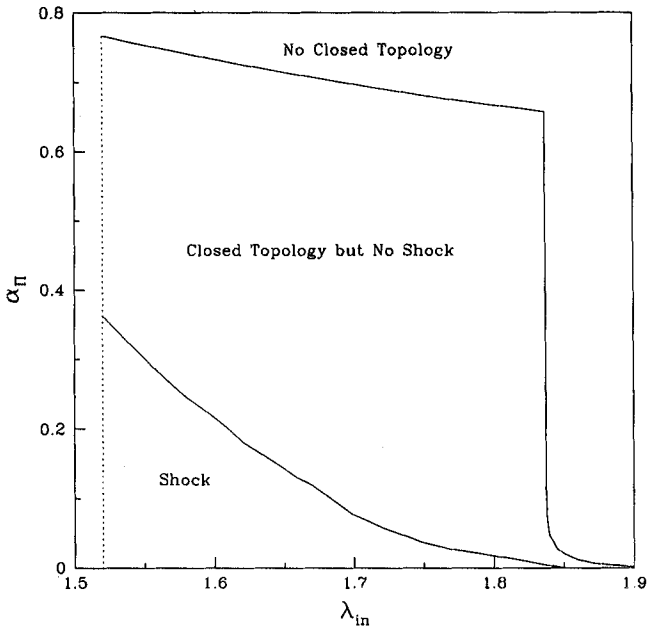

Figure 12. Critical viscosities separating standing from oscillating shocks and closed topologies from open topologies.

7 DEPENDENCE OF THE CRITICAL VISCOSITY PARAMETER

In our earlier discussion, we already hinted that there must be a critical viscosity parameter for which the flow topology must change its nature from an open topology to a closed topology. Here, we quantify the nature of this critical viscosity. Indeed, we find that there are in effect two critical viscosity parameters: one at the boundary which separates the closed topology from the open topology while the other splits the region of the closed topology in terms of whether shocks can form or not. Not surprisingly, these are dependent on the inflow parameter, and thus do not have universal values. Nevertheless, these are useful, since they give us insights into the cases in which shocks may be possible.

Fig. 12 shows the variation of the critical viscosity parameters with the angular momentum at the inner sonic point. Different regions are marked. We note that for higher viscosity parameters (α_Π), shocks are formed in the lower angular-momentum domain. As the angular momentum is increased, the shock disappears. This was also expected from our discussion of Fig. 1(c).

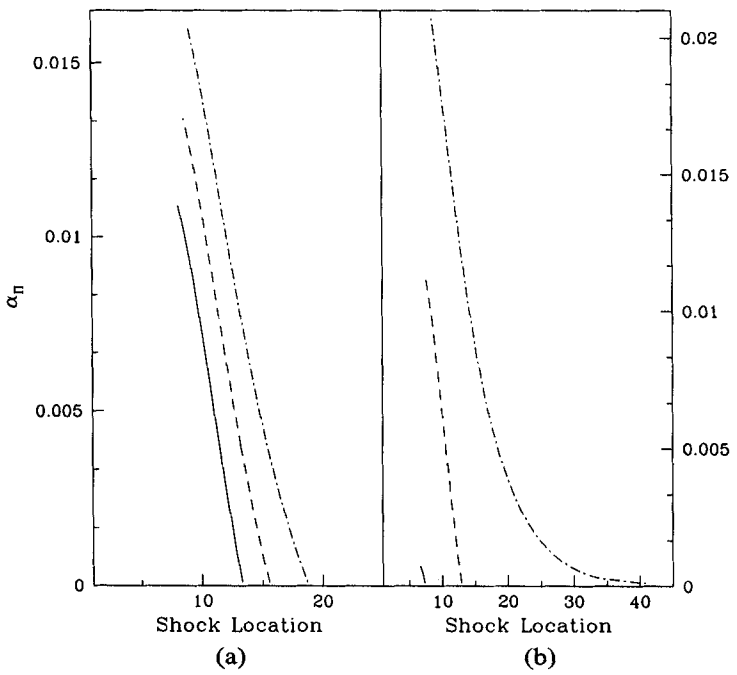

Figure 13. Variation of shock location with viscosity parameter and (a) inner sonic point and (b) specific angular momentum. The shock location always decreases with increase of viscosity until the critical viscosity parameter is reached, beyond which the shock ceases to exist.

8 DEPENDENCE OF THE SHOCK LOCATION ON VISCOSITY PARAMETER

In our study of shock properties, we have already mentioned that the shocks disappear when the viscosity is more than a critical value. In Figs 13(a) and (b) we show how the shock location depends on the viscosity parameter when the other two free parameters, i.e. the sonic point location (x_{in}) and angular momentum (λ_{in}), are kept fixed. In Fig. 13(a), the variation with the inner sonic point is shown when the angular momentum is kept fixed, while in Fig. 13(b), the variation with the angular momentum is shown, keeping the inner sonic point fixed. In all cases, the shock location is reduced with the increase in viscosity parameter till the critical viscosity parameter is reached, beyond which the shock ceases to exist. This is significant because in an accretion flow, when the viscosity is increased, the accretion rate is also increased and a black hole candidate goes from a spectrally hard to a spectrally soft state (CT95). Thus if the shock oscillation is indeed the cause of quasi-periodic oscillations (QPOs), then the frequency should increase with the accretion rate and finally as the shock ceases to exist, the QPOs also should disappear in softer states. Observation of such features could be used to verify if the shock oscillations may be the prime cause of the QPOs in black hole candidates.

9 CONCLUDING REMARKS

In this paper we have extended our earlier results of the study of shock formation to include the very difficult yet more realistic case of viscous polytropic flows. Some of the results have been touched upon in C96a but the new results in our work include a detailed study of the parameter space in which shocks form, even in the presence of viscosity. We found a large number of important results.

(i) There exist two critical viscosity parameters which separate the region of the parameter space into three parts: (1) in which the flow has a Bondi-type single sonic point; (2) in which there are three sonic points but no Rankine–Hugoniot relations are satisfied and (3) when the Rankine–Hugoniot relations are satisfied. These critical viscosity parameters decrease with the increase of the specific angular momentum of the flow at the inner sonic point.

(ii) At high viscosities, standing and oscillating shocks may form if the flow has very little angular momentum at the inner sonic point, while at low viscosities the situation is exactly the opposite. It is widely believed that accreting matter on galactic and extragalactic black holes could be of very low angular momentum, especially when the central compact object is accreting winds from a nearby star or stars. This brings out the possibility that shocks may be active ingredients of an accretion flow. Our results, with very plausible accretion flow models, indicate that standing and oscillating shocks are produced even for large viscosity parameters.

(iii) The shock location is reduced with enhancement of the viscosity parameter. This, coupled to earlier results (Chakrabarti & Manickam 2000) that the infall time is proportional to the period of quasi-periodic oscillation (QPO) of X-rays from black holes, implies that the QPO frequency should increase as the viscosity is increased. This is consistent with the observational findings that the QPO frequency is increased as the spectral slope softens, widely known to be due to an increase in viscosity and accretion rate.

One of the questions we have not addressed here is the stability properties of these shocks. A number of authors have pointed out that while the shocks are stable they should undergo oscillations, either radially, or vertically, or non-axisymmetrically (Molteni, Toth & Kuznetsov 1999; Gu & Foglizzo 2003). We anticipate that our shock solutions in viscous flows would suffer similar types of oscillations, especially when the viscosity is low. In particular, Gu & Foglizzo (2003) while studying shocks in inviscid, isothermal flows, found such instability and interpreted it as being due to cycles of acoustic waves between their corotation radius and the shock. In their interpretation this could be a form of Papaloizou–Pringle instability (Papaloizou & Pringle 1984) which is known to destabilize accretion tori when the angular momentum gradient is less than a certain value. If so, such an instability could disappear at high enough viscosity. This could have a bearing on the quasi-periodic oscillations of observed X-rays in galactic and extragalactic black hole candidates in that QPOs would cease to exist above a certain frequency. The interesting aspect is that these so-called 'instabilities' only cause oscillation of shocks and do not destroy the shock (Molteni et al. 1999).

ACKNOWLEDGMENTS

This work is partly supported by a project (Grant No. SP/S2/K-15/2001) funded by the Department of Science and Technology (DST), Government of India.

REFERENCES

Chakrabarti S. K., 1989a, MNRAS, 240, 7 (C89a)
Chakrabarti S. K., 1989b, ApJ, 347, 365 (C89b)
Chakrabarti S. K., 1990a, Theory of Transonic Astrophysical Flows. World Scientific, Singapore (C90a)
Chakrabarti S. K., 1990b, MNRAS, 243, 610 (C90b)
Chakrabarti S. K., 1996a, ApJ, 464, 664 (C96a)
Chakrabarti S. K., 1996b, MNRAS, 283, 325 (C96b)
Chakrabarti S. K., 1998, in Chakrabarti S. K., ed., Observational Evidence for Black Holes in the Universe. Kluwer, Dordrecht (C98)
Chakrabarti S. K., 1999, A&A, 351, 185
Chakrabarti S. K., Manickam S. G., 2000, ApJ, 531, L41

Chakrabarti S. K., Molteni D., 1993, ApJ, 417, 672
Chakrabarti S. K., Molteni D., 1995, MNRAS, 272, 80 (Paper I)
Chakrabarti S. K., Titarchuk L. G., 1995, ApJ, 455, 623 (CT95)
Chattopadhyay I., Chakrabarti S. K., 2002; MNRAS, 333, 454
Das S., Chattopadhyay I., Chakrabarti S. K., 2001, ApJ, 557, 983
Das S., Chakrabarti S. K., 2004, MNRAS, submitted
Gu W.-M., Foglizzo T., 2003, A&A, 409, 1
Holzer T. E., Axford W. I., 1970, ARA&A, 8, 31
Landau L. D., Lifshitz E. D., 1959, Fluid Mechanics. Pergamon, New York
Lanzafame G., Molteni D., Chakrabarti S. K., 1998, MNRAS, 299, 799 (Paper II)
Lu J. F., Yuan F., 1997, PASJ, 49, 525L
Matsumoto R., Kato S., Fukue J., Okazaki A. T, 1984, PASJ, 36, 7
Molteni D., Sponholz H., Chakrabarti S. K., 1996a, ApJ, 457, 805
Molteni D., Ryu D., Chakrabarti S. K., 1996b, ApJ, 470, 460
Molteni D., Toth G., Kuznetsov O. A., 1999, ApJ, 516, 411
Nobuta K., Hanawa T., 1994, PASJ, 46, 257
Paczynski B., Wiita P. J., 1980, A&A, 88, 23
Papaloizou J. C. B., Pringle J. E., 1984, MNRAS, 208, 721
Ryu D., Chakrabarti S. K., Molteni D., 1997, ApJ, 474, 378
Shakura N. I., Sunyaev R. A., 1973, A&A, 24, 337
Smith D. M., Heindl W. A., Markwardt C. B., Swank J. H., 2001, ApJ, 554, L41
Smith D. M., Heindl W. A., Swank J. H, 2002, ApJ, 569, 362
Yang R., Kafatos M., 1995, A&A, 295 238

This paper has been typeset from a TEX/LATEX file prepared by the author.

International Journal of Modern Physics D
Vol. 13, No. 9 (2004) 1955–1972

World Scientific
www.worldscientific.com

PROPERTIES OF ACCRETION SHOCKS IN VISCOUS FLOWS WITH COOLING EFFECTS

SANTABRATA DAS* and SANDIP K. CHAKRABARTI†

S.N. Bose National Centre for Basic Sciences,
JD-Block, Sector III, Salt Lake, Kolkata 700098, India
**sbdas@bose.res.in*
†*chakraba@bose.res.in*

Received 9 April 2004
Communicated by B. S. Sathyaprakash

Low angular momentum accretion flows can have standing and oscillating shock waves. We study the region of the parameter space in which multiple sonic points occur in viscous flows in presence of various cooling effects such as bremsstrahlung and Comptonization. We also quantify the parameter space in which shocks are steady or oscillating. We find that cooling induces effects opposite to heating by viscosity even in modifying the topology of the solutions, though one can never be exactly balanced by the other due to their dissimilar dependence on dynamic and thermodynamic parameters. We show that beyond a critical value of cooling, the flow ceases to contain a shock wave.

Keywords: Black hole physics; accretion; jets and outflows.

1. Introduction

Cooling and heating processes play an important role in studying the accretion disks around compact objects. In this paper, we consider both viscous heating and bremsstrahlung cooling as energy dissipative processes. In Chakrabarti and Das,[1] the problem of accretion and winds with small angular momentum was solved in a very comprehensive way when viscous heating was included. The entire parameter space was scanned and separated in terms of flows with and without shocks. A major scope for further work is to find and separate the parameter space which allows shock formations when cooling effects are also included. This will allow us to study flows with high accretion rate as well. The question arises because viscosity transports angular momentum and increases the possibility of shock formation at a larger distance from the black hole. However, cooling reduces the post-shock pressure and therefore the possibility of shock formation. Various cooling processes will and should change the parameter space in which shocks form.

†Also at Centre for Space Physics, Chalantika 43, Garia Station Rd., Kolkata 700084.

In Chakrabarti,[2] some of the effects of cooling was included. Assuming that cooling at a given radius of an accretion disk is proportional to the heating, all possible topologies were presented. While cooling will and should depend on heating, there is no reason to believe that this proportionality is independent of radial distance. It is therefore necessary to re-visit the problem with explicit form of heating and cooling included.

In the present paper, we make these important extensions of the previous work and show that shocks are still possible in a very large part of the parameter space. We find topologies of solutions which are similar to what was found for spiral shock study,[3] but otherwise new for axisymmetric situation. We also find new topologies which were not anticipated before. In more recent years, it has become evident that the standing shocks may be very important in explaining the spectral properties of black hole candidates[4] as the post-shock region behaves as the boundary layer where accreting matter dissipates its thermal energy and generates hard X-ray by inverse Comptonization. This region is also found to be responsible to produce relativistic outflows. Furthermore, numerical simulations indicated that the shocks may be oscillating at nearby regions of the parameter space in presence of cooling effects[5] and the shock oscillations can also explain intricate properties of quasi-periodic oscillations.[6] Recent observations do support the presence of sub-Keplerian flows in accretion disks.[7,8]

The present work is done around a Schwarzschild black hole by using pseudo-Newtonian potential.[9] We use a similar viscosity prescription as in Chakrabarti.[2] In Section 2, we present model equations which included both heating and cooling effects. In Section 3, we perform the sonic point analysis. In Section 5, we study the nature of the sonic points and how they vary with flow parameters. In Section 6, we study the global solution topologies with heating and cooling effects. In Section 7, we classify the parameter space in terms of whether shocks will form or not and how it depends on flow parameters. In Section 8, we briefly report how even the super-Keplerian flows may also be transonic. Finally, in Section 9, we discuss the importance of these solutions and make concluding remarks.

2. Model Equations When Cooling Effects are Included

As far as the cooling processes are concerned, they could be due to various physical reasons, such as the thermal and the non-thermal bremsstrahlung, synchrotron, Comptonization, etc. For simplicity, we assume that the Comptonization enhances the injected photon intensity due to bremsstrahlung by a factor of ζ which can take any value from 1 to $\sim$ few $\times$ 100 depending on the availability of soft photons.[4] In other words, we use ζ as a parameter to represent the net cooling.

We start with a thin, axisymmetric, rotating viscous accretion flow around a Schwarzschild black hole. The space–time geometry around a non-rotating black hole can be satisfactorily described by the pseudo-Newtonian potential[9] and is given by $g(x) = -\frac{1}{2(x-1)}$, where, x is the radial distance in dimensionless unit.

In the steady state, the dimensionless hydrodynamic equations that govern the infalling matter are the followings:[2]

(a) Radial momentum equation:

$$\vartheta\frac{d\vartheta}{dx}+\frac{1}{\rho}\frac{dP}{dx}-\frac{\lambda(x)^2}{x^3}+\frac{1}{2(x-1)^2}=0\,. \tag{1a}$$

(b) Baryon number conservation equation:

$$\dot{M}=\Sigma\vartheta x\,, \tag{1b}$$

apart from the geometric constant.

(c) Angular momentum conservation equation:

$$\vartheta\frac{d\lambda(x)}{dx}+\frac{1}{\Sigma x}\frac{d}{dx}(x^2W_{x\phi})=0\,. \tag{1c}$$

(d) The entropy generation equation:

$$\Sigma\vartheta T\frac{ds}{dx}=Q^+-Q^-\,. \tag{1d}$$

Here, ϑ is the radial velocity and $\lambda(x)$ is the specific angular momentum of the flow. The distances, velocities and masses are made dimensionless by using $r_g=2GM_{\rm BH}/c^2$, the Schwarzschild radius, c, the velocity of light and $M_{\rm BH}$, the mass of the black hole, respectively. Here Σ and $W_{x\phi}$ are the vertically integrated density and viscous stress, s is the entropy density of the flow, T is the local temperature, Q^+ and Q^- are the heat gained and lost by the flow, and $\dot{M}$ is the mass accretion rate. We assume that the accretion flow is in hydrostatic equilibrium in the vertical direction and the vertical velocity component is much smaller compared to the radial component. With this assumption, the local disk height is obtained by equating the pressure gradient force in the vertical direction with the gravitational force. The half thickness of the disk is then given by

$$h(x)=ax^{1/2}(x-1)\,, \tag{2}$$

where the sound speed is defined as $a=\sqrt{\gamma P/\rho}$, where γ, P and ρ being the adiabatic index, pressure and density respectively.

In the present paper, we follow a similar viscosity prescription as given in Chakrabarti[2] where $W_{x\phi}=-\alpha_\Pi\Pi$ is used. This prescription ensures that viscous stress remain continuous at the flow discontinuity (shock) in presence of significant radial motion of the accretion flow.

3. Sonic Point Analysis

A black hole accretes matter either from its binary companion or from the surrounding ambient medium. This matter starts with a negligible radial velocity at the outer edge of the disk. But it enters into the black hole with the velocity of light.[10] This ensures that inside the accretion disk there must be at least one point

where the radial velocity exactly matches with the sound speed. This point is known as the sonic point. Accretion flow which passes through a shock wave must cross sonic points at least twice. In other words, the flow may be called multi-transonic.

For the accretion flow, entropy equation (1d) can be simplified as

$$\frac{\vartheta}{\gamma-1}\left[\frac{1}{\rho}\frac{dP}{dx}-\frac{\gamma P}{\rho^2}\frac{d\rho}{dx}\right]=\frac{Q^- - Q^+}{\rho h}=C-H\,. \tag{3}$$

and then $H(=Q^+/\rho h)$ takes the form,

$$H=Ax(ga^2+\gamma\vartheta^2)\frac{d\Omega}{dx}\,, \tag{4}$$

where, $A=-\alpha_\Pi\frac{I_n}{\gamma}$ and $g=\frac{I_{n+1}}{I_n}$. Here, $\Omega(x)$ is the angular velocity of the accreting matter at the radial distance x, n is the polytropic index $\left(n=\frac{1}{(\gamma-1)}\right)$. The general expression of I_n is given by[11]

$$I_n=\frac{(2^n n!)^2}{(2n+1)!}\,. \tag{5}$$

Simultaneously with viscous heating, we use Comptonization of the bremsstrahlung radiation as the physical cooling process. The following analysis is carried out with non-dimensional cooling term $C(=Q^-/\rho h)$ as

$$C=\frac{\zeta B}{\vartheta x^{3/2}(x-1)}\,, \tag{6a}$$

with

$$B=1.4\times10^{-27}\left(\frac{\mu m_p}{2k}\right)^{1/2}\frac{\dot{M}}{2\pi m_p^2}\frac{1}{2GcM_{\rm BH}}\,, \tag{6b}$$

where μ is the mean molecular weight, m_p is the mass of the proton and k is the Boltzmann constant respectively.

3.1. *Sonic point condition*

From Eqs. (1a)–(1d), the sonic point conditions are derived following the general procedure[12] and are given by

$$\frac{d\vartheta}{dx}=\frac{N}{D}\,, \tag{7}$$

where the numerator N is

$$N=-\frac{\alpha_\Pi A(a^2g+\gamma\vartheta^2)^2}{\gamma x}-\left[\frac{\lambda^2}{x^3}-\frac{1}{2(x-1)^2}\right]\times\left[2\alpha_\Pi gA(a^2g+\gamma\vartheta^2)+\frac{(\gamma+1)\vartheta^2}{(\gamma-1)}\right]$$

$$-\frac{\vartheta^2 a^2(5x-3)}{x(\gamma-1)(x-1)}-\frac{\alpha_\Pi g A a^2(5x-3)(a^2 g+\gamma\vartheta^2)}{\gamma x(x-1)}$$
$$+\frac{2\lambda A\vartheta(a^2 g+\gamma\vartheta^2)}{x^2}+\frac{B}{x^{3/2}(x-1)}, \tag{8a}$$

and the denominator D is

$$D=\frac{2a^2\vartheta}{(\gamma-1)}-\frac{(\gamma+1)\vartheta^3}{(\gamma-1)}-A\alpha_\pi\vartheta(a^2 g+\gamma\vartheta^2)\left[(2g-1)-\frac{a^2 g}{\gamma\vartheta^2}\right]. \tag{8b}$$

At the sonic point, both the numerator and denominator vanish. For $D=0$, one can get the expression for the Mach Number $M(x_c)$ at the sonic point which is given by,

$$M(x_c)=\sqrt{\frac{-m_b-\sqrt{m_b^2-4m_a m_c}}{2m_a}}\approx\sqrt{\frac{2}{\gamma+1}}\quad\text{for}\quad\alpha_\Pi\to 0, \tag{9}$$

where,

$$m_a=-A\alpha_\Pi\gamma^2(\gamma-1)(2g-1)-\gamma(\gamma+1), \tag{10a}$$
$$m_b=2\gamma-2A\alpha_\pi g\gamma(\gamma-1)(g-1), \tag{10b}$$
$$m_c=A\alpha_\pi g^2(\gamma-1). \tag{10c}$$

In order for the Mach number to be physically acceptable, we do not use the negative sign within the square root. In the weak viscosity limit, Mach number at the sonic point reduces to the result as obtained in Chakrabarti.[12]

Setting $N=0$, we get an algebraic equation for sound speed at the sonic point which is given by

$$F(\mathcal{E}_c,\lambda_c,x_c)=\mathcal{A}a^4(x)+\mathcal{B}a^3(x)+\mathcal{C}a^2(x)+\mathcal{D}=0, \tag{11}$$

where,

$$\mathcal{A}=-\left[\frac{\alpha_\Pi A\{g+\gamma M^2\}^2}{\gamma x}+\frac{\alpha_\Pi A(5x-3)\{g+\gamma M^2\}}{\gamma x(x-1)}+\frac{M^2(5x-3)}{x(\gamma-1)(x-1)}\right], \tag{12a}$$
$$\mathcal{B}=\frac{2\lambda AM(g+\gamma M^2)}{x^2}, \tag{12b}$$
$$\mathcal{C}=-\left[\frac{\lambda^2}{x^3}-\frac{1}{2(x-1)^2}\right]\left[2\alpha_\Pi g A(g+\gamma M^2)+\frac{(\gamma+1)M^2}{(\gamma-1)}\right], \tag{12c}$$
$$\mathcal{D}=\frac{B}{x^{3/2}(x-1)}. \tag{12d}$$

We solve the above quadratic equation to obtain the sound speed at the sonic point. Das, Chattopadhyay and Chakrabarti[13] found that depending on a given set of initial parameters, accretion flow may have a maximum of four sonic points where one of the sonic points always lies inside the black hole horizon for non-dissipative accretion flow.[10,13] In our present study, we also expect a similar result if we are

interested in the weak viscosity and weak cooling limit. Below, we study the nature of the sonic points.

4. Nature of the Sonic Points

Accreting matter begins subsonically from the outer edge of the disk and becomes supersonic after passing through the sonic point before entering into black hole. A flow may contain multiple sonic points depending on the initial set of input parameters. Nature of sonic points depends on the value of the velocity gradients $(d\vartheta/dx)$ at the sonic points. At each sonic point, $(d\vartheta/dx)$ has distinctly two different values. If both the velocity gradients are real and of opposite signs, the sonic points is saddle type and one is used for accretion and the other used for winds. Nodal type sonic point belongs to the class when the derivatives are real and of the same sign. When the derivatives are complex, the sonic point is of spiral type. For a standing shock to form, an accretion flow must have more than one saddle type sonic point.

In Fig. 1(a), we plot the variation of specific angular momentum (λ_c) as a function of the logarithmic sonic point location (x_c) for a given viscosity parameter

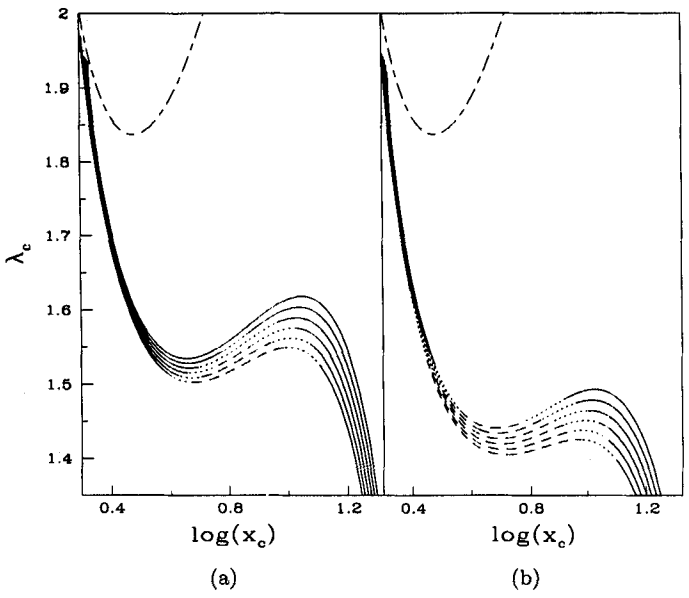

Fig. 1. Variation of specific angular momentum (λ_c) as a function of the logarithmic sonic point location (x_c) for the viscosity parameter (a) $\alpha_\Pi = 0.1$ (left panel) and (b) $\alpha_\Pi = 0.5$ (right panel). Dimensionless accretion rate $\dot{m} = 1.0$ and energy at the sonic point $\mathcal{E}_c = 0.0013$ are chosen. Long-dashed-dotted curve in the upper part is the Keplerian angular momentum distribution. Solid curves represent the saddle type sonic points, dotted curves represent the nodal type sonic points and the short-dashed curves are for the spiral type sonic points. The Comptonization cooling factor ζ is 1 (bottom curve), 20, 40, 60, 80 and 100 (top curve) respectively. Clearly, higher cooling and higher viscosity remove the outer sonic points. Eventually the disk becomes a Keplerian disk passing through the inner sonic point.

($\alpha_\Pi = 0.1$), and dimensionless accretion rate (made dimensionless by the Eddington rate) $\dot{m} = 1.0$ and a given specific energy $\mathcal{E}_c = 0.013$ at the sonic points. The variable used in cooling efficiency factor ζ (Eq. (6a)). From the bottom curve to the top, $\zeta = 1$, 20, 40, 60, 80 and 100 respectively. In Fig. 1(b), the same curve is shown for $\alpha_\Pi = 0.5$, other parameters remaining the same. The long-dashed curve at the top represents the Keplerian angular momentum distribution which is completely independent of the initial flow parameters and depends only on the geometry. Solid part of the curves represents the saddle type sonic points, dotted curve represents the nodal type sonic points and the short-dashed curves are for the spiral type sonic points. Here, at a higher viscosity, the number of sonic points becomes three even with very low angular momentum. For no Comptonization (lowermost curve), the viscous heating is so strong that only outermost sonic point (solid part of the curve at large radius) exists. Only a large degree of cooling can compensate for the viscous heating to bring back the innermost sonic point.

First, notice that the sonic points occur at angular momentum below Keplerian value. For lower values of cooling at the sonic point, an accretion flow contains all the three types of sonic points in a systematic order: saddle — nodal — spiral — nodal — saddle for monotonic increase of location of sonic points. With the increase of ζ, the region of spiral type sonic points gradually decreases and is finally replaced

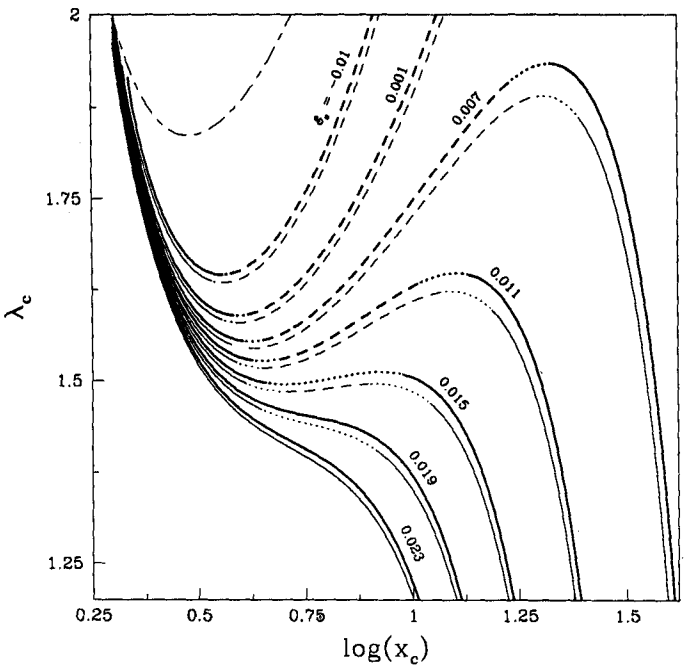

Fig. 2. Variation of the specific angular momentum (λ_c) at the sonic point (x_c) as a function of the specific energy ($\mathcal{E}_c$) of the flow. For each energy, two curves are drawn. The thick curves are drawn for the cases when both the heating and cooling are included while the thin curves are drawn when only the heating is included. For negative energies, there are only two sonic points.

by the nodal type sonic points, though multiple sonic points still exist. For further increase of ζ, all the nodal type sonic points also disappear and are replaced by saddle type sonic points. Note that the angular momentum is always sub-Keplerian. Later, we shall show that when the cooing is very strong, sonic points will form even for super-Keplerian flows.

We continue our investigation of the transonic nature of the flow by showing in Fig. 2 a series of curves where the specific energy at the sonic point is changed (marked). The long dashed curve is the Keplerian distribution as before. Meanings of solid, dashed and dotted curves are the same as before. For negative energies there are two sonic points, the inner one is saddle type (shown in the solid curve) and the dashed curve is the spiral type. For each energy, two curves are drawn. The thick curve is drawn when both the heating and cooling are included while the thin curve is drawn when only the heating is included. The motivation is to impress that the character of a solution can be changed when cooling is included. For instance, the solution for $\mathcal{E}_c = 0.019$ with heating and cooling has no spiral or nodal sonic points. But when the cooling is turned off, the saddle type sonic point becomes nodal type.

In our further study of the nature of the sonic points we draw in Figs. 3(a) and 3(b) the variation of energy at the sonic points with a cooling factor. In Fig. 3(a),

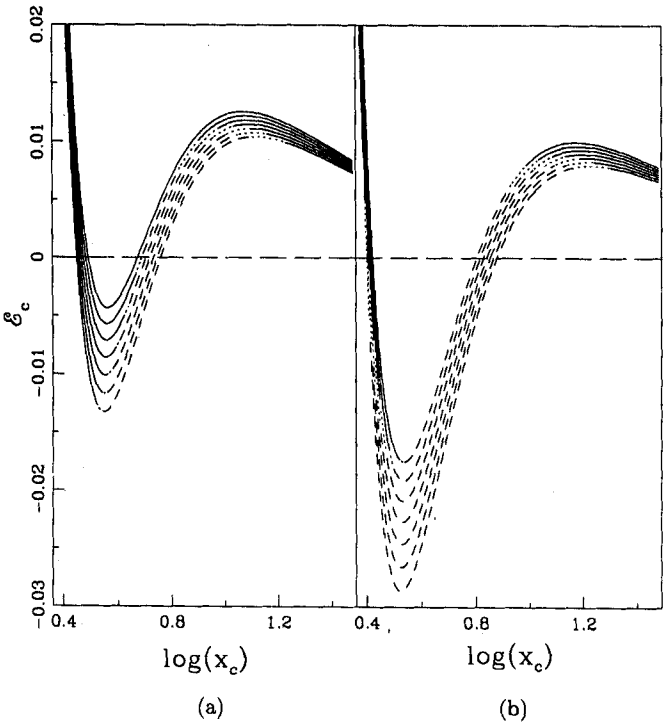

Fig. 3. Variation of the specific energy ($\mathcal{E}_c$) at the sonic point (x_c) as a function of the cooling rate of the flow. (a) $\alpha_\Pi = 0.1$ (left panel) and (b) $\alpha_\Pi = 0.5$ (right panel). For high viscosity, the outer sonic points almost disappear.

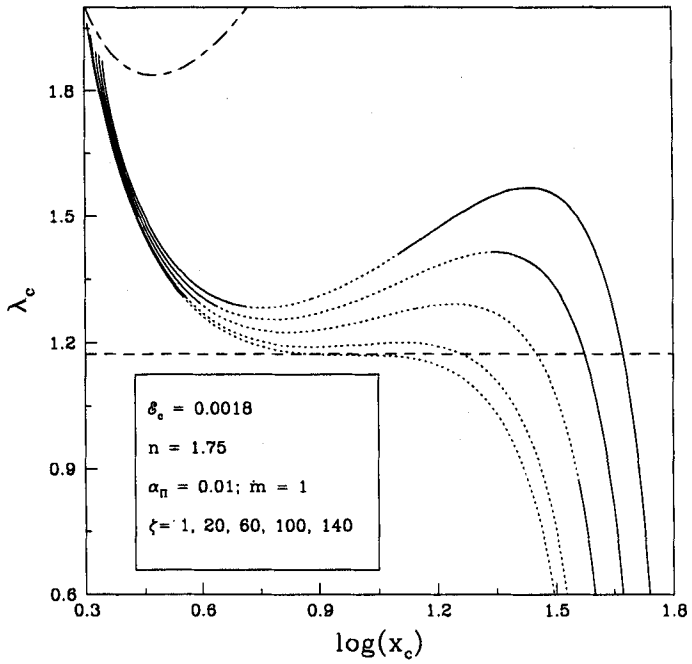

Fig. 4. Recovery of outer sonic point points as cooling process is introduced. Solid and dotted curves are for saddle and nodal type sonic points respectively. Parameters are marked on the plot. Long dashed curve at $\lambda_c = 1.1733$ gives a boundary below which there are no triple sonic points.

low viscosity ($\alpha_\Pi = 0.1$) is used, while in Fig. 3(b), high viscosity ($\alpha_\Pi = 0.5$) is used. Other parameters are: $\lambda = 1.65$ and $\dot{m} = 1$. The curves from bottom to the top are for the cooling factor $\zeta = 1$, 20, 40, 60, 80, 100 and 120. Notice that three sonic points occur only when the specific energy is positive, i.e., for sufficiently hot Keplerian disks or sub-Keplerian flows. For high viscosity, outer sonic points almost disappear from regions close to the black hole.

In Fig. 4, we show how the number of sonic points, reduced due to viscous heating process, is recovered back with the introduction of cooling. The curves are drawn, from the bottom to the top, for $\zeta = 1$, 20, 60, 80 100 and 140 respectively. The solid and dotted curves are for saddle and nodal type sonic points respectively. Other parameters are $\alpha_\Pi = 0.1$ and $\dot{m} = 1$. Polytropic index $n = 1.75$ and specific energy $\mathcal{E} = 0.0018$ are chosen. The long dashed curve gives the boundary of the angular momentum $\lambda_{\rm crit} = 1.1733$ and cooling factor $\zeta = 4.2$, below which there are no triple sonic points, i.e., no shocks in steady flows.

5. Global Solution Topology

Study of shock properties require multi-transonic accretion flow. Accretion flow passes through two different saddle type sonic points and discontinuous jump of the flow variable joins these two different branches — one passes through the inner sonic

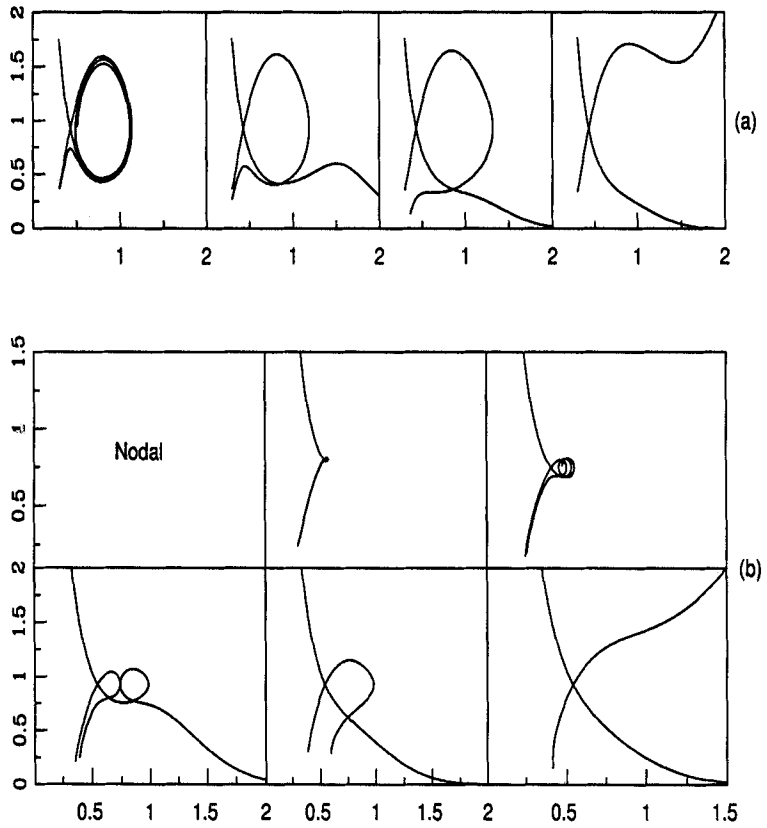

Fig. 5. Solution topologies in presence of heating and cooling. In (a), the parameters are $\zeta = 1$, 10, 25 and 50 respectively. Other parameters are $x_{\rm in} = 2.71$, $\lambda_{\rm in} = 1.68$, $\alpha = 0.01$, $\dot{m} = 0.5$. In (b), the parameters are $\zeta = 1$, 10, 25, 33.1, 50 and 70 respectively. Other parameters are; $x_{\rm in} = 3.5$, $\lambda_{\rm in} = 1.68$, $\alpha = 0.01$, $\dot{m} = 2.0$.

point and the other passes through the outer sonic point. This discontinuous jump usually known as standing shock transition. In this paper, we discuss the nature of solution topology in presence of viscous heating and bremsstrahlung cooling.

In Fig. 5(a), we show how the solution topologies change with cooling. Here we plotted the Mach number as a function of the logarithmic radial distance for $\zeta = 1$, 10, 25 and 50 respectively. Other chosen parameters are: $x_{\rm in} = 2.71$, $\lambda_{\rm in} = 1.68$, $\alpha_\Pi = 0.01$, $\dot{m} = 0.5$ respectively. We note that the topology opens up to allow flows to enter into black holes through the inner sonic points.

In Fig. 5(b), we show six panels in which we assume higher accretion rate and higher inner sonic point locations. The parameters are: $\zeta = 1$, 10, 25, 33.1, 50 and 70 respectively. Other parameters are: $x_{\rm in} = 3.5$, $\lambda_{\rm in} = 1.68$, $\alpha_\Pi = 0.01$, $\dot{m} = 0.2$. Here, as the cooling is increased, the topologies open up similarly, but the route to opening up is different. For instance, the solution in the fourth panel, with $\zeta = 33.1$ is completely new and intriguing. In this case, the flow has the potential to join

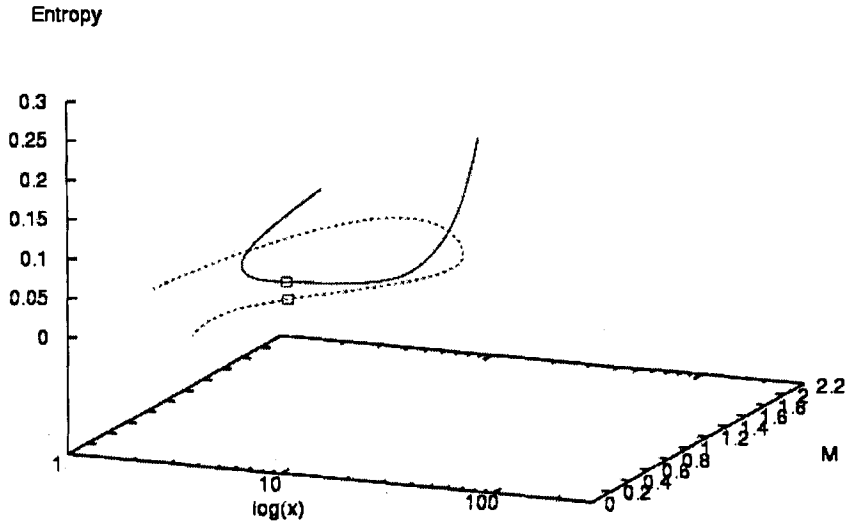

Fig. 6. Three-dimensional plot of the second panel ($\zeta = 10$) of Fig. 5(a) in which the specific entropy is also plotted as it varies along the flow. The boxes represent the pseudo-intersection point of that panel at around $M \sim 0.5$. The two branches have different entropies.

with a Keplerian disk far away (with low Mach number), while at the same time, it also passes through the inner sonic point. But it has multi-valued solution: there are two Mach numbers at a given radial distance in some region. We conjecture that this type of solution should be unstable and would cause non-steady accretion.

Many of these topologies show 'multiple crossings' very similar to what was found in the study of spiral shocks.[3] Actually, since entropy is changing along the flow, the two-dimensional nature of the plots in Fig. 5 is slightly misleading. In Fig. 6, we show a three-dimensional plot of the second panel ($\zeta = 10$) of Fig. 5(a) in which the specific entropy is also plotted as it varies along the flow. In particular, this diagram shows that at the true sonic point, the specific entropy is identical in both the incoming (solid) and outgoing (dotted) branches. But at the 'intersection' (at around $M \sim 0.5$) marked by two squares, the entropies are completely different. Thus, there is no 'sonic point' around $M \sim 0.5$.

6. Parameter Space Description

It is useful to study the global behaviour of the accretion solutions. For this we classify the parameter space spanned by the specific angular momentum and energy at the sonic point. Figure 7 shows the parameter spaces in which the solution passing through the inner sonic point contains a closed spiraling topology as in panel 1 of Fig. 5(a). This means that whether the Rankine–Hugoniot relation is satisfied or not, a shock could form in this region. The shock will be stationary if the Rankine–Hugoniot relation is satisfied[14] and will be oscillating if the relation is not satisfied. The solid, dashed, dot-dashed and dot-long-dashed regions are for

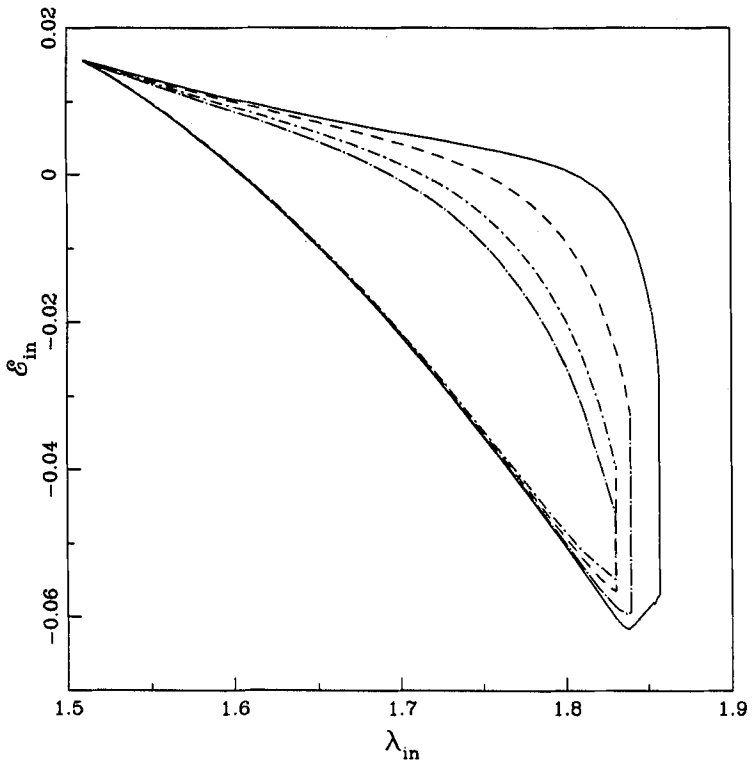

Fig. 7. Region of the parameter space in which the solution passing through the inner sonic point contains a closed spiraling topology. The solid, dashed, dot-dashed and dot-long-dashed regions are for cooling parameter 1, 10, 30, and 50 respectively. Other parameters are $\alpha_\Pi = 0.01$ and $\dot{m} = 0.1$.

cooling parameter 1, 10, 30, and 50, respectively. As the cooling is increased, the region shrinks and becomes smaller and smaller. This indicates that there exists a critical cooling parameter, beyond which a flow will cease to have three sonic points. Other parameters used are $\alpha_\Pi = 0.01$ and $\dot{m} = 0.1$. When the viscosity and cooling are reduced to zero, this region merges exactly to the corresponding region in Ref. 12.

In Figs. 8(a)–(c), we present a few complete solutions which are drawn with the parameters at $\lambda_{in} = 1.7$, $\alpha_\Pi = 0.05$, $\dot{m} = 0.2$ and $\zeta = 5$ and only the inner sonic point is varied: (a) $x_{in} = 2.545$, (b) $x_{in} = 2.55$ and (c) $x_{in} = 2.555$. The corresponding shock locations are (a) $x_s = 48.199$, (b) $x_s = 27.8854$ and (c) $x_s = 18.6445$, respectively. Vertical dashed lines show the shock transitions which connect two solutions, one passing through the inner sonic point and the other passing through the outer sonic point. The spiral loop through the inner sonic point rapidly shrinks with the increase in the sonic point location. The shock location also comes closer. This shows that even though the shock location may change by orders of magnitude, the inner sonic point virtually remains at the same place.

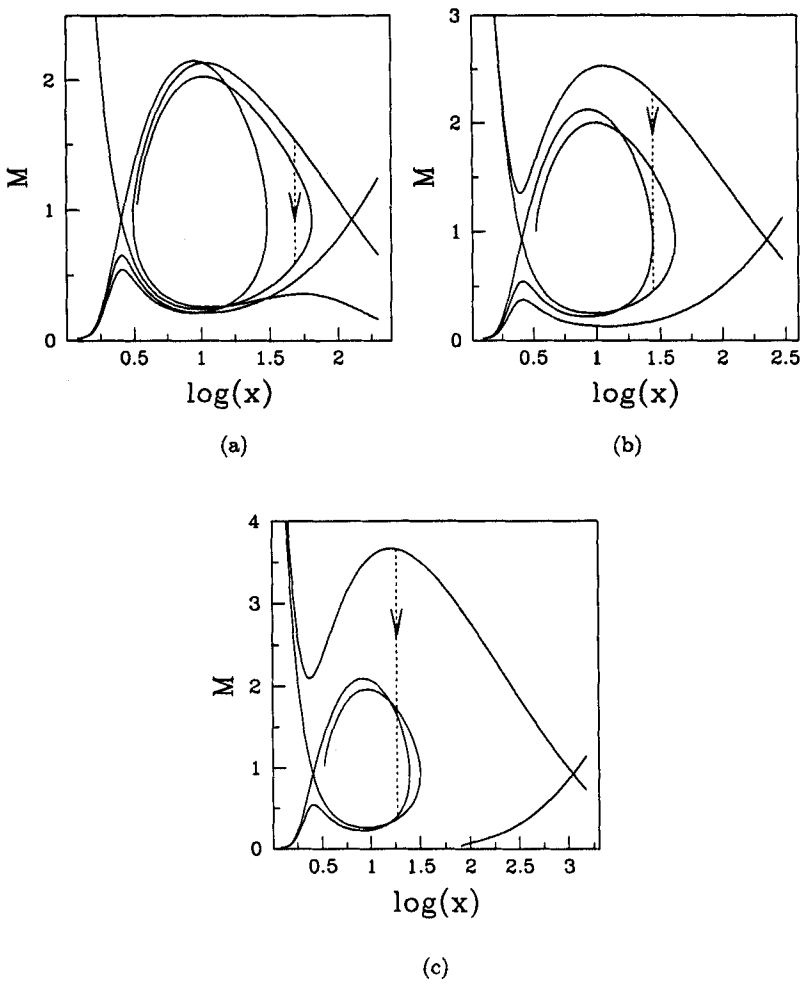

Fig. 8. A few complete solutions which are drawn with the parameters at $\lambda_{\rm in} = 1.7$, $\alpha_\Pi = 0.05$, $\dot{m} = 0.2$ and $\zeta = 5$ and only the inner sonic point is varied: (a) $x_{\rm in} = 2.545$, (b) $x_{\rm in} = 2.55$ and (c) $x_{\rm in} = 2.555$. The corresponding shock locations are (a) $x_s = 48.199$, (b) $x_s = 27.8854$ and (c) $x_s = 18.6445$, respectively. Vertical dashed lines show the shock transitions.

It is instructive to know the sub-division of the parameter space in terms of the topologies of the solutions. All the topologies seen in Paper I are also present in this case, but a new topology occurs (see, Fig. 5(b)) when the cooling is especially strong. Figure 9 shows the sub-division of the parameter space which are marked and the corresponding topologies are shown in the bottom left. When the cooling is very strong, the curve $\mathcal{ABC}$ shows further sub-divisions and a new topology shown in the box C13 occur. The number of loops in the inflow may increase depending on the cooling. The dotted curves indicate that the figure is drawn for different (high) cooling factors ζ. The regions marked S, OS, C11, C12, OAC, I*, O*

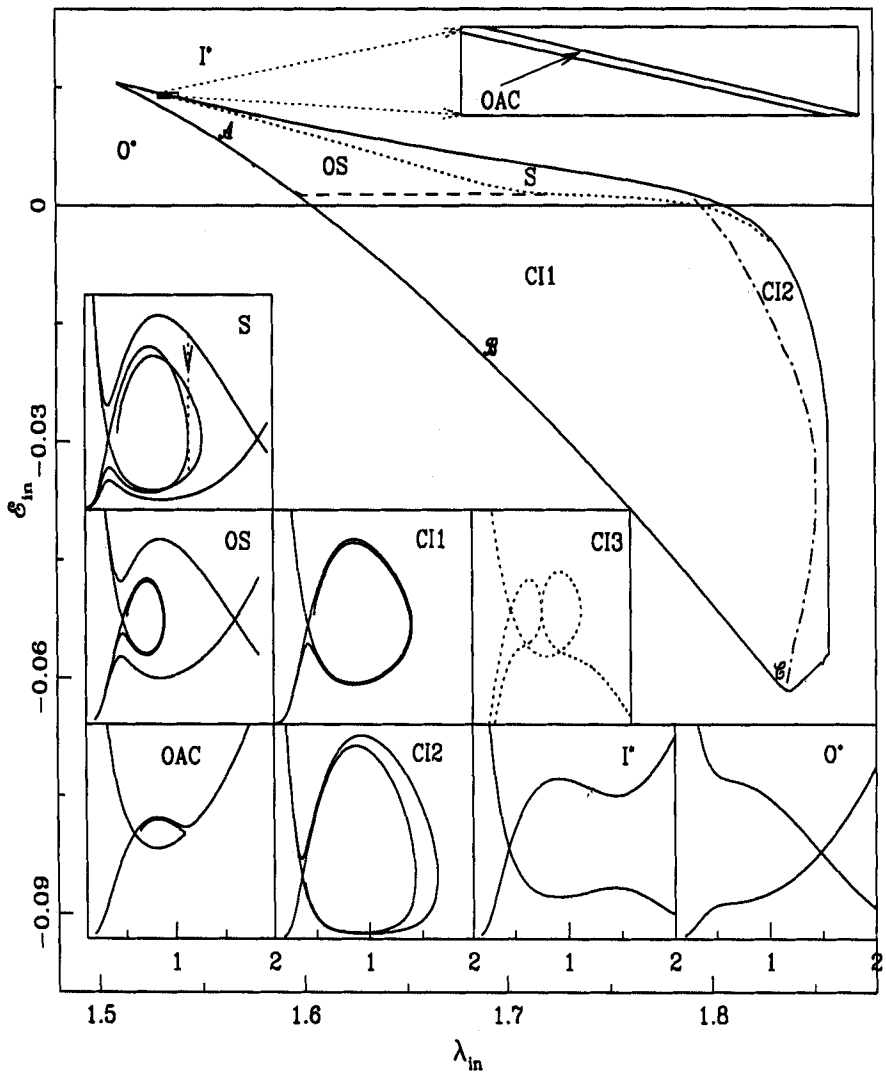

Fig. 9. Division of the parameter space according to the solution topologies shown in the inset. Details are in the text.

produce topologies which produce standing shocks in accretion, oscillating shocks in accretion, region which produces one type of closed topology (clockwise turn), region which produces the other type of closed topology (anti-clockwise turn), region which produces one open and the other closed topology, region which produces open solutions passing only through the outer saddle type sonic point, and the region which produces open solutions passing only through the inner saddle type sonic point respectively. The region producing the new dotted topology C13 is very close to the curve $\mathcal{ABC}$ and can be discernible only when cooling is strong.

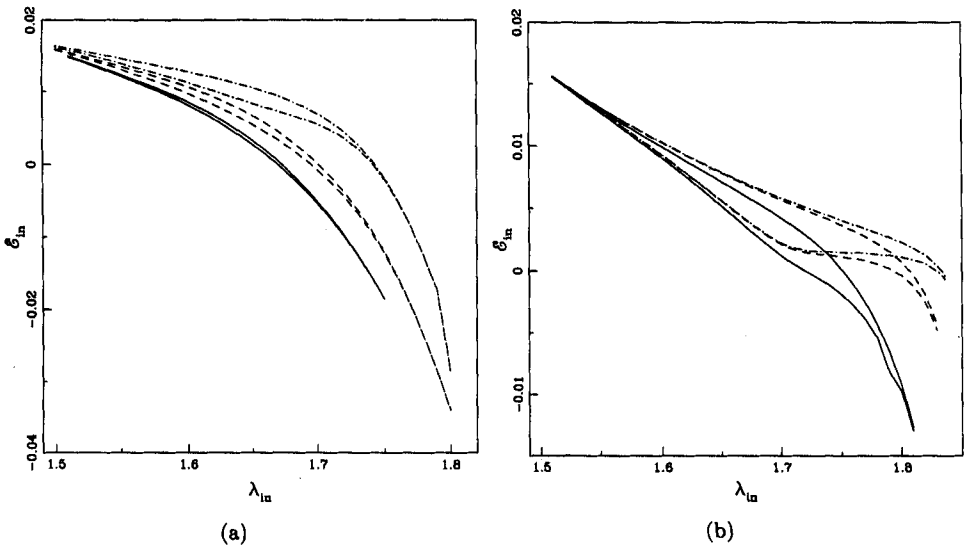

Fig. 10. Modification of the parameter space for shock formation when cooling is varied. (a) α_Π = 0.01 is chosen and $\zeta = 0.01$, (dot-dashed) 0.1 (long-dashed) and 1 (solid) (left panel). (b) $\alpha_\Pi = 0.05$ is chosen and $\zeta = 1$ (dot-dashed), 5 (long-dashed) and 10 (solid) (right panel).

It would be of interest, to concentrate on the modification of the parameter space for shock formation when cooling is enhanced. In Figs. 10(a) and 10(b) this is shown. In Fig. 10(a), $\alpha_\Pi = 0.01$ is chosen and the cooling parameters are $\zeta = 0.01$, (dot-dashed) 0.1 (long-dashed) and 1 (solid). We note that the region of the parameter space shifts to include negative energy regions as well. (For instance, for $\alpha_\Pi = 0$ and $\zeta = 0$, the parameter space contains only positive energy.) In Fig. 10(b), viscosity parameter is increased to $\alpha_\Pi = 0.05$. This causes a shrinkage in the parameter space. The cooling parameters are $\zeta = 1$ (dot-dashed), 5 (long-dashed) and 10 (solid) respectively. In this case, the parameter space shrinks drastically when cooling is enhanced.

7. Sonic Points for Super-Keplerian Flows?

It is generally accepted that at the sonic points, the flow must be sub-Keplerian.[3] However, if the cooling is very efficient, this requirement may be violated. In Fig. 11, we show that when ζ is very high, of the order of a few hundreds, the sonic point may have angular momentum *above* the Keplerian distribution (dotted curve). Particularly important is that this is possible if the sonic point is located near the black hole horizon. The implication of this is not obvious. Does it mean that very cold flow *can* be Keplerian or super-Keplerian throughout its journey? If so, can it spin up the black hole faster that what is presumed so far? This point is to be addressed in future.

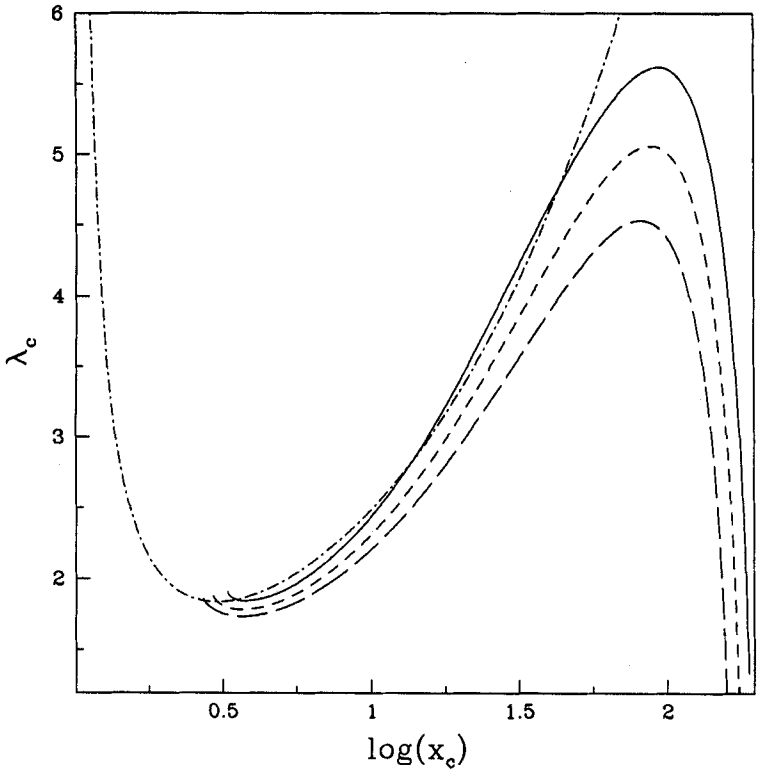

Fig. 11. Example of parameters which produce transonic solutions with super-Keplerian angular momentum. The dot-dashed curve is the Keplerian distribution. Solid curves, from the bottom to the top, are for $\zeta = 400$, 500 and 600 respectively.

8. Critical Cooling and Sub-Division of the Parameter Space

We have already indicated that cooling and heating have opposite effects in deciding the solution topologies, but one does not *exactly* cancel the other effect. When the cooling is enhanced for a given viscosity parameter, the possibility of shock formation is eventually reduced. This is shown in Fig. 12. Here the critical cooling parameter $\zeta = \zeta_{\rm crit}$ is plotted against the specific angular momentum for two different viscosity parameters. Solid curve is for $\alpha_\Pi = 0.01$ and the dashed curve is for $\alpha_\Pi = 0.05$. All possible inner sonic points are considered. The region below the curve contains topologies which are closed and therefore standing or oscillating shocks could be possible while the region above the curve allows solutions with open topologies. We note that for smaller $\lambda_{\rm in}$, the critical cooling factor is smaller. This is expected since the possibility of shock formation is enhanced with larger $\lambda_{\rm in}$ in general. When α_Π is higher $\zeta_{\rm crit}$ is lower. This indicates a general reduction of the parameter space due to higher viscosity[1] which is not totally compensated for by cooling effects.

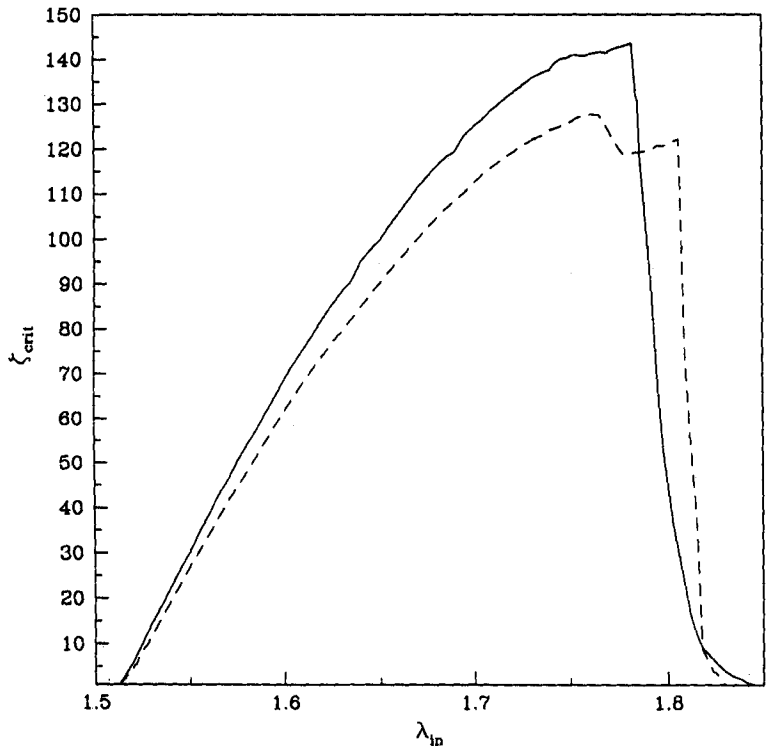

Fig. 12. The variation of the critical cooling parameter as a function of the specific angular momentum at the inner sonic point for two different viscosity parameters. Solid curve is for $\alpha_\Pi = 0.01$ and the dashed curve is for $\alpha_\Pi = 0.05$. The region below the curve contains topologies which are closed and therefore standing or oscillating shocks could be possible while the region above the curve allows solutions with open topologies.

9. Concluding Remarks

In this paper, we studied the dissipative accretion flow in presence of viscous heating and bremsstrahlung cooling processes. Viscosity tends to heat the flow, thereby reducing the Mach number. Cooling, on the other hand, increases the Mach number. Thus, formation of shock, which involves a supersonic to subsonic transition is affected by heating and cooling. We classified the parameter space in terms of whether three sonic points or shocks can form or not. We discovered a completely new topology in which matter, coming from a large distance, is connected to the black hole horizon as a normal solution, but it has multiple valued Mach number solution. We find that cooling can 'undo' the effect of heating on topological properties, only to a certain extent. If the viscosity is high enough, then no matter how much cooling is used, the parameter space shrinks. We have also found that for a given set of flow parameters, there is always a critical cooling factor which separates the parameter space into closed regions, one with a closed and the other with an open topology.

It is generally believed that only the sub-Keplerian flows can pass through the sonic points. However, we find that when the flow is very strongly cooled, even super-Keplerian flows can also pass through the inner sonic point. This is a new result and may be significant in evolution of the spin of the accretion black holes.

Acknowledgment

This work is partly supported by a project (Grant No. SP/S2/K-15/2001) funded by Department of Science and Technology (DST).

References

1. S. K. Chakrabarti and S. Das, *Mon. Not. R. Astron. Soc.* **349**, 649 (2004).
2. S. K. Chakrabarti, *Astrophys. J.* **464**, 664 (1996).
3. S. K. Chakrabarti, *Astrophys. J.* **362**, 406 (1990).
4. S. K. Chakrabarti and L. G. Titarchuk, *Astrophys. J.* **455**, 623 (1995).
5. D. Molteni, H. Sponholz and S. K. Chakrabarti, *Astrophys. J.* **457**, 805 (1996).
6. S. K. Chakrabarti and S. G. Manickam, *Astrophys. J.* **531**, L41 (2000).
7. D. M. Smith, W. A. Heindl, C. B. Markwardt and J. H. Swank, *Astrophys. J.* **554**, L41 (2001).
8. D. M. Smith, W. A. Heindl and J. H. Swank, *Astrophys. J.* **569**, 362 (2002).
9. B. Paczyński and P. J. Wiita, *Astron. & Astrophys.* **88**, 23 (1980).
10. S. K. Chakrabarti, *Theory of Transonic Astrophysical Flows* (World Scientific, Singapore, 1990).
11. R. Matsumoto, S. Kato, J. Fukue and A. T. Okazaki, *Pub. Astron. Soc. Japan* **36**, 7 (1984).
12. S. K. Chakrabarti, *Astrophys. J.* **347**, 365 (1989).
13. S. Das, I. Chattopadhyay and S. K. Chakrabarti, *Astrophys. J.* **557**, 983 (2001).
14. L. D. Landau and E. D. Lifshitz, *Fluid Mechanics* (Pergamon, New York, 1959).